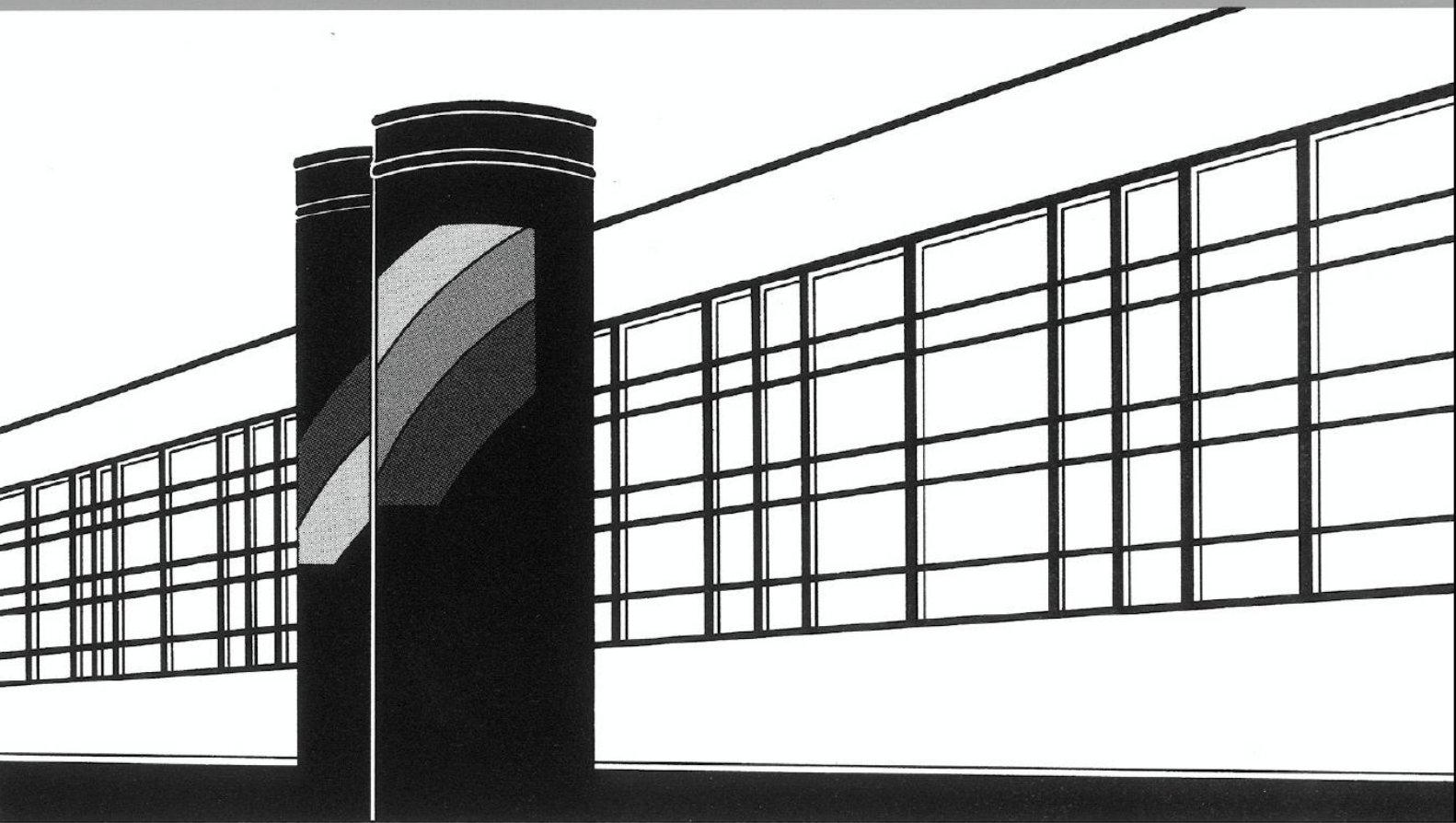


Universität Stuttgart



Institut für Wasser- und Umweltsystemmodellierung

Mitteilungen



Heft 270 Moritz Thom

Towards a Better Understanding of the
Biostabilization Mechanisms of Sediment
Beds

Towards a Better Understanding of the Biostabilization Mechanisms of Sediment Beds

von der Fakultät Bau- und Umweltingenieurwissenschaften der
Universität Stuttgart zur Erlangung der Würde eines Doktor-Ingenieurs
(Dr.-Ing.) genehmigte Abhandlung

vorgelegt von
Moritz Thom
aus Neuss, Deutschland

Hauptberichter: Prof. Dr.-Ing. Silke Wieprecht
Mitberichter: Prof. Dr.-Ing. Jochen Aberle

Tag der mündlichen Prüfung: 17. Juli 2019

Institut für Wasser- und Umweltsystemmodellierung
der Universität Stuttgart
2019

Heft 270 **Towards a Better
Understanding of the
Biostabilization Mechanisms
of Sediment Beds**

von
Dr.-Ing.
Moritz Thom

Eigenverlag des Instituts für Wasser- und Umweltsystemmodellierung
der Universität Stuttgart

D93 Towards a Better Understanding of the Biostabilization Mechanisms of Sediment Beds

Bibliografische Information der Deutschen Nationalbibliothek

Die Deutsche Nationalbibliothek verzeichnet diese Publikation in der Deutschen Nationalbibliografie; detaillierte bibliografische Daten sind im Internet über <http://www.d-nb.de> abrufbar

Thom, Moritz:

Towards a Better Understanding of the Biostabilization Mechanisms of Sediment Beds, Universität Stuttgart. - Stuttgart: Institut für Wasser- und Umweltsystemmodellierung, 2019

(Mitteilungen Institut für Wasser- und Umweltsystemmodellierung, Universität Stuttgart: H. 270)

Zugl.: Stuttgart, Univ., Diss., 2019

ISBN 978-3-942036-74-0

NE: Institut für Wasser- und Umweltsystemmodellierung <Stuttgart>: Mitteilungen

Gegen Vervielfältigung und Übersetzung bestehen keine Einwände, es wird lediglich um Quellenangabe gebeten.

Herausgegeben 2019 vom Eigenverlag des Instituts für Wasser- und Umweltsystemmodellierung

Druck: DCC Kästl e.K., Ostfildern

Danksagung

Zunächst einmal möchte ich mich bei Frau Professor Wieprecht bedanken. Sie haben mir während meiner Promotionsphase viele Freiheiten gelassen und gleichzeitig meine Motivation gefördert um dann aber doch an entscheidenden Stellen einzugreifen. Nur so konnte ich mein Ziel konsequent verfolgen.

Dann würde ich mich gerne bei Herrn Professor Jochen Aberle bedanken, für unsere anhaltenden und sehr fruchtbaren Diskussionen während diverser Konferenzen und für die wertvollen Tipps die du mir gegeben hast.

Ein weiterer Dank geht an Frau Dr. Gabriele Hartmann, dafür, dass du mir dabei geholfen hast, die vielen organisatorischen und bürokratischen Hürden rund um meine Promotion ein wenig angenehmer zu machen.

Ein besonderer Dank geht an Frau Dr. Sabine Gerbersdorf für die Betreuung meiner Arbeit und für unendlich lange kurze Gespräche, ob im Büro oder per Telefon. Kurze Fragen wurden so zu endlosen und sehr interessanten Diskussionen und ich hoffe sehr darauf, dass dies auch in Zukunft so bleiben wird.

Ich danke auch allen Kollegen und Kolleginnen des Lehrstuhls die ich während meiner Promotionsphase kennenlernen durfte. Durch euch hat das Promovieren richtig Spass gemacht und ich hoffe wir bleiben in Kontakt. Ein spezieller Dank geht hierbei an meinen direkten Kollegen Dr. Holger Schmidt für die teils sehr inspirierenden Gespräche. Ich möchte auch den Werkstätten einen besonderen Dank zukommen lassen. Eure Arbeit hat stets meine Erwartungen bei Weitem übertroffen und ohne eure Hilfe hätten viele meiner Ideen gar nicht erst umgesetzt werden können. Gleiches gilt auch für viele Hiwis, die mich bei den Arbeiten unterstützt haben.

Dann danke ich noch Dr. Marc Scheffler, der als exzellenter Physiker und netter Kollege, die Geduld hatte sich mit den teils sehr unterschiedlichen Sichtweisen von Ingenieuren und Biologen auseinanderzusetzen und mich in die komplexe Welt des Magnetismus einzuführen. Auch hier hoffe ich, dass der Kontakt aufrecht erhalten bleibt.

Dann danke ich auch meinen Eltern, die mich auf meinem langen Weg zur Promotion immer unterstützt aber auch immer mit mir gelitten haben.

Der mit Abstand allergrößte Dank allerdings, geht an meine kleine Familie und allen voran an Ursula. Es ist keinesfalls selbstverständlich eine solche kompromisslose Unterstützung und Geduld zu erfahren. Ich bin euch unendlich dankbar und widme euch meine Dissertation.

"Hätte ich drei Wünsche frei, dann wüsst ich grad keinen"

- Weiss, Wunderlich, Heinzmann, Schuster, Manglus -

Notice

All images in this thesis are either produced by the author or reproduced or modified with permission from the respective copyright holders.

Table of contents

List of Figures	viii
List of Tables	xiv
Notations	xvii
Abbreviations	xxi
Abstract	xxv
Zusammenfassung	xxix
A BACKGROUND AND BASICS	1
A.1 Introduction	1
A.1.1 Background	1
A.1.2 Research gaps	2
A.1.3 Research aims	6
A.1.4 Outline of the work	8
A.2 Background information on biofilms in aquatic systems	10
A.3 Background information on biostabilization	13
A.4 Environmental impacts on biofilm growth	17
A.4.1 Abiotic impacts	17
A.4.2 Biotic impacts	19
A.5 Biofilm mechanics and material properties	20
A.5.1 Rheology	20
A.5.2 Adhesion and cohesion	22
A.5.3 Methods to determine adhesive properties	24
A.6 The critical shear stress for motion of sediments	31
A.6.1 The stability of uniform non-cohesive abiotic sediments	33
A.6.2 The stability of biostabilized sediments	38
A.6.3 The modified Shields approach after Righetti and Lucarelli (2007)	42
B BIOSTABILIZATION UNDER DIFFERENT ENVIRONMENTAL CONDITIONS	47
B.1 The experimental setup	49
B.1.1 The setup for the cultivation of biofilms on artificial sediments	49

B.1.2	Validation of the hydrodynamic regime	51
B.1.3	Erosion measurements in the SETEG Flume	52
B.2	The experimental program of the conducted experiments	53
B.3	Evaluation of the erosion measurements	54
B.3.1	Impact of hydrodynamics, light intensity and seasonality	54
B.3.2	The mechanical process of erosion	58
B.4	Discussion on erosion measurements	60
B.4.1	The impact of environmental conditions on biostabilization in freshwaters	60
B.4.2	The mechanical process of erosion for biostabilized sediments	63
B.5	Conclusions	64
C	AN ADVANCED METHOD TO MEASURE SURFACE ADHESION OF BIOFILMS	67
C.1	The original method to approximate surface adhesion	68
C.1.1	The basic concept	68
C.1.2	Needs for further development	71
C.2	The advanced setup to determine surface adhesion forces (MagPI-IP)	72
C.3	The calibration procedure	74
C.3.1	Electromagnetic forces and magnetic particle properties	75
C.3.2	The calibration of the MagPI-IP device	82
C.4	Data evaluation by image processing	86
C.5	Calculating surface adhesion from the mean pull off force	91
C.6	Evaluating the performance of the MagPI-IP	96
C.6.1	Determination of the reference force on non adhesive surfaces	97
C.6.2	Adhesion forces measured on a surrogate EPS surface	99
C.6.3	Adhesion forces measured on a biofilm surface	100
C.6.4	Comparison to other methods reported in literature	100
C.7	Limitations/uncertainties and needs for further development	101
D	TEMPORAL DEVELOPMENT OF SURFACE ADHESION AND STABILITY	103
D.1	Preliminary considerations	103
D.2	The experimental setup	105
D.2.1	The setup for biofilm cultivation	105
D.2.2	Erosion measurements in the SETEG flume	106
D.2.3	Surface adhesion measurements	106
D.3	The experimental program of the conducted experiments	107
D.4	Evaluation of the experiments	110
D.4.1	Characterization of the temporal development of surface adhesion	110
D.4.2	The development of stability divided in phases	115
D.4.3	The correlation between critical bed shear stress and surface adhesion	117
D.5	Hypotheses on the role of surface adhesion for biostabilization	120
E	APPLICATION OF A THEORETICAL MODEL TO PREDICT BIOSTABILIZATION	123

E.1	Additional methods for the quantification of floc geometry and bulk density	124
E.1.1	Floc size analysis	124
E.1.2	Bulk density analysis	129
E.2	Application of the modified Shields approach	129
E.3	The impact of individual parameters	139
E.4	Limitations and recommendations for further research	142
E.5	Concluding remarks	144
F	CONTINUOUS SURVEY OF BIOFILM TOPOGRAPHY	147
F.1	Setup for topographical measurements and calibration	148
F.1.1	The experimental program of biofilm topography measurements	151
F.2	Evaluation of the temporal changes of biofilm topography	152
F.3	Modified roughness in the erosion flume	156
F.3.1	Comparison of hydraulics between a smooth and a sandpaper bed	157
F.4	Proposed further investigations on biofilm roughness	159
G	SUMMARY, CONCLUSIONS & OUTLOOK	165
	References	169
	Appendix	183
A	Additional materials: MagPI-IP	183
B	Additional methods	193
C	Additional data	195

List of Figures

A.1	Diagrammetric side view representation and photograph of the biofilm-sediment matrix.	16
A.2	Low-temperature scanning electron microscopy (LTSEM) images of sand grains and glass beads covered by EPS	19
A.3	A developing biofilm from the planktonic to the matured stage (from left to right, modified after Vasudevan, 2014)	20
A.4	Seasonal succession of phytoplankton (from Horne & Goldman, 1994).	21
A.5	Different bulk biofilm/EPS responses to applied stress and strain (modified from Guelon et al., 2011).	22
A.6	Schematic drawing of the centrifugation device and the acting forces to measure the adhesion strength of biofilm attached to plates (modified from Ohashi & Harada, 1994).	25
A.7	Diagrammetric representation of the setup to investigate adhesion with a T-shaped probe (modified after Chen et al., 1998)	26
A.8	Schematic drawing of the microject impingement device and forces (from Böl et al., 2013)	27
A.9	Diagrammetric representation of the method to measure adhesion based on atomic force microscopy and applied by Lau et al. (2009)	28
A.10	The measuring principle of the original MagPI after Larson et al. (2009)	30
A.11	Schematic representation of the erosion, transportation, deposition and consolidation cycle and the contribution of biofilms (modified from Gerbersdorf & Wieprecht, 2015)	32
A.12	Forces balance on a spherical sediment at the surface of a bed (modified after Righetti & Lucarelli, 2007)	34
A.13	Popular diagrams relating the mean velocity to sediment transport (after Grabowski, Droppo, & Wharton, 2011)	36
A.14	The Shields diagram (after Raudkivi, 1982)	37
A.15	The relationship between chlorophyll a and the critical bed shear stress studied at different stations located in an intertidal flat (diagram after Le Hir et al., 2007)	40
A.16	Schematic diagram of oscillations of a biofilm-mat caused by fluid flow (modified after Vignaga et al., 2013)	42

A.17 Forces balance on a spherical grain at the surface of a bed considering additionally adhesive forces (modified after Righetti & Lucarelli, 2007)	44
A.18 Comparison between the “traditional” Shields curve and measured values of biostabilized sediments.	46
B.1 The experimental setup for biofilm cultivation	49
B.2 Details of the cultivation setup	50
B.3 Setup for the erosion of biostabilized sediments and applied stepwise increase of forces	52
B.4 Spring and late autumn experiments on the impact of hydrodynamics on τ_c and biostabilization index (BI).	55
B.5 Summer experiments on the impact of light intensity on τ_c and biostabilization index (BI).	56
B.6 Top view of biofilm samples cultivated under the same conditions in the August experiment.	56
B.7 Photographs of biofilm development taken twice a week in the March experiment under three different levels of bed shear stress.	57
B.8 Different biological stabilization mechanisms and erosion processes as observed during the experiments.	58
B.9 Photographs showing the different appearances of biofilms in spring (<i>Left</i> , image from Gerbersdorf & Wieprecht, 2015) and summer (<i>Right</i>).	63
C.1 Basic concept of particle attraction by the MagPI.	68
C.2 Schematic representation of the MagPI system (from Larson et al., 2009) . .	69
C.3 Schematic representation of the novel MagPI-IP system	73
C.4 A typical data set consisting of images captured by the MagPI-IP system. . .	74
C.5 Graph illustrating the relation between the gradient of the magnetic flux density (∇B) and the applied electric current (I) of an electromagnet	76
C.6 Changes of the magnetic flux density with vertical distance from the center of the tip of the electromagnet	77
C.7 Sensitivity of the electromagnetic force to a vertical distance deviation from the targeted distance between electromagnet and ferromagnetic particles (= 4mm)	78
C.8 Changes of the magnetic flux density by horizontal distance of the particles from the centre of the tip	79
C.9 Chains of particles, indicative for an increased propensity for magnetization (photograph from Bierbaum, 2015)	79
C.10 The attraction behavior of two different types of particles by an electromagnet on the same surface	80
C.11 A typical hysteresis plot of a ferromagnetic material	81
C.12 Differences in magnetization of particles with different geometries but manufactured from the same core material	82

C.13 Ferromagnetic particles permanently glued on a PVC cylinder.	83
C.14 Methods used during calibration.	84
C.15 Calibration curve illustrating the relation between the tensile force exerted by the electromagnet on one particle and the applied gradient of MFD	85
C.16 Calibration curve illustrating the relation between the tensile force exerted by the electromagnet on one particle and the applied electric current	85
C.17 The coefficients of variation at the applied increments of tensile forces	86
C.18 Step 1 of the image processing: Identification of the area of interest (AoI).	87
C.19 Step 2 of the image processing: Screenshot showing the initial picture and the same picture converted to binary images for different thresholds	88
C.20 Step 3 and 4 of the image processing: Screenshot showing the surface area covered by particles (in px) plotted against the applied electric current	89
C.21 Screenshot showing the original images as captured by the MagPI-IP device (colored) and the corresponding computed binary images which are further processed	89
C.22 Step 5a of the image processing. The final results are presented. This graph illustrates the final relationship between SCP and I (in red). The blue curve is the unprocessed raw data.	90
C.23 Step 5b of the image processing. The final results are presented. Bar graph of the decrease of SCP at each increment of electric current.	90
C.24 A refined model of the impact of surface adhesion on the pull off force.	92
C.25 Graph showing the values of the reciprocal area of contact (ζ) for different depths of penetration	94
C.26 Determination of the r/h value for particles spread on a silicone surface by image analysis.	95
C.27 Ferromagnetic particles left on an adhesive surface for different periods of time before measuring the pull off force to determine the h/d ratio	96
C.28 Example of an individual measurement on a flat glass slide without adhesion	98
C.29 Example of an individual measurement on glass beads without adhesion	98
C.30 Surface adhesion of an EPS surrogate (Xanthan gum) at different concentrations.	99
D.1 A comparison between measured surface adhesion and adhesion responsible for resisting the attacking forces in the event of erosion	104
D.2 Generic plot of the development of mean surface adhesion forces in the Jul14 experiment	111
D.3 Generic plot of the development of mean surface adhesion forces in the Mar14 experiment	111
D.4 Generic plot of the development of mean surface adhesion forces in the Mar15* experiment	112
D.5 Temporal development of $\tau_{c,bio}$ as typical for the Jul14 experiment.	116

D.6	Temporal development of $\tau_{c,bio}$ as typical for the Mar14 experiment	116
D.7	Temporal development of $\tau_{c,bio}$ as typical for the Mar15* experiment	117
D.8	The interrelationship between erosion threshold and surface adhesion in Phase I as measured in experiment Mar14.	118
D.9	The correlation between erosion threshold and surface adhesion in Phase II as measured in experiments Mar14 and Jul14	119
D.10	The interrelationship between erosion threshold and surface adhesion in Phase III as measured in experiments Jul14 and Mar15*.	119
E.1	Definition sketch of important parameters considered in the physics-based model of Righetti and Lucarelli (2007)	124
E.2	Schematic drawing of the Gust chamber (Gust, 1990) used for the collection of eroded flocs	125
E.3	The settling column and camera system to investigate floc geometries and settling velocity	126
E.4	Example of processing the images of settling flocs (screenshots)	127
E.5	Example of histogram plot showing the distribution of spherical-equivalent diameters from one eroded biofilm sample	128
E.6	Temporal development of eroded floc diameters D for biofilms cultivated under low flow velocities	130
E.7	Temporal development of eroded floc diameters D for biofilms cultivated under high flow velocities	130
E.8	Temporal development of measured floc bulk density in the Jul14 experiment	131
E.9	Comparison between the traditional Shields parameter and experimental results of Jul14.	133
E.10	The correlation between calculated effective adhesion and measured surface adhesion in Jul14	137
E.11	The critical Shields parameter at different values of surface adhesion	140
E.12	The critical Shields parameter at different values of aggregate bulk density	141
E.13	Graph comparing the measured and predicted erosion threshold by using the parameterization of the modified Shields equation based on the measured surface adhesion values	144
E.14	Conceptual model of important mechanical impacts on biostabilization	146
F.1	Side view image of a biofilm from one of the experiments (photograph by Bojan Skodic). Contour lines represent the biofilm topography qualitatively	147
F.2	The developed measuring device for surveillance of submerged biofilm topography and an exactly milled stairway for calibration	149
F.3	The basic principle of laser triangulation (modified after Löffler-Mang, 2012)	150
F.4	Graph comparing the real heights of the submerged milled stairway with the digital output of the laser triangulation sensor	151

F.5	Development of biofilm topography over time of growth in two experiments . . .	152
F.6	Mean elevation and standard deviation of four different biofilm DEMs over time of growth	155
F.7	Implementation of a sandpaper roughness in the erosion flume to adapt the inlet section with a biofilm similar roughness	156
F.8	Velocity distribution in flow direction over depth in the erosion flume (reference level is the bottom of the flume $z = 0$) at different discharges	158
F.9	Shear stress distribution in flow direction over depth in the erosion flume at different discharges	158
F.10	Updated and original calibration curve (τ_b versus Q) for the erosion flume over a rough and a smooth bed	159
F.11	Qualitative comparison between a biofilm and a sandpaper topography	160
F.12	Histograms of elevations measured on a generic biofilm surface and a sandpaper.	161
F.13	Second-order structure functions for a sandpaper and a biofilm topography in flow and transverse direction	162
A.1	Circuit diagram of the “filter” for smoothing the PWM signal to control the increase of electric current	183
A.2	Image of the Electromagnet “Ersatz1000” (from Bierbaum, 2015)	184
A.3	Mechanical characteristics of the electromagnet “Ersatz1000” as determined in the calibration procedure	184
A.4	Image of the Electromagnet “Original1000” (from Bierbaum, 2015)	185
A.5	Mechanical characteristics of the electromagnet “Original1000” as determined in the calibration procedure	185
A.6	Image of the Electromagnet “Original1500” (equivalent to the “Ersatz1500”) (from Bierbaum, 2015)	186
A.7	Mechanical characteristics of the electromagnet “Ersatz1500” as determined in the calibration procedure	186
A.8	Flow chart of the general procedure to control the MagPI-IP and conduct measurements	187
A.9	The basic functioning principle of the Arduino software to control the changes in electric current and communication with the Raspberry PI to take pictures.	188
A.10	The basic functioning principle of the MATLAB [®] code to process images (part 1)	189
A.11	The basic functioning principle of the MATLAB [®] code to process images (part 2)	190
B.1	Developed form to note all relevant processes of erosion.	194
C.1	Mar13: Critical bed shear stress versus time of growth.	198
C.2	May13: Critical bed shear stress versus time of growth.	199

C.3 Jul13: Critical bed shear stress versus time of growth	200
C.4 Aug13: Critical bed shear stress versus time of growth	201
C.5 Nov13: Critical bed shear stress versus time of growth	202
C.6 Mar13: Critical bed shear stress versus time of growth	203
C.7 Jul14: Critical bed shear stress versus time of growth	204
C.8 Mar15*: Critical bed shear stress versus time of growth	205
C.9 Mar14: Surface adhesion versus time of growth	206
C.10 Jul14: Surface adhesion versus time of growth	207
C.11 Mar15*: Surface adhesion versus time of growth	208
C.12 Mar14, Jul14, Mar15* experiments: Critical bed shear stress versus surface adhesion	209

List of Tables

A.1	Different definitions for the term “biostabilization” from literature	13
A.2	An overview on the results of biostabilization from literature (modified and updated from Vignaga, 2012)	14
A.3	Overview on different methods to measure biofilm-adhesion forces and results from literature (updated from Böl et al., 2013).	29
B.1	Boundary conditions applied in the experiments and the specific notations used in the following text.	50
B.2	Overview on the experiments with objectives and applied boundary conditions.	53
B.3	The three predominant erosion processes	59
C.1	Summary of results of surface adhesion measurements on different surfaces and random positions.	97
C.2	Updated overview on different methods to measure biofilm-adhesion forces and results from literature (updated from Böl et al., 2013).	101
D.1	Boundary conditions applied in the experiments and the specific notations used in the following text	106
D.2	Detailed overview on experiments (Mar14, Jul14, Mar15*), their study objectives and applied boundary conditions	108
D.3	Summary of results on surface adhesion and erosion threshold development over time for the experiments Jul14, Mar14, Mar15*	114
E.1	Measured input parameters for the modified Shields equation, calculated results and additional information (Jul14)	134
E.2	Parameters, quality and valid range of the linear fits between the calculated effective adhesion and the measured surface adhesion in Jul14	137
F.1	Details of the topographical survey of four biofilm surfaces in Jul14	154
F.2	Sandpaper with different grit sizes to represent biofilm roughness.	156
F.3	Statistical moments of elevations, measured on a generic biofilm surface and a sandpaper	160
A.1	General information on materials: “Ersatz1000” (from Bierbaum, 2015)	184
A.2	General information on materials: “Original1000” (from Bierbaum, 2015) . . .	185
A.3	General information on materials: “Ersatz1500” (from Bierbaum, 2015)	186

A.4	Input files needed to define important parameters for the MATLAB® image processing code.	191
C.1	Overview on the experiments: Mar13, May13, Jul13, Aug13, Nov13, their study objectives and applied boundary conditions	196
C.2	Overview on the experiments: Mar14, Jul14, Mar15*, their study objectives and applied boundary conditions	197
C.3	Detailed experimental program of Mar15*	197

Notations

The following symbols are used in this thesis:

Symbol	Unit	Description
a	[px]	Visible vertical extent of a particle on a silicone surface
a_1, a_2, a, b	[m]	Distances in the balance of forces
A	[m ²]	Surface area
A_c	[mm ²]	Area of contact
A_{eff}	[N/m ²]	Effective adhesion or adhesion coefficient (Righetti & Lucarelli, 2007)
A_{fp}	[mm ²]	Averaged surface area of one ferromagnetic particle
$A_{s,30}$	[N/m ²]	Surface adhesion as measured in this study
$B, \nabla B$	[mT], [mT/mm]	Magnetic flux density, gradient of the magnetic flux density
B_{ext}, B_{int}	[mT]	External and internal magnetic field
c	[N/m]	Cohesion coefficient
c_1, C_1, c_2	[–]	Coefficients
C_{XG}	[g/l]	Concentration of Xanthan gum powder dissolved in water
d	[mm]	Particle diameter
d^*	[–]	Particle dimensionless characteristic diameter
D	[mm]	Equivalent Diameter of an eroded macroaggregate
D^*	[–]	Aggregate dimensionless characteristic diameter
D_{50}	[mm]	Median diameter of the particle size distribution
d_f	[mm]	Spherical-equivalent diameter
D_{G2}	[mm ²]	Second order structure function
$d_{spot,min}$	[mm]	Minimum horizontal extent of the elliptical laser spot

Symbol	Unit	Description
f	[N/m ²]	Adhesion strength (Ohashi & Harada, 1994)
F	[N]	Horizontal force to pull away a biofilm (Chen et al., 2005)
F_c	[N]	Centripetal force (Ohashi & Harada, 1994)
F_1	[N/m ²]	Lift force at bed due to buoyancy
F_A	[μ N/particle]	Particle-specific adhesive force
F_{ad}	[μ N/particle]	Net mean pull off force due to adhesion of a single ferromagnetic particle ($F_{ad} = F_m - F_{m,0}$)
F_{adh}	[N]	Adhesion force as defined by Lau et al. (2009)
F_D	[N]	Drag force
F_{em}	[μ N/particle]	Tensile force on a ferromagnetic particle exerted by the electromagnet
F_G	[N]	Particle submerged weight force
F'_G	[N/particle]	Particle-specific submerged weight force (Dade et al., 1992)
F_L	[N]	Lift force
F_m	[μ N/particle]	Mean pull off force needed to attract an adhered magnetic particle
$F_{m,0}$	[μ N/particle]	Mean pull off force needed to attract a not-adhered magnetic particle
F_{scale}	[N]	Weight force measured by a scale
g_1	[m/s ²]	Centrifugal acceleration (Ohashi & Harada, 1994)
g	[m/s ²]	Acceleration due to gravity
h_1, h_2	[mm]	Vertical distances between Hall probe and electromagnet
h, h_{mean}	[mm]	Depth of penetration, mean depth of penetration
I	[mA]	Electric Current
Ku	[–]	Kurtosis
l_x	[mm]	Lag in flow direction
l_y	[mm]	Lag in transverse direction
M	[A/m]	Magnetization
m_1, m_2, m_3	[g]	Different weights in pycnometer analysis
M, N	[–]	Number of measuring points of bed elevations in flow/transverse direction
m, n	[–]	Variables in second order structure function
m	[kg]	Mass

Symbol	Unit	Description
O_{sensor}	[-]	Digital output of the laser triangulation sensor
P_{min}, P_0, P_{max}	[m]	Minimal, stand off and maximum distance to laser
P'_{min}, P'_0, P'_{max}	[m]	Minimal, stand off and maximum distance to laser's detector
Q	[l/s]	Discharge
r	[N/m ² d]	Adhesion rate
r_{mean}	[mm]	Mean radius of the ferromagnetic particles
Re^*	[-]	Particle Reynolds number
Sk	[-]	Skewness
SCP	[px], [%]	Surface area covered by particles
t	[d]	Time of Growth
t_P, t_Q	[s]	Respective time to remove a biofilm (Chen et al., 2005)
u	[m/s]	Fluid velocity in flow direction
u^*	[m/s]	Shear velocity
v	[m/s]	Fluid velocity in vertical direction
v	[m/s ²]	Probe pulling speed (Chen et al., 2005)
W	[J/m ²]	Work required to remove a biofilm from a surface (Chen et al., 2005)
z_{real}	[mm]	Actual or real height of the calibration stairway

The following Greek symbols are used in this thesis:

Symbol	Unit	Description
α	[°]	Angle between a horizontal line and direction of movement of a particle
α_3	[–]	Particle shape factor
α_A	[–]	Fraction of a surface area covered by a biofilm (Chen et al., 2005)
δ	[mm]	Layer thickness where van der Waals forces act (Righetti & Lucarelli, 2007)
$\delta x, \delta y$	[mm]	Sampling interval in flow direction, sampling interval in transverse direction
Δ	[–]	Relative density of the eroded particle/aggregate
Θ_C	[–]	Critical Shields parameter
Θ_{C0}	[–]	Traditional abiotic non-cohesive expression of the Shields parameter
Θ_{CA}	[–]	Parameter representing the additional contributions to the critical Shields parameter due to adhesive forces
Θ_{CC}	[–]	Parameter representing the additional contributions to the critical Shields parameter due to cohesive forces
μ_0	[H/m]	Magnetic permeability
ν	[m ² /s]	Kinematic viscosity of water
ρ	[kg/m ³]	Density of water
ρ_b	[kg/m ³]	Bulk density of an eroded aggregate
ρ_s	[kg/m ³]	Density of a particle
$\rho_{w,t}$	[t/m ³]	Density of the water at the fluid temperature (pycnometer analysis)
σ_z	[mm]	Standard deviation of bed elevations
ς	[1/mm ²]	Reciprocal lateral area of a sphere
τ_b	[N/m ²]	Bed shear stress
τ_c	[N/m ²]	Critical bed shear stress
$\tau_{c,0}$	[N/m ²]	Critical bed shear stress for abiotic sediments
$\tau_{c,bio}$	[N/m ²]	Critical bed shear stress for biostabilized sediments
χ	[m ³ /kg]	Magnetic susceptibility

Abbreviations

The following abbreviations are used in this thesis:

Abbreviation	Description
2A	Formation of a second layer beneath the surface (erosion process)
A	Crust eroded in aggregates (erosion process)
ADV	Acoustic Doppler Velocimetry
AFM	Atomic Force Microscopy
AoI	Area of Interest
B	Bubble entrainment (erosion process)
BI	Biostabilization Index
BIO16, BIO48	Natural biofilm at the age of 16/48 days
BLANK	Blank surface
C	Surficial carpet-like erosion (erosion process)
CFD	Computational Fluid Dynamics
<i>chl a</i>	<i>Chlorophyll a</i>
CSM	Cohesive Strength Meter
CV	Coefficient of Variation
DEM	Digital Elevation Model
DWDS	Drinking Water Distribution Systems
EPS	Extracellular Polymeric Substances
ETDC	Erosion, Transport, Deposition and Consolidation cycle
FP	Ferromagnetic Particle
fps	Frames Per Second
ID	Identifier
JKR	Johnson, Kendall and Roberts - theory

Abbreviation	Description
LDA	Laser Doppler Anemometry
LED	Light-Emitting Diode
LI	Light Intensity
LTSEM	Low-Temperature Scanning Electron Microscopy
MagPI	Magnetic Particle Induction
MagPI-IP	Magnetic Particle Induction - Image Processing
MFD	Magnetic Flux Density
n	Number of measurements
OM	Organic Matter
PAR	Photosynthetic Active Radiation
PCA	Principle Component Analysis
Ph.	Phase (categorized by surface adhesion)
PWM	Pulse-Width Modulation
rpm	Revolutions Per Minute
S	Individual particle movement (erosion process)
SCP	Surface area Covered by Particles
SD	Standard Deviation
SE	Standard Error
SETEG	Strömungskanal zur Ermittlung der tiefenabhängigen Erosionsstabilität von Gewässersedimenten
SfM	Structure From Motion
USDA	United States Department of Agriculture
XG	Xanthan Gum

The following abbreviations are used for the experiments:

Abbreviation	Description
Mar13	Experiment in March 2013
May13	Experiment in May 2013
Jul13	Experiment in July 2013
Aug13	Experiment in August 2013
Nov13	Experiment in November 2013
Mar14	Experiment in March 2014
Jul14	Experiment in July 2014
Mar15	Experiment in March 2015

Abstract

The stability of sediments exposed to the fluid forces is a key research topic in hydraulic engineering and also has considerable implications for the ecological functioning of aquatic systems. While several abiotic properties of the mineral grains influence the stability (geometry, density) it is nowadays increasingly recognized that biology can influence the sediment stability likewise. In this context, biofilms which are the study objective of this thesis play an important role. Biofilms, comprising e.g. bacteria, microalgae and their secreted substances, grow in-between and on top of surficial sediments and act like a natural glue. Even though these glueing effects can lead to considerable sediment stabilization, a prediction of this “biostabilization” potential is impeded so far due to a lack of a proper understanding of the underlying mechanics.

Studying biostabilization therefore requires fundamental laboratory studies in which the complex interactions between environmental conditions and growth, the impact of spatial/temporal variability and the mechanical forces that lead to a strengthening of the sediment, are investigated systematically. The objectives of this thesis are to a) study the impact of environmental conditions on biostabilization, b) develop advanced methods to measure important parameters and provide suitable experimental programs and c) provide data from robust measurements on mechanical properties.

Biofilms are cultivated on glass beads in a sophisticated flume setup using natural river water as an inoculum. In a first set of experiments the biostabilization potential of biofilms exposed to different defined environmental conditions (hydrodynamics, light intensity and seasonality) is investigated by determination of the critical bed shear stress in a straight erosion flume (SETEG). The most striking differences in biostabilization occurred between seasons with the highest values in spring and the lowest in late autumn. The temporal development of biostabilization and observed biofilm growth is further influenced by the hydrodynamic conditions during cultivation even though the effects are less than expected. Interestingly, no substantial biostabilization effect is detected where biofilms are cultivated in darkness, possibly a result of slower development. Generally it is found that the biostabilization effect is highly heterogeneous, both temporal and spatial which underlines the need for a better understanding of the underlying mechanisms and mechanical forces in biostabilization.

One of the mechanical forces which are frequently made responsible for the biostabilization effect but which is only very poorly studied is the adhesion force. The adhesion force is the binding force between the sticky EPS and the sediments. To investigate these adhesion forces a promising method (the MagPI - Magnetic Particle Induction) is further developed and applied in several experiments. The primary objective of this advanced method (called MagPI-IP for Magnetic Particle Induction - Image Processing) is to measure the surface adhesion in a mechanical unit [N/m^2] to allow the results to be used in mechanical models to predict biostabilization. The device consists of an electromagnet which attracts magnetic particles from an adhesive surface and an elaborate procedure to follow the attraction of these particles. A calibration procedure is presented which relates the electromagnetic force to the desired mechanical force which, in combination with a partly automation and an image processing software, allows to measure adhesion forces on the surface of biofilms in a quick, reproducible and highly detailed way.

This novel approach is applied in three experiments aiming at characterizing the temporal development of surface adhesion forces during the growth of biofilms. Interestingly, the development of surface adhesion forces follows a similar trend as is already observed for the critical bed shear stress (as measured with the SETEG flume) indicating a possible relationship between both parameters.

From the adhesion and erosion measurements it is indicated that the here investigated biofilms are strongly adhesive with adhesion forces exceeding the weight force of sediments by up to 590 % and enhancing the stability by up to a factor of 10 as compared to the abiotic sediment.

Consequently, and to the authors' knowledge for the first time, the adhesion data is used in a theoretical mechanical model to predict the biostabilization potential and unravel the applicability of this novel approach. It is demonstrated that the model produces reasonable results for relatively young biofilms while for older biofilms, which are often structurally different, other approaches should be considered. Furthermore it is shown that besides adhesion forces other parameters play an equally or even more important role. The most important is the size of the eroded flocs but also the bulk density of these flocs. In principle it is indicated that predicting the stability by physical measurements should be possible even though more data is needed to finally confirm the applicability of the model.

Finally, a method is developed to measure the topographical changes of developing biofilms under water on a sub-millimeter scale. A laser triangulation sensor is mounted on a movable rack and a housing is constructed which allows the biofilm to be submerged during the measurements to prevent it from desiccation. It is found that the first topographical changes occur after two weeks with a steep increase in roughness before it reaches a level of saturation. The results are used to improve the accuracy of the erosion measurements.

Keywords: Biostabilization, environmental conditions, biofilm, critical bed shear stress, bioadhesion, biofilm topography.

Zusammenfassung

Die Frage nach dem Bewegungsbeginn von Sedimenten, also ab welchen Strömungskräften sich Sedimente, die sich auf einer Gewässersohle befinden, in Bewegung setzen, ist ein zentraler Aspekt des Wasserbaus. Während man diesen Bewegungsbeginn unter bestimmten Randbedingungen ausreichend genau mithilfe von Formeln ermitteln kann, ist dies bislang kaum für Sedimente möglich, die entweder sehr fein oder biologisch stabilisiert sind. Obwohl mittlerweile bekannt ist, dass Biofilme, bestehend aus Bakterien, Mikroalgen und deren Ausscheidungsprodukten, einen enormen Einfluss auf die Sedimentstabilität haben können, fehlt ein grundlegendes Verständnis für die mit der sogenannten "Biostabilisierung" zusammenhängenden mechanischen Prozesse.

In der vorliegenden Arbeit werden Ergebnisse von Laboruntersuchungen an Biofilmen, die unter kontrollierten Bedingungen aufgewachsen sind, analysiert und Methoden entwickelt, mit dem Ziel, ein besseres Verständnis für die, der Biostabilisierung zugrundeliegenden mechanischen Prozesse zu erlangen. Im Speziellen werden a) die Einflüsse unterschiedlicher Umweltbedingungen (Hydrodynamik, Lichtintensität) auf die stabilisierende Wirkung von Biofilmen untersucht, b) Messmethoden und -abläufe (weiter-) entwickelt, um wichtige (mechanische) Parameter zu bestimmen, und c) Daten erhoben und im Kontext der Biostabilisierung diskutiert.

In den Laboruntersuchungen werden Biofilme in eigens hierfür entwickelten Fließrinnen kultiviert. Hierzu wird natürliches Flusswasser in sechs baugleichen Rinnen über einen längeren Zeitraum (4 - 8 Wochen) zirkuliert. In den Fließrinnen befinden sich Schälchen, die mit künstlichem Sediment (Glaskugeln mit Durchmessern zwischen 0.1 und 0.2 mm) befüllt sind und auf denen die Biofilme nach einer gewissen Zeit wachsen. Sowohl die Fließgeschwindigkeit als auch die Lichtintensität über den Biofilmen kann verändert werden, um unterschiedliche Umweltbedingungen zu simulieren. Die Wassertemperatur wird mithilfe von Wärmetauschern konstant auf 15 °C gehalten. Die Schälchen werden während der Kultivierungsphase entnommen um zum Beispiel mit einem Erosionsgerinne (SETEG) Messungen der Stabilität der Biofilm-Sedimentmatrix durchzuführen.

Die Ergebnisse dieser Untersuchungen zeigen, dass die Jahreszeit, in der das Wasser dem Fluss entnommen wird, den größten Einfluss auf das Biostabilisierungspotential hat.

Im Frühling wird die höchste Stabilität gemessen, während im Spätherbst die Stabilitätszunahme gegenüber den unbewachsenen Sedimenten nahezu vernachlässigbar ist. Die Abhängigkeit von der Jahreszeit kann durch die natürliche Sukzession der Mikroben im Fließgewässer erklärt werden. Dieser saisonale Trend der Biostabilisierung ist grundsätzlich im Einklang mit Ergebnissen aus der Literatur. Trotz deutlicher Erhöhung der Fließgeschwindigkeiten in den Rinnen können keine nennenswerten Stabilitätsunterschiede zwischen Biofilmen, die unterschiedlichen Fließgeschwindigkeiten ausgesetzt sind, festgestellt werden. Zwar kann gezeigt werden, dass Biofilme unter hohen Fließgeschwindigkeiten eine verzögerte Entwicklung haben, jedoch kann die allgemeine Hypothese, dass diese Biofilme stabiler sind als Biofilme, die unter niedrigen Fließgeschwindigkeiten kultiviert werden, nicht bestätigt werden. Entgegen der Erwartungen, haben Biofilme die unter Ausschluß von Licht aufgewachsen sind und somit größtenteils von Bakterien gebildet werden, kaum zu einer Erhöhung der Stabilität beigetragen. Ein Grund hierfür ist möglicherweise, dass diese Biofilme mehr Zeit benötigen, um ihr volles Potential auszuschöpfen. Für zukünftige physikalische Versuchsaufbauten und Durchführungen ist zwingend zu berücksichtigen, dass die Biostabilisierung sowohl räumlich als auch zeitlich starken Schwankungen ausgesetzt ist. Diese Schwankungen erschweren deutlich die Aussagekraft von Einzelexperimenten, sodass empfohlen wird, eine große Anzahl von Replikaten zu untersuchen, um diese dann mit statistischen Mitteln auszuwerten.

Obwohl es mittlerweile grundsätzlich akzeptiert ist, dass die stabilisierende Wirkung von Biofilmen vor allem auf eine "Verklebung" der Sedimentkörner zurückzuführen ist, gibt es kaum Studien, die sich damit befassen, die damit zusammenhängenden mechanischen Kräfte zu messen und mit der Biostabilisierung in Verbindung zu bringen. Grundsätzlich werden die Klebekräfte unterteilt in kohäsive (zwischen gleichen Materialien) und adhäsive Kräfte (zwischen unterschiedlichen Materialien), wobei bislang unklar ist, wie diese Kräfte zur Biostabilisierung beitragen.

Im Fokus dieser Arbeit steht die Messung der adhäsiven Kräfte. Hierzu wird ein bereits existierendes Verfahren (der sogenannte MagPI: Magnetic Particle Induction, nach Larson et al., 2009) angewendet, in dem mithilfe eines Elektromagneten magnetische Partikel, die zuvor auf die Biofilmoberfläche aufgestreut wurden, angezogen werden. Sobald sich diese Partikel von der Oberfläche lösen, ist die Adhäsionskraft des Biofilms überschritten. Mithilfe einer neu entwickelten Kalibrierung und unter Berücksichtigung von weiteren mechanischen Kräften, wurde dieses Verfahren mit dem Ziel weiterentwickelt, die Ergebnisse der Adhäsionsmessungen mechanischen Modellen zur Vorhersage des Stabilisierungspotenzials von Biofilmen zur Verfügung zu stellen. Weiterhin wird das MagPI System noch mit einer Kamera und einer eigens entwickelten Software ausgestattet, um detailliertere Messungen durchführen zu können. Diese Modifikationen tragen auch dazu bei, dass sich die Ergebnisse leichter nachvollziehen lassen und Messungen aus unterschiedlichen Laboren besser

verglichen werden können. Das Potenzial des modifizierten Systems (MagPI-IP: Magnetic Particle Induction-Image Processing) wird mit Hilfe von künstlichem EPS untersucht. Es kann gezeigt werden, dass es sich für die Adhäsionsmessungen auf Biofilmoberflächen gut eignet, eine hohe Sensitivität besitzt und sich Messergebnisse gut reproduzieren lassen.

Um die Oberflächen-Adhäsionskräfte von sich entwickelnden Biofilmen über die Zeit zu messen, wird das MagPI-IP System in drei Experimenten angewendet. Es zeigt sich, dass die Entwicklung der Adhäsionskräfte durch drei Phasen charakterisiert werden kann. In der ersten Phase, die ungefähr zwei Wochen dauert, sind die Adhäsionskräfte gering oder nicht existent ($\lesssim 1.0 \text{ N/m}^2$). Hiernach steigen diese Kräfte linear bis maximal $\approx 7.0 \text{ N/m}^2$ an, um dann in Phase drei um einen konstanten Wert zu schwanken. Besonders interessant hierbei ist, dass sich ein ähnlicher Trend auch aus den Erosionsmessungen ableiten lässt, was wiederum die Hypothese unterstützt, dass die Adhäsionskräfte eine zentrale Rolle in der Biostabilisierung spielen.

Zudem stimmt die Größenordnung der Messwerte mit den Ergebnissen aus einem theoretischen Modell (Righetti & Lucarelli, 2007) überein, sodass dieses näher untersucht wird. Das Modell basiert auf dem bekannten Shields Ansatz, berücksichtigt aber zusätzlich auch noch Adhäsionskräfte und ist dimensionshomogen. Da nahezu keine Informationen über real gemessene Adhäsionskräfte in der Literatur existieren, konnte das Modell bislang nur dazu verwendet werden, um die Adhäsionskräfte zu berechnen, womit auch ein Beweis, dass es mechanisch korrekt ist, bislang nicht erbracht werden konnte.

Basierend auf den Daten eines Experiments und zusätzlichen Informationen über die Stabilität (kritische Sohlschubspannung, Größe der erodierten Aggregate und deren Dichte) wird herausgefunden, dass der modifizierte Shields Ansatz prinzipiell geeignet ist, um die Stabilität ausgehend von Adhäsionsmessungen vorherzusagen, dies jedoch einigen Restriktionen unterliegt. Es hat sich auch gezeigt, dass die beiden anderen Parameter (Aggregatgröße und -dichte) einen ebenso bedeutenden oder sogar größeren Einfluss haben als die Adhäsionskräfte und somit in zukünftigen Experimenten noch genauer untersucht werden müssen.

Ein weiterer Teil dieser Dissertation beschäftigt sich mit der Entwicklung einer Messmethode, um die topographischen Veränderungen von Biofilmoberflächen während des Wachstums bestimmen zu können. Da Biofilme, wenn sie an die Luft kommen, schnell austrocknen und dies zu einer Veränderung ihrer Eigenschaften führen kann, müssen alle Messungen an eingetauchten Biofilmen durchgeführt werden. Hierzu wird ein Laserdistanzsensor verwendet und der zu vermessende Biofilm in einer wassergefüllten Vorrichtung untergebracht. Mithilfe einer Glasscheibe, die auf die Wasseroberfläche aufgesetzt ist, wird zudem verhindert, dass beim Übergang des Lasers zwischen Luft und Wasser Abweichungen durch

eventuelle Wasserbewegungen entstehen. Das System musste hierzu neu kalibriert werden, da es ursprünglich nur für den Einsatz "unter Luft" konzipiert ist. Die topographischen Daten der Biofilmoberflächen zeigen unter anderem eine starke Zunahme der Oberflächenrauheit, die allerdings erst nach circa zwei Wochen eintritt. Diese Informationen werden dazu verwendet, die Aussagekraft zukünftiger Erosionsmessungen zu erhöhen, indem eine biofilmähnliche Rauheit in das Erosionsgerinne eingebracht und somit ein nahtloser Übergang zwischen Rinnenboden und zu erodierendem Biofilm hergestellt wird.

Zusammengefasst lässt sich sagen, dass mit der vorliegenden Arbeit ein wichtiger Schritt in Richtung des Verständnisses der mechanischen Prozesse, die der Biostabilisierung zugrunde liegen, gegangen wird. Es ist die Hoffnung des Autors, dass die hier beschriebenen Methoden, Vorgehensweisen und Daten in zukünftigen Forschungsprojekten Berücksichtigung finden, um dem Phänomen der Biostabilisierung weiter auf den Grund gehen zu können.

Part A

BACKGROUND AND BASICS

A.1 Introduction

A.1.1 Background

Since long times, scientists are engaged with investigating the dynamics of sediments in aquatic systems. A holistic understanding of these dynamics (reflected by the erosion, transportation, deposition, consolidation cycle (ETDC)) is of fundamental value for many disciplines dealing with water. For example, engineers need to estimate the stability of sediments around piles (e.g. bridge piers) to protect them from scouring (Roulund et al., 2005). Likewise, the navigability of harbors and channels is threatened by sedimentation and consequently need frequent dredging (Owens et al., 2005). Ecologists are concerned with the health of aquatic systems and with the distribution of vegetation/animals, which in turn is strongly related to the morphology of the system (Gerbersdorf et al., 2009; Rice et al., 2010). Furthermore, pollutants and their transportation pose a risk to aquatic habitats when they become bioavailable (Schüttrumpf et al., 2011; Heise & Förstner, 2007).

The first indications that microbes attached to sediments potentially alter the mechanical properties of sediments were made approximately half a century ago by Meadows and Anderson (1969). From that day on, the general conception is that biofilms excrete glue-like substances (extracellular polymeric substances - EPS) which stick together sediment grains to induce an increased benthic stability (Gerbersdorf & Wieprecht, 2015). Since then engineers are trying to understand the complex interactions between biofilms and sediments focusing predominantly on the combined stability of both (Dade et al., 1990), often with the goal to predict their stabilization potential (hereafter named “biostabilization”) and their contribution to the erosion, transportation, deposition and consolidation cycle.

Biofilms, which colonize intertidal (cohesive-) sediments (Stal, 2010) but also fine grained riverine sediments (Gerbersdorf et al., 2007), typically form a protective thin layer by adhering to the surficial sediment grains and thereby increase their stability (Le Hir et al., 2007).

Biostabilization has a direct impact on the onset of bed-load transport while once eroded the underlying (abiotic) sediment will follow typical abiotic erosion patterns (Le Hir et al., 2007; Piqué et al., 2016). In a morphological sense, biostabilization is more important to attenuate the erosion processes in normal flows rather than in catastrophic events (surges, floods) (Le Hir et al., 2007). As a consequence, biostabilization might promote germination and growth of aquatic plants, which depend on an immobile bed in the inter-flood period (e.g. seagrass see Lee & Park, 2008) and in turn increase the erosion threshold significantly to resist catastrophic events (Paola, 2001).

But biofilms are even more than sediment stabilizers. Growing or established biofilms at the sediment-water interface have major consequences for the functioning of the whole aquatic ecosystem by providing important ecosystem services (Gerbersdorf & Wieprecht, 2015; Battin et al., 2003b). They are the base of the food chain enabling organisms of higher trophic levels to survive and reproduce, they purify water (a process which is commonly known from waste water treatment) and biodegrade anthropogenic pollutants (Gerbersdorf et al., 2011).

The consequences of these processes extend far beyond the aquatic environments and influence human health and welfare. The monetary value of these ecosystem services is not easily traceable but is estimated by Costanza et al. (1997) to exceed billions of dollars (waste treatment alone in lakes and rivers is estimated for 1994 to be $665 \text{ US\$}/\text{ha}\cdot\text{yr}$).

It is because of these reasons that a number of research projects, especially in Europe, investigate the complex tripartite biofilms-sediments-hydraulics (e.g. ECOFLAT, INTRMUD and the recently launched Hydralab+). This thesis originates from the DFG funded project “Ecosystem Engineering: Sediment entrainment and flocculation mediated by microbial produced extracellular polymeric substances (EPS)”.

A.1.2 Research gaps

Despite an overwhelming number of publications on the topic of biostabilization, its underlying mechanical processes are not well understood (Grabowski et al., 2011). And this is partly because most studies have been conducted *in-situ* where causal relationships between different factors are not easily isolated from uncontrolled environmental conditions. Accordingly, Le Hir et al. (2007) emphasize the need for laboratory studies to investigate biostabilization under controlled conditions to unravel the basic mechanisms of biogenic stabilization. In their paper, Le Hir et al. (2007) evaluate the chances of accounting for biota effects in sediment transport modeling *inter alia* by reviewing the recent advances in biostabilization research. They summarize that most results on erosion threshold and erosion rates originate from field studies where the numerous uncontrolled environmental impacts on biofilm growth can hardly be correlated to the biostabilization effect.

The lack of systematic laboratory studies can be attributed to the difficulty of correctly representing the complexity of biological systems (e.g. reciprocal interactions between environmental conditions and biology) and conversely simplifying/idealizing the system to study fundamental feedback mechanisms (often preferred by engineers, Rice et al. (2010)). As a consequence, a common strategy to answer fundamental questions in biofilm research is looking at monospecies biofilms even though it is consensus nowadays that these biofilms do not resemble natural biofilms too well (Gerbersdorf et al., 2009)¹. This simplification strongly underestimates the feedback mechanisms in natural systems impacting also their mechanical behavior (Gerbersdorf et al., 2009).

Systematic fundamental research on the interface of ecology and hydraulics is a tightrope walk and necessarily to be conducted in interdisciplinary research teams. On the one hand it must simplify/idealize as much as possible to allow an easier parameterization while on the other hand great care must be taken in abstracting too much to not disturb the basic biological functioning (Rice et al., 2010).

While this line of thought is not particularly new, it is still discussed in prominent position in this thesis, as a number of laboratory studies from the disciplines investigating biostabilization fail in an appropriate experimental design. However, in recent times, more and more research has been conducted combining all relevant disciplines (e.g. Singer et al., 2006; Vignaga, 2012; Graba et al., 2010) to investigate the interactions of biofilm-sediment-hydraulics in sophisticated experimental setups. Still, systematic investigations on the biostabilization potential using e.g. laboratory flumes are in their infancy and the reasons are manifold and mostly related to the complex structure of the biofilm:

Biofilms and EPS production is sensitive to environmental conditions

Amongst the conditions that influence biofilm growth are hydrodynamics, light intensity, nutrient availability, pH, temperature and cations to name but the most important conditions (Gerbersdorf & Wieprecht, 2015). Addressing all of these conditions in controlled experiments (e.g. flume experiments) is at least very difficult and appropriate flumes are not necessarily a standard repertoire of hydraulic laboratories (Rice et al., 2010; Thomas et al., 2014; Jonsson et al., 2006).

Biofilms are spatially heterogeneous and affected by local hydrodynamics

Local hydrodynamics influence biofilm growth from the micro- to the macroscale. For example, Graba et al. (2013) reported that flow velocity is a selective factor in algal composition and Battin et al. (2003a) found an impact of velocity on the structure of the biofilm. These findings are further supported by Stoodley et al. (1998) who reported significant differences

¹Probably the most studied bacteria is *Pseudomonas aeruginosa*

between biofilms grown under laminar and turbulent conditions. Biofilm surfaces have been titled “microbial landscapes” (Battin et al., 2007) indicating that these landscapes also physically affect their environment themselves which introduces even more levels of complexity (Stewart, 2012).

Biofilms have a high temporal heterogeneity

Biofilm growth can be divided into several phases, from initial attachment to matured biofilms. It is intuitive to assume, that the stabilization potential differs in these phases. Investigations on the temporal development of biostabilization are however scarce (e.g. Fang et al., 2014; Droppo et al., 2007; Ubertini et al., 2015), even though knowledge on this aspect could be very beneficial for an understanding of the phenomenon. Furthermore, biostabilization is strongly impacted by seasonality. A number of studies demonstrated a significant difference between the stabilization potential at different seasons (e.g. Dickhudt et al., 2009; Amos et al., 2003; Righetti & Lucarelli, 2010). The reasons can, amongst others, be related to the differences in microbial community composition (Schmidt et al., 2016).

Le Hir et al. (2007) and Grabowski et al. (2011) demonstrated that the recent attempts to predict biostabilization from measured parameters fail at providing a universal relationship, which on the one hand can be assigned to the complexity as indicated above, but may also be related to the unavailability of appropriate measurement techniques or a lack of knowledge on the key parameters. Different approaches and models have been developed during the last decades, often based on the correlation of *chlorophyll a* (*chl a*) and/or colloidal carbohydrates (as a proxy for EPS) to sediment stability. A comparison of the results of these regression models using *chl a* as an input parameter clearly demonstrates that a universal relationship to stability cannot be derived from this parameter (Le Hir et al., 2007) as the data from different literature based models scatters significantly. This is not very surprising as *chl a* is not a direct measure of any mechanical property that is responsible for biostabilization. Instead *chl a* is a measure for photosynthetic activity and used as a proxy for algal biomass. This however is assumed to be indirectly correlated with stability as has been indicated by rather good correlations from the individual experiments.

Another and perhaps more promising approach are physics-based models, i.e. models which are based on mechanics and are dimensionally correct. While the stability of non-cohesive non-biostabilized sediments are well understood and can be modeled with often satisfactory accuracy (e.g. by application of the Shields approach), the effect of biostabilization is yet to be evaluated (Grabowski et al., 2011). And this is despite the fact that the additional forces which are made responsible for biostabilization have been assigned names for since long time: cohesion and adhesion. In fact, *adhesiveness* has already been mentioned in the late sixties of the last century (Webb, 1969) and since then both terms adhesion and cohesion are made responsible for the biostabilization process in many publications (e.g.

Black et al., 2002; Dade et al., 1990; Ubertini et al., 2015). In recent times, some progress has been made in the development of models incorporating these forces (Grabowski et al., 2011), mostly based on the seminal work of Lick et al. (2004). They developed a theoretical model based on data from literature where bentonite is added to quartz grains to mimic cohesion effects. Another promising approach, based on the model presented in Lick et al. (2004) and accounting for the modifications proposed by You (2004) was developed by Righetti and Lucarelli (2007). It combines an adhesion and cohesion coefficient with floc bulk density and -size to predict the erosion threshold. Righetti and Lucarelli (2007) applied their model using data from field studies to predict the adhesion coefficient. Even though the calculated values for the adhesion coefficient seem reasonable (in context with literature), they could not be related to “real” measured adhesion values presumably due to a lack of appropriate measuring devices and data. In fact, Grabowski et al. (2011) note that these approaches “represent important advances in our theoretical understanding of inter-particle attractions” but, at the same time their applicability is limited by a) the empirical character of adhesion/cohesion and bulk density effects and b) a limited data set that the models are validated on.

Considering its importance, surprisingly few attempts have been made to correlate adhesion or cohesion forces to biostabilization. The first exception is the work of Vignaga et al. (2012) who investigated the tensile strength (or cohesive strength) of microbial mats. Their work is still restricted to cyanobacterial biofilms comprising intertwined filaments which form bio-mats. Hence, biofilms which do not form mats or are still in an early developing phase may not be addressed by this method (because they are not strong enough or break in small pieces). The second exception is the studies of Lubarsky et al. (2010) who used a new method (first described in Larson et al., 2009) to determine a proxy for surface adhesion (Magnetic Particle Induction - MagPI) and compared the results to the critical erosion stress determined with the help of the Cohesive Strength Meter (CSM). Even though the invention of this method that allows relatively quick and non-destructive measurements by using an electromagnet which attracts ferromagnetic particles, can be regarded as a major step towards an improved understanding of the mechanical properties of biofilms, its full potential is still not reached and requires exploration. For example, it lacks an appropriate calibration² into a mechanical force (also noted by Vignaga et al., 2012) to compare the results to literature values and to use the data as a basis for predicting biostabilization in physics-based models.

²Larson et al. (2009) use the strength of the magnetic field (Magnetic flux density MFD in mTesla) as a proxy for surface adhesion. The MFD cannot directly be translated into a mechanical force as it does not consider the ferromagnetic particle characteristics (see Section C)

In short, the research gaps that will be addressed in this thesis are:

1. Knowledge on how to conduct experiments concerned with investigating biostabilization and its complexity is limited to only a few studies; appropriate protocols and methods need further development
2. No unifying model exists to predict the stabilization mediated by biofilms, at the same time a mechanical understanding of the process is unavailable
3. An understanding of the mechanical biostabilization processes would greatly benefit from developing appropriate methods to measure cohesion and adhesion

In the course of this thesis the knowledge gaps will be addressed in more detail.

A.1.3 Research aims

This thesis is based on laboratory experiments in which biofilms are cultivated in a novel flume setup to investigate the impact of different environmental conditions (fluid forces and light intensity during growth) on the temporal development of biostabilization. Furthermore, this work aims at contributing to a generic mechanical understanding of biofilm formation and stabilization by providing methods, data and analysis for a systematic research on biostabilization - a prerequisite for the development of a universal physics-based model to predict the effects of biostabilization.

The general objectives of this thesis are to a) study the impact of environmental conditions on biostabilization, b) develop advanced methods to measure important parameters and provide suitable experimental programs and c) provide data from robust measurements on mechanical properties.

Quasi-natural multispecies biofilms are cultivated on artificial non-cohesive sediments. Their development is monitored from the initial state (suspended microbes in the inoculum) to fully grown biofilms (duration of the experiments between 4 and 8 weeks). The intention of the cultivation procedure is to control the most influential environmental boundary conditions to draw inferences about their impact on biostabilization. It is noteworthy that no specific fluvial environment is simulated, the results therefore are not necessarily transferable to natural systems, but serve to provide an improved understanding of the processes. However, when possible, the environmental conditions are chosen to be comparable to natural conditions.

The specific objectives can be summarized as follows:

1. Induce biofilm formation in a flume setup ensuring that both hydrodynamics as well as biological requirements are met. This includes: defined hydraulics and environmental boundary conditions, the viability of biological as well as mechanical measurements.

2. Investigate the impact of different controlled environmental conditions on biostabilization over time using natural freshwater as an inoculum.
3. Improve methods capable of measuring important parameters for the prediction of biostabilization in physical experiments
4. Measure surface adhesion forces in a reproducible way and relate it to the stabilization potential of growing biofilms.
5. Assess the potential of surface adhesion forces in predicting the biostabilization potential by application of a physics-based, thus intentionally universally applicable model (the modified Shields approach; after Righetti & Lucarelli, 2007).
6. In addition: assess the surface topography of developing biofilms over time to a) investigate the surface roughness and potential impact on near-bed hydraulics and b) upgrade commonly used straight erosion flumes for more precise investigations on biostabilization.
7. Add data on erosion thresholds, surface adhesion and biofilm roughness as well as on methods and procedures to the relatively young field of physical laboratory experiments on biostabilization.

Important remark

The here presented experiments are conducted under idealized conditions to test causal relationships between selected parameters and stability. Although natural river water is used as an inoculum, a number of artificial boundary conditions restrict the transferability of the results to the field. Firstly artificial sediments are used as substratum with a narrow range of size distributions and almost spherical shapes. This is in strong contrast to natural environments where differences in particle sizes are likely. Secondly, the water is withdrawn from the river at one distinct point in time and then circulated over several weeks (at a constant water temperature). In contrast, in a natural system the water is supplied continuously: seasonal effects are hypothetically superimposed and probably less obvious as compared to the experiments. Thirdly, benthic sediments and biofilms in natural systems are colonized by other microorganisms, plants and animals which are also known to influence sediment stability. In contrast, in the experiments the water is sieved prior to circulation to focus purely on the development of the biofilms. On the other hand, especially in Part B it will be demonstrated that the trends reported from field studies are reasonably well reflected in the physical experiments. More research is needed in which both, *in-situ* and physical experiments are combined to investigate the transferability between both conditions.

A.1.4 Outline of the work

This section outlines the content of the thesis briefly, to provide the reader with the workflow. The thesis is divided into 7 main parts, named A, B, C, D, E, F and G. Starting with background information (this Part A), the second part (Part B) is an introduction to the basic experimental setup and the first findings which form the basis of the thesis. Part C deals with the further development of a device to measure surface adhesion forces, whose application is subsequently presented in Part D. Part E further analyzes the results of the surface adhesion measurements by application of a physics-based model to predict biostabilization. Part F is an additional chapter on surface roughness measurements, providing information on how to modify frequently used straight erosion flumes for biostabilization measurements. Finally the thesis is summarized and concluded in Part G, together with future research recommendations.

In detail:

After the introduction, Part A is divided into 4 sections. Sections A.2 and A.3 give an explanation on what biofilms are, where biofilms (both favorable and detrimental) form and further reviews the state of the art knowledge on biostabilization in aquatic environments. The next Section (Section A.4) reviews the impact of environmental conditions (both biotic and abiotic) on biofilm growth and expected influences on biostabilization. Section A.5 is an overview on biofilm material properties and explains the difference between cohesion and adhesion forces. Hereafter the currently available methods to measure adhesion forces are presented as those forces play a central role in this thesis. The last Section (A.6) explains the modeling approaches to predict biostabilization, with an overview on empirical and physics-based models, while also the most common approach to predict non-cohesive abiotic erosion threshold is explained briefly serving as background information.

Following these background information, Part B provides the reader with information on the experimental setup constructed specifically for the project (Section B.1). Hereafter the experimental program for the first set of experiments is described (Section B.2) and the results are presented and discussed (Sections B.3 and B.4). In this first set of five experiments (conducted in March, May, July, August and November 2013), the erosion threshold of biostabilized sediments is related to the environmental boundary conditions (hydrodynamics, light intensity and seasonality). Moreover the observed erosion mechanisms are discussed before Section B.5 presents a conclusion.

The further development of a device to measure surface adhesion forces of biofilms with the goal to increase objectivity and gather information that can be used in mechanical models is a focal point and described in Part C. This Part firstly introduces the original concept (Section C.1) and frames the need for modifications. Secondly, in Section C.2 the upgraded device

is presented briefly followed by a description of the procedure for calibration, to obtain a mechanical force (Section C.3). The latter section additionally contains background information on electromagnetism. In Section C.4 the method replacing the manual observations on adhesion-thresholds with an image processing based approach is explained. The calibration as well as the image processing is a prerequisite for obtaining reliable measurements on surface adhesion forces, which are defined in Section C.5. Finally the performance of the device is tested by measurements on surrogate materials. These tests might be useful as benchmark tests and are described in Section C.6. Uncertainties and limitations of the new method are then given in Section C.7.

As the upgraded device to measure surface adhesion forces was finalized in the beginning of 2014, the method was first available in the second set of experiments (conducted in March 2014, July 2014 and March 2015). Part D consequently focuses on the analysis of the surface adhesion data obtained during these experiments using the upgraded device. At first important preliminary considerations on the general interrelationship between the measured surface adhesion forces and the erosion threshold are given in Section D.1. This is followed by a description of the experimental setup and program for the measurements (both erosion threshold and surface adhesion in Sections D.2 and D.3). Thereafter, Section D.4 describes the correlation between the erosion threshold, surface adhesion and the time of growth by means of a regression analysis followed by a discussion (Section D.5) and a hypothesis on the relationship between the measured parameters.

In Part E the modified Shields approach after Righetti and Lucarelli (2007) is tested on a detailed dataset of one experiment; including data on bulk density, floc size, erosion threshold and surface adhesion. To the authors' knowledge it is the first time that the mechanical adhesion forces are directly applied in a model considering all of the above mentioned parameters. Section E.1 contains information on the methods used to obtain these data (including size analysis for irregular shaped flocs, developed especially for this purpose). Section E.2 illustrates the results followed by a discussion on applicability of the adhesion data within the model and outlining the most important parameters to be considered in future experiments (Section E.3). The experimental limitations are discussed in Section E.4 before Part E is concluded in Section E.5.

Part F is an additional chapter describing the development of a device to measure the surface topography (or roughness) of biofilms. The method is applied in one experiment. This additional data from the topographic survey is used to modify the existing erosion flume to the requirements for erosion of biostabilized surfaces. Further data contains information about the temporal development of quasi-undisturbed biofilm roughness, unique in current literature. Firstly, Section F.1 provides an overview on the method that was specifically developed for that purpose. Secondly, the results of one experiment conducted in July 2014

are presented (Section F.2) and discussed. And thirdly (Section F.3), the modifications made to the erosion flume are described (including information on the modified flow field obtained by the modifications). Finally Part F provides an outlook and recommendations for an alternative method and analysis (Section F.4).

The thesis is concluded and summarized in Part G including future research needs related to physical experimentation on biostabilization processes.

A.2 Background information on biofilms in aquatic systems

Biofilms are complex assemblages of bacteria, microalgae and fungi (e.g. diatoms, cyanobacteria, heterotrophic bacteria, e.g. Le Hir et al., 2007; Battin et al., 2003b) and their secreted EPS. These microbes accumulate on all kinds of surfaces (e.g. the solid-liquid interface) where they can form films or mats (Noffke et al., 2001; Flemming & Wingender, 2010) of thicknesses between some micrometer and a few millimeters (Okkerse et al., 2000). Biofilm growth is largely depending on nutrient availability (Gerbersdorf & Wieprecht, 2015).

The microbes, which only make up a small percentage of the whole biofilm, secrete the so called extracellular polymeric substances (EPS) in which they are encased (Flemming & Wingender, 2010). The EPS fulfils a number of important functions for the biofilm: It serves as a nutrient storage and -transportation system (through its pores), it retains water against desiccation, and enables the exchange of genetic information (Flemming & Wingender, 2010). It consists of polysaccharides, proteins, lipids, nucleic acids and humic substances and is highly hydrated with a wet density close to that of water (Gerbersdorf et al., 2011; Wäsche et al., 2000; Horn & Hempel, 1997). The EPS fraction may account for 90 % of the total biofilm matrix (by dry weight), while only 10% is occupied by microorganisms (Flemming & Wingender, 2010).

Another function of this biopolymer, which is of uttermost importance for this study, is its glue-like property especially important for the adhesion of microbial cells to a surface and gluing of sediment grains to resist environmental forcing (Gerbersdorf & Wieprecht, 2015; Dade et al., 1990). This biogenic binding can be further divided into adhesion and cohesion, while a clear distinction must be made between these terms (discussed in Section A.5.2).

Significance of biofilms in aquatic systems - and related research

Biofilms are ubiquitous in nature and their existence and functionalities can have positive (advantageous) or negative (detrimental) consequences for their surroundings. The detrimental bioadhesion is mostly referred to as “biofouling” (Palacio & Bhushan, 2012). In the medical area, for example, the term biofilm is largely negatively associated with e.g. dental

plaque and biofilms on medical implants. On the other hand, the most famous advantageous biofilm can be found in waste water treatment where it is responsible for clarifying the water by nitrification and denitrification. From an engineering point, especially flocculation processes of activated sludge (e.g. aggregation and disaggregation of flocs, settling velocities) are being subject of many research studies (e.g. Andalib et al., 2010). In the following a brief overview on engineering-related research areas associated with biofilms is given (as the reader will notice, these research fields are, to some extent, related to the stability of biofilms, however “biostabilization” will be covered further below):

Biofouling of ship hulls

Schultz and Swain (1999) and Schultz et al. (2015) investigated the skin-friction reduction of biofouled ship hulls. In their experiments, Schultz et al. (2015) found that biofilm growth (even on fouling release hull coatings) resulted in skin friction increases of up to 70% thereby inducing an enhanced power demand between 1.5 and 10.1%. In an earlier study Schultz and Swain (1999) even reported an increase of skin friction of 33 to 187 % on antifouling paints.

Biofouling in drinking water distribution systems

Biofouling in hydraulic conduits generally may result in a significant reduction of efficiency, which has been demonstrated by Barton et al. (2010) using a photogrammetrical method. Additionally, biofilms in drinking water distribution systems (DWDS) can be a threat to human health as they promote capture, growth and release of pathogens. Shen et al. (2015) investigated the complex interactions between hydrodynamics, adhesion and roughness of DWDS biofilms (*inter alia* by computational fluid dynamics - CFD), and found that the physical structure and local hydrodynamics control adhesion and detachment. Furthermore, they reported that biofilms can have a significant impact on the discharge capacity due to the increased roughness of the walls. However, it must be mentioned that roughness changes depend on the initial (abiotic) roughness, biofilms may even result in smoother walls. For example, Barton et al. (2010) observed that diatoms grew between roughness elements (grit size: 0.5 . . . 4 mm) and developed a mat that was smoother than the initial surface.

Biofouling in open hydro power canals

Andrewartha et al. (2010) investigated the increases in drag coefficient for an Australian open hydro power canal due to the growth of a diatom biofilm. They reported increases of total drag coefficient of up to 99 % (versus the clean surface) and observed that vibrations of the biofilm lead to additional energy dissipation.

Biofilms and ecotoxicology

Benthic biofilms are linked to pollutant dynamics in aquatic systems through a number of mechanisms, whereby the EPS plays an important role: Firstly, bacteria inhabiting the

biofilm may be harmed by the pollutants but likewise Gerbersdorf et al. (2011) hypothesize that some species might tolerate or even be able to degrade the pollutants. Secondly, the glue-like EPS helps in binding pollutants to biofilms (a process named “biosorption”) and biofilm-coated sediments. Consequently pollutants are immobilized with an impact on bio-availability and degradation (e.g. heavy metals, nanoparticles, anthropogenic trace compounds, see Pal & Paul, 2008; Tournay & Ngwenya, 2014; Gerbersdorf et al., 2015). Thirdly, the immobilized pollutants can get re-mobilized through erosion processes (Schüttrumpf et al., 2011; Heise & Förstner, 2007; Noack et al., 2015), while the biostabilization effects pose an additional resistance to the fluid force. Fourthly, the biosorpted pollutants are transferred to other sites, while the transportation mechanisms are likewise affected by the structure and composition of the biofilm-flocs.

Biofilms and ecosystem services

The term “ecosystem services” describes the benefits that functioning ecosystems provide for human beings. Biofilms in aquatic systems (both benthic or free floating) are a key component of ecosystems as they regulate the availability of nutrients to higher trophic levels³, purify water and generally contribute to the biogeochemical fluxes of carbon, nitrogen and phosphorous (Battin et al., 2003b; Gerbersdorf et al., 2011; Gerbersdorf & Wieprecht, 2015). Moreover, as has been suggested by Packman (2013) biostabilization (i.e. the immobilization of sediments for example after flood events) might lead to improved conditions for other organisms to grow. As most vegetation needs stable bed conditions for the seeds to germinate and develop shoots which can resist the typical fluctuations of hydrodynamic forcing, benthic biofilms might play an important ecological role in this regard⁴.

Benthic biofilms and clogging/colmation

When biofilms grow on river beds they can occupy the pore spaces between single sediments which might induce changes in the permeability of the bed, a process called bio-clogging. Thereby it may reduce the hydraulic conductivity to an aquifer (Newcomer et al., 2016; Battin & Sengschmitt, 1999) with far-reaching implications for biogeochemical processes (Brunke & Gonser, 1997). In a general context, clogging might lead to unfavorable conditions for the reproduction of gravel-spawning fish as the fish eggs and larvae depend on the transport of well-oxygenated surface water (Noack et al., 2016b).

Flocculation and settling of biofilm aggregates

Aggregates of biofilm-bound sediments which are eroded are called flocs. Besides being a research topic in waste water treatment (for an extensive review see Liu & Fang, 2003) floc transport is also associated with the ETDC cycle (erosion, transport, deposition and consolidation cycle, to be discussed in Section A.6). The difficulties in predicting the transportation of the flocs originate from the complexity of these systems. Biofilms mediate the size, shape,

³Biofilms are in fact the base of the food chain

⁴To the authors' knowledge this aspect has not yet been covered by science

density and surface texture of the primary particles and thereby affect the mode, rate and distance of transportation (Dietrich, 1982). Characterizing floc geometries and relating them to settling velocities is a major challenge. A number of studies are related to parameterize the different (geometrical) effects by introducing different shape factors and investigate their impact on settling behavior (Tran-Cong et al., 2004; Shang et al., 2014; Cuthbertson et al., 2016). As the properties of biofilm flocs allows conclusions on the process of erosion, the two fields are closely related, which will be demonstrated in Section E.

As can be seen, research on biofilms is widespread, consequently the tools and procedures developed in the present thesis may help in a number of different research areas besides the here investigated biostabilization.

A.3 Background information on biostabilization

While observations made half a century ago already suggested an impact of microbes on sediment stability (see Meadows & Anderson, 1969) the potential of biofilms to impact sediment stabilization was only recognized in the 90's of the last century by Paterson and Daborn (1991) who introduced the term "biostabilization" to describe these processes. Paterson and Daborn (1991) defined biostabilization as "a decrease in sediment erodibility caused directly or indirectly by biological action". Since then the original definition was redefined and modified several times (a short overview is given in Table A.1).

Table A.1 Different definitions for the term "biostabilization" from literature. Note: Gargaud et al. (2011) subdivided the definition into three types: types 2 and 3 are not directly related to erosion processes and therefore only type 1 is presented here.

Source	Definition of biostabilization
Paterson and Daborn (1991)	"[...] a decrease in sediment erodibility caused directly or indirectly by biological action"
Droppo et al. (2001)	"[...] the process whereby microbial growth and production of extracellular polymeric substances (EPS) in conjunction with sediment colonization by other organisms such as fungi and algae result in the increased stabilization of a bed sediment due to the sticking together of individual particles and flocs. In essence, biostabilization represents a biofilm incorporated into the surface sediment."
Gargaud et al. (2011)	"Type 1 biostabilization is the response by benthic microbiota to erosion. Bacterial filaments are oriented horizontally, and EPS (extracellular polymeric substances, if present) change their chemical structure to a more erosion-resistant phase [...]."
CoastalWiki (2016)	"Biological processes increasing sediment stability or reducing potential for erosion by tidal currents and wave action (e.g. enhanced cohesion, binding by filaments / roots, surface protection / armoring, flow and wave attenuation by biota)."

In essence, most definitions mention either "increased stability", "increasing erosion resistance" or "decreasing erodibility" or a combination hereof as an effect of either "biological action/processes" or "benthic microbial growth". In this thesis, "biostabilization" is clearly mediated by benthic microbial growth (no grazing, no higher plants) to increase the stability

of the biofilm-sediment matrix or increase the erosion threshold of this matrix towards a horizontally directed step-wise increasing flow.

In the 1990's research on biostabilization became increasingly popular. Especially noteworthy is the work of research teams around Prof. Paterson (University of St. Andrews, UK) and Prof. Amos (now at the University of Southampton, UK) who conducted *inter alia* a number of field studies (mainly on intertidal flats) by the use of *in-situ* erosion devices to determine the impact of biofilms on sediment stability. While theoretically even destabilization effects (e.g. due to the lifting forces of produced gas bubbles: Sutherland et al., 1998) are possible, all studies reported an increasing stability relative to the control (abiotic) sediment. In this context the biostabilization index (BI) (after Manzenrieder, 1985) is an often used indicator for the efficiency of biostabilization. The BI is defined as:

$$BI = \frac{\tau_{c,bio}}{\tau_c} \quad (\text{A.1})$$

where $\tau_{c,bio}/\tau_c$ is the ratio between critical bed shear stress of the biostabilized sediment and the abiotic reference. Table A.2 gives a non-exhaustive overview on results of different experiments investigating biostabilization in different environments. Both, approaches as well as evaluation of the data differed a lot between the studies, therefore the table gives a more qualitative overview.

Table A.2 An overview on the results of biostabilization from literature (modified and updated from Vignaga, 2012) including information on the substratum type, the environment where the measurements were conducted and the erosion devices used. Note: The column "Substratum" is the type of sediment which was biostabilized. Here, "c" stands for cohesive sediments and "nc" for non-cohesive sediments. "CSM" is the abbreviation for Cohesive Strength Meter

Study	BI[-]	Substratum	Environment	Research method
Neumann et al. (1970)	6	nc	subtidal	<i>in-situ</i> flume
Grant and Gust (1987)	4.9, 4.5	nc	marine	sediment cores
Dade et al. (1990)	3	nc	media with sea salt	laboratory study
Madsen et al. (1993)	4	nc	subtidal	laboratory flume
Yallop et al. (1994)	> 10.6	nc	marine	CSM
Parchure and Mehta (1985)	3	c	estuary	laboratory study
Yallop et al. (1994)	4	c	intertidal sandy beach	CSM
Righetti and Lucarelli (2007)	1.5	c	freshwater (lakes)	sediment cores
Amos et al. (2004)	3.4	c/nc	tidal flats	<i>in-situ</i> flumes
Fang et al. (2014)	1.7	c/nc	stabilization pond	laboratory study
Vignaga (2012)	2.5	nc	freshwater	laboratory study

It is apparent that the biostabilization indices scatter over a wide range. This can be attributed to a) the differences in methods applied, b) an impact of the sediment size and c)

differences between biofilms in the studies. Regarding the latter, it is widely accepted that biostabilization is heterogeneous, both temporally (e.g. differences between seasons) as well as spatially (between field sites) (see e.g. Dickhudt et al., 2009; Widdows et al., 2000; Kornman & de Deckere, 1998). This important feature of biostabilization may be the result of the different environmental boundary conditions in the field. An overview of the most important impacts will be given in Section A.4, before Section B explores the biostabilization potential of biofilms cultivated under different conditions.

Investigated substratum

A number of field studies were conducted in estuaries or tidal flats on cohesive sediments (e.g. Amos et al., 2004). In fact cohesive sediments (i.e. sediments with a high amount of clay and silt, bound by cohesive forces) provide ideal conditions for biofilm growth, which can be related to their high organic content (serving as a nutrient supply) and surface area (see also Section A.4). As cohesive sediment stability is depending on a large number of sediment properties, a generally accepted model to predict their erosion threshold is still subject of research (Grabowski et al., 2011). Consequently, the additional uncertainties and parameters introduced by the biofilm formation make the prediction even more challenging, so it is decided that non-cohesive sediments are used as substratum in this study.

A common perception of biostabilization in cohesive, but also in non-cohesive sediments, is that the biofilm and associated EPS fills up the pore spaces between sediments, as can be seen in Figure A.1 (*Left*: a diagrammatic representation, *Right*: a photograph from the project) and binds the grains together. This mechanism is effective (i.e. comes along with a significant impact on biostabilization) when fine material is glued. In fact it can be assumed that a certain critical diameter exists at which the glueing force is outcompeted by the weight of the sediment. For example, a cobblestone will be stabilized by its weight whose force is likely to exceed the glueing force of a biofilm by several orders of magnitude. It must be further noted, that in many cases (also including this study) the biofilm-sediment matrix is only a thin layer (thicknesses between some micrometer and a few millimeters) which protects the underlying sediment (Okkerse et al., 2000; Boulêtreau et al., 2011; Black et al., 2002). However, depending on nutrient availability and other factors, EPS can also be found in much deeper layers (> 500m depth, Black et al. (2002)).

Investigated environments

Research on biostabilization in freshwater systems is still in its infancy. Even though it is commonly accepted that biofilms theoretically grow on all kinds of surfaces and are virtually ubiquitous (Proia et al., 2012), Table A.2 demonstrates that research has primarily focused on marine habitats (see also Gerbersdorf & Wieprecht, 2015). One reason is that it was long believed, that due to high ion concentrations in marine water, the binding is generally more effective. However, recent studies (e.g. Gerbersdorf et al., 2007) indicate that freshwater

biofilms may mediate a similar stabilization potential.

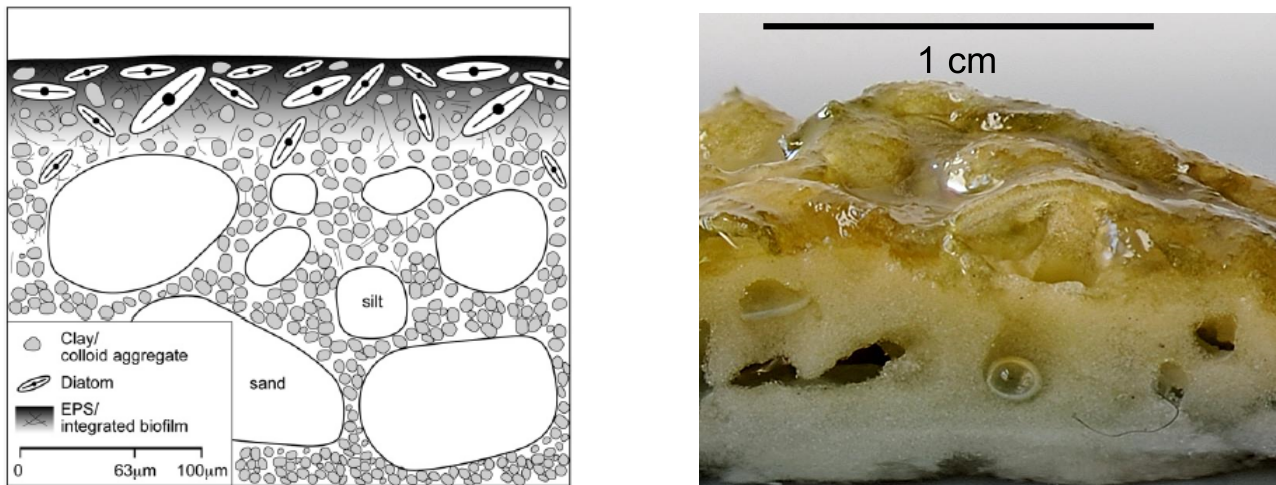


Figure A.1 Diagrammatic side view representation and photograph of the biofilm-sediment matrix. *Left:* Microbes (diatoms) and EPS between clay particles. Only the upper few millimeter are affected by the biofilm (from Grabowski et al., 2011); *Right:* Side view image of a biofilm cultivated in the experiments. The biofilm is clearly visible on top of the sediment (green slimy layer) while also existing in the uppermost few millimeter (indicated by a greenish color of the white sediment). Further below, the pure white sediment is visible. Two more aspects are well visible: 1) The impact of the biofilm on the surface topography and 2) gas bubbles below the surface retained by the biofilm (Photograph by Bojan Skodic).

Lift force and surface roughness

As can be seen on Figure A.1 *Right*, biofilms produce gas (e.g. oxygen from primary production) which accumulates below the surface to form bubbles. In this case the biofilm experiences an additional lift force, as the bubbles are trying to escape but are retained by the biofilm surface layer (Sutherland et al., 1998). Only very few studies address this phenomenon. In one of these studies experiments were conducted by cultivating biofilm mats and monitoring their buoyant behavior. Mendoza-Lera et al. (2015) found that the impact of gas bubbles was highest for sandy sediments (compared to gravel).

Another aspect concerns the impact of biofilms on surface roughness (also visible in Figure A.1 *Right*) which consequently also impacts the turbulence conditions in the near bed region, thereby affecting the erosion threshold. As already mentioned a number of studies have focused on determining the surface roughness changes (Nikora et al., 1997; Larned et al., 2011; Walker et al., 2013) by different methods. However, only few studies correlate the friction changes to the erodibility. One exception is the study of Graba et al. (2010) who studied chronic detachment of biomass due to local hydrodynamic effects and underlined the importance of roughness changes for an understanding of biofilm dynamics. Biofilm topography will also be addressed in Part F discussing an improved method for continuous monitoring.

A.4 Environmental impacts on biofilm growth

Parts of this section originate from a contribution to a Hydralab+ deliverable (unpublished).

The environmental conditions in which biofilms grow influence their characteristics and properties with possible influences on their biostabilization potential. In the following an overview on the most important abiotic and biotic environmental conditions is given. Furthermore the current knowledge on expected effects is provided.

A.4.1 Abiotic impacts

Hydrodynamics

The role of hydrodynamics is particularly important for the formation of a biofilm, as 1) it triggers the efficiency of initial attachment of suspended microbes to the sediment, 2) it is closely linked to the availability of nutrients to the biofilm during colonization and growth, and 3) exerts a force to potentially detach the biofilm-sediment matrix.

Especially in the early formation of a biofilm the first contact between advected microbes and the substratum surface depends on the turbulent conditions of the flow. In the pioneering work of Stoodley et al. (1998) it was reported that under laminar conditions cell attachment to a surface happened earlier as compared to turbulent conditions. While generally, under turbulent conditions, more cells are transported to the surface than under laminar conditions, their attachment efficiency is reduced due to their ongoing detachment by turbulent forces. During growth, however, higher flow velocities predominantly enhance the availability of nutrients due to higher mixing rates (see also Larned et al., 2004).

In fact, biofilms may even suffer from nutrient availability in stagnant waters or at low flow velocities, even in eutrophic systems. However, higher flow velocities also induce higher drag forces on the biofilm and may result in detachment.

This trade-off between enhanced mass transfer and detachment is widely accepted (e.g. Stewart, 2012) and applies also for higher plants (e.g. Nikora, 2010). It has been demonstrated that biofilms adapt to their specific environment. For example at low flow velocities the biofilm produces filaments protruding into the water column to increase nutrient availability. At higher flow velocities biofilms are observed to be more compact and also potentially more stable (Pereira et al., 2002; Graba et al., 2013).

Light regime

The effective light quantity (= intensity) as well as quality (= intensity at different wavelength) on the biofilm surface is highly variable in natural systems (e.g. turbidity and depth of the water, shadowing). Light is the main source of energy for algae and even some bacteria (e.g.

cyanobacteria) to fix carbon and build up organic substances (Gerbersdorf & Wieprecht, 2015). The photosynthetic active radiation (PAR, typically: 400 . . . 700 nm) is the range of radiation that can be used by photosynthetically active organisms whereas the light intensity [$\mu\text{mol}/\text{m}^2\text{s}$] is a measure for its strength. Increased light intensities can result in enhanced growth, but potentially also in an enhanced production of oxygen bubbles that are produced below or on top of the surface of the biofilm and create a destabilizing lift force (as described above). Too much light intensity might also have a negative effect on biostabilization, as it produces photo-oxidative stress (Gerbersdorf & Wieprecht, 2015). It is important to note that even under no-light conditions (e.g. in a deep river, or in deep sediments: “deep biota” Black et al., 2002) a biofilm will develop, consisting predominantly of heterotrophic bacteria. Measurements made by Lubarsky et al. (2010) showed that bacteria produced a sticky EPS which indicates the high potential for bacterial biofilms to stabilize sediments.

Water temperature

Temperature affects growth rates of biofilms. It is well-documented that metabolic rates increase exponentially with temperature (Brown et al., 2004). For example, Villanueva et al. (2011) investigated biofilm formation by variation of nutrient availability and temperature and reported that the biofilm formation at higher temperatures was faster. They also hypothesized that “Increasing the temperature of river water might lead to faster biofilm recolonization after disturbances”, probably indicating impacts on e.g. lowland river morphodynamics. Regulating water temperature in physical experiments is challenging as most flumes are not equipped with e.g. heat exchangers. However, due to the often long durations of the experiments, water temperature is likely to increase due to the heat produced by pumping the water. In the experiments presented in this thesis, the water temperature is kept constant at 15 °C.

Sediments

The selection of substrate for biofilm cultivation is essential when the erosion threshold of the biofilm-sediment matrix is studied. Natural substrate (e.g. from a river or estuary) typically has a high content in organic matter, nutrients and associated microbes, which is favorable for biofilm growth but with the downside, that these constituents need to be analyzed to determine their impact on biofilm growth. To relate these additional parameters to biostabilization effects is especially difficult if experimental conditions need to be reproduced in a later experiment (e.g. to study the influence of seasonality). A useful approach to this is to use artificial inert sediment as has been done in the experiments reported by Lubarsky et al. (2010). Figure A.2 *Left* shows Low-Temperature Scanning Electron Microscopy (LTSEM) images from biofilms on glass beads. It can be clearly seen that the EPS fills the voids between the beads and covers their surfaces resulting in a conglutination of the sediment. For comparison Figure A.2 *Right* shows a similar situation with natural sand grains.

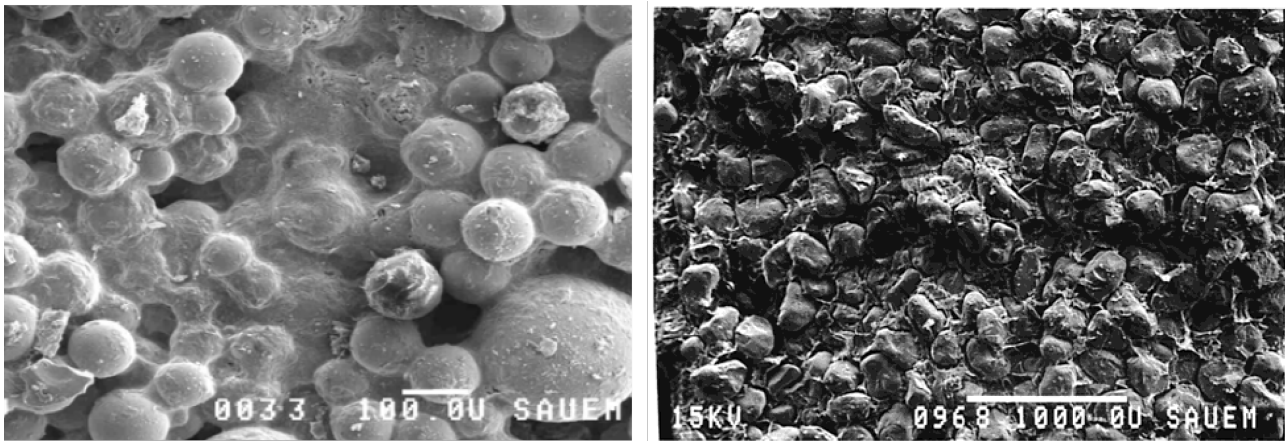


Figure A.2 Low-temperature scanning electron microscopy (LTSEM) images of sand grains and glass beads covered by EPS (from Lubarsky et al., 2010; Black et al., 2001). *Left* artificial sediment (glass beads) (Lubarsky et al., 2010). *Right*: natural sand grains (Black et al., 2001). The EPS fill up the intermediate pore spaces and covers the sediments.

The size of the sediment is crucial for erosional studies as with either too large or too small sizes (where electro-chemical forces exceed the glue-like forces of the EPS) the biostabilization effect might not be relevant. In their seminal paper, Lick et al. (2004) analyzed the initiation of movement of differently sized quartz particles with added bentonite (to mimic cohesion/adhesion effects) and reported that the major increase of critical bed shear stress is for particle sizes between 100 . . . 400 μm . In further investigations Fang et al. (2014) found that for particle diameters between 10 . . . 200 μm adhesive and cohesive forces are dominating over weight and electrostatic forces. Additionally, it needs to be considered, that with finer sediments the surface area offered for microbial settlement and colonization is increased as well (as reviewed in Gerbersdorf & Wieprecht, 2015) and pore spaces between sediments are smaller which is in turn beneficial for the EPS to completely smother the grains and thereby potentially enhance stability (Black et al., 2002).

A.4.2 Biotic impacts

Biofilm growth

On freshly deposited sediments (e.g. after a storm event), the formation of a biofilm in a natural system can be subdivided in phases, namely “attachment” (adhesion of cells to surface), “colonization” (formation of monolayer and microcolony) and “growth” (see Figure A.3)⁵.

It is intuitive to assume that also the biostabilization potential differs at these stages (from initial sediment-without biofilm stability, to matured biofilm stability). However, the time needed for the biofilm to develop a stabilization potential depends on the environmental boundary conditions. For example Droppo et al. (2007) reported significant stabilization effects (factor 3) after 5 days of growth. In another study, Tolhurst et al. (2008) concluded that: “Changes in biogeochemical properties can be expected after just one day”.

⁵For more information on these phases please see Vasudevan (2014) and references therein

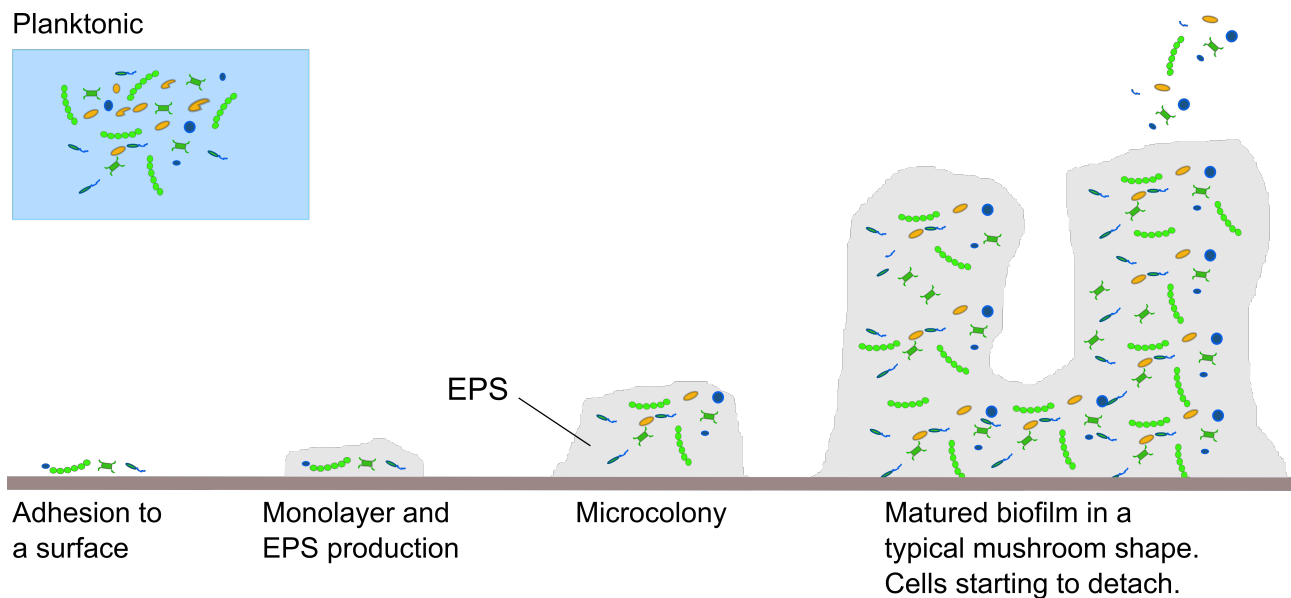


Figure A.3 A developing biofilm from the planktonic to the matured stage (from left to right, modified after Vasudevan, 2014)

A general trend of biofilm growth is that it increases the erosion threshold over time (again depending on the environmental conditions and seasonality) to potentially maintain a relatively stable state as reported by Fang et al. (2014). However, experimental studies investigating the temporal development of sediment stability are still extremely scarce.

Succession

During the course of the year, physical, biological and chemical conditions change in systems where biofilms are present and this also impacts their community composition. Some organisms are outcompeted by others as due to, for example warmer water temperature, nutrient availability or increased light intensity. This so called successional processes (an example of a seasonal succession of phytoplankton is illustrated in Figure A.4) also influences the biostabilization potential as was demonstrated by a number of researchers in different environments (e.g. Dickhudt et al., 2009; Amos et al., 2003). In most studies, the stabilities are higher during the warm seasons as compared to the colder seasons.

A.5 Biofilm mechanics and material properties

A prerequisite for understanding the failure of biofilm-sediment matrices is knowledge on the material properties of biofilms and especially on the secreted extracellular polymeric substances (EPS). Here, a brief overview of the state of current knowledge is given.

A.5.1 Rheology

Rheology is defined as the study of flow of materials. A number of studies deal with the rheological nature of biofilms and biofilm constituents to unravel their response to applied

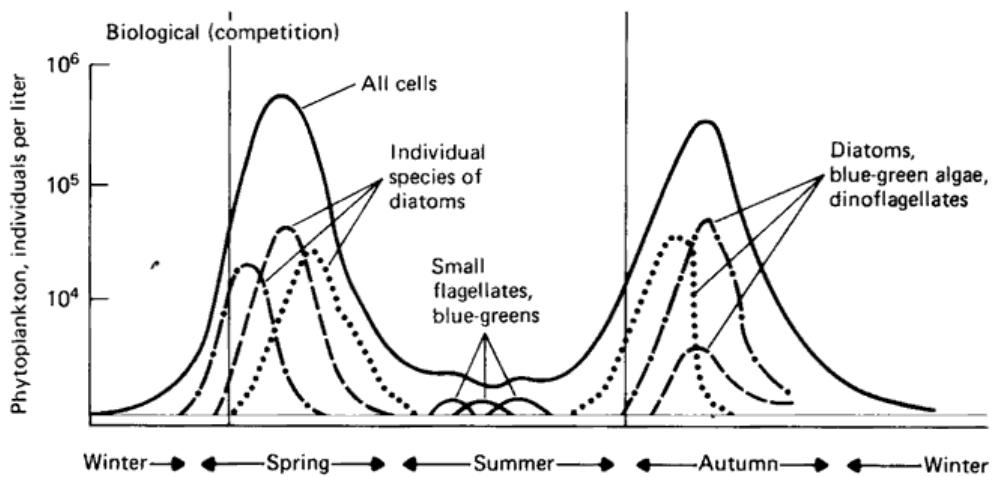


Figure A.4 Seasonal succession of phytoplankton (from Horne & Goldman, 1994).

stresses. However, rheological characteristics are especially interesting for studying failure of the bulk material (without sediments involved). Even though the rheology will not be further addressed in this study the following information are useful for studying biostabilization at the microscale (e.g. binding, deformation and failure of EPS on a single grain) and mentioned here for the sake of completeness.

Three different types of rheological behavior have been identified: elasticity, visco-elasticity and plasticity (Guelon et al., 2011; Böl et al., 2013). Elastic behavior is characterized by stretching of the material when a stress is applied. Unloading the stress results in the material to return to its original dimensions (see Figure A.5a).

Plasticity on the other hand, stands for an irreversible deformation of the material with applied stress (see Figure A.5d). This behavior is rather rarely reported in literature (Guelon et al., 2011).

The most common characterization is a viscoelastic behavior which is also time dependant (Billings et al., 2015; Guelon et al., 2011). Viscoelasticity includes both irreversible viscous deformation and a reversible elastic response (Guelon et al., 2011). For example, Stoodley et al. (2002) found that *Pseudomonas aeruginosa* biofilms behaved like viscoelastic fluids with elastic behavior with an applied stress over a few seconds and viscous behavior when the stress was applied over a longer period of time. Figure A.5b illustrates the idealized response of a biofilm to a constant stress over time, with a creeping behavior (deformation increases with time) and Figure A.5c illustrates “relaxation” of the applied stress when a constant strain is applied.

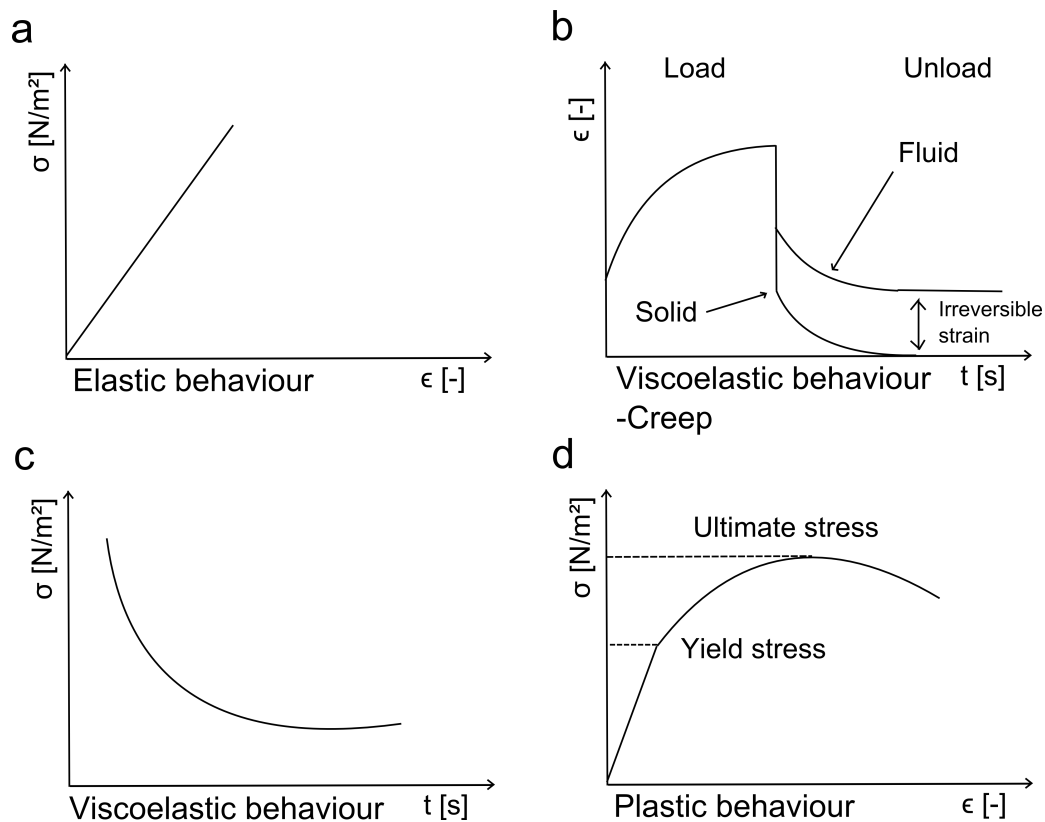


Figure A.5 Different bulk biofilm/EPS responses to applied stress and strain (modified from Guelon et al., 2011). *a*) elastic behavior: after unloading the material returns to its original state; *b*) viscoelastic behavior under constant stress: an elastic behavior followed by a stretching over time; *c*) viscoelastic behavior under applied constant strain: the stress dissipates over time; *d*) plastic behaviour: after a certain threshold the material undergoes irreversible changes

A.5.2 Adhesion and cohesion

In the context of this study, which mainly deals with investigating adhesional effects, it is important to first highlight the difference between adhesion and cohesion. The most commonly used definitions of the two terms are:

Adhesion

Adhesion describes the sticking of dissimilar materials to one another (Grabowski et al., 2011; Flemming, 2011), for example EPS sticking to Sediment. Different mechanisms can be responsible for adhesion and may be appearing simultaneously, amongst them mechanical, chemical, dispersive mechanisms. Mechanical adhesion for example is the filling of voids of a surface by the adhesive material intertwining the two materials, as a result the strength of this bond is depending on the surface morphology (Palacio & Bhushan, 2012). Chemical adhesion is associated with the swapping of electrons between two materials (also called ionic bonding), and dispersive adhesion includes van der Waals forces. When biological systems are involved the term “bioadhesion” is commonly in use.

Cohesion

Cohesion on the other hand describes the sticking of similar materials to one another (for example EPS to EPS). In hydraulic engineering, cohesion and cohesive effects are often associated with the attraction between fine particles (e.g. clay) by electro-chemical forces (van der Waals forces, electrostatic attraction, Jumars and Nowell (1984)). Hypothetically, cohesive forces (EPS-EPS) might also play a decisive role in biostabilization, especially when bio-mats⁶ are considered (Vignaga et al., 2012).

It is generally of no doubt that biofilms cause both, adhesive (EPS-substratum) as well as cohesive (EPS-EPS) effects. But it is not clear which effect dominates in stabilizing sediments⁷. Even a combined biostabilization-effect (cohesion and adhesion) cannot be excluded. Moreover, it is possible that other effects have a likewise (or higher) impact on biostabilization (destabilization by gas bubbles, the variation of bulk density by growing biofilms or the effect of changed floc sizes).

Data to confirm or discard single hypotheses on the impact of adhesion/cohesion is extremely scarce. In fact, to the authors' knowledge, only one study compared cohesion measurements to the biostabilization potential of a cyanobacterial biofilm (Vignaga et al., 2012) at a relevant scale. Considering adhesion some studies were performed (e.g. Lubarsky et al., 2010, 2012; Gerbersdorf et al., 2009), but the results are of little use to quantify the effect of mechanical adhesion on biostabilization (in terms of critical bed shear stress) in natural flows: In these studies a proxy for adhesion was compared to data obtained with the cohesive strength meter (CSM). As has been also noted by Black et al. (2001) the CSM is not mimicking natural geophysical flows, where fluid forces are a combination of horizontal and vertical components, as the CSM solely blasts a vertical jet on a surface to determine an erosion threshold.

An indication of the specific role of adhesion/cohesion is provided by Vignaga et al. (2012). In their study tensile tests were conducted on cyanobacterial biofilm-mats for both, biofilm-only samples and composite materials (i.e. biofilm + glass beads/sand). They report that the composite materials were 3 . . . 6 times weaker than biofilm-only samples, concluding that adhesion (between glass beads/sand and the biofilm) is weaker in bio-mats than cohesion (EPS-EPS). The hint that adhesion is weaker than cohesion is further underlined by comparison of literature values on both effects. From the excellent review of Böl et al. (2013) on advances in the mechanical characterization of biofilms it can be concluded that cohesion values are in the range $10^0 \dots 10^5 \text{ N/m}^2$ while adhesion values range between $10^{-1} \dots 10^2 \text{ N/m}^2$.

By assuming that biofilm-sediment matrices will fail at their weakest points, it can be hypothesized that this failure will occur at the sediment-EPS interface as the adhesion forces

⁶Strong mats of bacteria/diatoms which are entrained as coherent patches on the cm^2 scale.

⁷To the authors' knowledge only the publication of Grabowski et al. (2011) tries to shed a light on this aspect.

are seemingly lower than the EPS-EPS bonds. This would mean that adhesion forces play the more important role in biostabilization processes than cohesion forces. Still, more research is needed as the reported values generally vary over a wide range and are strongly depending on the investigated scale and measuring method applied (as will be discussed below).

A.5.3 Methods to determine adhesive properties

In recent years research on the adhesive/cohesive properties of biofilms has gained considerable momentum, reflected by the number of reviews that were published (e.g. Billings et al., 2015; Böl et al., 2013; Guelon et al., 2011; Palacio & Bhushan, 2012; Garrett et al., 2008; Otto, 2008).

These reviews agree on two aspects: That only little data on cohesion/adhesion is currently available (when considering the high heterogeneities of biofilms) and furthermore these data differ considerably. Böl et al. (2013) explains these deviations by a) the structural heterogeneity of biofilms and b) the differences in the evaluation between the different methods applied and c) the different length scales that were tested. Even though the authors mention that investigations carried out at different scales can be beneficial for the development of complex mechanical models, it is intuitive to assume that material properties at the nanoscale (as for example measured by atomic force microscopy (AFM) e.g. Ahimou et al., 2007) are of little use in the context of biostabilization as the scale differs significantly from the scale at which erosion processes are investigated. Consequently, Vignaga et al. (2012) underlines the importance of considering the scales for biostabilization research.

Measuring material properties of biofilms is especially difficult as it requires customized testing equipment and procedures. Guelon et al. (2011) point out that biofilms are easily desiccated when exposed to air (which is often necessary for conducting the measurements) and it is still unclear how this influences the material properties. Moreover, unlike liquids or gels, biofilms cannot be poured into classical rheometers as they need substratum to grow on. A number of “creative methods” (Guelon et al., 2011) have therefore been developed to investigate material properties of (attached-) biofilms.

The focus of this thesis is on measuring adhesion forces, consequently the devices which are currently available to obtain adhesion data are reviewed below, emphasizing their advantages/disadvantages related to the research objectives of this thesis and providing background information on how adhesion is traditionally measured. Guelon et al. (2011) and Böl et al. (2013) provide extensive overviews on the different methods and obtained results and according to them only 4 methods are actually capable of measuring (proxies for) adhesion forces. These physical methods are briefly summarized in the following.

Centrifugation device (Ohashi & Harada, 1994, 1996)

The study of Ohashi and Harada (1994) is considered pioneering as belonging to the earliest work on biofilm mechanical testing. Using a centrifugation device Ohashi and Harada (1994) investigated the adhesion strength of denitrifiers attached to a plate and cultivated in an open channel reactor. Moreover, a number of different other parameters were measured (e.g. biofilm thickness, -viscosity and EPS). Investigations were carried out on young developing biofilms and the results are related to the time of growth. Figure A.6 is a schematic diagram of the centrifugation device.

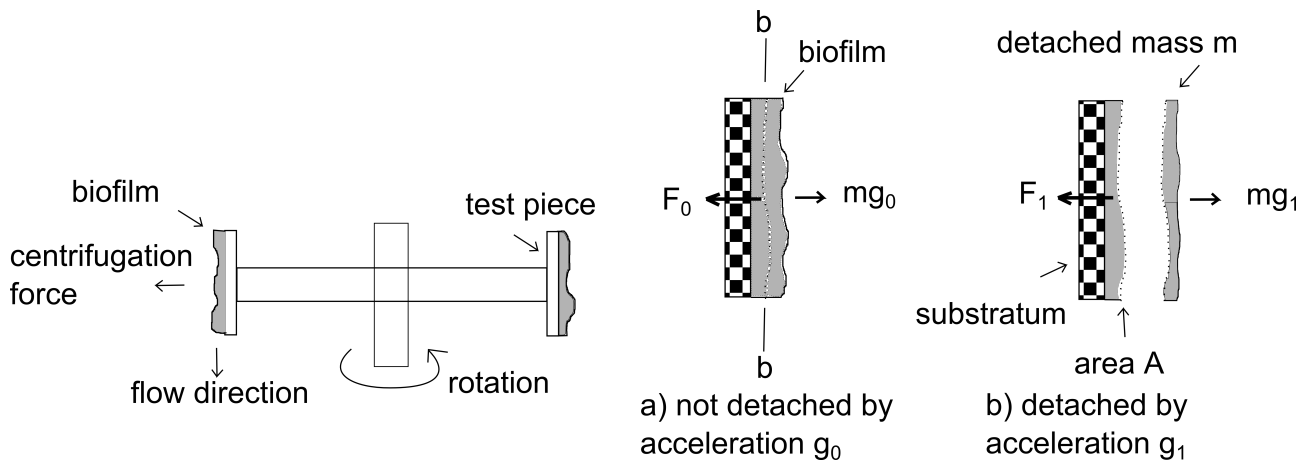


Figure A.6 Schematic drawing of the centrifugation device and the acting forces to measure the adhesion strength of biofilm attached to plates. (modified from Ohashi & Harada, 1994). *Left*: the plates with biofilms attached are rotated around a vertical axis. *Right*: the forces acting on the biofilm due to centrifugation. At detachment (*b*) the horizontally directed centrifugation force $m \cdot g_1$ exceeds the reaction force F_1 (further details on calculating the adhesion force are given in the text).

The sample is fixed perpendicular to a rotary table. Detachment is caused by the centrifugal acceleration mg_1 (see Figure A.6 *Right*). The adhesion strength (f) is then calculated from the reaction or centripetal force F_c at the event of detachment as⁸:

$$f = \frac{F_c}{A_c} \quad (\text{A.2})$$

where A_c is the contact area of the detached biofilm (*b-b*, see Figure A.6 *Right a*). In their first study Ohashi and Harada (1994) reported the resulting strength of adhesion to range between $0 \dots 49 \text{ N/m}^2$ and between $0 \dots > 8 \text{ N/m}^2$ (the upper limit of the measuring device was reached) in (Ohashi & Harada, 1996) for the same type of biofilm, but with differences in cultivation time and hydrodynamic conditions. Ohashi and Harada (1994) reported that adhesion strength increases with time of cultivation and with biofilm depth (low at the surface, high at the sediment/biofilm interface). Concerning the experimental procedure, a number of critical points are raised by Böl et al. (2013) resulting in a relatively low reliability of the obtained data.

⁸This definition is further used in this study to calculate the surface adhesion $A_{s,30}$, as will be explained in Chapter C

Micromanipulation (Chen et al., 1998, 2005)

Micromanipulators are devices consisting of one or more axes and a motor which controls the movement of the axes in a very precise manner. These devices have been used in a number of studies on testing of biofilm-mechanics (e.g. micro-indentation technique, see Guelon et al., 2011).

In the studies of Chen et al. (1998) and Chen et al. (2005) a micromanipulator is connected to a specially designed T-shaped probe to investigate the strength of adhesion of a biofouling deposit produced by *P. fluorescens* biofilms either on the inner surface of a pipe (Chen et al., 1998) or on a glass test stud (Chen et al., 2005). The basic principle is illustrated in Figure A.7.

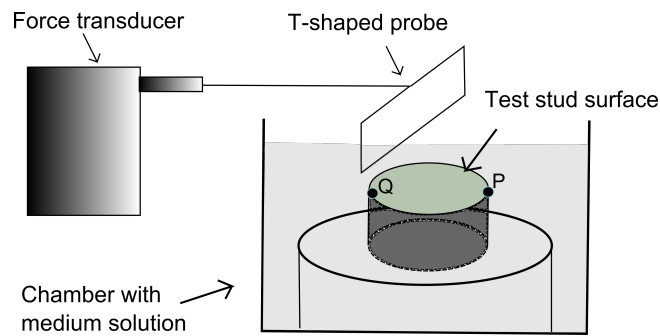


Figure A.7 Diagrammatic representation of the setup to investigate adhesion with a T-shaped probe (modified after Chen et al., 1998)

The biofilm on the test object is pulled away horizontally by the T-shaped probe and the force imposed on the biofilm is measured. The strength of adhesion (σ [J/m^2]) is herein defined as the work (W [J]) per unit area ($\alpha \cdot A$ [m^2]) required to pull away the biofilms from the surface (Chen et al., 2005):

$$\sigma = \frac{W}{\alpha_A \cdot A} \text{ and } W = v \int_{t_P}^{t_Q} F dt \quad (\text{A.3})$$

with α_A being a factor for the fraction of the area covered by biofilm, F is the force measured at time t needed to move the probe from point P to Q and A is the area of the glass stud. W is the work required to remove the biofilm from the glass stud (over the distance \overline{PQ} with the time $\Delta t_{PQ} = t_P - t_Q$ needed at constant probe pulling speed v [m/s]).

Their results suggest an impact of growing conditions on the adhesive strength. Chen et al. (2005) found a higher adhesive strength for biofilms e.g. cultivated at higher flow velocities, having higher suspended cell concentrations and surface roughness, with flow velocities being the most significant impact. Biofilm age (between days 10-20 of cultivation) did not considerably influence the adhesive strength, while a slight increase was measurable after day 20. The adhesive strength ranged between $0.06 \dots 1.0 \text{ Nm}/\text{m}^2$. A critical point related to

the measuring setup is raised by Böl et al. (2013) who argue that it is not clear whether the results will change if differently thick biofilms are tested.

Microjet impingement (Kreth et al., 2004)

Microjet impingement describes a method where adhesives are removed by a fluid jet directed normally to the surface (see Figure A.8 *Left*). The forces (i.e. shear stress and pressure) acting on the biofilm due to the vertical jet have been evaluated numerically (*inter alia* by Deshpande & Vaishnav, 1983) for different Reynolds numbers, jet heights, fluid flow rates (see Figure A.8 *Right*).

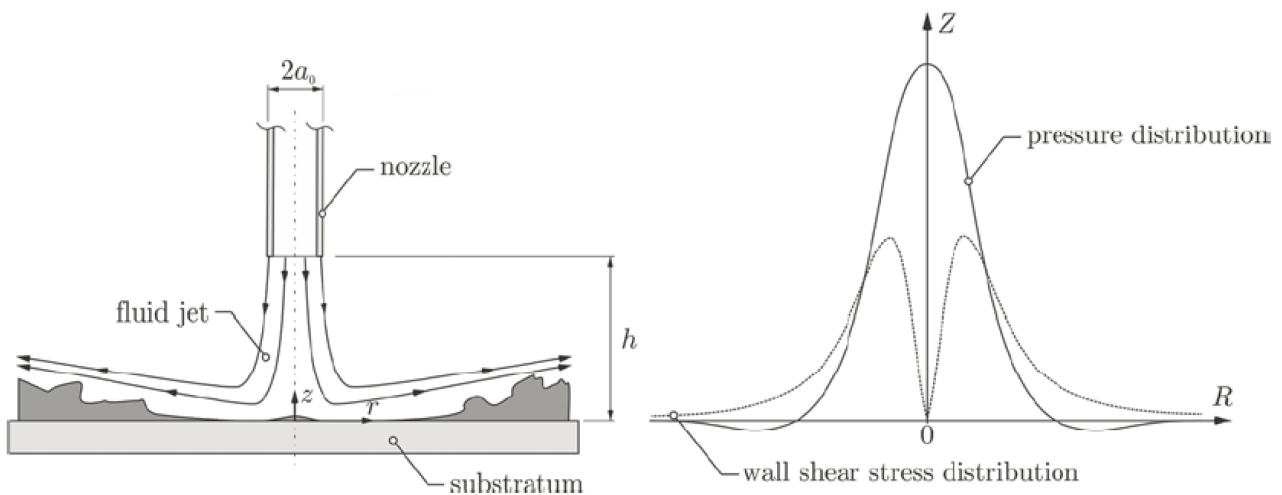


Figure A.8 Schematic drawing of the microjet impingement device and forces (from Böl et al., 2013). *Left*: A vertical jet of fluid is directed on a biofilm surface to detach the biofilm. *Right*: The distribution of pressure and wall shear stress (not to scale) exerted by the jet after Deshpande and Vaishnav (1983)

Kreth et al. (2004) use the shear stress experienced at the perimeter of the removed biofilm surface as a proxy for biofilm adhesion strength. In their study, the fluid (phosphate buffered saline) is delivered via a $\varnothing = 0.2 \text{ mm}$ nozzle at a vertical distance to the surface of 0.4 mm . The imposed flow rate of 0.077 ml/s is applied for 5 s and the area of lesion is determined by image analysis. Kreth et al. (2004) studied the impact of sucrose (a sugar) concentration on the shear stress needed to detach the biofilm. They reported that the critical shear stress increased with sucrose concentration (ranging between $20 \dots 640 \text{ N/m}^2$) in a non-linear fashion. According to Böl et al. (2013) one drawback of the method is that the results depend on e.g. the duration of exposure of the jet. A material characteristic (e.g. adhesion) on the other hand, is per definition independent from applied loads.

Atomic force microscopy (AFM) (Lau et al., 2009)

Atomic force microscopy (AFM) was originally developed for topographical measurements up to the sub nanometer scale (Israelachvili, 2011). In principle, a small tip attached to the end of a cantilever is moved along a surface following its contour. The movement of the tip is recorded by the displaced reflection of a laser beam projected on the tip. Furthermore

the normal and/or lateral forces acting on the tip are measured with a high sensitivity of around $1 \dots 10 \text{ pN} \hat{=} (1 \dots 10) \times 10^{-12} \text{ N}$ (Israelachvili, 2011). AFM can be used for a number of different investigations (topographical, mechanical and manipulative) and is also applied for characterizing mechanical properties of biofilms at scales of nanometers. One example is the study of Lau et al. (2009) who presented a new approach named the “microbead force spectroscopy”. A biofilm-coated glass bead ($\varnothing = 50 \mu\text{m}$, thickness of biofilm = $0.5 \dots 3 \mu\text{m}$) is attached to the cantilever and pressed on a glass surface with a specific load (see figure A.9) and for a specified period of time.

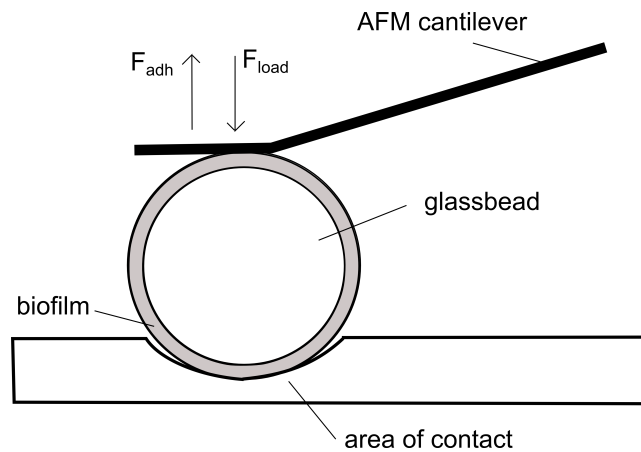


Figure A.9 Diagrammatic representation of the method to measure adhesion based on atomic force microscopy and applied by Lau et al. (2009) (modified from Lau et al., 2009). A biofilm-coated microbead is first pressed on a surface. Subsequently the microbead is retracted and the force needed is plotted against the separation distance to obtain the adhesion force.

The tip is then retracted at different specified velocities. Force-separation plots (force plots) were generated for a great number of experimental conditions and evaluated to determine the adhesive force (F_{adh} in nN). The adhesive pressure is then calculated by dividing F_{adh} by the time dependent area of contact. In this case the contact area was calculated based on Hertzian theory (for a comprehensive overview on Hertzian and JKR theory, see Israelachvili, 2011). Lau et al. (2009) reported that average adhesive pressures decreased during maturation (0 to 3 days) for two types of *P. aeruginosa* biofilms. Adhesive pressures ranged from $19 \dots 330 \text{ N/m}^2$.

Summary

Most of the methods described above are based on the same principle; to remove the biofilm from a surface with a known force and relating that force to the area of contact between the biofilm and the surface. In this way, the material property adhesion can be calculated. The methods differ in that they measure adhesion at different scales and with completely different mechanisms (adapted to the specific research objectives) resulting in adhesion values that span orders of magnitude (see Table A.3 for a summary).

What these methods have in common is that they require a mechanical failure of the biofilm and in some cases, they are not appropriate for measurements on mixed materials (e.g.

Table A.3 Overview on different methods to measure biofilm-adhesion forces and results from literature (updated from Böi et al., 2013).

Parameter	Range	Magnitude	Unit	Reference
Centrifugation device				
Adhesion strength	0.0 ... 4.9	10^1	N/m^2	Ohashi and Harada (1994)
Tensile strength	0.0 ... (> 8.0)	10^0	N/m^2	Ohashi and Harada (1996)
Micromanipulation				
Adhesive strength	0.6 ... 2.0	10^{-1}	Nm/m^2	Chen et al. (1998)
Adhesive strength	0.0 ... 1.0	10^0	Nm/m^2	Chen et al. (2005)
Microjet impingement				
Adhesive strength	0.2 ... 6.4	10^2	N/m^2	Kreth et al. (2004)
Atomic force microscopy				
Adhesion pressure	1.9 ... 33	10^1	N/m^2	Lau et al. (2009)
MagPI				
Surface adhesion	0.2 ... 1.5	10^1	mTesla	Larson et al. (2009)
Model application				
Adhesion coefficient	0.0 ... 2.5	10^0	N/m^2	Righetti and Lucarelli (2007)
Adhesion coefficient	2.0 ... 11.0	10^0	N/m^2	Righetti and Lucarelli (2010)
Adhesive strength	0.4 ... 4.5	10^0	N/m^2	Dade et al. (1990)
Adhesion coefficient	1.5 ... 3.0	10^0	N/m^2	Fang et al. (2014)

biofilm-sediment) as the samples must grow on surfaces that can be fixed to the devices (e.g. micro manipulation, centrifugation). In other cases, sediments would greatly influence the measuring results (e.g. micro jet impingement). In fact, the described methods could be used to complement data on biofilm adhesion, but they are not appropriate for the continuous monitoring of biofilm-sediment matrix adhesion on an appropriate scale (either sediment or erosion-process scale) investigated in this study. For this specific purpose the MagPI has excellent basic prerequisites (as described below).

For the sake of completeness, table A.3 also includes results of mathematical models (see “Model application”) initially developed to investigate the stability (τ_c) of biostabilized sediments from sedimentological and adhesion parameters (Righetti & Lucarelli, 2007, 2010; Dade et al., 1990; Fang et al., 2014). The proposed equations have been solved to determine the involved adhesion forces. A comparison of calculated (from the model) and physically measured adhesion forces is still not available in current literature. The model developed by Righetti and Lucarelli (2007) will be explained in detail in Section A.6 and its application is described in Section E.

Magnetic particle induction (MagPI) (Larson et al., 2009)

The MagPI is based on the principle that a number of magnetic particles which have been recently placed on an adhesive surface are retrieved by an electromagnet at a known magnetic force (magnetic flux density MFD or B [mTesla]). Figure A.10 illustrates the measuring principle of the MagPI.

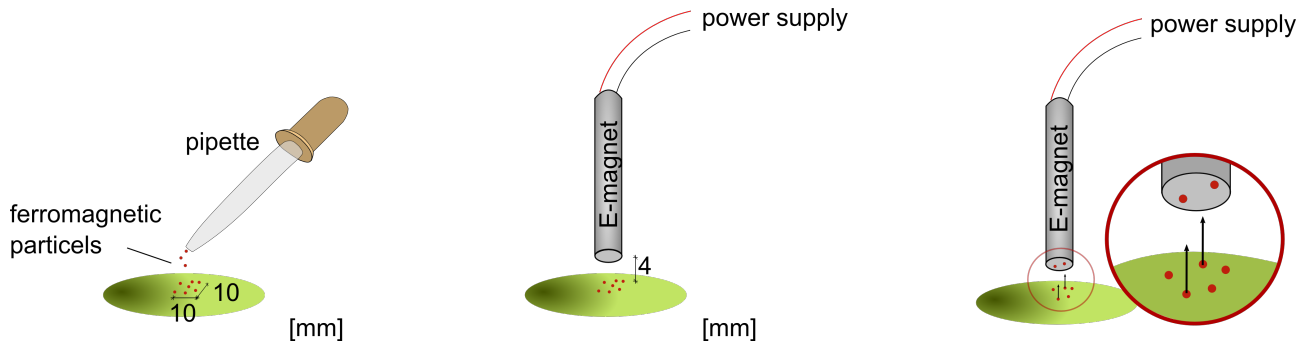


Figure A.10 The measuring principle of the original MagPI after Larson et al. (2009). *Left:* ferromagnetic particles are carefully placed on an adhesive surface. *Middle:* An electromagnet is positioned at a defined vertical distance from the particles. *Right:* The electric current of the magnet is increased and the particles are retrieved. A human operator observes the gradual detachment of the particles and relates it to predefined thresholds (e.g. “the first particle is retrieved”, “the last particle is retrieved”). These thresholds are then related to the magnetic forces which are considered as proxies for adhesion.

All measurements are conducted under water. When a particle jumps up at a given magnetic force, the retaining (i.e. adhesive) force of the surface is exceeded and the corresponding magnetic flux density is a proxy for surface adhesiveness. Due to reasons, which have not been discussed by Larson et al. (2009), not all particles are attracted simultaneously at a given MFD. Instead particle retrieving is a gradual process over a wide range of magnetic flux densities. Consequently, Larson et al. (2009) introduced four thresholds, each indicative of a different property of the surface. These thresholds (A: “initial orientation” of particles, B: “first particle is attracted”, C: “a small number of particles (around 5) are attracted” and D: “total removal of particles”) are evaluated by a human operator.

The idea of the MagPI is unique in that it is nearly non-destructive, it can be applied in-situ (a permanent magnet was also tested for that purpose but even the electromagnet setup is highly transportable) and under water (important as biofilms easily get desiccated). Its application is relatively easy and quick: an important feature in biostabilization research to account for the biofilms heterogeneity. Breaking down the principle of attracting a number of particles (n = number of particles) at a time, each single measurement provides n data on surface adhesion on a scale similar to the sediment size. Additionally, the MagPI is highly flexible, as the magnetic particle size can be adjusted to the size of the investigated sediments for different research purposes. These advantages have inspired a number of studies on biofilm adhesiveness to use the MagPI (e.g. Lubarsky et al., 2010, 2012; Anderson et al., 2011; Gerbersdorf et al., 2009).

However, the MagPI is still in its infancy as a number of issues remain unclear: The most critical issue concerns the calibration. In most of the aforementioned studies the magnetic flux density (MFD) of the electromagnet is employed as a proxy for adhesion. The MFD describes the strength of the magnetic field of the electromagnet but not the interaction between the electromagnet and the magnetic particles. The magnetic particles, however, may have magnetic properties (i.e. their capability of being attracted) varying over a wide range. Using the same electromagnet but employing different particles will not change the MFD, but may influence the results significantly. For example, particles which are more easily to be attracted will require a much lower MFD compared to other particles on the very same adhesive surface. This prohibits the comparability of values for adhesion between different laboratories when different particles (with undefined magnetic properties) and/or different particle size ranges are used. A first step into considering the mechanical forces has been done in Gerbersdorf et al. (2009) by measuring the combined lift force of several particles with a laboratory scale.

The second issue is also related to the calibration and concerns the unit of results (B in [mT]), which is not useful in the context of mechanical modeling (Vignaga et al., 2012) and currently prohibits a comparison to literature reported values of adhesion. Adhesion, as described above and illustrated in table A.3 is usually a force per area of contact. Even, when considering the MFD to be a proxy for the force needed to retrieve the particles (for example, by employing the very same electromagnet and the same particles as Larson et al., 2009) one important piece of information is missing, as the area over which the adhesion forces act on the magnetic particles is not considered. This information, however, is absolutely necessary to meet the requirements of a “material property”: As outlined by Böl et al. (2013) “the results of the characterization should be immanent to the material and independent of the applied testing method”. A comparison between the forces needed to retrieve particles of different sizes with different methods (MagPI and AFM) underlines the importance of relating these forces to the contact area. As will be demonstrated for example in Part C, the force needed by the electromagnet to retrieve a particle $\varnothing \approx 150 \mu\text{m}$ is in the micro Newton range (10^{-6}N) while the AFM force (for a biofilm-covered glass bead of $\varnothing \approx 50 \mu\text{m}$) is in the nano Newton range (10^{-9}N). A difference in the order of 10^3N .

In the present study the MagPI is modified accordingly (see part C) and the modified version is employed in experiments to relate the surface adhesion to the stabilization potential of biofilms (see Parts D and E).

A.6 The critical shear stress for motion of sediments

As outlined in the beginning, sediment entrainment or erosion of sediments is one aspect of the ETDC cycle (see Figure A.11) and since long times engineers are engaged with the task

to set up models for predicting the erosion threshold of different types of sediments. This is for practical reasons as a number of engineering structures and problems are related to sediment transport (e.g. reservoir management, scour around piles, dredging for navigation in channels and harbors, Noack et al., 2015). Moreover, understanding sediment stability is crucial for understanding ecosystem processes/function (e.g. Gerbersdorf & Wieprecht, 2015; Owens et al., 2005) and contaminant transport (e.g. Heise & Förstner, 2007; Droppo, 2009, 2001).

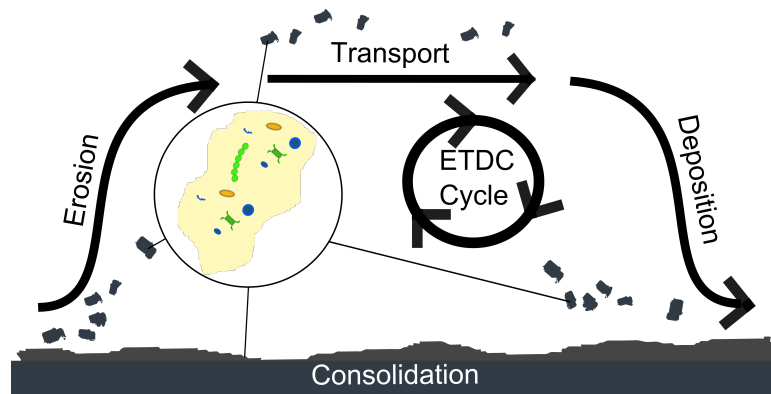


Figure A.11 Schematic representation of the erosion, transportation, deposition and consolidation cycle and the contribution of biofilms (modified from Gerbersdorf & Wieprecht, 2015). Biofilms on cohesive sediments impact sediment stability (erosion), the characteristics of suspended flocs (transportation and deposition) and chemical changes during consolidation.

According to Gerbersdorf and Wieprecht (2015) biofilms that form on or between sediments impact all components of the ETDC cycle. Sediment transportation and deposition, for example is another popular field of research as biofilms can significantly impact the characteristics of flocs (see e.g. Droppo et al., 1997; Black et al., 2001). Droppo (2001) mentions that biological constituents may influence particle size, shape, density, porosity and composition of eroded sediments with effects on their mode of transportation (bed-load, suspended load). However, as this thesis focuses on the erosion of biostabilized sediments (and not their transport), these aspects will not be further discussed, even though, as will be demonstrated in the course of this thesis (especially in Part E), the geometries of eroded flocs will play an important role.

While current models are well developed to predict erosion of clastic or granular (uniformly sized) sediments, a generally accepted theory to predict the stability of either very fine sediments ($d < 63 \mu\text{m}$, additionally stabilized by electrochemical forces, see e.g. Dade et al., 1992; Aberle et al., 2004) or biologically affected sediments (Grabowski et al., 2011; Le Hir et al., 2007) is currently not available. This is further complicated by the fact that both effects are often to be found side by side in cohesive sediments as these sediments often have high organic matter content (Dade et al., 1992; Aberle et al., 2004; Grabowski et al., 2011). For the systematic investigation on biostabilization presented in this study, biofilms are consequently cultivated on non-cohesive sediments to avoid complexity.

This section firstly provides background information about one commonly applied model to predict the stability of non-cohesive abiotic sediments (the Shields approach) followed by an overview on the current state of the art in predicting biostabilization effects (subdivided into empirical models and physics-based models to predict the erosion threshold).

A.6.1 The stability of uniform non-cohesive abiotic sediments

Sediment motion is initiated when the erosive forces exceed the resisting forces of the sediment. The erosive forces, in downstream and upward direction, are caused by the moving fluid and typically denoted as the bed shear stress (τ_b), which is *inter alia* depending on the roughness of the sediment surface. A distinction can be made between two general cases: Case 1, hydraulically smooth: The sediment size is small in comparison to the thickness of the viscous sublayer (Particle Reynolds number $Re^* < 5$ after Schlichting & Gersten, 2006) such that the roughness elements are completely enclosed. Roughness of the surface has no or little impact on the resistance to the flow and viscous shear stress plays a dominating role. Case 2, hydraulically rough: The height of Roughness elements (e.g. sediments) is larger than the thickness of the viscous sublayer, turbulent effects dominate over viscous shear ($Re^* > 70$ after Schlichting & Gersten, 2006). The flow separates behind the sediment with a turbulent wake. The roughness of the surface has a significant effect on the resistance to the flow. Moreover a transitional zone exists ($5 < Re^* < 70$ after Schlichting & Gersten, 2006), where both effects play a role. The particle Reynolds Re^* number is calculated as:

$$Re^* = \frac{u^* d}{\nu} \quad (\text{A.4})$$

with the shear velocity $u^* = \sqrt{\tau_b/\rho}$, where ρ is the fluid density, d is the particle diameter and ν is the kinematic viscosity.

Generally, the fluid forces can be divided into a horizontal drag component (F_D) and a vertical lift component (F_L). The resisting forces of the sediment are the particle submerged weight (F_G) and contact forces between the particle and adjacent/underlying particles (see Figure A.12).

Balance of forces for a single particle exposed to the flow

In order to derive the incipient motion of a single particle an analysis of the balance of forces is useful, and serving as a basis for studies on sediment entrainment under different conditions (e.g. for heterogeneous sediments: Wiberg & Smith, 1987 or for biostabilized sediments: Righetti & Lucarelli, 2007, as will be demonstrated in Section A.6.3).

Figure A.12 illustrates schematically the forces that act on a single particle exposed to a fluid in motion. Frictional forces between the particles are not considered here. In other words,

the particle pivots around point P in the direction of easiest movement (Southard, 2006) instead of sliding on the adjacent particles.

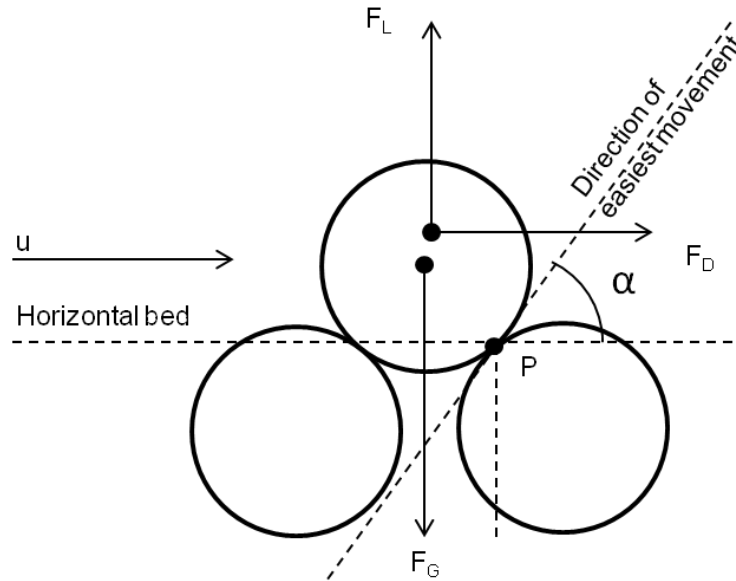


Figure A.12 Forces balance on a spherical sediment at the surface of a bed (modified after Righetti & Lucarelli, 2007)

Furthermore the lift force due to fluid flow is neglected (as was done by Shields, 1936) and a horizontal bed is assumed. Calculating the balance of forces at the initiation of movement, the overturning moment (due to drag) as well as the restoring moment (due to gravity) around point P, yields:

$$a_1 \cdot (F_G \sin \alpha) = a_2 \cdot (F_D \cos \alpha) \quad (\text{A.5})$$

with α the angle between the horizontal bed and the direction of easiest movement of a particle, a_1 and a_2 are here the normal distances to the point P and are depending on the particle geometries and in case of a_2 also on the characteristics of the flow (due to the complex distribution of pressure and viscous shear on the surface of the particle the exact position of F_D is unknown (Southard, 2006)). F_G can be written as:

$$F_G = c_1 \cdot d^3 (\rho_s - \rho) g \quad (\text{A.6})$$

where c_1 is a particle-shape parameter and $(\rho_s - \rho)$ is the difference in densities of the particle and the fluid. Equation A.7 on the other hand further defines the drag force of the fluid as depending on the square of the particle diameter d , the bed shear stress at initiation of motion τ_c and c_2 - a coefficient taking the variation of drag on the surface into account, as

well as the geometry and packing of the particles (Southard, 2006):

$$F_D = c_2 \cdot d^2 \tau_c \quad (\text{A.7})$$

Substitution of equations A.6 and A.7 into equation A.5 and solving for the critical bed shear stress (τ_c) yields:

$$\tau_c = \frac{a_1 c_1}{a_2 c_2} (\rho_s - \rho) g d \tan \alpha \quad (\text{A.8})$$

According to Southard (2006) division of both sides by $(\rho_s - \rho) g d$ the Equation A.8 is made dimensionless, which yields the Shields parameter Θ_C :

$$\Theta_C = \frac{\tau_c}{(\rho_s - \rho) g d} = \frac{a_1 c_1}{a_2 c_2} \tan \alpha = f(Re^*) \quad (\text{A.9})$$

which will be further discussed in the following paragraphs. It is important to note that the described model is an oversimplification of erosion under strictly idealized conditions. Still, this model is the basis for the commonly applied Shields equation and a number of modifications hereof. The right hand side of equation A.9 further demonstrates that the Shields parameter is depending on the particle geometries but also the distribution of pressure and viscous shear which in itself can be expressed as a function of the particle Reynolds number Re^* or as a function of the dimensionless particle characteristic diameter d^* . Before discussing the Shields approach, two other famous plots explaining the relationship between the particle diameter and erosion/deposition are briefly explained.

The Hjulstrøm and Postma diagrams (Hjulstrom, 1939; Postma, 1967)

An intuitive approach to investigate sediment dynamics is to relate the mean flow velocity to the particle size as both parameters are relatively easy to determine (in the laboratory as well as *in-situ*). Figure A.13 *Left* illustrates such a relationship as was published in the early work of Hjulstrom (1939).

An advantage of this plot is that it readily illustrates the common perception that higher mean flow velocities are needed for erosion as the particle size increases. The same holds true for decreasing particle sizes. Hjulstrom (1939) explained the latter phenomenon by the cohesive effects of very fine material. In fact, electrochemical forces such as van der Waals forces, are responsible for the cohesion between e.g. the clay particles (Grabowski et al., 2011). Additionally, fine sediments are composed of organic materials such as living organisms, detritus, fecal pellets, extracellular polymeric substances (EPS), and organic colloids, which impact sediment stability to a more or less degree (Grabowski et al., 2011). It is noteworthy

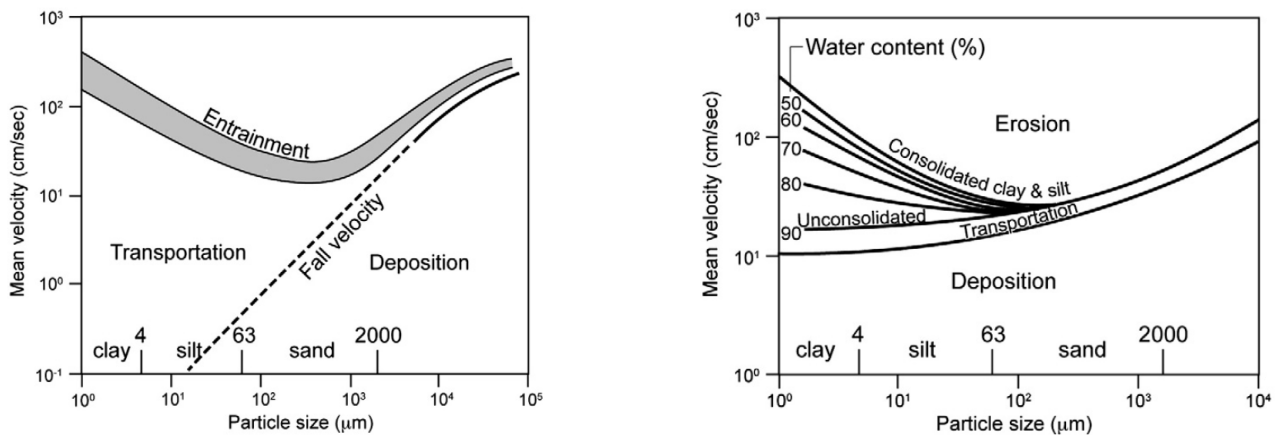


Figure A.13 Popular diagrams relating the mean velocity to sediment transport (after Grabowski et al., 2011). *Left:* The Hjulstrøm diagram (Hjulstrom, 1939). *Right:* The Postma diagram (Postma, 1967)

that, these constituents not only increase the biostabilization potential, as biodestabilization due to bioturbation of e.g. burrowing worms is also possible (Meysman et al., 2006).

Besides these biological impacts, it has been demonstrated in a number of studies (e.g. Jepsen et al., 1997) that the bulk density or water content can have a decisive effect on the stabilization potential. Accounting for these “density-effects” the Postma plot (Figure A.13 *Right*) has been developed (Postma, 1967). It illustrates that for fine sediments, the mean velocity necessary to erode sediments increases with decreasing water content which is well in line with the general trend reported in literature (Grabowski et al., 2011).

The information that is provided by these two diagrams is somewhat misleading concerning the quantitative predictability of erosion thresholds from these measured variables especially for the fine sediment fraction: 1. The data for particles $< 100 \mu\text{m}$ is based on observations rather than on empirical data (Dade et al., 1992) 2. the processes in the fine sediment region are too complex to be expressed in this simple form (comprehensive lists of parameters which might influence stability are available in e.g. Berlamont et al., 1993; Grabowski et al., 2011) and 3. while it seems appealing to use a depth averaged velocity, this parameter is insufficient to describe the complex interactions between hydrodynamics and roughness in the near bed region. As a consequence, these plots predominantly serve illustrative purposes and “no great numerical value should be attached to [the left side of these figures]...” as fairly mentioned also by Postma (1967) (Dade et al., 1992).

The Shields approach (Shields, 1936)

In the 1930’s the American engineer A. Shields published his seminal work “Anwendung der Ähnlichkeitsmechanik und der Turbulenzforschung auf die Geschiebebewegung” (Shields, 1936) based on dimensional analysis and fluid mechanics considerations. The famous Shields diagram (see Figure A.14) has since then been applied and modified frequently

(Miedema, 2010).

As outlined before (see equation A.9) the Shields parameter Θ depends on the critical shear stress τ_c , the difference between the sediment density and the fluid density $\rho_s - \rho$, as well as the gravity g and the particle diameter d . The diagram (Figure A.14) illustrates that Θ can be expressed as a function of the particle Reynolds number (see equation A.4). Taking into account the scattering of his experimental results Shields (1936) presented his curve as a range (the dotted area in Figure A.14) rather than a direct functional relationship.

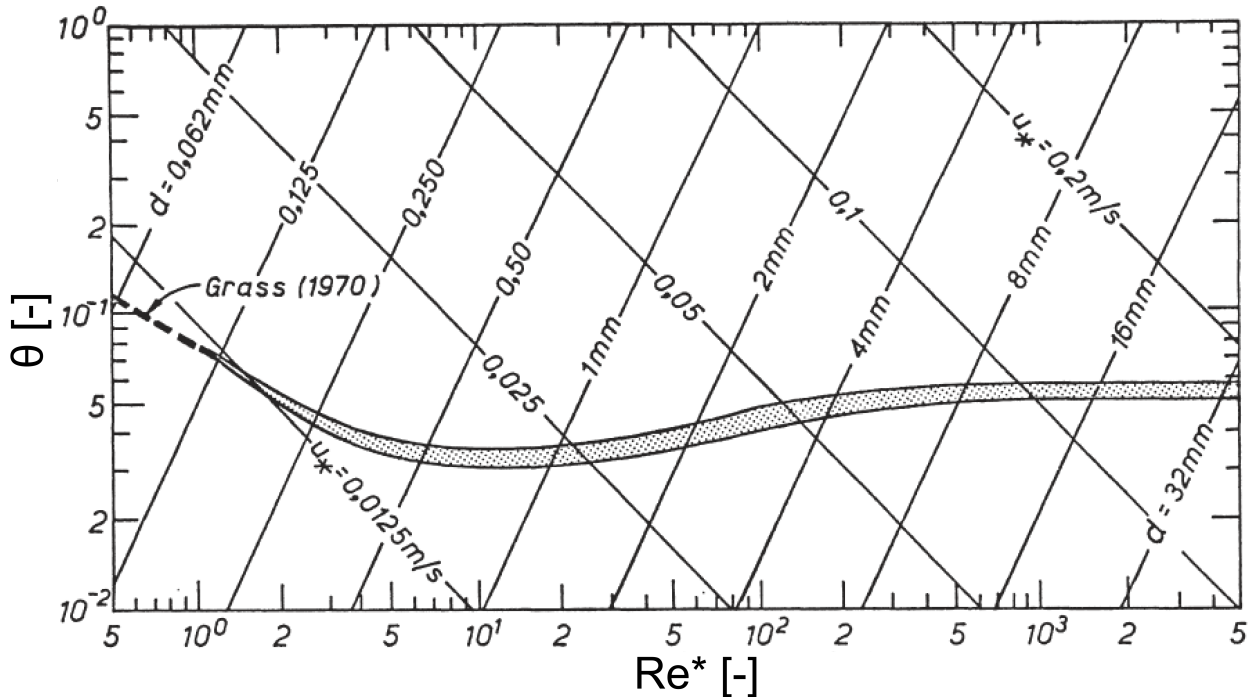


Figure A.14 The Shields diagram (after Raudkivi, 1982)

At high particle Reynolds numbers (where the near bed hydrodynamics are characterized by turbulence) the Shields parameter approaches asymptotically a value of $\approx 0.05 \dots 0.06$. On the other side of the diagram (the left side), Θ increases with decreasing Re^* , indicative for the additional binding forces for fine sediments due to electrochemical forces between the grains but probably also due to biological binding. As outlined before, for $Re^* < 5$ the surface can be considered to be hydraulically smooth, as a result the particles are additionally “protected” from the impact of pressure forces caused by turbulence (outweighed by the cohesive/adhesive forces). At $Re^* \approx 10$ (corresponding to the transitional zone) the Shields parameter reaches a minimum ($\Theta \approx 0.03$).

To construct the curve Shields (1936) conducted a number of flume experiments with differently sized sediments (0.85 \dots 3.4 mm) which also differed in their density (1.06 \dots 4.2 g/cm³). The erosion threshold was calculated by means of measuring the rates of transport and extrapolation to the zero rate value (Southard, 2006). The data set on which the curve was constructed is limited to $2 < Re^* < 600$ and rather uniformly sized sediments, furthermore

the lift force was neglected. This inspired a number of further research and modifications of the Shields curve (Wiberg & Smith, 1987; Raudkivi, 1982; Miller et al., 1977). Buffington and Montgomery (1997) further demonstrated significant differences between an observational determination of incipient motion and the reference bed load transport rate method.

Furthermore, different approaches have been made to parameterize the Shields curve (Miedema, 2010). One approach is a parameterization with a dimensionless characteristic diameter d^* . The following fit equation was introduced by Brownlie (1981), based on the Bonneville parameter:

$$\Theta_C(d^*) = 0.22d^{*-0.9} + 0.06e^{-17.77*d^{*-0.9}} \quad (\text{A.10})$$

with $d^* = d(g\Delta/\nu^2)^{1/3}$ and the relative density of the particle $\Delta = (\rho_s - \rho)/\rho$. There are numerous other fit equations published (e.g. Wu & Wang, 1999). In this study the “Brownlie fit” will be used following the approach of Righetti and Lucarelli (2007) to modify the Shields approach taking into account cohesive/adhesive forces (see Section A.6.3 and Part E).

A.6.2 The stability of biostabilized sediments

As outlined above, the traditional (and mostly accepted) theories to predict the stability of sediments are limited to non-cohesive abiotic sediments therefore new approaches have to be developed for biostabilized sediments. According to Grabowski et al. (2011) “the development of a unifying equation to predict erodibility [of cohesive biotic sediments] based on sediment properties is difficult, if not impossible, because of a lack of a complete mechanistic understanding of how the key sediment properties interact to influence erodibility”. In this regard, the list of key properties is long (Grabowski et al., 2011; Berlamont et al., 1993), and further extending depending on the disciplines involved.

Moreover, Grabowski et al. (2011) explicitly recommends laboratory experiments where the environmental conditions can be controlled as a ranking of the key sediment properties is impeded so far by the great variability of site specific properties measured *in-situ* (a combination of physical, geochemical, and biological properties). This conclusion is perfectly in line with Le Hir et al. (2007) who published an insightful review on the state of the art in predicting the erodibility of biostabilized sediments (at that time) to account for biota effects in sediment transport modeling.

Nevertheless, an overview on the different approaches to predict biostabilization based on biological and/or physical properties is presented below with the aim to inform the reader about the progress that has recently been made but also the drawbacks of individual approaches. This section is divided into two paragraphs: empirical models and physics-based

models, following the structure of Grabowski et al. (2011).

Empirical approaches

In the context of this thesis, empirical approaches are defined as investigating the correlation between different measurements or observations and sediment stability, without necessarily being physically correct. In most such approaches one or more sediment properties (e.g. EPS) that are believed to be a proxy for a physical phenomenon (e.g. the binding between grains, De Brouwer et al., 2002), are correlated to the critical bed shear stress. This approach has considerable advantages over physics-based models as the number of parameters that must be investigated could be hypothetically lower, the measuring methods well established and their results can be evaluated quickly.

One example for an empirical model is relating the chl *a* (chlorophyll *a*) content to sediment stability as was frequently done in the beginning of the 21st century. This approach is especially interesting as chl *a* can be mapped via remote sensing (Le Hir et al., 2007), which would allow to predict sediment stability quickly and over large areas. Lucas et al. (2003) showed that chl *a* content is a reasonable measure for colloidal carbohydrate content and furthermore, both chl *a* and colloidal carbohydrates were high when the threshold for erosion was high. Widdows et al. (2000) deployed a small annular flume on a research vessel to conduct erosion tests and found that both chl *a*/colloidal carbohydrate had a significant correlation to sediment stability.

Still, the correlation between chl *a*/carbohydrates and erosion threshold seems to be ambiguous. Riethmüller et al. (2000), studied areas of tidal flats of the Danish and German Wadden Sea by means of chl *a* content, analysis of the microphytobenthos composition and erosion measurements with a round shaped mesocosm. Their results indicate that the relationship between chl *a* and erosion threshold is highly site specific to be explained by differences in the microbial community and intensity of surface reworking (by e.g. grazing). This is well in line with the meta analysis of Le Hir et al. (2007), who conclude that no universal relationship can be established between chl *a* content and erodibility. Please see also Figure A.16 illustrating the spatial differences between the correlation chl *a* - erosion threshold at different stations of the German Wadden Sea and additional information from other sources.

According to Le Hir et al. (2007) this deficit can be explained by the sampling procedure for chl *a* determination, inconsistencies in the method to determine the stability and (spatial/temporal) differences in physical properties of the sediments (rheology, water content, etc.). Considering the latter, a more reasonable approach would be a multivariate regression, considering more than one parameter to estimate the biostabilization potential. Friend et al. (2003) conducted a principle component analysis (PCA) and reported that not chl *a* but

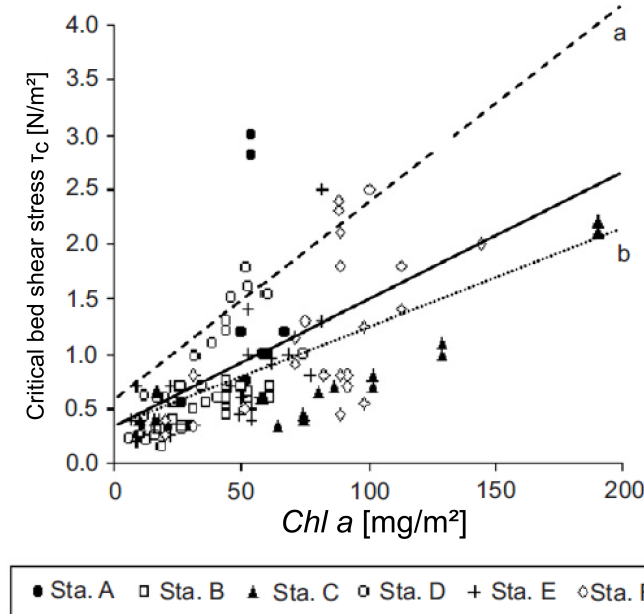


Figure A.15 The relationship between chlorophyll a and the critical bed shear stress studied at different stations (abbreviated by “Sta.”) located in an intertidal flat (data from Lanuru, 2004, diagram after Le Hir et al., 2007). The solid line is the corresponding linear regression. Additional regression curves from literature. Dashed line: Defew et al. (2003). Dotted line: Riethmüller et al. (1998).

both elevation (above mean low water spring) as well as colloidal carbohydrates are the best predictors for biostabilization. Additionally, Yallop et al. (2000) presented a preliminary multivariate regression model to predict the erosion threshold from chl *a*, colloidal-S EPS and water content. These approaches may be especially useful in investigating the importance of potential impacts on stabilization and to identify key sediment properties (Grabowski et al., 2011). Nevertheless, a prerequisite for such an analysis is comparability between the different methods and techniques (Grabowski et al., 2011) applied in biostabilization research.

Physics-based approaches

According to Grabowski et al. (2011) considerable progress has been made recently towards the development of physics-based models to predict biostabilization. These models try to explain the mechanical failure of biofilm-sediment matrices from a physical point of view, analogous to models on predicting abiotic non-cohesive sediment entrainment (e.g. the Shields approach, as presented above). It is noteworthy though that even the physics-based models rely on empirical parameters. For example, the Shields parameter is empirical as it summarizes effects which cannot be measured accurately (at least to solve the problem for a natural heterogeneous bed and turbulent flow).

Still, the basic principles of sediment erosion are known and only little militates against adapting the theories to biostabilization (the exceptions will be discussed later) by introducing adhesion/cohesion effects and testing them (Grabowski et al., 2011).

Dade et al. (1992)

Probably the first physics-based model for biostabilization was introduced by Dade et al. (1992). The model is based on the balance of forces between hydrodynamics and the resisting forces of a single particle on a geometrically flat bed. The forces under considerations are: the immersed weight of the grain, net particle adhesive/cohesive forces, the drag and lift forces and the particle packing angle. Dade et al. (1992) developed their model on the assumption of a hydraulically smooth bed ($Re^* < 3$) as particles are small relative to the thickness of the viscous boundary layer. Their mathematical expression contains a term, namely F_A/F_G that relates the particle-specific adhesive force, F_A [N/grain] to the immersed weight of a grain (F_G [N/grain]). In a previous study (Dade et al., 1990) evaluated the results of erosion measurements on quartz grains mixed with either extracted exopolymers or *in-situ* secreted polymers from the culture of *Pseudomonas Atlantica* to estimate the F_A/F_G ranging between 0.9 . . . 11.4 (in Table A.3 the F_A was divided by the surface area of one quartz grain to present comparable values). According to Dade et al. (1992) a ratio $F_A/F_G > 1$ indicates that erosion resistance is primarily due to particle interaction, while for $F_A/F_G < 1$ both gravitational forces and adhesion/cohesion is responsible. Further Dade et al. (1992) promote the use of yield stress measurements to determine F_A , an interesting approach that is yet to be tested, but probably not applicable to natural biostabilized sediments which are naturally highly heterogeneous.

Fang et al. (2014)

In 2014 Fang et al. (2014) reported on two approaches to predict the erosion threshold of biostabilized sediment. While the model, considering the rolling of biostabilized aggregates, is basically identical with the model that will be discussed below (Righetti & Lucarelli, 2007) the second approach considers sliding. Consequently Fang et al. (2014) introduced an additional frictional force which they accounted for by the use of film water theory. By conducting experiments in a straight flume Fang et al. (2014) calculated the adhesion coefficient that ranged between 0.4 . . . 4.5 N/m² for biofilms cultivated on two differently sized sediments.

Vignaga et al. (2013)

The approach described by Vignaga et al. (2013) differs significantly from all other discussed approaches. Vignaga et al. (2013) assume that the traditional models (at incipient motion the bed failure is characterized by rolling, sliding or lifting of single grains) fail in describing the process of “biofilm-mat” erosion. A “biofilm-mat” is one specific type of biofilm (gelatinous, as a “carpet” on top of the bed, see Figure A.16) which is to be found in marine environments⁹.

Vignaga et al. (2013) reported that the biofilm-bound mat oscillates in the flow at increasing flow velocities until it suddenly fails. In their model they accounted for that behavior

⁹This type of biofilm has also been observed during the experiments of this thesis; its erosion mechanism is described in Part B

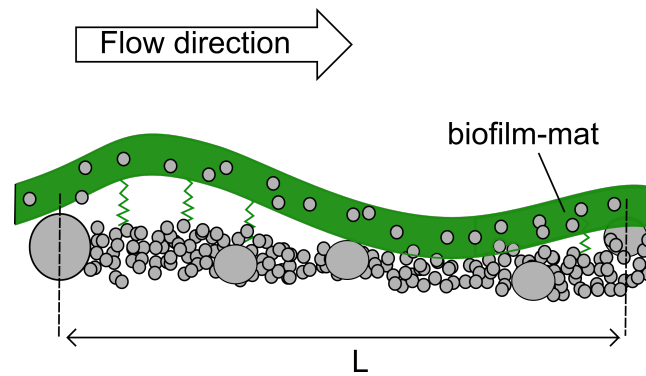


Figure A.16 Schematic diagram of oscillations of a biofilm-mat caused by fluid flow (modified after Vignaga et al., 2013)

by means of an oscillating membrane and found that the “the horizontal length scale over which oscillations occur is a controlling factor for incipient sediment entrainment”. While the development of the model may greatly assist in understanding bio-mat failure, it is questionable if the proposed model is (at the current time) of practical engineering relevance, as the proposed variables the model relies on, can currently only be measured under laboratory conditions.

A.6.3 The modified Shields approach after Righetti and Lucarelli (2007)

In 2007 Righetti and Lucarelli published their paper with the title: “May the Shields theory be extended to cohesive and adhesive benthic sediments?”. Righetti and Lucarelli (2007) modified the Shields approach by further considering adhesive and cohesive forces together with the near-bed hydraulic conditions. Righetti and Lucarelli (2007) emphasize that the proposed approach complies with dimensional analysis - a critical point which was raised in the discussion by You (2004) on the seminal publication of Lick et al. (2004) and which is a basis for the modified Shields approach for Righetti and Lucarelli (2007).

Particularly interesting is that the proposed approach considers aggregates/flocs properties instead of primary particles (Grabowski et al., 2011). By carefully evaluating data obtained from sediment cores (including: the critical bed shear stress τ_{cs} , macroaggregate density ρ_b and macroaggregate diameter D), they were able to calculate an adhesion coefficient (A , which will be later on referred to as the effective adhesion A_{eff}) which they then correlated to the organic matter content (OM) of the samples. In a follow up study Righetti and Lucarelli (2010) took samples of three more alpine lakes at different seasons to demonstrate seasonal differences.

The modified Shields model will be applied in Section E of this thesis by correlating real measured surface adhesion with the adhesion coefficient. The theoretical background is given below. It is important to note, that the proposed model comprises both terms for adhesive as

well as cohesive effects. Righetti and Lucarelli (2007), however defined “cohesion” only “as the result of attractive van der Waals interactions between particles of the same medium, saturated with clear water”, while “the adhesion can be defined as any additional binding forces due to variation in composition of the second interparticle medium [e.g. the biofilm], with respect to the clear water”. In fact, this definition is unclear, as the binding between flocs, can, besides the mentioned cohesive van der Waals forces between primary particles and the adhesive forces between particles and EPS, also originate from bio-cohesive forces between EPS-EPS.

In this thesis, however, the cohesive EPS-EPS forces are likewise neglected (as was also done by Righetti and Lucarelli (2007, 2010)), as the focus is on measuring sediment-EPS adhesion. Still, for future research, it is highly recommended to also identify cohesive EPS-EPS interactions to unravel the phenomenon of biostabilization.

Following the definition of Righetti and Lucarelli (2007), the cohesive (particle-particle) term is irrelevant to this study, as the biofilm is cultivated on non-cohesive glass beads ($100 < d < 200 \mu\text{m}$). Therefore, the model will be explained focusing solely on the adhesive and excluding the cohesive term (this is possible, and has also been done by Righetti and Lucarelli (2010), as the approach is dimensionally consistent).

Theoretical framework for adhesive individual particle entrainment

Figure A.17 shows the resisting (the submerged gravitational force: F_G) and external forces (lift force: F_L and drag force: F_D) on a single particle (as already discussed in Section A.6.1) considering additionally a vertical adhesive force F_A .

The particle is expected to pivot around point P at initiation of movement. The balance of forces around point P is then:

$$F_D \cdot b = (F_G + F_A - F_L) \cdot a \quad (\text{A.11})$$

with a, b the normal distances to point P. Further F_G can be defined as $F_G = (\rho_s - \rho)g\alpha_3 d^3$ as the volume of the particle is proportional to $\alpha_3 d^3$, where α_3 is a shape factor that is assumed to be equal to $\pi/6$ for near spherical particles. The drag and the lift force can be expressed by means of the shear velocity:

$$F_D = C_1 \rho u_*^2 d^2 \quad (\text{A.12})$$

$$F_L = \eta F_D \quad (\text{A.13})$$

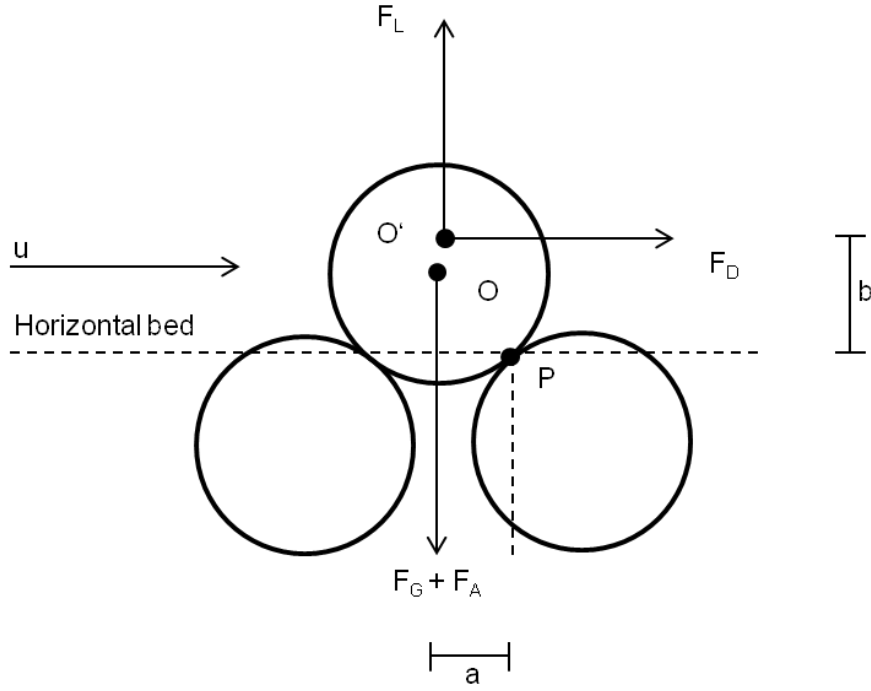


Figure A.17 Forces balance on a spherical grain at the surface of a bed considering additionally adhesive forces (modified after Righetti & Lucarelli, 2007)

with C_1, η being appropriate functions of Re^* (see Righetti & Lucarelli, 2007). The shear velocity is defined as $u^* = \sqrt{\tau_b/\rho}$. Combining equation A.11 with A.12 and A.13 and the definition of u^* yields:

$$\frac{\tau_c}{(\rho_s - \rho)gd} = \frac{\alpha_3^{a/b}}{(1 + \eta^{a/b})C_1} \left(1 + \frac{1}{\alpha_3} \frac{F_A}{(\rho_s - \rho)gd^3} \right) \quad (\text{A.14})$$

Neglecting the adhesion force (i.e. $F_A = 0$) yields the traditional Shields parameter (here renamed to Θ_{C_0} as Θ_C is now a combination of the traditional Θ_{C_0} and an adhesive contribution):

$$\Theta_{C_0}(d^*) = \frac{\alpha_3^{a/b}}{(1 + \eta^{a/b})C_1} \quad (\text{A.15})$$

where d^* can be calculated from the fit equation developed by Brownlie (equation A.10). Substitution of A.15 into A.14 yields:

$$\frac{\tau_c}{(\rho_s - \rho)gd} = \Theta_{C_0}(d^*) + \frac{\Theta_{C_0}(d^*)}{\alpha_3} \frac{F_A}{(\rho_s - \rho)gd^3} \quad (\text{A.16})$$

So far, F_A is the binding force of a single grain to its surrounding material and the direction of that force is vertical. One can easily imagine, that F_A depends not only on the adhesion but also on the size of the grain. For example, a larger grain has a larger area of contact to

the surrounding adhesive material and consequently, the adhesive force F_A is also greater. After Lick et al. (2004) the adhesion scales with the square of the particle diameter:

$$F_A = A_{eff} \cdot d^2 \quad (\text{A.17})$$

where $A_{eff} [\text{N}/\text{m}^2]$ is the adhesion coefficient as defined by Righetti and Lucarelli (2007). It is intuitive to assume that more parameters, besides the diameter and the adhesion, influence the adhesive force F_A . One example would be the surface morphology and -chemistry of the grain (see e.g. Palacio & Bhushan, 2012; Zafar et al., 2014). Therefore A_{eff} shall be treated as an “effective” adhesion, incorporating all the aforementioned impacts (and probably more), which, multiplied with the square of the particle diameter gives the additional vertically directed force due to adhesion. In contrast, a “real” adhesion is a material property which is immanent to the material and not depending on e.g. the characteristics of the surface it sticks to (Böl et al., 2013). To be more clear about the difference between a (measured) “real” adhesion and A_{eff} , the adhesion coefficient is written with the index “*eff*” for “effective”.

Theoretical framework for adhesive floc entrainment

According to Righetti and Lucarelli (2007) equation A.16 can likewise be applied for floc erosion simply by replacing the particle diameter d with the aggregate/floc diameter D , d^* with D^* and the particle density ρ_s with the aggregate/floc bulk density ρ_b . Combining now equation A.16 with equation A.17 and considering the above mentioned yields:

$$\Theta_C = \frac{\tau_c}{(\rho_b - \rho)gD} = \Theta_{C0}(D^*) + \frac{\Theta_{C0}(D^*)}{\alpha_3} \frac{A_{eff}}{(\rho_b - \rho)gD} \quad (\text{A.18})$$

or in a general form:

$$\Theta_C = \Theta_{C0}(D^*) + \Theta_{CA}(D^*) \quad \text{with} \quad \Theta_{CA}(D^*) = \frac{\Theta_{C0}(D^*)}{\alpha_3} \frac{A_{eff}}{(\rho_b - \rho)gD} \quad (\text{A.19})$$

Equation A.19 illustrates that the additional contribution to the Shields parameter due to adhesion $\Theta_{CA}(D^*)$ can be calculated by the determination of the traditional Shields parameter for flocs (i.e. based on D^* using the Brownlie fit, equation A.10) and subtraction from the measured $\Theta_C = \frac{\tau_c}{(\rho_b - \rho)gD}$. Further, A_{eff} can be calculated by solving Equation A.19 *Right*.

Besides the development of the theoretical framework, Righetti and Lucarelli (2007) proposed an original method to evaluate data, based on a set of samples (sediment cores) they took from different lakes. For the definition of the incipient motion threshold they applied image processing on images of eroded flocs to obtain the total area of eroded flocs with bed

shear stress. Further they used microscope pictures to obtain the eroded floc size distribution and defined a criterion for the macroaggregate size D (will be discussed in part E). Their results clearly demonstrate the additional stability due to adhesive forces as compared to the traditional Shields curve (see Figure A.18) as the measured Θ_C is well above $\Theta_{C0}(D^*)$.

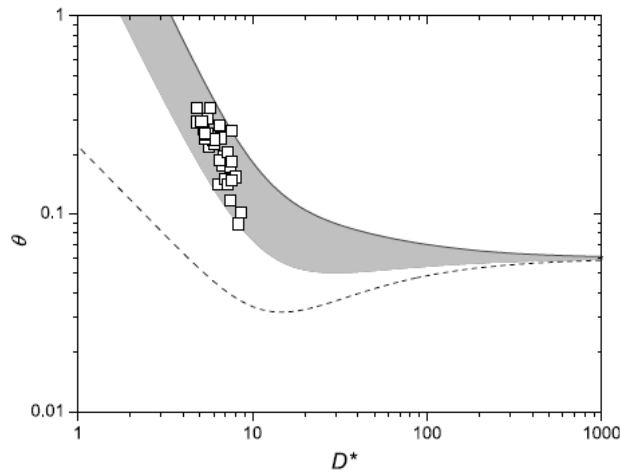


Figure A.18 Comparison between the “traditional” Shields curve and measured values of biostabilized sediments. The measured values are well above the traditional curve (from Righetti & Lucarelli, 2007)

By solving equation A.18 Righetti and Lucarelli (2007) calculated the adhesion coefficient ranging between $A_{eff} = 0 \dots 2.5 \text{ N/m}^2$, while in the follow up study (Righetti & Lucarelli, 2010) adhesion coefficients between $A_{eff} = 2 \dots 11 \text{ N/m}^2$ were obtained. In both studies the adhesional effects were related to the production of EPS in biofilms.

Part B

BIOSTABILIZATION UNDER DIFFERENT ENVIRONMENTAL CONDITIONS

This part is a slightly modified version of Thom et al. (2015a)

Biofilms consisting of microphytobenthos (e.g., diatoms, cyanobacteria), heterotrophic bacteria, and their secreted extracellular polymeric substances (EPS), grow on boundary surfaces, for instance on the river bed. The EPS matrix fulfills various ecological functions for the microbes (Flemming & Wingender, 2010) and the adhesive properties of the polymers “virtually glue sediment particles together” to increase bed stability (Gerbersdorf & Wieprecht, 2015); a process named biostabilization (Paterson, 1989). These binding forces depend on EPS quantity and quality, both of which are influenced by numerous biotic (succession, grazing, competition, etc.) and abiotic (light regime, hydrodynamic regime, temperature, nutrients, sediment composition, etc.) parameters. Complex mutual feedback mechanisms between biofilm growth and the environmental conditions impeded so far the general understanding of the phenomenon biostabilization. Consequently, to date, no reliable model exists to predict biostabilization in a morphological context (Grabowski et al., 2011).

The DFG (Deutsche Forschungsgemeinschaft) project “Sediment entrainment and flocculation mediated by microbial produced extracellular polymeric substances (EPS)” combines hydraulic engineering and (micro-) biological science to investigate biostabilization in different niches of freshwater with the long-term goal to develop a morphological model. In contrast to limnic systems, biostabilization has been extensively investigated within the marine and brackish water environment, which revealed the high microbial binding capacity as opposed to less stable, abiotic sediments. For example, Tolhurst et al. (1999) reported a five-fold increase of critical bed shear stress in an intertidal area colonized by diatoms as compared to uncolonized sediments. Interestingly, biostabilization varies significantly between the investigated field sites, which might be explained by highly variable environmental conditions and their impact on biota development. For example, Widdows et al. (2000) reported a higher stability in the central part of a tidal flat as compared to its edges. Addi-

tionally, they reported that biostabilization capacity differed during the course of a year with higher biostabilization during June compared to September. In situ measurements in the Venice Lagoon by Amos et al. (2004) confirmed that bed strength in summer exceeded winter stability up to five times.

Field studies are important to understand biostabilization under natural conditions, but it is nearly impossible to unravel the influence of individual environmental parameters in these complex systems. This, however, is a prerequisite for models which aim to predict the impact of changes in biotic and abiotic conditions on biofilm growth and functionality. While most fundamental laboratory studies link environmental conditions to microbial settlement and biofilm growth there is little information available regarding consequences on the stabilizing effect of the biofilm. An exception can be found in Fang et al. (2014) who investigated the impact of sediment particle sizes on the critical bed shear stress of a developing biofilm in a laboratory setup and reported increasing stability up to a threshold level after which the stability declined again. Another laboratory experiment was conducted by Droppo et al. (2007) who explained fluctuations in bed stability by alternating development and decay processes of biofilm layers.

Few studies have emphasized the complex mechanisms between biofilm growth and bed shear stress. In this context, the role of hydrodynamics on biofilm growth shows a certain degree of complexity. For example, Stoodley et al. (1998) determined a higher bed colonization rate of microbial cells under laminar conditions. On the other hand, it is well known that microbes actually profit from the higher nutrient availability due to higher mixing rates as flow rates increase (Nikora, 2010). However, high energy impact by flow might induce the detachment (“sloughing off”) of biofilms (Characklis & Cooksey, 1983) with possible consequences for biostabilization. In the study of Pereira et al. (2002), higher flow velocities during cultivation led to a reduction in biofilm thickness and simultaneously increased biofilm density which has implications for nutrient access and sediment stability. Hence, hydrodynamic forces shape the biofilm topography while the biofilm structure itself may impact its own physical environment by modifying the near-bed hydrodynamic conditions, e.g. by shifts in the roughness length (Nikora, Goring, & Biggs, 2002) or reducing drag at high flow velocities while enhancing nutrient transport at low flow velocities (Larned et al., 2011).

Erodibility of biostabilized sediments also depends on the structures that the biofilms form under different environmental conditions. Consequently, the understanding of mechanical properties is an important prerequisite for the development of a unifying equation to predict erodibility (Grabowski et al., 2011). Unfortunately, very little information is available on the relation between environmental conditions and the mechanical structure of the biofilm/sediment matrix and its response to increasing bed shear stress. One exception is Vignaga et al. (2013) who investigated cyanobacterial mats exposed to increasing bed shear

stress and compared their mechanical behavior to an elastic, oscillating membrane that suddenly fails.

The intention of this paper is 1) to show the impacts of hydrodynamics and light regime on biostabilization of river bed sediments in different seasons and 2) to give an overview of the mechanical processes of the biofilm/sediment mixture observed during erosion. For this purpose, biofilm is grown over 4 . . . 8 weeks within specifically designed straight flumes by the circulation of natural river water over artificial sediments. This paper demonstrates the results and observations from stability measurements made in five experimental runs in different seasons; each of them focusing on the impact of either hydrodynamics or light intensity, both varied at three different levels during cultivation. The data presented here contribute to a fundamental understanding of the phenomenon of biostabilization under varying abiotic conditions.

B.1 The experimental setup

B.1.1 The setup for the cultivation of biofilms on artificial sediments

The experimental setup consists of six identical straight glass flumes ($l \times w \times h = 3.00 \times 0.15 \times 0.15 \text{ m}^3$) with individual water and cooling circuits, regulated discharges, and adjustable light intensities (Figure B.1 *Left*). Two containers encase three flumes each to avoid any possible contamination and the influence of ambient light (Figure B.1 *Right*). Each flume consists of an inlet flow section and a biofilm growth section with fully turbulent flow conditions.

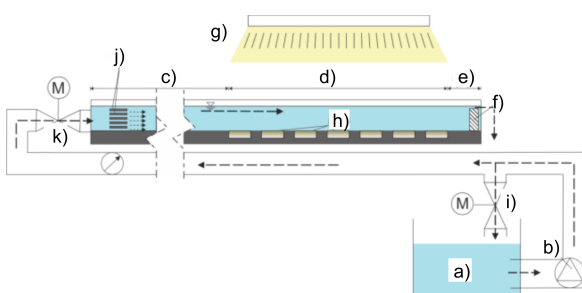


Figure B.1 The experimental setup for biofilm cultivation. *Left*: (a) Outflow tank, (b) pump, (c) inlet flow section with baffles, (d) biofilm growth section, (e) outlet flow section, (f) weir, (g) fluorescent tubes, (h) sediment cartridges, (i) bypass, (j) current abatement, (k) fine tuning valve (after Thom et al., 2012). *Right*: View into one of the two containers with three identical straight flumes.

To ensure various but defined light intensities, two parallel OSRAM Biolux[®] fluorescent tubes can be adjusted in height according to the calibration by a high resolution spectroradiometer (SR-9910, Macam Photometric Ltd., Scotland) done prior to the experiments. At the same time, these calibrations revealed a homogeneous light intensity distribution in the PAR (photosynthetic active radiation, 400 . . . 700 nm) range over the whole growth section. During the experiments, three different light intensities are set-up to mimic natural illumination in various

niches according to Table B.1, while applying an 8/16 hours day/night cycle.

Table B.1 Boundary conditions applied in the experiments and the specific notations used in the following text.

Notations used in the text	Light intensity (LI) [$\mu\text{mol}/\text{m}^2\text{s}$]	Bed shear stress τ_b [N/m^2]	Temperature [$^{\circ}\text{C}$]
Low/None	0	0.02	15
Medium	50	0.04	15
High	100	0.08	15

The water temperature that is vital for biological processes is kept at 15°C by heat exchangers supplied with colder water (8°C). This initial temperature is needed to compensate for the additional heating by the activity of the pumps. The biofilm growth section contains sixteen removable PVC cartridges ($l \times w \times h = 88 \times 58 \times 18 \text{ mm}^3$, Figure B.2 *Left*) holding the sediment for biofilm growth. To ensure minimal disturbance of the hydraulic regime, the cartridges are fitted into PVC frames that are planar with the flume bottom, as illustrated in Figure B.2 *Right*. However, as biofilm grows on the sediment, this setup leads to flow perturbations on the up- and downstream edges of the cartridges due to changes in roughness (transition between sediment and the PVC frames), resulting in localized higher bed shear stress. Consequently, in the beginning of the experiments when the sediment is not yet biostabilized, the samples need to be handled with great caution to avoid scour development. After some weeks the biofilm covers both the sediment and the PVC frames so that the roughness change impacts become negligible.

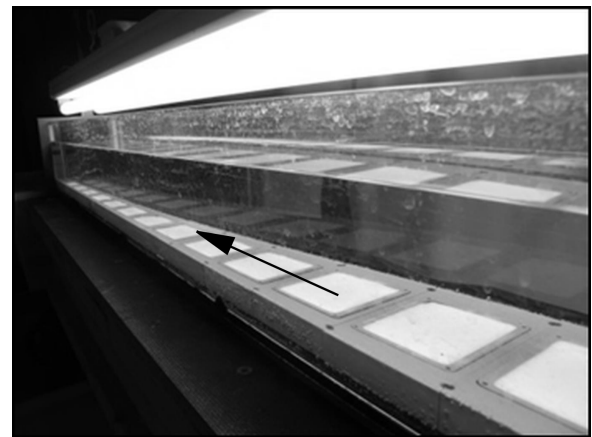
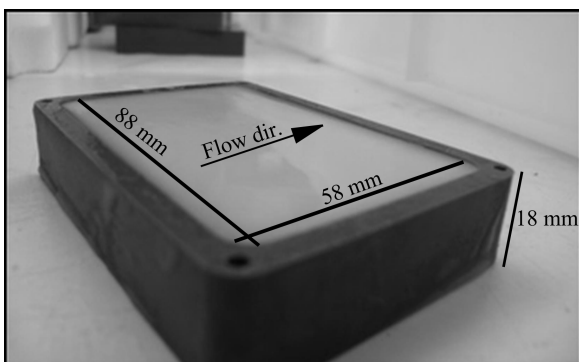


Figure B.2 Details of the cultivation setup. *Left*: Removable cartridge containing the sediment on which the biofilm grows. *Right*: Side view of the test section (uncolonized) under illumination.

The sediment particles (inert glass beads, $\rho = 2.5 \text{ g}/\text{cm}^3$, Muehlmeier, Germany) have a diameter between $0.1 \dots 0.2 \text{ mm}$ which is well in the range of diameters where the binding forces of the EPS could dominate over gravitational forces as reported by Fang et al. (2014) and should be considered as non-cohesive. This is an important prerequisite for investigations

on biostabilization as it is assumed that no additional effects on transport mechanisms need to be considered. The sediment size corresponds to sediments usually found in lowland rivers.

B.1.2 Validation of the hydrodynamic regime

As the hydrodynamic regime controls two important parameters for biofilm formation, namely mass transfer and drag forces (Stewart, 2012; Stoodley et al., 1998), special attention is paid to the establishment of well-defined hydraulic boundary conditions. Since near-bed mass transfer (of, e.g., nutrients to the biofilm surface) is primarily driven by turbulence (Nikora, 2010), direct measurements of the flow velocity components and calculated fluctuations thereof are conducted using a LDA system (Laser Doppler Anemometry, Coherent, USA) at different positions while applying different discharges but equal water levels (due to the low discharges in the flumes the flow can be assumed to be uniform in the following considerations). The turbulent shear stress (τ) is calculated as the time averaged product of velocity fluctuations (after Reynolds decomposition, in longitudinal (u') and normal (v') directions) from the mean velocity multiplied with the fluid density:

$$\tau = -\rho \overline{u'v'} \quad (\text{B.1})$$

To determine the bed shear stress (τ_b) in the flumes the turbulent shear stress measured at 5, 6, 8 and 10 mm height above the bed are averaged. As τ_b is constant in the rearward-half of the flumes fully turbulent conditions are assumed here. Consequently, the biofilm growth section including the cartridges and illumination is placed into this area. Reproducibility of the hydraulic boundary conditions in all flumes is confirmed by ADV (Acoustic Doppler Velocimetry, Sontek, USA) measurements. The following empirical relationship is established between the discharge and bed shear stress over the biofilm growth section ($R^2 = 0.9968$):

$$\tau_b = 0.00119Q^2 + 0.0079Q \quad (\text{B.2})$$

Where $\tau_b [\text{N}/\text{m}^2]$ is the bed shear stress and $Q [\text{l}/\text{s}]$ is the discharge which is continuously measured by a flow meter (Buerkert 8030, Germany). The three levels of τ_b that are applied during the experiments are also listed in Table B.1. It is important to note that the investigations are solely carried out under turbulent conditions since laminar flow can rarely be found in a natural stream. Since light intensities and -quality may vary at different water depths, the water level is kept constant (8.1 cm) in the setup, i.e. in all flumes and at different discharges. This is achieved by deploying weirs positioned at the end of the flumes that are adapted to the designated discharges by varying their height.

B.1.3 Erosion measurements in the SETEG Flume

The determination of the critical bed shear stress for biostabilized sediments is conducted in the SETEG flume (“Strömungskanal zur Ermittlung der tiefenabhängigen Erosionsstabilität von Gewässersedimenten” Witt & Westrich, 2003, Figure B.3 *Left*). The SETEG flume is a pressure duct ($l \times w \times h = 8.3 \times 0.145 \times 0.1 \text{ m}^3$) where samples (here: the sediment cartridges) are inserted through an open bottom so that the flume bed is level with the surface of the sample. One downside of this setup is that the initial roughness of the flume bed may differ from the roughness of the biofilm sample (depending on the maturity of the biofilm) inevitably leading to unwanted edge effects like a local increase in bed shear stress and scour development. Consequently, in a current study investigations on roughness development are being conducted aimed at minimizing the aforementioned edge effects during erosion¹.

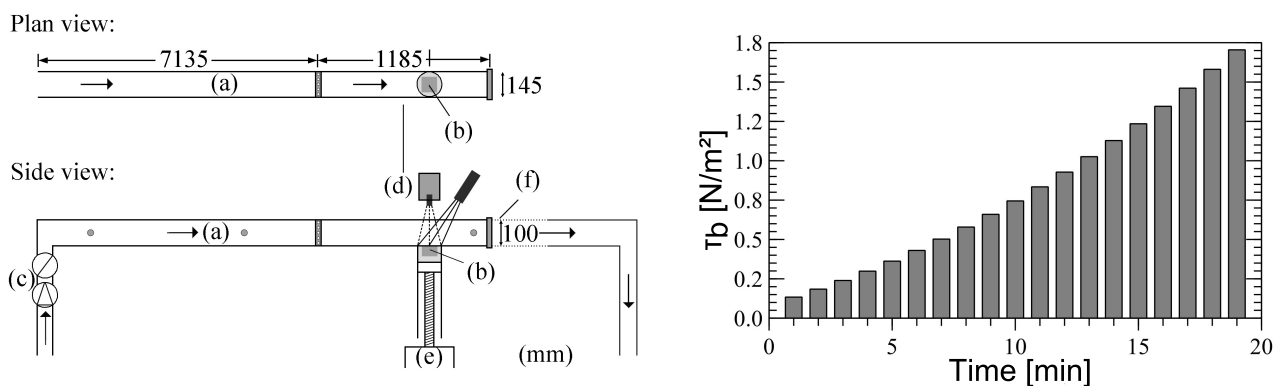


Figure B.3 Setup for the erosion of biostabilized sediments and applied stepwise increase of forces. *Left*: Schematic view of SETEG erosion flume, modified after Witt and Westrich (2003): (a) pressure duct, (b) sediment cartridge fitted into a frame (c) pump and magnetic inductive flow meter (d) laser triangulation system (not applied) (e) jack with stepping motor (f) outflow weir. *Right*: Applied increments of bed shear stress in the SETEG flume over time.

However, to determine the critical bed shear stress (τ_c), the discharge is increased stepwise in small increments and each discharge is maintained for one minute (Figure B.3 *Right* for corresponding τ_b). In this study, the critical bed shear stress is defined as the point of incipient particle/aggregate motion where the detachment exposes the underlying abiotic sediment. This definition is basically identical with the erosion type Ib after Amos et al. (2003). By focusing on the morphologically relevant de-armoring of the sediment, the release of the surficial fluffy layers is not taken into account here. At present, the experimental system is complemented by integrating laser triangulation in order to measure erosion rates and relate these data to visual observations. A critical bed shear stress of 0.23 N/m^2 is determined for the abiotic sediment used in the experiments which is slightly higher than the one derived from the Shields' equation ($\tau_c = 0.145 \text{ N/m}^2$ after Shields, 1936). In the following, the determined $\tau_c = 0.23 \text{ N/m}^2$ for abiotic sediment serves as a reference value to classify the effects of biostabilization.

¹The results are presented in Part F

B.2 The experimental program of the conducted experiments

From the River Enz (county of Baden-Württemberg, Germany) 1.2 m³ of natural freshwater is withdrawn, transported to the laboratory, well-mixed, filtered (removing larger particles) and transferred in equal shares into the outflow tanks of the flumes. River water is used to seed the experiments with natural assemblages of microbes in order to investigate the effect of natural variations (e.g., seasonal succession). Light intensities are adjusted according to the selected boundary conditions (Table B.1). The glass beads, which mimic fine sediments, are saturated with riverine water and inserted carefully into the cartridges, where they are compacted and flattened to achieve a surface planar to the cartridge edges. Afterwards, the loaded cartridges are placed into the growth section of the flumes. To avoid immediate erosion of the artificial sediment, the discharge is increased in small increments up to the desired threshold by regulating valves and the bypass. The water is then circulated continuously to promote biofilm growth by settlement of microbes.

In total, five experiments (each lasting between 4 and 8 weeks) are conducted to address the two most influential abiotic boundary conditions, τ_b and light intensity, on biofilm growth and sediment stability. The hydrodynamic impact is investigated by varying τ_b (according to Table B.1: low, medium, high) in three experiments in March, May, and November while the light intensity is kept constant at a medium level (Table B.2). In two further experiments in July and August, the light intensities are varied (Table B.1: none, medium, high) and the τ_b is kept low in all flumes (Table B.2). In all five experiments, every treatment condition is applied to two flumes (replicate A and replicate B) to account for possible variations between the flumes.

Table B.2 Overview on the experiments with objectives and applied boundary conditions.

Name	ID	Study objectives	Light intensity	Bed shear stress τ_b
March 2013	Mar13	Hydrodynamics	Medium	Low, Medium, High
May 2013	May13	Hydrodynamics	Medium	Low, Medium, High
July 2013	Jul13	Light intensity	None, Medium, High	Low
August 2013	Aug13	Light intensity	None, Medium, High	Low
November 2013	Nov13	Hydrodynamics	Medium	Low, Medium, High

Retrieving the samples and subsequently eroding them within the SETEG flume, takes place once a week; however, it is worth noting that this procedure is destructive and the number of cartridges is limited. Consequently, the beginning of the erosion tests and/or the number of cartridges to be eroded is adapted to the special objectives of the particular experiments. For example, in the May experiment, more biological data were needed, so that only one,

instead of two samples per flume are eroded after one month of cultivation (see Figure B.4 d-f).

B.3 Evaluation of the erosion measurements

B.3.1 Impact of hydrodynamics, light intensity and seasonality

A total of five experiments are conducted in which either the impact of hydrodynamics or light intensities on biostabilization is investigated. Figures 4 and 5 illustrate the mean temporal development of sediment stability ($n = 2$, \pm standard deviation) for two replicate flumes (replicate A and replicate B) in different experiments. In the following, the biostabilization index (after Manzenrieder, 1983) is used:

$$BI = \frac{\tau_{c,bio}}{\tau_{c,0}} \quad (\text{B.3})$$

where BI is the biostabilization index, and $\tau_{c,bio}/\tau_{c,0}$ is the ratio between critical bed shear stress of the biostabilized sediment and the abiotic reference (here: $\tau_{c,0} = 0.23 \text{ N/m}^2$).

The results of the experiments show that the biostabilization index ranges between 1 (no effect) and ≈ 10 (a tenfold increase of sediment stability) depending on applied boundary conditions and the investigated season. In the beginning of the measurements (i.e. in the first two weeks) the stability is largely comparable to abiotic sediment stability ($1 < BI < 2$). With a few exceptions, the critical shear stress increases hereafter (e.g. Figure B.4 d. In one experiment the stability declines after initially high biostabilization values, when exposed to high light intensity in July (Figure B.5c).

In the experiments the biofilm growth (as observed) as well as its stability is spatially heterogeneous. Even though applying the exact same boundary conditions in two flumes at a time the differences in stability between these flumes are remarkable (e.g. a difference of approximately $BI = 2$ in Figure B.4d, after one month). Even in a single flume the values partially differ between two samples, expressed by high standard deviations (e.g. standard deviation of approximately 0.6 in Figure B.5e, in the fifth week). Figure B.6 shows an example of the heterogeneous appearance of biofilm coverage. The main causes for this variability in the experiments are most likely differences in the erosion behavior and small scale spatial heterogeneities in biofilm growth observed during erosion, which is discussed in Sections B.3.2 and B.4.2.

Figure B.7 is an example of the temporal development of biofilm growth under different hydrodynamic conditions indicating that a higher hydrodynamic stress seems to delay the formation of a biofilm coverage (e.g. a first biofilm coverage is visible after three weeks for medium bed shear stress (Figure B.7 b) in contrast to two weeks for low bed shear stress (Figure B.7 a). This trend can be also observed for biostabilization. For example, in the May

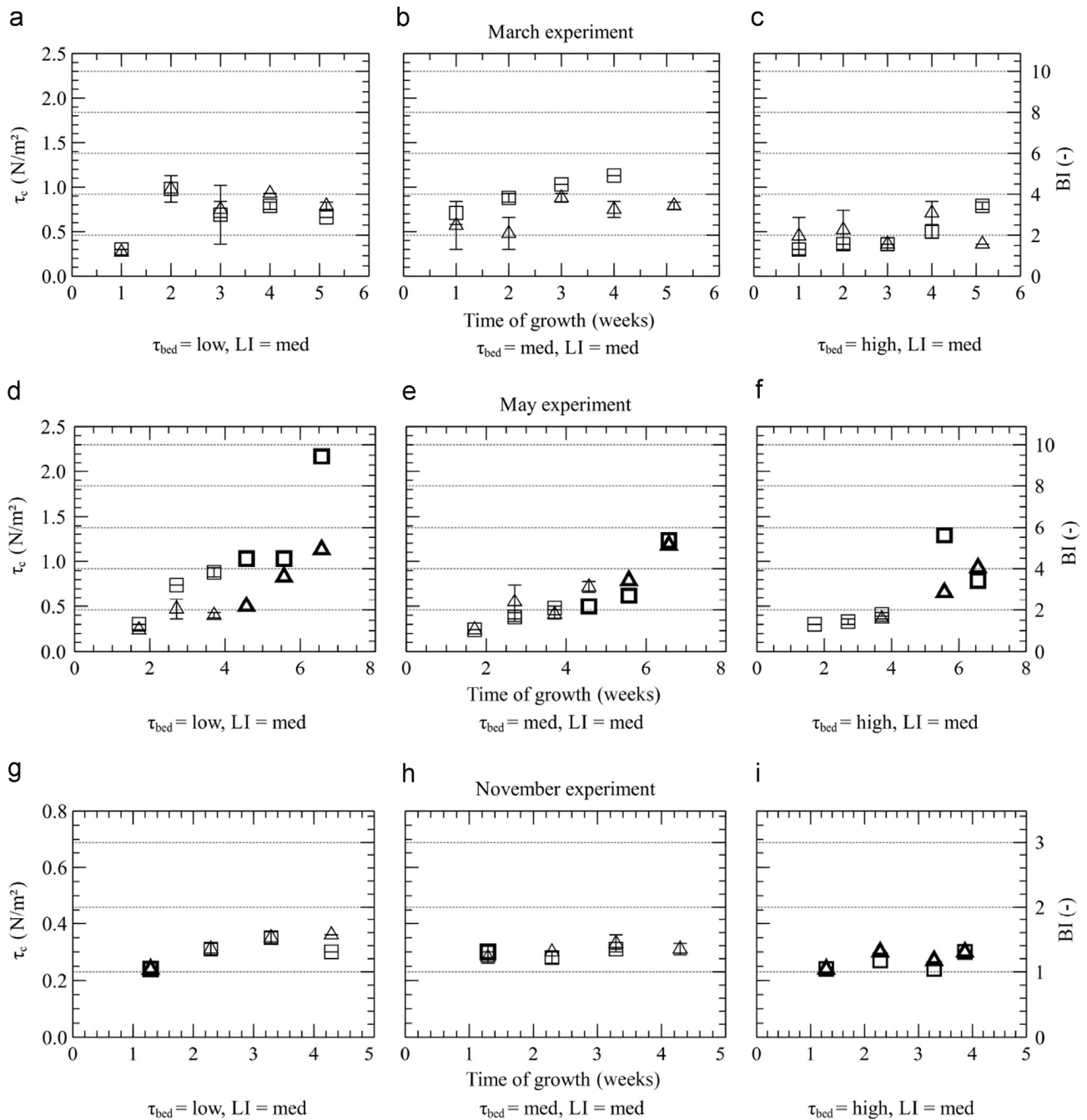


Figure B.4 Spring and late autumn experiments on the impact of hydrodynamics on τ_c (left vertical axis) and BI (right vertical axis): Each graph shows the temporal development of mean ($n = 2$, \pm standard deviation) τ_c for two replicate flumes (triangles: replicate A; squares: replicate B). LI is constantly set at a medium level ($= 50 \mu\text{mol}/\text{m}^2\text{s}$). Thicker symbols indicate where only one sample is eroded (see Section B.2). Please notice the different axis scaling.

experiment, a noticeably higher value of BI is reached earlier under low τ_b than under higher hydrodynamic stress (e.g. a $BI > 2$ after 2.5 weeks in Figure B.4 d and only after 5.5 weeks in Figure B.4 f).

In two experiments (Figure B.5) the impact of light intensity and darkness is investigated. While the biological analysis confirms the existence of a bacterial biofilm (measurable content of EPS carbohydrates, no chlorophyll *a*), the stability measurements reveal that dark-

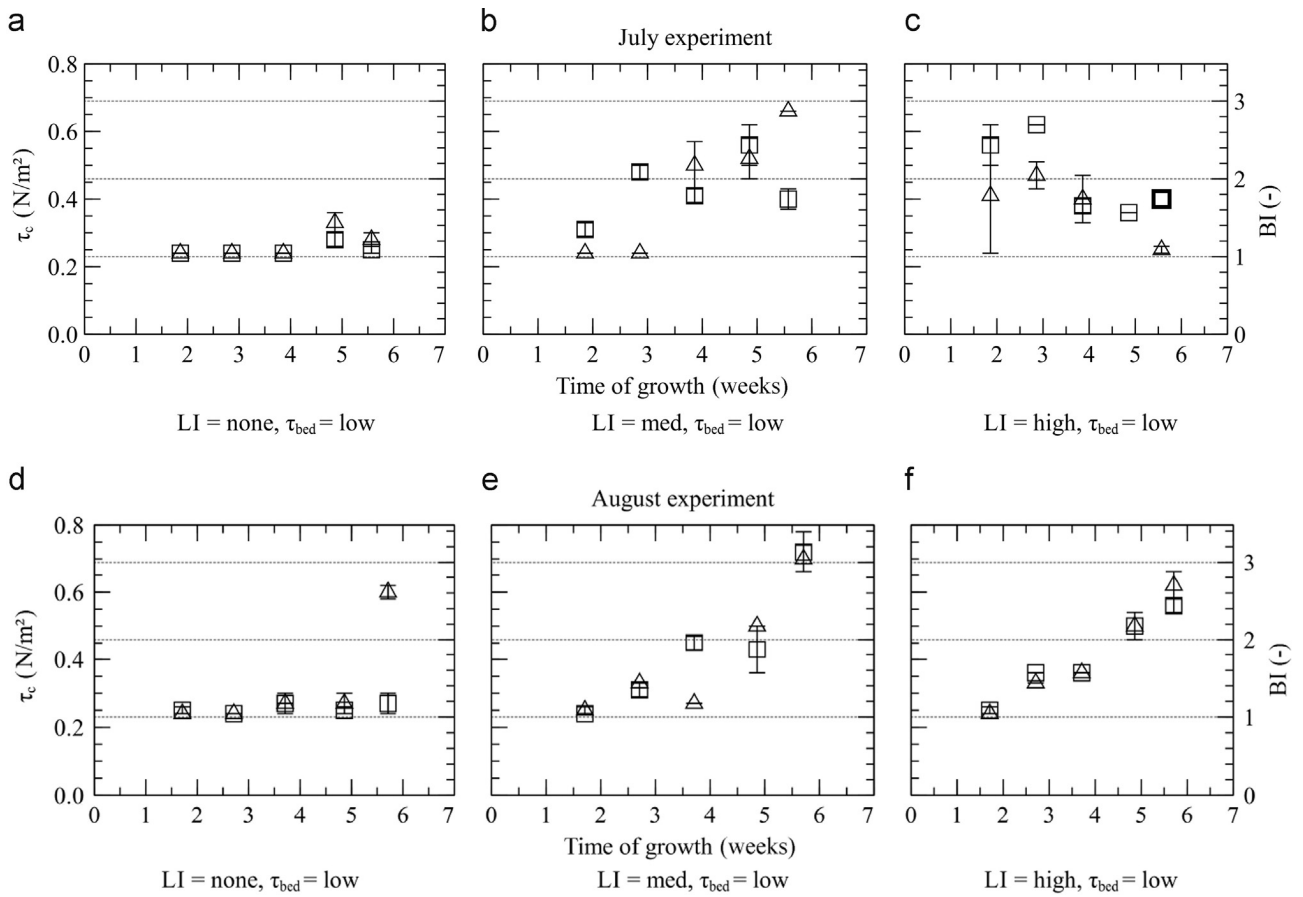


Figure B.5 Summer experiments on the impact of light intensity on τ_c (left vertical axis) and BI (right vertical axis): Each graph shows the temporal development of mean τ_c ($n = 2$, \pm standard deviation) for two replicate flumes (triangles: replicate A; squares: replicate B). τ_b is constantly set at a low level ($= 0.02 \text{ N/m}^2$). Thicker symbols indicate where only one sample is eroded (see Section B.2).

a) Replicate flume A

b) Replicate flume B

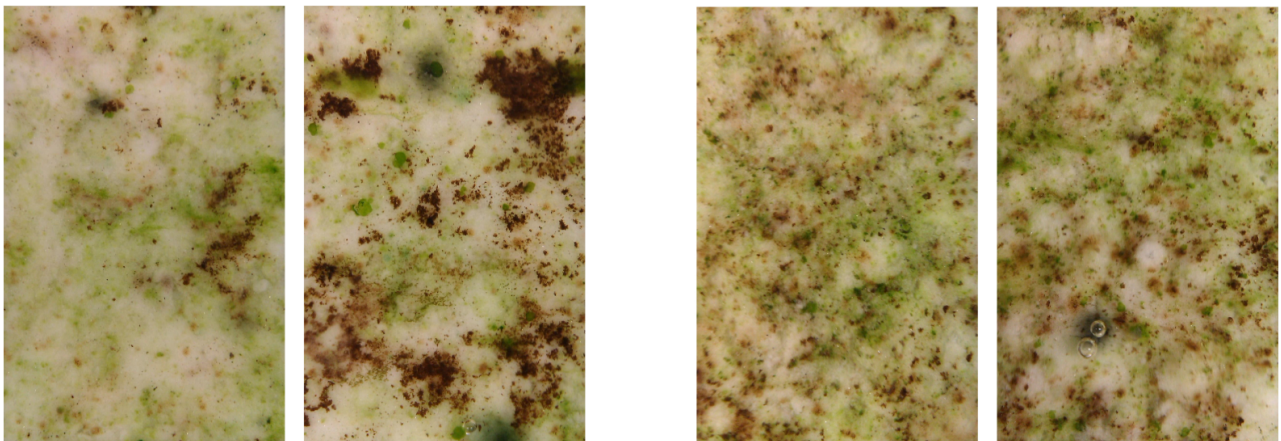


Figure B.6 Top view of biofilm samples cultivated under the same conditions in the August experiment ($\tau_b = \text{low}$, LI = medium). a) two samples from replicate flume A, b) two samples from replicate flume B. All photographs are taken on day 36 of cultivation. A high spatial heterogeneity is indicated by scattered spots of diatoms (brown spots) and green algae (green spots) colonization.

ness does not support biofilm growth to induce significant biostabilization. Still a minor impact is detected ($1 < BI < 1.5$). Only after five weeks of growth (in the August experiment)

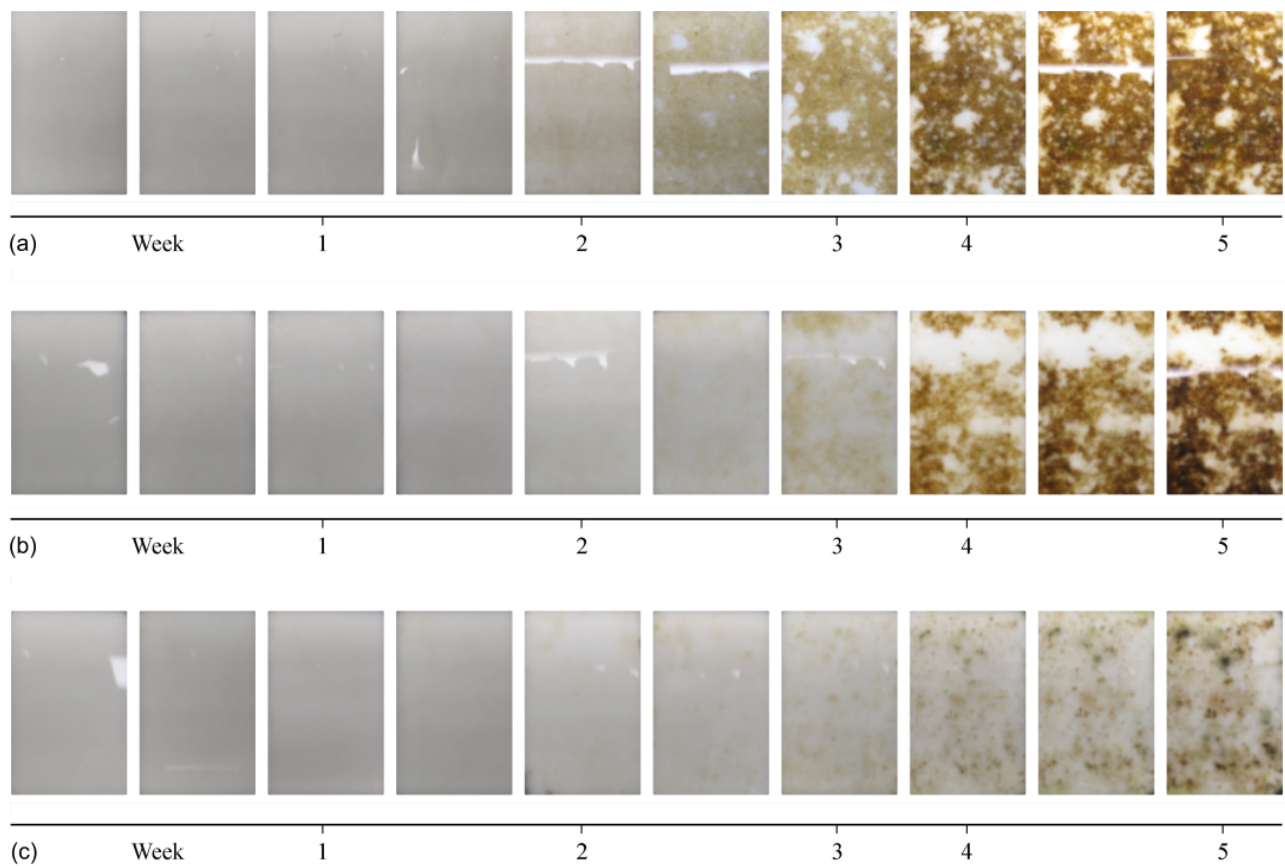


Figure B.7 Photographs of biofilm development taken twice a week in the March experiment under three different levels of bed shear stress. A) low, b) medium and c) high.

an increase of stability is measured in one flume ($BI = 2.6$). Apart from the decreasing stability under high light intensities in July (Figure B.5c) no clear trend is observable in the treatments where light is applied (Figure B.5b, e, and f).

Comparing all five experiments, the most pronounced stabilization potential can be reported from the experiments in early and late spring (March and May) with a maximum biostabilization index of 4.8 and approximately 10, respectively. This high stabilization (May experiment, after the sixth week, Figure B.4d) is explained by a very stable carpet-like biofilm which could also be observed in other experiments in spring and summer. With a maximum BI of approximately 3 and 3.1 the stability in summer (July and August, see Figure B.5) is lower than in spring. In late autumn (November) an experiment was conducted investigating the hydrodynamic impact with a rather short duration of four weeks. After four weeks of growth, the effect of biostabilization is still very low, as the biostabilization index ranges between 1 and 1.5. It is suggested, that the main reason for these seasonal differences is the microbial succession in riverine systems and its impacts on the mechanical process of erosion as will be discussed in B.3.2 and B.4.2.

B.3.2 The mechanical process of erosion

During the SETEG measurements detailed information about the erosion mechanisms are gathered by direct visual observations of each individual process of entrainment and a subsequent extensive description². Two dominant types of biofilm-influenced entrainment and additional characteristics are identified (see Figure B.8 for an illustration). This information is used in conjunction with the results on biostabilization to get a better understanding of the mechanical process of erosion. Please also see Table B.3 for further details.

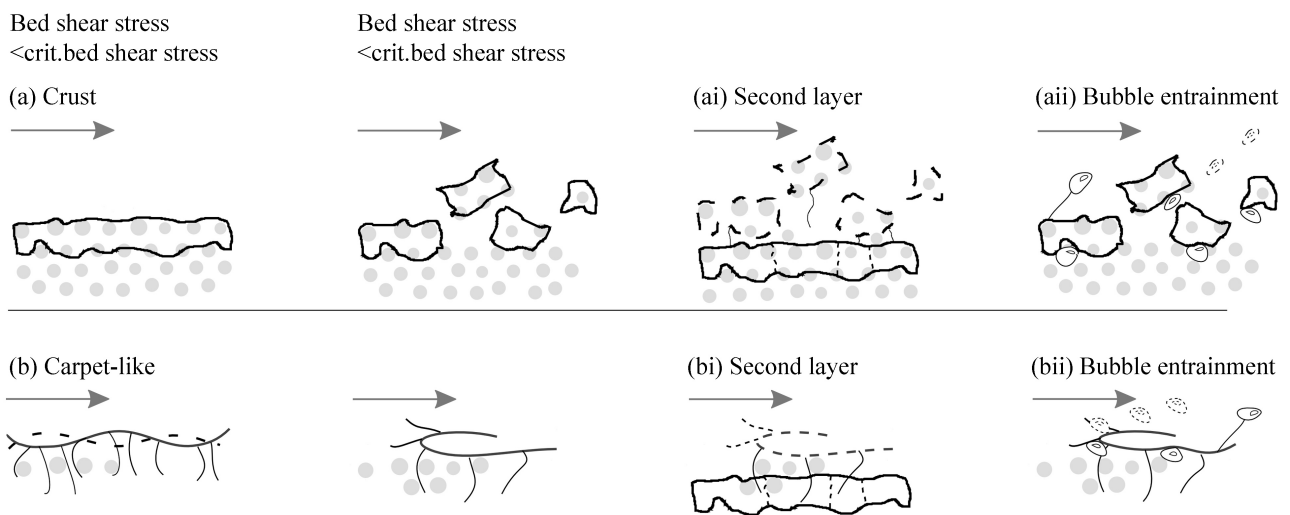


Figure B.8 Different biological stabilization mechanisms and erosion processes as observed during the experiments.

For the surface layer, one type of entrainment is a biofilm crust that is eroded in smaller aggregates (Figure B.8a) and the second type is an elastic carpet-like erosion where an increasing τ_b leads to a sudden failure (Figure B.8 b). Additionally the erosion process was influenced by destabilizing bubble entrainment (Figure B.8 *aii* and B.8 *bii*) and the subsequent erosion of the layer beneath, mainly breaking up in aggregates (similar to the crust-like erosion, see Figure B.8 *ai* and B.8 *bi*). Filamentous structures which are protruding into the water column, are often observed, but are found to be easily eroded and do not contribute to biostabilization in the experiments reported here, and, thus, are not further considered in this study. It is worth mentioning that different mechanical erosion processes occur in samples from different seasons, treatments, and replicates but even within one sample, indicating the highly heterogeneous biofilm growth in the experiments and possibly explaining the deviations in stability mentioned in Section B.3.1.

The different erosion processes seem to correspond to varying bed stability. In the first days of the experiments the predominant entrainment mechanism is the movement of individual particles as bed load (characteristic for abiotic non-cohesive sediments) before the biofilm growth influences the mechanical behavior. The crust-like erosion of aggregates frequently is found and can be related to a wide range of bed stabilities (e.g. in the second week of Au-

²please see Appendix B.2 for an evaluation sheet

Table B.3 The three predominant erosion processes: (S) individual particle movement, (A) a crust that is eroded in aggregates and (C) a surficial carpet-like erosion. Additionally the erosion process is influenced by (B) bubble entrainment and (2A) the formation of a second layer beneath the surface. Additionally, the corresponding ranges of biostabilization indices are illustrated in grayscale.

BI range			Color legend						
$BI < 1.5$									
$1.5 \leq BI < 2.5$									
$2.5 \leq BI < 3.5$									
$3.5 \leq BI < 4.5$									
$4.5 \leq BI$									
			Week						
ID	Conditions	Rep	1	2	3	4	5	6	7
Mar13	τ_b Low	A	S	S,C,2A	S,2A	S,2A	-	S	-
		B	S	A,S,2A	S,2A	S,2A	-	C	-
	τ_b Med	A	S,B,2A	A,S,2A	S,2A	S,A,2A	-	C,2A	-
		B	S,2A	S,2A	S,2A	C,2A	-	-	-
	τ_b High	A	S,2A	S,2A	S,A,B	S,2A	-	S,2A	-
		B	S	S	A,S,B	A,2A	-	C,2A	-
May13	τ_b Low	A	-	S	A,S,B,2A	A,S,B	C,A,B	C	C
		B	-	S,B	S,B,2A	C,A	A,S,B	C,B	C,B
	τ_b Med	A	-	S	A,S,B,2A	A,2A	A,C,B	C,A,B	A
		B	-	S,B	S,B	A,S,B	A,S,B	A,B	C,A,B
	τ_b High	A	-	-	-	A,S,B	-	A	A
		B	-	S,B	S,B	S,A	-	A,S	C,A
Jul13	LI None	A	-	S	S	S	S	S	-
		B	-	S	S	S	S	S	-
	LI Med	A	-	S	S	A,B	A,C,B	A,C	-
		B	-	S	A,B	A,B	A	A,B	-
	LI High	A	-	S,2A	S,2A	A	-	A,B	-
		B	-	S,2A	S,2A	A,B	A,C	A	-
Aug13	LI None	A	-	S	S	S	S	S,2A	-
		B	-	S	S	S	S	S	-
	LI Med	A	-	S,A	S,A	S,A	A,S,B	A,2A	-
		B	-	S,A,B	A,S	S,A,B	A	A,B,2A	-
	LI High	A	-	S,A,B	S,A,B	S,A,B	S,A,B	A,2A	-
		B	-	S,A	S,A,B	A,B	A,2A	A,C,2A	-
Nov13	τ_b Low	A	-	S	S	S,A	A,S	-	-
		B	-	S	S	S,A	A,S	-	-
	τ_b Med	A	-	S	S	S,A	A,S	-	-
		B	-	S	S	S,A	S,A	-	-
	τ_b High	A	-	S	S	S,A	A,S	-	-
		B	-	S	S	A,S	-	-	-

gust with a $BI < 1.5$ and after 6 weeks with a BI between 2.5 and 3.5). On the contrary, the carpet-like erosion is mostly related to a higher biostabilization and is detected only in the spring and summer experiments. One example, that was already mentioned, is the biostabilization after the sixth week of growth in May where the sediment is mostly stabilized by a surficial carpet. Both the formation of various biofilm layers and the appearance of bubbles cannot be related to specific conditions (except that bubbles are absent in the treatments where biofilms are cultivated in darkness). While bubble entrainment destabilizes the sediment (further discussed in Section B.4.2), the existence of a second biofilm layer beneath the surface results in an enhancement of stability.

B.4 Discussion on erosion measurements

One of the main goals of this study is to evaluate biostabilization under varying hydraulic conditions and light intensities and to reveal its meaning for riverine sediments which is, in contrast to marine and estuarine sediments, insufficiently studied. It has long been believed that biostabilization which is mainly due to microbially secreted sticky polymers, depends largely on the amount of ions to help binding (Spears et al., 2008). This would imply that the stabilization potential in freshwater is significantly lower than in the marine environment. Only recently more attention was drawn to riverine biostabilization by eroding natural sediment cores and correlating stability to microbial activities (Gerbersdorf et al., 2007). The results of the two experiments conducted in spring clearly demonstrate a high biostabilization potential in and after the fifth week ($BI = 3.7$) which is well in the range of maximum marine biostabilization indices found by, e.g. Amos et al. (2004) ($BI_{max} : 2.4$), De Brouwer et al. (2000) ($BI_{max} : 3$) and Tolhurst et al. (1999) ($BI_{max} : 6.2$), even though, it must be admitted, that a comparison to in situ measurements is generally difficult because of the complexity in a natural system. Still, it remains unclear how biostabilization works and how it varies in different niches of freshwater.

B.4.1 The impact of environmental conditions on biostabilization in freshwaters

Hydrodynamic boundary conditions affect biofilm growth and biostabilization in complex ways by influencing the settlement of suspended microbes on the substratum and their subsequent attachment, the availability of nutrients, and the erosion (or detachment) of biofilm aggregates. In the initial phase of biofilm formation the number of cells getting into contact with the sediment surface increases with higher turbulence intensities (Stoodley et al., 1998). In contrast to this, their attachment efficiency is reduced by higher bed shear stress (Bryers & Characklis, 1981), consequently, net attachment (difference between cells getting into contact with the surface and cells detached by the hydrodynamic forces) is also reduced. In laboratory studies Stoodley et al. (1998) found that in laminar flow the colonization rate

was higher than under turbulent conditions (and obviously higher than the detachment), resulting in an earlier development of biofilm. Similar results for a delayed colonization were obtained recently by Graba et al. (2013). They reported higher detachment rates in the early stages of biofilm formation induced by higher bed shear stress during cultivation. Figure B.7 shows the development of the biofilm over time and confirms the aforementioned hypotheses for delayed growth under higher hydrodynamic impact. The results presented in this study suggest for the first time that this delay not only affects biofilm growth but also the temporal development of biostabilization (also supported by the biological analysis, revealing a delayed development of EPS protein content).

After settlement, the rate of biofilm growth depends on the availability of nutrients and substrate, along with light quantity and quality. Therefore, nutrients must be transported to the biofilm surface, and transport is significantly influenced by the near-bed turbulence. Similar to the processes of cell attachment, increasing turbulence intensities transport more nutrients to the biofilm surface by higher mixing rates and by reducing the thickness of the viscous benthic boundary layer (Characklis & Cooksey, 1983). In other words, higher turbulence intensities promote nutrient uptake processes and lower intensities limit biofilm growth. On the contrary, bed shear stress exceeding the stability of the biofilm-sediment matrix leads to erosion of biomass and is consequently considered to be the upper limit for biofilm development, while (cell-) detachment processes might even occur for lower shear stresses. This “trade-off” between enhanced mass transfer and enhanced detachment (Stewart, 2012) under higher hydrodynamic stress is expected, in the authors’ opinion, to result in a more or less constant rate of biostabilization for matured biofilms. Indications for such a dynamic equilibrium can be found in Fang et al. (2014) who reported a maximum increase of incipient velocity for erosion to 70 % (after 4 weeks), after which the stability drops to a nearly constant level of 40 % for the following weeks. Furthermore, fluctuating stabilities were also reported in Droppo et al. (2007) (BI varied between 3 . . . 7) but were explained by “new layers of biofilm integrating into the sediment beneath older decaying biofilm layers”. Indications for this multiple layer formation are also discovered in this study (see Sections B.3.2 and B.4.2). However, in the present study the stability is mostly increasing (see e.g. Figure B.4d-f) until the last day of measurements. Consequently, as there is no constant level of BI, it is hypothesized that the biofilm was still developing in the timeframe of the experiments (4 . . . 8 weeks). It is suggested, that the high variability in biostabilization observed in the experiments can be attributed to this early phase of biofilm formation, in which spatial heterogeneities in coverage, community, and erosion mechanisms require the highest level of attention.

Another aspect concerns the light climate in a riverine system, which is affected by various environmental factors. Light intensity on the sediment surface changes with water depth and turbidity. Further the light climate is influenced by shading effects of trees and last

but not least by the day/night cycle during different seasons. While higher light intensities enhance the growth of microalgae and photo-autotrophic bacteria (Roeselers et al., 2006), too much light might also result in migration activities of microalgae from the surface into the sediment with possible implications for biostabilization (as reviewed in: Gerbersdorf & Wieprecht, 2015).

It is intuitive to assume that significant differences exist between illumination and darkness treatments as the former promote photosynthetic activity and the latter result in a biofilm consisting solely of heterotrophic bacteria. In the two summer experiments investigating the impact of light intensities, it is shown that biofilms grown in darkness do not substantially influence the stability. However, in one experiment (Figure B.5d) a single increase is detected on the last measuring day, indicating that bacterial biofilms possibly need more time to develop a stabilization potential compared to biofilms exposed to light. Even though Roeselers et al. (2006) reported increasing growth rates for higher light intensities, no such trend can be derived from the biofilm under illumination. Unfortunately, final conclusions regarding the impact of light intensity on biostabilization can only be drawn after further experiments are conducted in another season.

The data show considerable differences of biostabilization depending on the season, which has also been reported from various field studies in intertidal environments. Dickhudt et al. (2009), for example, found a higher erodibility in winter and spring than in summer and autumn. A five-fold increase of the BI in summer as compared to winter was reported by Amos et al. (2004). The experiments largely confirm these trends from the intertidal environment, possibly indicating a cyclic behavior of erodibility. It is found that in spring the biostabilization is considerably higher than in summer.

The differences between seasons are further supported by the results of the biological analysis. For example, in the spring experiments, EPS protein content is significantly higher than in summer and autumn. In late autumn biostabilization is nearly absent and also carbohydrate as well as protein concentrations are much lower as compared to all other experiments. Furthermore, first results of the micro-biological analysis reveal differences in the microbial community (from diatom dominated populations to increasing portions of green algae during the course of the year), that are likely to result in different biostabilization potentials and erosion mechanisms. Figure B.9 *Left* shows photographs of biofilm coverage from a spring experiment consisting primarily of diatoms while the summer biofilm shown in Figure B.9 *Right* has a more fluffy appearance and is mainly composed of green algae. Apart from these obvious structural differences, biostabilization is considerably influenced by differences in EPS production. For example, epipellic diatoms produce colloidal EPS carbohydrates during migration activities, which are known to contribute significantly to binding (Gerbersdorf & Wieprecht, 2015). The complex relationship between EPS compounds, seasonal succes-

sion of the microbial community, and biostabilization is another focus of research within the current project and results of this analysis are published in Schmidt et al. (2016).

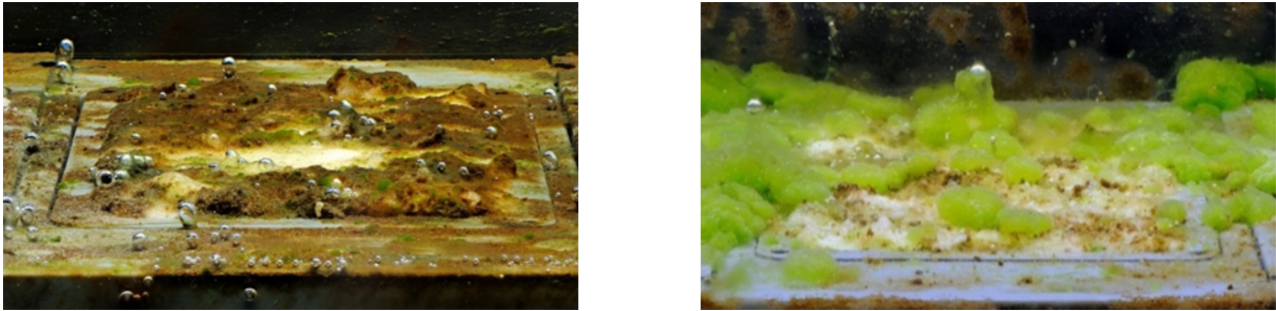


Figure B.9 Photographs showing the different appearances of biofilms in spring (*Left*, image from Gerbersdorf & Wieprecht, 2015) and summer (*Right*).

B.4.2 The mechanical process of erosion for biostabilized sediments

In recent years many researchers successfully correlated physical and biological parameters (and combinations thereof) to biostabilization (e.g. bulk density: Amos et al., 2003; organic matter content: Righetti & Lucarelli, 2010; Chl *a*: Yallop et al., 2000; colloidal carbohydrates: Friend et al., 2003). But the empirical relationships found are site specific and cannot be generalized. Differences in the mechanical structure and the resulting processes of erosion are often disregarded but may be partly responsible for the wide range of stabilization potential. As highlighted by Grabowski et al. (2011) the development of a unifying equation to predict erodibility is limited by the absence of a complete mechanistic understanding of the biostabilization process and its interactions between key parameters.

To get a better understanding of the fundamental processes an analysis on the observed erosion processes is carried out revealing significant differences between mechanisms and possible impacts on stability. Two predominant types of stabilizing structures are identified: The most frequent mode of incipient motion in the experiments is the erosion of chunks or aggregates (Figure B.8a, denoted as crust-like erosion). The data show that this type of erosion can be correlated to a wide range of stabilities. By gluing individual sediment particles a crust is formed on the top few millimeters. These types of structures are additionally detected below the surface of the sediment (i.e. a second underlying biofilm layer) adding even more resistance to the flow (Figure B.8ai). In the event of erosion this crust breaks apart at the weakest spots (in the experiments cracks in the crust are frequently found already during cultivation) and aggregates of different sizes (sub mm to mm scale) are eroded. This leads subsequently to a chain reaction where even more aggregates are exposed to the hydraulic forces and eroded. Righetti and Lucarelli (2007) ascribed the enhanced biostabilization potential to the impact of changed aggregate sizes (and density) and adhesion forces between these aggregates and developed a promising model based on the Shields equation (Shields, 1936) to account for the biogenic impacts.

The second type is a carpet-like structure (Figure B.8b) which is largely detected at a more matured biofilm age by a different type of organism. In contrast to the crust-like erosion it is less common but more correlated to a higher stability (mostly $BI > 3.5$). Most strikingly is the formation of such a mat in one experiment (in May), with a BI of approximately 10 before suddenly failing. Loosely bound to the underlying sediment (or biostabilized layer) via filaments the biofilm forms an elastic mat armoring the river bed. It is worth mentioning that differences compared to classical erosion models are huge and until now only one model exists describing this behavior, developed by Vignaga et al. (2013). For future experiments in the field of biostabilization these different mechanisms of erosion are to be considered, especially to interpret data from biological analysis and relate them to stabilizing effects.

In contrast to the previously mentioned mechanisms gas bubbles that are visible both on the surface of the biofilm as well as in the top few millimeters below the surface destabilize the sediment (Figure B.8a_{ii} and b_{ii}). Bubble formation in biofilms is a natural process driven by either photosynthetic activity of algae (oxygen), bacterially mediated organic matter decomposition (methane), and/or bacterial respiration (carbon dioxide). When the concentration of the produced dissolved gas exceeds the solubility in the medium (supersaturation) bubbles can form (Boudreau et al., 2001) which create lifting forces and thereby reduce the bulk density of the biofilm-sediment matrix (Amos et al., 2003; Jepsen et al., 2000). For a more elaborated description of the mechanical processes see, e.g. Boudreau (2012) and Johnson et al. (2002). As a result, the sediment is more vulnerable to bed shear stress and more easily eroded as also reported by Amos et al. (2004) and Sutherland et al. (1998).

The occurrence of these gas bubbles in the presented experiments is highest in May and absent in the November experiment (see Table B.3), but cannot be related to specific environmental conditions (except that no bubbles are present in darkness conditions). From the authors' own observations, the lifting forces of these gas bubbles certainly influence sediment erodibility and should get more attention in future experiments.

B.5 Conclusions

Both literature reviewing and the physical experiments presented here indicate that seasonal effects clearly influence the biostabilization of bed sediments under different hydrodynamic and light intensity conditions. It is found that the sediment stability is higher in spring than in summer, while in late autumn only little stability enhancements are detected compared to the case without a biofilm. Apart from EPS compounds that are known to influence the adhesion forces of the biofilm, it is concluded that the different mechanical structures and types of erosion are partially responsible for the high variability of the observed biostabilization. Understanding these processes is a prerequisite to develop a model for predicting

erodibility of biostabilized sediments. In addition to micro-biological analyses to identify the microbial key players along with a detailed breakdown of the bio-chemical compounds of the EPS, it is suggested that the mechanical properties certainly need more attention in future experiments.

Furthermore, it is shown that a higher bed shear stress during cultivation delayed the stability development of the biofilm/sediment matrix. From the data, it can be concluded that the investigated biofilms were still developing and that in this early stage the heterogeneities have a strong impact on the biostabilization potential. Bacterial biofilms only showed little stabilization effects in the timeframe of the experiments, which is possibly the result of a slower development. While certainly only covering a small part in the complexity of biostabilization in freshwaters, the present findings help to increase the fundamental knowledge that is needed for an understanding of the phenomenon biostabilization.

Part C

AN ADVANCED METHOD TO MEASURE SURFACE ADHESION OF BIOFILMS

Accurate measurements of mechanical properties are of uttermost importance for the development of physics-based models on biostabilization. It is nowadays generally accepted that either cohesive (EPS-EPS)/adhesive (EPS-sediment) or both forces impact the stabilization of sediments in biostabilization (Grabowski et al., 2011; Dade et al., 1990, 1992). Still, methods to measure these forces at scales relevant to biostabilization are scarce or their results (e.g. proxies) are difficult to be translated into physical units needed to calibrate a mechanical model (Vignaga et al., 2012).

In this part, modifications made to a device (MagPI, first published by Larson et al., 2009) capable of measuring a proxy for surface adhesion forces is described. The presented modifications aim at 1. translating the proxy into a material property “adhesion” expressed in N/m^2 , and 2. enhancing the evaluation of the obtained data qualitatively (increase objectivity and reproducibility of results in different laboratories) and quantitatively (increase the resolution of obtained data for determination of a meaningful representation of adhesion). These improvements are considered necessary to achieve the main goal of producing reliable data that can be used to calibrate/validate or develop a mechanical model of biostabilization.

This Part starts with a more detailed description and discussion of the MagPI system, illustrating the capabilities, uncertainties and the needs for further improvements. The following section then gives a brief overview on the modifications made before Section C.3 describes fundamental knowledge on electromagnetism needed for calibration of the device. The improvements on evaluability using Image Processing are described hereafter in Section C.4. Finally in Section C.5 a method is proposed to calculate the surface adhesion $A_{s,30}$ [N/m^2] from the obtained data. The performance of the improved system (MagPI-IP, magnetic particle induction - image processing) is then evaluated using appropriate surrogate materials for EPS (Section C.6). Lastly, in Section C.7, the potential sources of error, uncertainties and limits of the procedure are discussed.

C.1 The original method to approximate surface adhesion

C.1.1 The basic concept

A detailed description of the device and the original measuring procedure was first published by Larson et al. (2009). The measurement principle of the MagPI is based on the concept that an object whose surface is in contact with an adhesive substance is pulled away until the object loses its contact. After Larson et al. (2009) the magnetic force that is needed for this separation is interpreted as a proxy for surface adhesion.

As already outlined in Section A.5.2, ferromagnetic particles (FP) are spread on an adhesive surface (Figure C.1 *Left*).

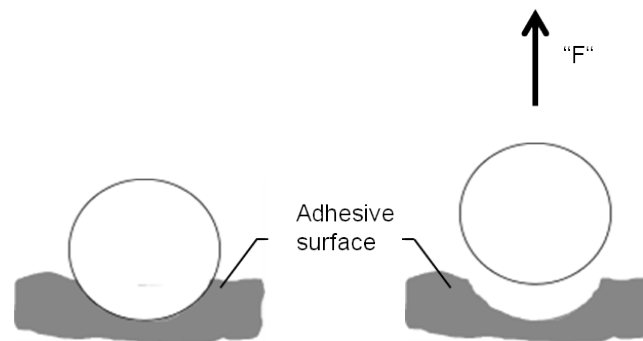


Figure C.1 Basic concept of particle attraction by the MagPI. *Left:* A ferromagnetic particle (FP) is in contact with an adhesive surface. *Right:* The FP is attracted by an electromagnet, detaches from the surface and the magnetic field that is produced by the electromagnet (here illustrated by the force “F”) at detachment is a proxy for surface adhesion

The particles get into contact with the adhesive surface and depending on the degree of stickiness of that surface they are more or less easy to be removed. Directly after spreading, an electromagnet is placed at a defined distance above the FP and the magnetic force is increased manually in increments. It needs to be emphasized that particle attraction happens directly after spreading the particles on the adhesive surface. Hypothetically only a part of the particle surface gets into contact with the adhesive surface. This means that the particles are not fully incorporated or overgrown as would be the case when the particles are left on the surface for a while.

When the magnetic force exceeds the forces that hold the particles in place, the particles jump up towards the electromagnet (Figure C.2). Consequently, the magnetic force needed to retrieve the particles is related to the stickiness of the surface, as highly adhered particles are more difficult to be detached (i.e. need a higher magnetic force) than less adhered particles.

According to Larson et al. (2009) the magnetic flux density (MFD or B in mTesla) is an ap-

appropriate measure of the magnetic force. The MFD of an electromagnet can be determined by a Hall sensor connected to a gauss meter and the MFD can thus be correlated to the electric current which is set at the power supply (red arrow in Figure C.2). Figure C.2 illustrates the setup of the MagPI. Besides the correlation of electric current and MFD, the MFD is additionally depending on the vertical distance of magnets to the FP.

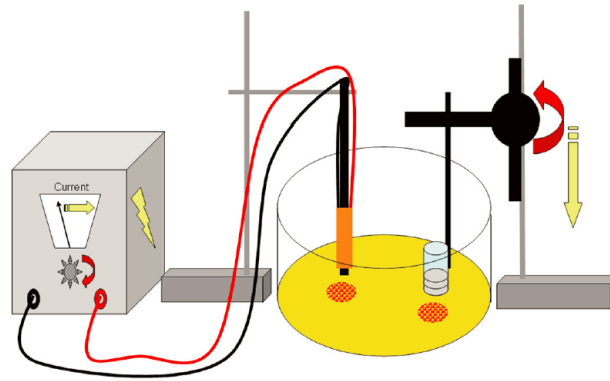


Figure C.2 Schematic representation of the MagPI system (from Larson et al., 2009). An electromagnet is used to attract ferromagnetic particles. The magnetic force can be increased by increasing the electric current.

Evaluation of the measurements and discussion on thresholds

The ferromagnetic particles are gradually retrieved by the electromagnet, which complicates the determination of one single proxy for surface adhesion. For this reason Larson et al. (2009) introduced four thresholds of particle response:

- (A) particle orientation to the magnetic field
- (B) first magnetic particle captured by the magnet
- (C) larger groups of particles attracted
- (D) total clearance of particles under the magnet

During the measurements the operator has to keep track of the particle attraction by observation and note the MFD for the different thresholds. According to Larson et al. (2009) each threshold is representative for “a slightly different property of the surface”. The meaning of the thresholds and their downsides in definition and practicability are discussed below.

Threshold A

The first threshold is of no practical relevance for the purpose of adhesion measurements. At a low magnetic force the particles align to the magnetic field lines produced by the electromagnet. During this process the particles remain in contact with the adhesive surface.

Threshold B

This threshold marks the lowest magnetic force at which a particle is retrieved by the electromagnet. As a consequence, one can assume that the first particle that was attracted exhibited the lowest adhesion forces. This threshold can be obtained by visual inspection. During the experiments it is observed that sometimes particles which are not in full contact with the adhesive surface, can be another reason for this first attraction (e.g. several particles overlap). In that case the operator has to decide on the first threshold by keeping track of the following particle attractions.

Threshold C

Larson et al. (2009) refined the definition of this threshold as “a small number of particles (around 5) are attracted to the magnet”. In the experiments (and also in accordance to Larson et al., 2009) this threshold was the most subjective: Firstly, the number of particles used was different at different measurements. This was a practical aspect, as counting particles in a size range of $d = 200 \dots 355 \mu\text{m}$ for hundreds of measurements was not feasible. As such “a small number of particles (around 5)” can potentially mean very different things. For example, when dropping 50 particles on the biofilm, retrieving 5 particles may not represent the same threshold as when dropping 20 particles on the surface.

Secondly, in the majority of measurements “a small number of particles (around 5)” was retrieved during several increments of MFD and consequently it was up to the operator to select the most appropriate threshold C. And thirdly, the manual increase of the magnetic force differs from operator to operator and even from measurement to measurement, with the strongest influence on the threshold C. The particle attraction behavior is different with different step sizes: when the increments are large, there are hypothetically MFDs at which 20 particles are attracted as opposed to very small increments at which only less than 5 particles are attracted at each increment.

However, from a general perspective threshold C could be representative for a “mean” adhesiveness, a seemingly useful proxy for adhesion of a surface and theoretically the most robust against outliers (see threshold B and D).

Threshold D

Threshold D is the total clearance, meaning that the last particle is retrieved by the electromagnet. Larson et al. (2009) recommend using this threshold as it is the least subjective when a human observer is involved and as such the most reproducible. The MFD needed to retrieve the last particle is necessarily higher than for the other thresholds. In following this line of argumentation, threshold D is reflecting the highest adhesion of the investigated biofilm spot. However, during the experiments this threshold could not always be related to the stickiness of the biofilm surface as particles have also been physically trapped. This

means that particles are captured e.g. between sediment grains or by filaments. If so, the operator should consider the second last particle as threshold D.

C.1.2 Needs for further development

To apply the concept of the MagPI for the purpose of this thesis a number of modifications are put forward. The need for these modifications arises from the special requirements of the research.

An appropriate calibration

Adhesion is a mechanical force and also referred to as “pull-off”, “binding”, “separation”, or “detachment” force per area, consequently a typical unit of measure is N/m^2 . Even though, the MagPI system does not provide the technical capabilities of measuring adhesion after the common definitions of adhesion theory (this would for example include: measuring the force-distance functions, i.e. the distance the two media are separated from each other as a function of the applied load, see e.g. Israelachvili, 2011) the basic concept is similar: an object that sticks to an adhesive is exposed to an external force and this force at separation of the object is a measure of adhesion.

The original MagPI is calibrated with the help of a gauss meter by measuring the magnetic flux density, which characterizes the magnetic field. Apart from the fact that the gradient of the MFD (i.e. ∇B) is the correct measure for the magnetic force (as was investigated in collaboration with the 1. Physics Institute, University of Stuttgart) the magnetic flux density can obviously not be used in mechanical models. Consequently, there is an urgent need for a mechanical calibration.

Furthermore, MFD or the gradient of the MFD only represent the strength of the electromagnet but not the characteristics of the attracted particles, which is not only a problem when different ferromagnetic particles (FP) are used but also impacts the mechanical force (will be demonstrated later). Therefore an appropriate calibration must ultimately consider both: the magnetic forces and the particle characteristics.

Reliable quantification of particle detachment

Even though being an essential part of the measurements, the definition of the thresholds and their practical applicability is difficult. Thresholds B and D which can be interpreted as proxies for the lowest and highest adhesion, respectively, are the least subjective ones and consequently, (Larson et al., 2009) recommends them over threshold C. On the other hand these thresholds are prone to misinterpretation, if physically trapped or not in contact with the adhesive surface. This is especially true as the number of particles at these thresholds (the “first” or the “last”) is small compared to the number of particles which have been spread on the surface and are attracted. The tendency of single particles being outliers is higher

than when analyzing a greater number of particles.

In this context, threshold C, which can be interpreted as a mean value (especially when looking at one measurement as a combination of a number of measurements) makes more sense. Unfortunately, threshold C is also the most subjective and it was nearly impossible to find an unambiguous definition that could be realized by human observation. Consequently, the best solution is to track the whole process of particle attraction (e.g. with a camera system), which ensures that a mean value can be evaluated and beyond that, the whole dataset can be used for further interpretation in future experiments. To achieve this objective, images of the particles below the electromagnet are taken and evaluated by means of Image Processing.

A partly automation to control the magnetic force

Manual adjustment of the applied magnetic force may result in additional uncertainties as the exact increments are hardly reproducible. As outlined above, the application of different increments may influence the results (or thresholds) significantly. Especially in combination with an improved quantification of particle detachment an automated system is of absolute necessity. Furthermore, the applied magnetic force will influence the magnetic propensity of the ferromagnetic particles. For defined forces the measuring program must likewise be exactly set (as will be described in the next section).

Considering all factors of influence

As fairly mentioned by Larson et al. (2009) the method they described results in a proxy for surface adhesion. In fact, Larson et al. (2009) simplified the mechanical adhesion considerably by not considering 1) the area of contact between the FP and the adhesive surface and 2) the dead weight of the ferromagnetic particles. Regarding 1) one can easily imagine that different particle sizes have a different area of contact and consequently also the force needed to attract them differs considerably. And regarding 2) the force needed to retrieve the particles is a combination of the force to overcome the adhesion forces but also the deadweight of the particle. If the deadweight of the FP is in the same order of magnitude as the adhesion forces, their neglectation will result in an overestimation of the adhesion forces. In the following section the modifications made to the MagPI are briefly presented, and further discussed in later sections.

C.2 The advanced setup to determine surface adhesion forces (MagPI-IP)

To address the requirements discussed above the MagPI system underwent significant modifications. The novel setup is termed MagPI-IP (Magnetic particle induction - image processing). In order to capture the images and automatically increase the magnetic force, an

additional camera (RaspberryPI camera module, 5 megapixel), a microcontroller (Arduino Leonardo) and a single-board computer (RaspberryPI 1 model B+) are added to the original setup (consisting of the electromagnet, power supply and micromanipulator for height adjustment). The complete setup is illustrated in Figure C.3.

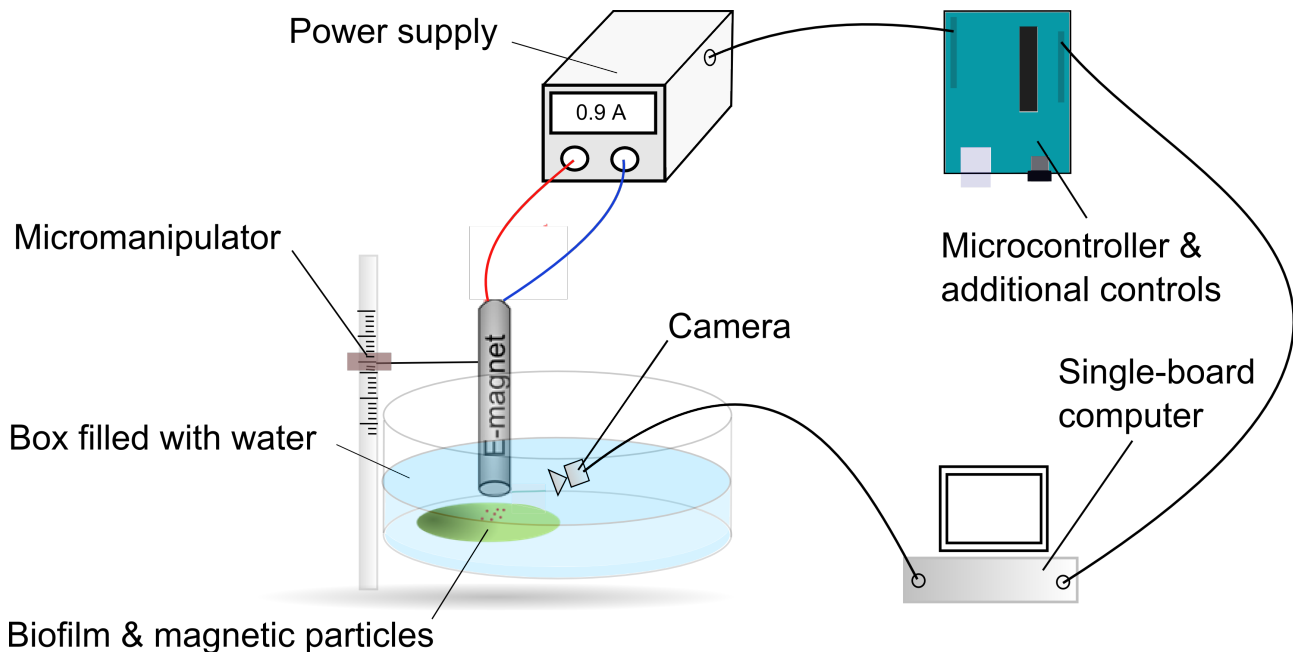


Figure C.3 Schematic representation of the novel MagPI-IP system. In addition to the original setup (electromagnet, power supply and micromanipulator) a camera automatically captures the particles below the electromagnet when the next increment of magnetic force is triggered. Both, the camera and the power supply are triggered by a combination of a single-board computer and a microcontroller. The specific measuring programs can be adapted to the research objectives.

The single-board computer sends a command both to the microcontroller and the camera. After receiving the command, the microcontroller increases the magnetic force of the electromagnet in pre-defined increments (here: $\Delta \nabla B = 1.5 \text{ mTesla/mm}$ every six seconds). This is done by sending a pulse-width modulated signal (PWM) passing through a filter (to smooth the signal: the circuit diagram can be found in the Appendix A.1.1) to the power supply. During each increment one image is captured by the camera (here three seconds after increasing the magnetic force). The programs are fully flexible and can be adjusted to the specific needs. Once the programs are installed on the single-board computer and the microcontroller, the user is guided through the whole process via the computer screen. The data (essentially the captured images) is then stored on a USB stick that can be transferred to a desktop PC for evaluation of the data. The data evaluation is described in detail in Section C.4.

A typical dataset, consisting of captured images at each increment of magnetic force is presented in Figure C.4.

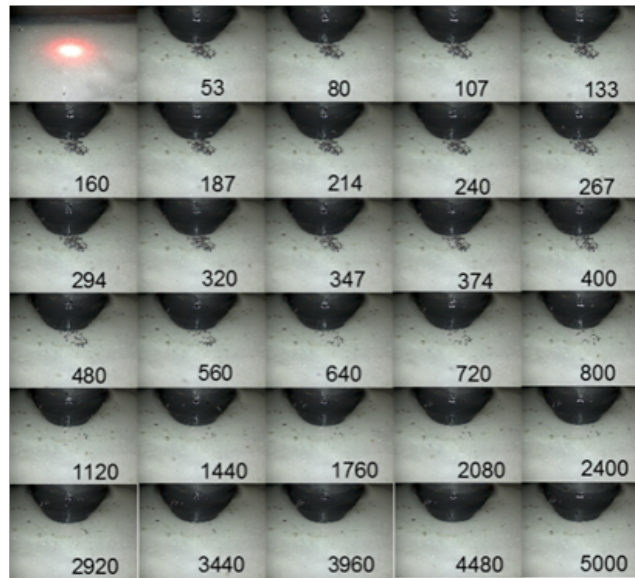


Figure C.4 A typical data set consisting of images captured by the MagPI-IP system. The ferromagnetic particles are in the center of the images. Further denoted in the bottom right corner is the electric current (I [mA]) applied at image capturing. The images illustrate the gradual reduction of particles with increasing magnetic force (especially after $I = 400$ mA). The red laser spot was initially used for defining the area which will be evaluated later and was replaced by a more practical solution during the course of the development of the device.

The basic procedure of measuring the surface adhesion forces is presented as a flow chart in the Appendix (A.2) and briefly explained here. In the first step a Python script is executed which is installed on the single-board computer. The user needs to enter details of the experiment which will later be relate the data to the specific experiment. Then, a background picture is taken by positioning the electromagnet at a defined distance to the measuring area and starting the program by pressing the start button. Hereafter, the particles are spread on the surface and the program initiates the measuring routine on command (more details in Section C.4).

C.3 The calibration procedure

As outlined before, the force which attracts the particles is both depending on the force of the electromagnet and the material properties of the attracted ferromagnetic particles (FP). Before the calibration procedure is described in Section C.3.2 these dependencies will be demonstrated with the help of examples to provide a general understanding of the electromagnetic background. To unravel the physics behind the device, three studies were conducted in close cooperation with Dr. Marc Scheffler from the 1. Physics Institute of the University of Stuttgart (Kikillus, 2012; Bierbaum, 2015; Dany, 2015). Some basic findings from these studies are presented below.

C.3.1 Electromagnetic forces and magnetic particle properties

The physically correct electromagnetic force

In their original publication on the MagPI Larson et al. (2009) claimed that the magnetic flux density (B in mT) is responsible for the particle attraction by the electromagnet, where the magnetic flux density is the magnitude of the magnetic field. On the basis of a simple experiment Bierbaum (2015) could demonstrate that in physical terms not the MFD but the gradient of the MFD (∇B in mT/mm) is responsible for the attraction of the particles, which means that the spatial changes of the MFD (close to the tip of the electromagnet the MFD is high and decreases with vertical distance) lead to the retrieval of FP.

In the experiment a homogeneous magnetic field was produced by two permanent magnets. In this setup the MFD was artificially increased while no gradient was produced (i.e. $\nabla B = 0$). If one considers that the magnetic flux density is the driving force of particle attraction (as proposed by Larson et al., 2009), the particles should be attracted at the very same value of B^1 as compared to a normal measurement without the additional permanent magnets. However, it could be demonstrated that the magnetic flux density needed to retrieve the particles from differently adhesive surfaces was always higher using the additional permanent magnets. Consequently it was concluded that B is not an appropriate measure of the electromagnetic force, instead strong hints indicate the role of ∇B as the driving force.

Figure C.5 is an example of a typical curve where the electromagnetic force ∇B is plotted versus the applied electric current.

Regarding the determination of ∇B Bierbaum (2015) conducted two measurements. Using a Hall probe connected to a gauss meter, the magnetic flux density is measured at a vertical distance of $h_1 = 3.5$ mm and $h_2 = 4.5$ mm from the tip of the electromagnet. The gradient of the MFD is calculated as $\nabla B = (B(h_2) - B(h_1)) / (h_2 - h_1)$. From Figure C.5 it is apparent that a) the electromagnetic force increases with applied electric current and b) the curve is linear between 0 and approximately 750 mA. At higher electric currents, the curve is significantly flattened. This saturation is a typical behavior of electromagnets and is induced by a full magnetization of the core material and introduces difficulties in adjusting the electromagnetic force in a linear way. In the original procedure the electric current is controlled via turning the potentiometer of the electric current located on the power supply. In doing so, the force of the electromagnet is significantly increased at lower electric currents (I), while at higher electric currents the same rotation of the potentiometer nearly has no consequences.

Even though it has been demonstrated that ∇B is physically correct, it is to be mentioned that B is proportional to ∇B under the normal measuring conditions. Consequently, the magnetic flux density is still adequate for demonstrating e.g. the impact of the distance to

¹In the setup with the permanent magnets the magnetic flux density was measured considering the impact of both, the permanent magnets and the electromagnet

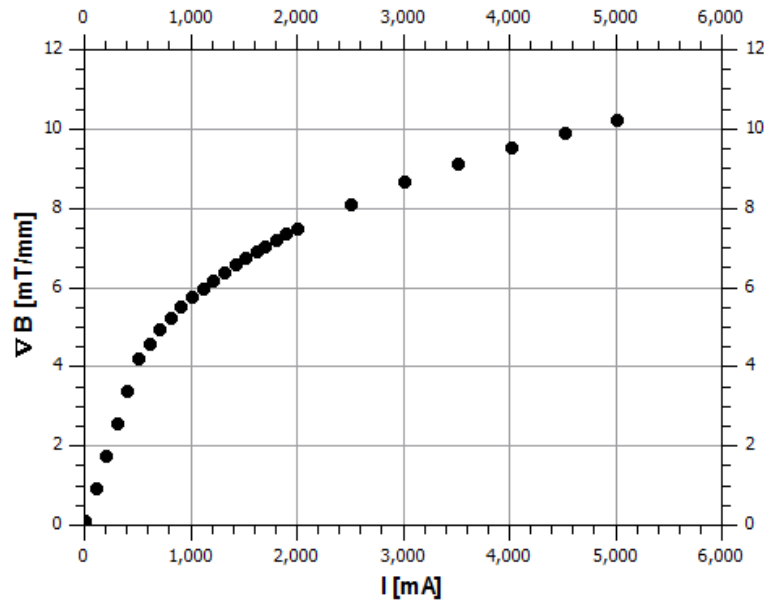


Figure C.5 Graph illustrating the relation between the gradient of the magnetic flux density (∇B) and the applied electric current (I) of an electromagnet with 1000 turns of wire. For more details on the electromagnet see Appendix A.1.2. Data from Bierbaum (2015)

ferromagnetic particles on the electromagnetic forces (as will be shown in the next paragraph).

The correlation between the electromagnetic force and the distance to the ferromagnetic particles

As reported by Larson et al. (2009) the electromagnetic force strongly depends on the distance between the tip of the electromagnet and the ferromagnetic particles. This dependency is confirmed by the measurements of Kikillus (2012), see Figure C.6.

The figure readily illustrates that the highest electromagnetic force is to be found at the closest distance to the tip and decreases with increasing distance. At a distance of 3 cm the magnetic force nearly vanishes completely. At a distance of 4 mm (the dashed line in Figure C.6), which corresponds to the distance between FP and the electromagnet in the experiments, the magnetic flux density is equal to $B \approx 20$ mT. Furthermore the figure shows that the sensitivity of the electromagnetic forces towards increasing distance from the tip is higher at lower distances than at distances more far away. Consequently, there is a tradeoff between high electromagnetic forces/high sensitivity and low forces/low sensitivity.

As the biofilms surface is highly heterogeneous (with peaks and valleys) and it is thus not always possible to position the tip of the electromagnet exactly at a predefined distance, it is of particular interest to quantify the loss or gain of electromagnetic forces due to a deviation from the targeted distance. Figure C.7 illustrates the percental deviation of the electromagnetic force with deviations from the 4 mm reference distance.

The graph demonstrates the high sensitivity that is to be taken into account to achieve a

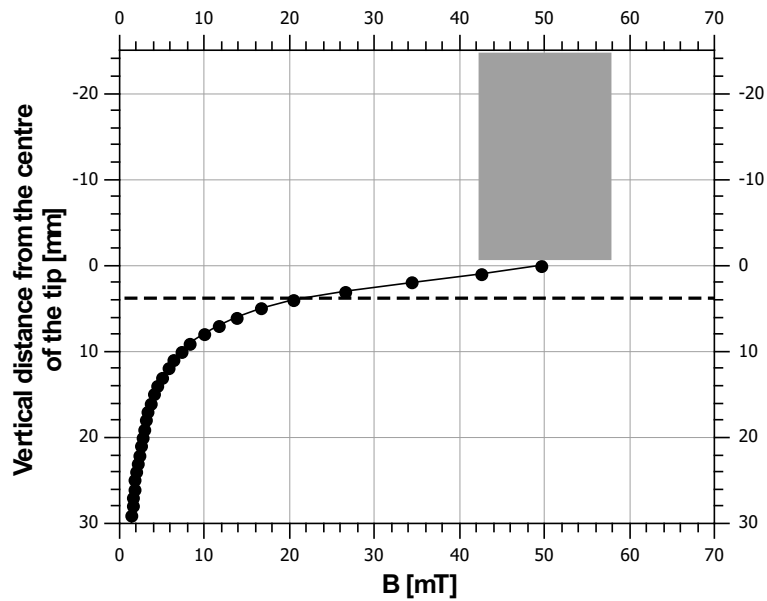


Figure C.6 Changes of the magnetic flux density with vertical distance from the center of the tip of the electromagnet. The grey bar is representative for the geometry of the electromagnet's tip. Measurements are conducted by applying an electric current of $I = 600 \text{ mA}$. The dashed line is the distance the electromagnet is currently set to ($= 4 \text{ mm}$) in the experiments. Data from Kikillus (2012).

particle attraction with the constructed electromagnets, as increasing the distance to the particles did not result in FP attraction on highly adhesive biofilms. For this specific electromagnet a ferromagnetic particle which is 0.3 mm closer to the tip experiences a 10% increase of attracting force.

Besides the vertical distance, the horizontal distance from the centre of the tip impacts the measuring results as is illustrated in Figure C.8. While the electromagnetic force is highest in the centre of the magnet, it decreases in a bell shaped form towards a higher horizontal distance. The coefficient of variation (CV; i.e. the standard deviation divided by the mean electromagnetic force below the centre of the tip) increases likewise.

When the particles are positioned outside of the projected area of the electromagnet (the dashed lines in Figure C.8) they experience a coefficient of variation greater than 10% and a significantly reduced B . In other words these particles are attracted later in the experiments (when the electromagnetic forces are high enough) which might also influence the determination of the thresholds. As a consequence these particles should not be taken into consideration to achieve a higher accuracy of the method.

In summary, the results obtained with the current setup are still prone to significant deviations which shall be considered when evaluating the data. While the uncertainties which are produced by horizontal deviations are minimized with a technical solution, the deviations induced by vertical mis-positioning could not be addressed. As a future recommendation a

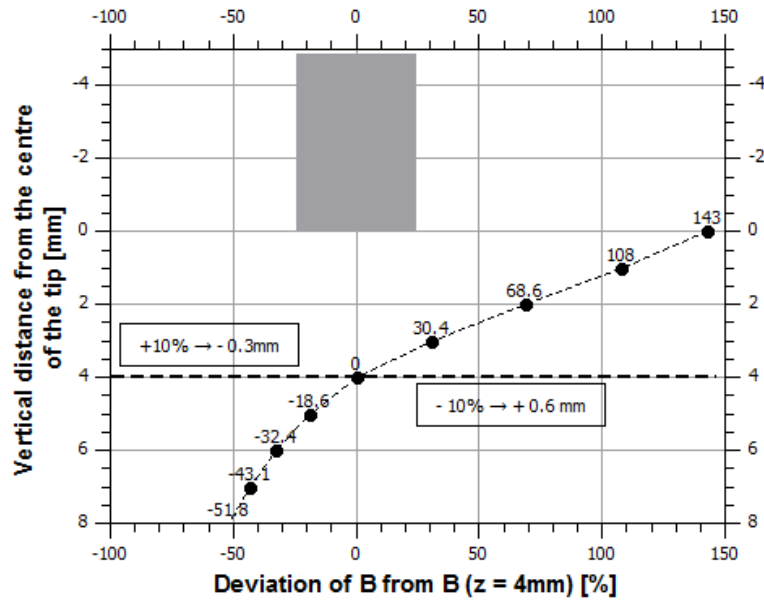


Figure C.7 Sensitivity of the electromagnetic force to a vertical distance deviation from the targeted distance between electromagnet and ferromagnetic particles ($= 4\text{mm}$). The grey bar is representative for the geometry of the electromagnets tip. Measurements are conducted by applying an electric current of $I = 600\text{mA}$. The deviations of electromagnetic force are presented in percentage of $B(z = 4\text{mm})$. Data from Kikillus (2012).

possible solution could be the use of other core-materials, stronger magnets or FP which can be retrieved at lower ∇B .

Electromagnetic forces and ferromagnetic particle properties

As already mentioned in Section C.1.2, the magnetic force alone is not sufficient to investigate the mechanical force of adhesion. The particles properties must be considered as well. In this context, the particles geometries (size, shape, surface roughness, see e.g. Zafar et al., 2014), their density/weight and particularly their magnetic properties are a decisive factor.

To illustrate the importance of considering the particle characteristics, a simple test on two types of FP is carried out, applying the same setup of electromagnet and measuring routine: The first set of particles is manufactured by PARTRAC[®] (UK) and sieved to a size range of $d = 200 \dots 355 \mu\text{m}$. The particles are ferromagnetic and have a fluorescent coating. In preliminary experiments they were considered to be suitable and applied as standard particles in the rest of the experiments in this thesis. The second test particles (F-red lake) have a more or less similar size ($d = 150 \dots 300 \mu\text{m}$) and consist of iron grit colored with water insoluble food dyes. They are manufactured by Micro-Tracers Inc. and usually used in mixing of e.g. food products to test if all ingredients are mixed correctly.

Magnetization of the particles is an important magnetic property. In simple words, mag-

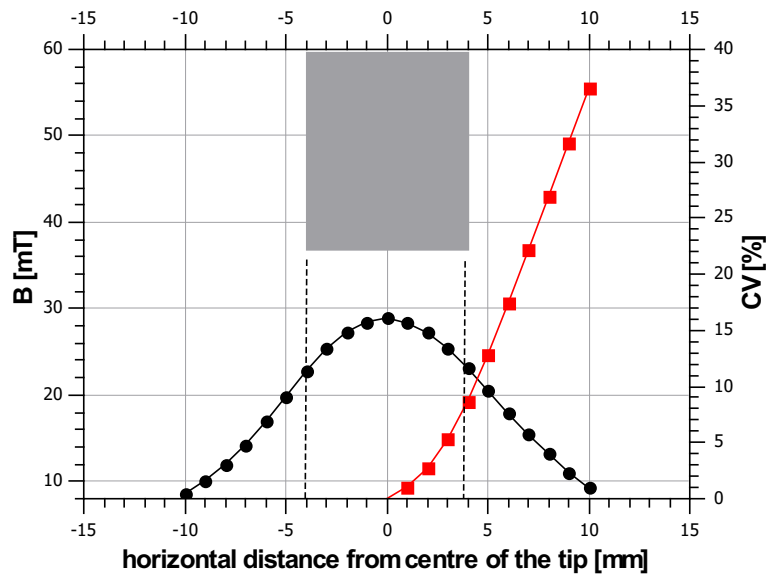


Figure C.8 Changes of the magnetic flux density by horizontal distance of the particles from the centre of the tip. Additionally the coefficient of variation (CV) of the magnetic flux density is plotted in red by considering the force in the centre of the tip as the reference value. All measurements conducted at a vertical distance of (4 mm) from the tip. The grey bar is representative for the geometry of the electromagnets tip. Measurements are conducted by applying an electric current of $I = 1000$ mA. Data from Bierbaum (2015).

netization describes the propensity of material to be attracted or to attract other materials. Apparently, the F-red particles are more easily to be magnetized as they produce chains (similar to the chains illustrated in Figure C.9) which continue to exist after removal of the external magnetic field.

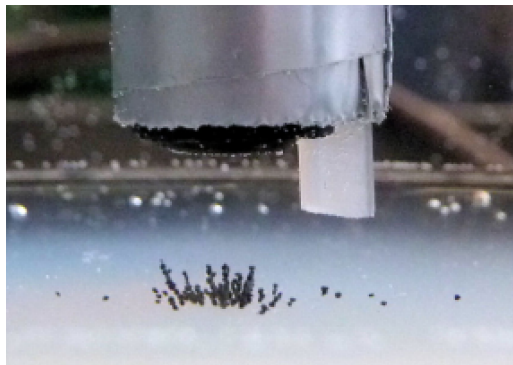


Figure C.9 Chains of particles, indicative for an increased propensity for magnetization (photograph from Bierbaum, 2015)

For the simple demonstrational experiments, both types of particles (three replicates each) have been spread on an adhesive surface (Xanthan gum with 1wt.% powder mixed with water) and subjected to an increasing magnetic force (following the standard measuring procedure described in Section C.2) to determine differences in the attraction of the particles. Figure C.10 illustrates the enhanced detachment of particles as percentage detachment of the particle surfaces with increasing ∇B . A similar form of representation will be used widely

in the thesis and is explained in more detail Section C.4.

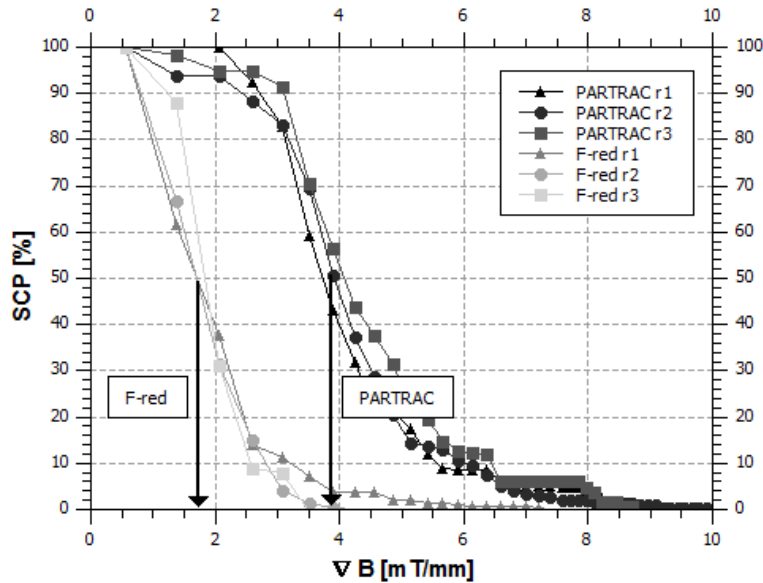


Figure C.10 The attraction behavior of two different types of particles by an electromagnet on the same surface. Generally the particles are retrieved with increasing ∇B illustrated by a decrease of the surface covered by particles (SCP) in %. The light grey curves represent 3 measurements (replicates: r1, r2, r3) using the PARTRAC® particles and the dark grey curve stands for the F-red particles. The particles predominantly differ in their magnetization characteristics. The vertical arrows indicate the electromagnetic force needed to retrieve the first half of the particles

The experiment demonstrates effectively that a lower magnetic force is needed to attract the F-red particles than the standard particles (PARTRAC®). For example, to attract the first half² of the F-red particles a $\nabla B = 1.7 \text{ mT/mm}$ is needed while the magnetic force more than doubled to attract the same percentage of PARTRAC® particles ($\nabla B = 3.8 \text{ mT/mm}$).

The tendency of a ferromagnetic particle to be attracted increases with the strength of the externally applied magnetic field. When exposed to this field the particle is magnetized and can be attracted more easily. If the magnetic field is even higher (in certain boundaries) the particles are magnetized to an even higher degree and their attraction is further enhanced. This effect (i.e. the magnetization $M \text{ [A/m]}$ is a function of B) is different for different materials.

To characterize the behavior of materials being magnetized physicists utilize a hysteresis plot (as shown in Figure C.11).

The figure illustrates a typical hysteresis of a ferromagnetic material (Tipler & Mosca, 2015). It shows the internal magnetic field (B_{int}) of e.g. a particle as a function of an externally applied magnetic field (B_{ext}). The curve progression between the origin “O” and “ P_1 ” can

²Actually it is not the first half of the particles but a reasonable proxy, further explained in Section C.4

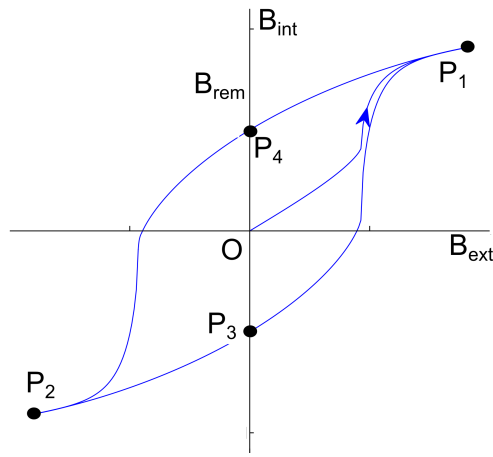


Figure C.11 A typical hysteresis plot of a ferromagnetic material. The curve from point “O” to “P₁” represents the response of the internal magnetization (B_{int}) to an external electromagnetic field (B_{ext}).

be regarded as a first application of an increasing external magnetic field (B_{ext}) on a ferrous material. While exposed to an external magnetic field (B_{ext}) the particle is magnetized (its internal magnetic field B_{int} is a function of the B_{ext}). When the external field is reduced or switched off, the material keeps on being magnetized to a certain degree which is termed the remanence of the material (see Figure C.11 point B_{rem}).

The magnetization M is additionally influenced by the time of exposure to the external magnetic field. This fact further underlines the importance of an automated system in which the increments of ∇B can be controlled and standardized for each experiment. In the measurements each increment is applied exactly for six seconds.

According to Gardel et al. (2005) the mechanical force (i.e. the force which the calibration aims at) can be expressed as the product of magnetization and the gradient of MFD:

$$f(t) = \vec{M}(t) \cdot \frac{\delta \vec{B}(t)}{\delta x} \quad (\text{C.1})$$

where $\vec{B}(t)/\delta x$ is the time dependant ∇B . The magnetization M is further depending on magnetic susceptibility: χ and the permeability μ_0 (Tipler & Mosca, 2015) of the material. In simple words, the forces on the particle or the forces that are needed to retrieve one particle might differ significantly by a) the time of exposure to the electromagnet and b) the material the particles are made of. To further complicate things, even particles made of the same material can have a very different magnetization M (or m in emu), which is illustrated in Figure C.12 by the differences in hysteresis character of three geometrically different PARTRAC[®] particles.

Figure C.12 illustrates that the magnetization of particles is correlated with their size. The

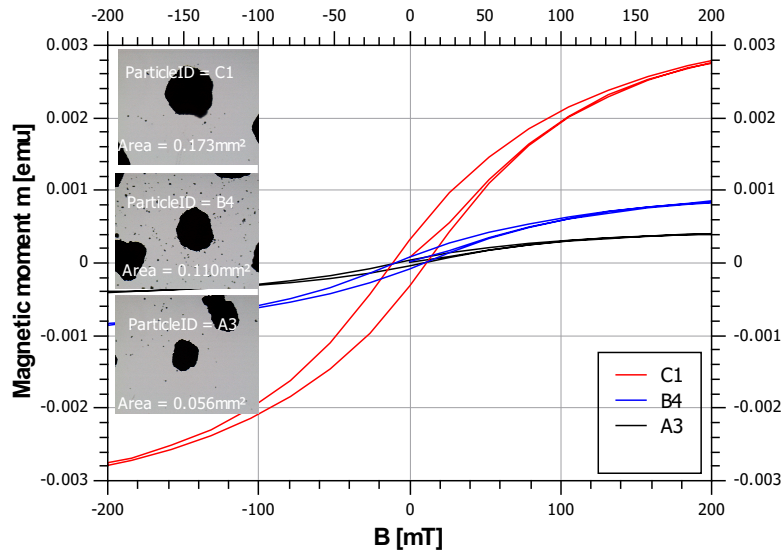


Figure C.12 Differences in magnetization of particles with different geometries but manufactured from the same core material. Particle C_1 has the largest surface area and has the highest propensity towards magnetization, followed by B_4 and the smallest particle A_3 (data from Dany, 2015).

highest degree of magnetization is experienced by the largest particle and the lowest by the smallest particle. According to Dany (2015) this can be explained by the differences in particle-volumina as the volumina is proportional to the magnetization. Consequently, it is recommended to use particles of the same or comparable sizes to reduce the differences in magnetization in future experiments. This assumes that the size and the volume of the material that is attracted are proportional. In fact, the magnetic core material of the FP is coated with a fluorescent color and unfortunately it is not clear how uniform this color was applied on the particles.

In the following section a simple and effective calibration procedure is described. In this procedure the resulting mechanical force is measured which is according to equation C.1 a function of the magnetization of FP and the electromagnetic force. Consequently, this procedure makes the determination of both individual parameters redundant. This is acceptable as only the mechanical force is of importance for the here presented adhesion measurements. Still, without the fundamental insights reported here, an interpretation and proof of concept of the calibration procedure could have never been realized.

C.3.2 The calibration of the MagPI-IP device

The following text is modified from Thom et al. (2016)

The main goal of the here presented calibration procedure is to obtain the mechanical tensile force on one particle at different applied electric currents to the electromagnet. This vertical tensile force is denoted as F_{em} [$\mu\text{N}/\text{particle}$] and is a key value for the determination of surface adhesion as will be discussed in Sections C.4 and C.5. The basic idea is, that the

vertical tensile force F_{em} at detachment of one particle from the surface can be related to the retentive force of that surface.

It is important to mention that the design of the electromagnet, the properties of the ferromagnetic particles and even the measuring program (temporal length of the applied electromagnetic force and quantity) can have an impact on the resulting magnetic force. It is therefore strongly recommended to recalibrate the device for each possible scenario.

The here described calibration setup is designed in such way, that it is reproducible in modern laboratories: A random number of ferromagnetic particles is permanently glued on a small PVC cylinder (see Figure C.13).



Figure C.13 Ferromagnetic particles (red) permanently glued on a PVC cylinder. The diameter of the cylinder is equal to the core diameter of the electromagnet. The upper side of the cylinder is painted with a white color to provide a good contrast between the particles and the background, in order to evaluate the number of particles by Image Processing.

The diameter of the cylinder should be equal to the core diameter of the electromagnet, as only this area will be evaluated later (see Section C.4). The cylinder is then placed in a small box on a laboratory scale (PCE-LS 500C, resolution 0.001 g, reproducibility 0.002 g). The box is placed approximately 12 cm above the scale (using a PVC column) to prevent the electromagnet from attracting the metallic scale plate (see Figure C.14 a). At this distance no influence of the electromagnet is detectable by the gauss meter.

The electromagnet is positioned with a vertical distance of 4 mm above the particles (the same distance is used for the measurements). In contrast to the real measurements where the surface, the particles as well as the tip of the electromagnet are submerged, all calibration measurements are conducted under dry conditions. From a physical point of view this will not impact the electromagnetic force as both in water and air, the magnetic permeability, which is responsible for supporting a magnetic field, of the respective media is almost identical (permeability of water: $\mu = 1.256627 \times 10^{-6} \text{ H/m}$, permeability of air: $\mu = 1.25663753 \times 10^{-6} \text{ H/m}$). As a consequence the magnetic force "submerged" and "in dry conditions" is equivalent. The reason for this simplification in the calibration procedure is that submerged measurements are subjected to temperature changes of the water, by the influence of the heated electromagnet and the ambient temperature. This results in a) expansion of the electromagnets coating b) expansion of the water and c) evaporation of water which all influence the measuring results and complicate the calibration unnecessarily.

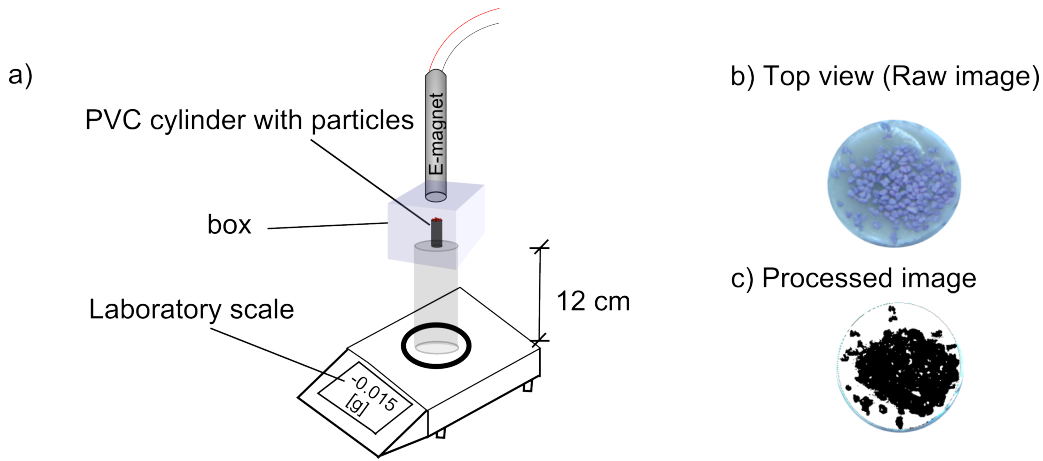


Figure C.14 Methods used during calibration. *a)* sketch showing the calibration setup, *b)* and *c)* A raw and processed top view image of the particles (pink) glued to the cylinder for the determination of the projected surface area (black pixels are the FP).

To determine the tensile force F_{em} the gradient of the magnetic flux density (∇B) is increased incrementally. At each increment the sum of the particles are attracted more strongly. As the particles are firmly attached, they lift the PVC cylinder (without losing contact to the ground) and thus reduce the weight on the scale by ΔF_{scale} [N]. To determine the tensile force on a single particle ΔF_{scale} needs to be divided by the number of FP:

$$F_{em} = \frac{\Delta F_{scale}}{n} \quad (C.2)$$

where n is the number of particles determined by dividing the total projected surface area of the particles with the projected surface area of one single spherical particle. The total projected surface area is measured by analyzing top view images of the upper side of the cylinder (see Figure C.14 *b* and *c*).

Figure C.15 illustrates a typical calibration curve where the tensile force (F_{em}) is plotted against ∇B for one specific combination of electromagnet and particles (the • symbols). The graph shows that the tensile force on a single particle ranges between $0 \dots 1.3 \mu\text{N}/\text{particle}$ corresponding to $(0 \dots 1.3) \times 10^{-6} \text{ N}/\text{particle}$.

The graph further illustrates a non-linear relationship between F_{em} and ∇B . Especially at $\nabla B > 4.5 \text{ mT}/\text{mm}$ the tensile forces are considerably greater than the indicated linear relationship (the dashed line). This behavior is explained by the magnetization of the particles (see previous section) resulting in an increased propensity to being attracted. For FP which have a lower propensity towards magnetization, the curve would be more linear - as can be seen, the magnetization obviously has a non-negligible impact on the measuring results. For practical reasons, F_{em} is better expressed as a function of the electric current I (see Figure C.16), as the latter will later be controlled with the help of a microcontroller (or in the manual version, by turning the potentiometer).

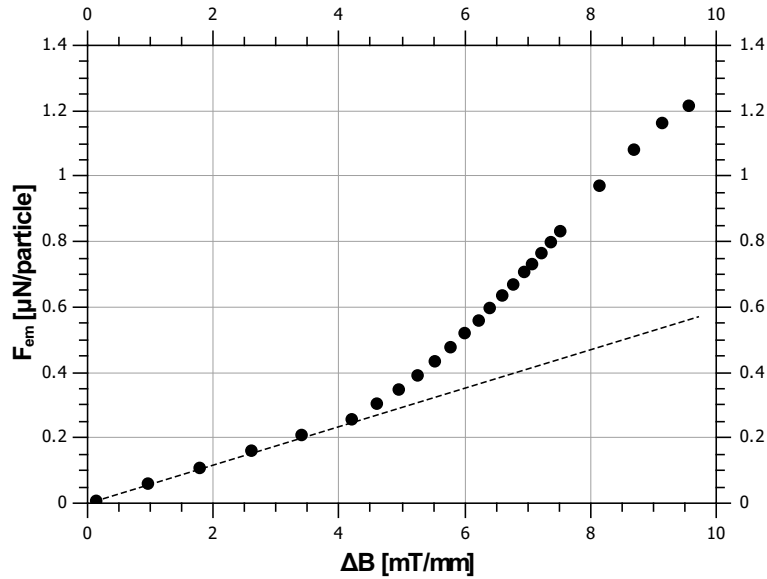


Figure C.15 Calibration curve illustrating the relation between the tensile force exerted by the electromagnet on one particle and the applied gradient of magnetic flux density (the \bullet symbols). The dashed line is a theoretical curve for ferromagnetic particles which are less magnetizable. The deviations from this theoretical curve underline the importance of further considering the magnetic properties of the attracted particles.

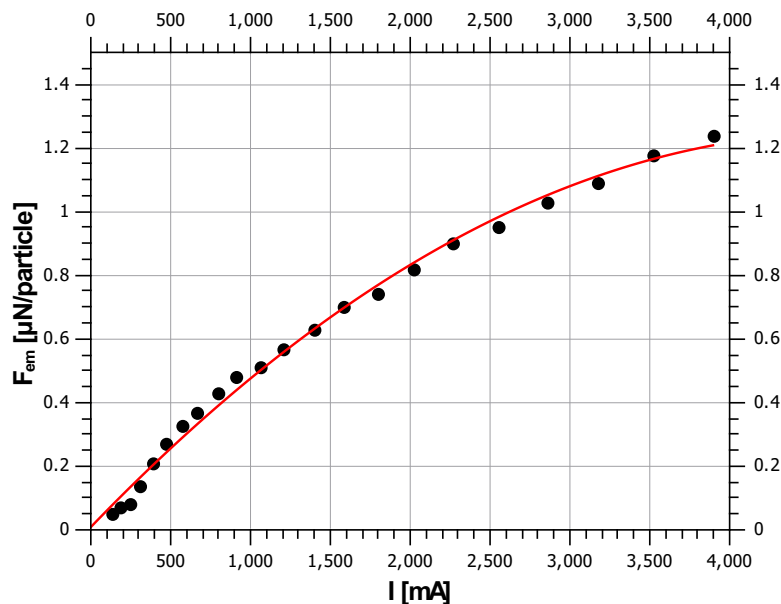


Figure C.16 Calibration curve illustrating the relation between the tensile force exerted by the electromagnet on one particle and the applied electric current. The \bullet symbols are the averaged values of six measurements and the red line is the fitted quadratic regression.

Illustrated in Figure C.16 are the averaged values of six individual calibration runs (the \bullet symbols). The fitted regression curve (in red) can be used to transform the electric current

(I) into the tensile force ($R^2 = 0.994$, $n = 6$):

$$F_{em} = 8.819 \times 10^{-3} + 5.216 \times 10^{-4}I - 5.488 \times 10^{-8}I^2 \quad (\text{C.3})$$

The precision of the single measurements is reasonably good in the range of expected values for adhesive surfaces ($F_{em} > 0.25 \mu\text{N}/\text{particle}$), as illustrated in Figure C.17.

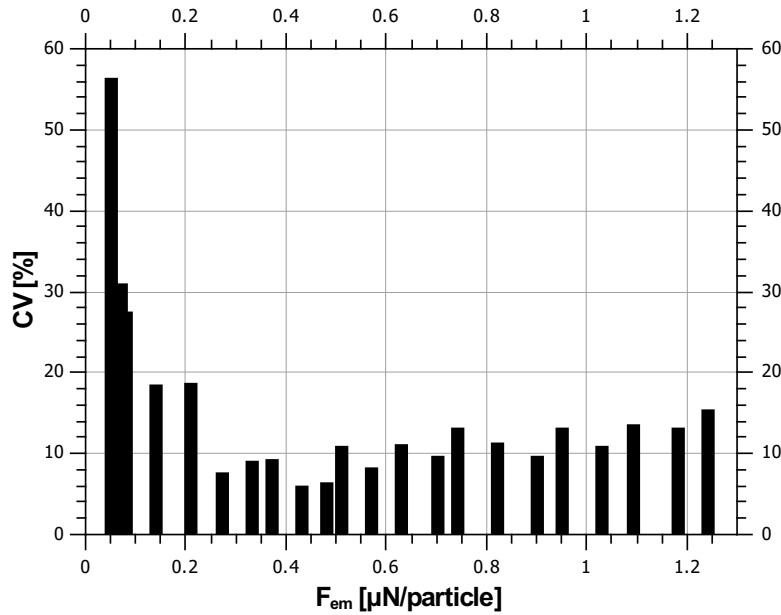


Figure C.17 The coefficients of variation for tensile forces on a single particle at the applied increments of tensile forces. Six measurements are conducted and the standard deviation at each increment is divided by the mean value to obtain the CV as a measure for precision of the calibration procedure.

In this range the coefficient of variation is approximately 10%. Below $F_{em} = 0.25 \mu\text{N}/\text{particle}$, however, the averaged CV is higher ($\approx 24\%$). This may be explained by the accuracy of the scale. At the lower ranges of ∇B the weight reduction ΔF_{scale} is in the order of magnitude of the scales' resolution of 0.001 g and unfortunately smaller than the reproducibility (0.002 g).

C.4 Data evaluation by image processing

Note: The content of this section is modified from: Thom et al. (2015b)

The quantification of ferromagnetic particle retrieval by the electromagnet is an essential feature of the advanced system. Quantification enables to relate the tensile force on individual particles to the detachment processes and allows deeper insights into the surface adhesion characteristics of biofilms. This is especially useful for a determination of a mean adhesiveness (which was hardly possible with the unmodified device) but also for increasing the reliability of data and comparability between different laboratories. Moreover, the quantification is helpful for further improvements of the method (e.g. to compare the attraction

behavior of different particles as has been demonstrated in the previous section).

Image Processing

The images that have been captured by the MagPI-IP device (see Section C.2) are transferred to a desktop PC and loaded into the MATLAB® program which was developed for this purpose. When the program starts, the user is guided through the whole process. The single steps of this process are described briefly in the following.

It is important to note that, due to the limitations in the processing of images, the MagPI-IP system currently cannot differentiate between individual particles. Instead, the Surface area Covered by Particles (in the following denoted as SCP [px]) is used as a proxy.

Step 1

The first picture that is presented to the user of the software, shows the particles below the electromagnet and an additional rectangle. This rectangle defines the area of interest (Aoi), which means that only the particles inside this area are evaluated (see Figure C.18 *Right*). The dimensions of the Aoi were determined *a priori* by e.g. placing a drawing with the exact dimensions of the electromagnets core below the electromagnet, capturing an image and then placing the rectangle in the program on that exact position (see Figure C.18 *Left*). The reason for the identification of the Aoi is that particles located inside this area are exposed to a nearly constant magnetic force (as described in Section C.3.1). All other particles are disregarded in the next steps. All images of one run are now trimmed to this area (see Figure C.19) for the further analysis.

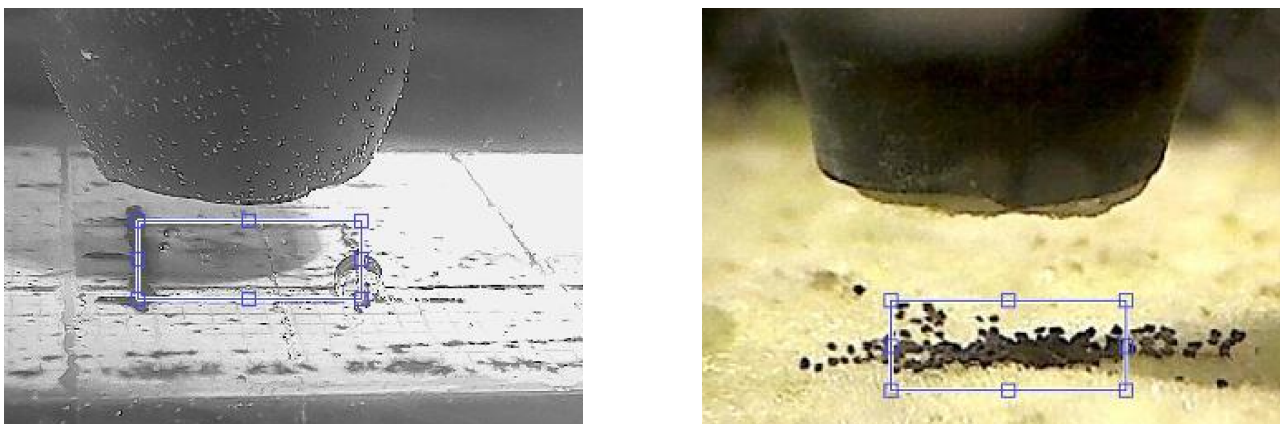


Figure C.18 Step 1 of the image processing: Identification of the area of interest (Aoi). *Left*: Identification of area directly below the electromagnet. The Aoi (rectangle) is positioned and resized; *Right*: Initial picture ($I = 0$ mA) with selected Aoi.

Step 2

To differentiate between the ferromagnetic particles and the biofilm, the images are converted to binary image (black and white) after manually choosing an appropriate threshold value and subtraction of a background image. The FP then appear black and the biofilm is

white. Figure C.19 illustrates the original image and the computed binary images for different thresholds. It can be seen that the sensitivity in interpreting a colored pixel as a black pixel is higher for lower thresholds. This manual step is important, since in the process of biofilm formation, the contrast between particles and background may change considerably. To reduce subjectivity in this step, the program displays binary images of different thresholds and the operator compares this to the original colored image; thus the correct choice of an appropriate threshold value is straightforward.

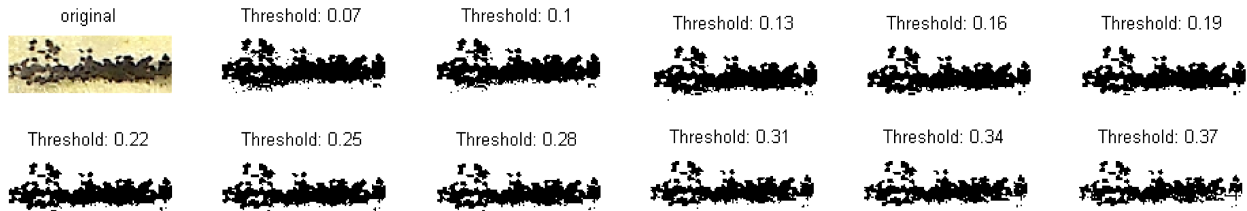


Figure C.19 Step 2 of the image processing: Screenshot showing the initial picture ($I = 0$ mA) and the same picture converted to binary images for different thresholds. The operator chooses the most appropriate threshold value so that only the particles (not the biofilm) are represented as black pixels.

Step 3

Determination of SCP: The black pixels (i.e. the surface covered by particles, SCP) are counted and plotted into one graph together with the corresponding magnetic flux density (circles in Figure C.20). Pixels which are left as black pixels after one run are either noise (a part of the background is identified as particles) or particles which are left because the electromagnet could not attract them. The number of these pixels is automatically subtracted (this process is hereafter called “subtraction”). It is strongly recommended to check and compare the original pictures with the binary images and note any anomalies. For this purpose the program provides all necessary data from each individual step of processing (e.g. see Figure C.21 illustrating the original images and the corresponding computed binary images).

Step 4

Analysis of the data: The operator identifies the step just before the first particles are attracted. This is usually the maximum SCP as the particles orient themselves towards the magnet before being attracted³. Sometimes, either due to noise or due to a bad quality of the images, SCP values at increment i are higher than one increment before. These values are unrealistic as this would mean that more FP are suddenly present below the electromagnet than in the increment before. These erroneous data however, can under certain conditions impede the subsequent analysis. Therefore, in this step, SCP values (SCP_i) which are higher than their neighboring previous values (SCP_{i-1}) are set to (SCP_{i-1}). This process is hereafter called “filtering” At the end of step 4 the SCP is converted into percentages of the maximum SCP for a better interpretability of the results.

³As the camera is positioned at the side of the device (with a camera angle of approximately 20°), this initial orientation results in an increase of SCP

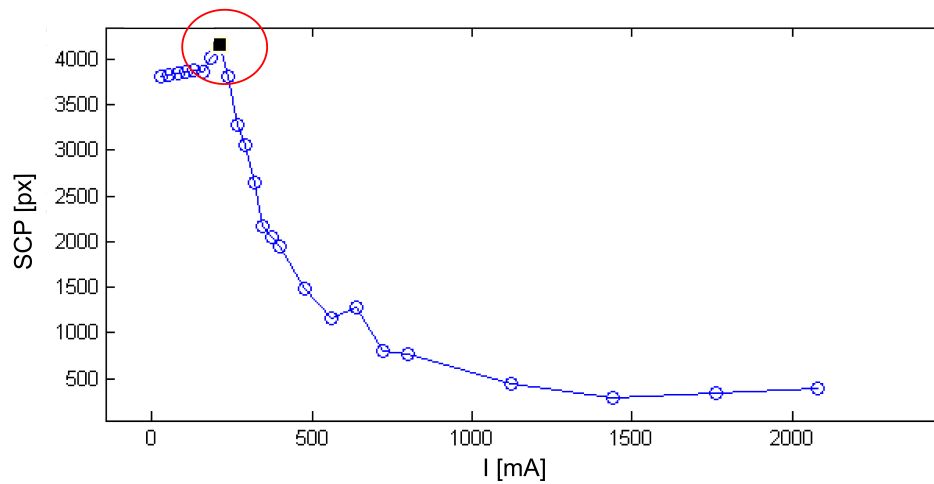


Figure C.20 Step 3 and 4 of the image processing: Screenshot showing the surface area covered by particles (SCP in px) plotted against the applied electric current. The operator identifies the last value before the SCP decreases, due to particle retrieval (see ■ in red circle). Only the data which lies between this value and the end of the measurements is evaluated.

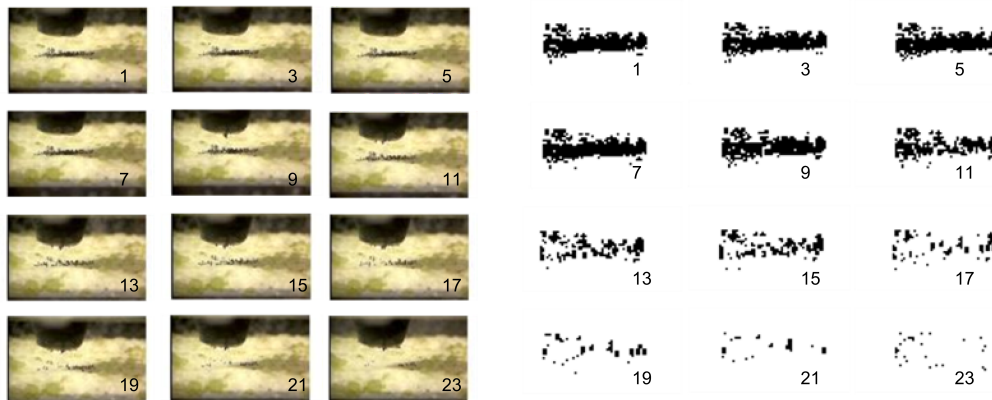


Figure C.21 Screenshot showing the original images as captured by the MagPI-IP device (colored) and the corresponding computed binary images which are further processed. Please note that the binary images have been trimmed to the extensions of the predefined AoI. To improve visibility only 12 of 24 images are shown. The numbers in the bottom right corners denote the respective increment (0...24) in which the images are captured

Step 5

In the final step the processed data is illustrated in two graphs (see Figures C.22 and C.23). The first graph (Figure C.22) shows the development of SCP [%] with increasing electric current I . The red curve in the figure illustrates the final results and the blue curve represents the raw data (before “subtraction” and “filtering”) to provide the operator with the opportunity to check the data. Furthermore, this step is also useful for evaluating the quality of the data as too high deviations between the curves indicate a significant quality loss due to a low contrast between the FP and the biofilm. The second graph (see Figure C.23) illustrates the reduction of SCP (ΔSCP) in each increment of applied electric current. The columns in this

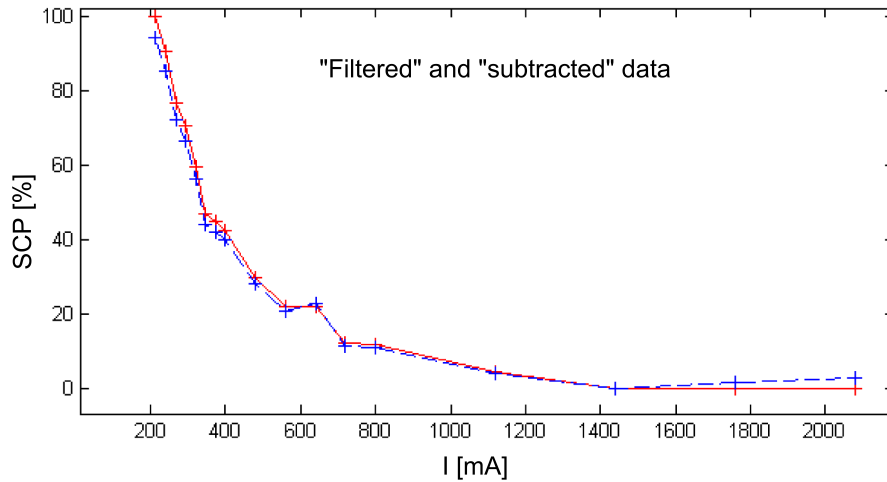


Figure C.22 Step 5a of the image processing. The final results are presented. This graph illustrates the final relationship between SCP and I (in red). The blue curve is the unprocessed raw data.

bar graph readily illustrate at which increment the most particles are retrieved.

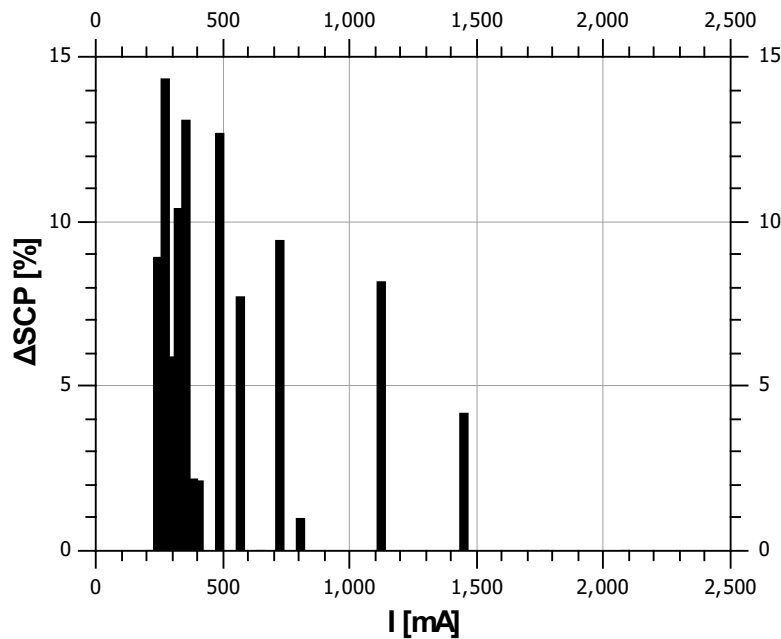


Figure C.23 Step 5b of the image processing. The final results are presented. Bar graph of the decrease of SCP at each increment of electric current.

All data is saved to comma-separated text files for further evaluation. Generally this data allows a wide range of analyses (e.g. lowest/highest adhesion, heterogeneity of the surface adhesion). In the present evaluation, however, a mean surface adhesion will characterize the biofilm. Therefore, a mean pull off force (F_m [$\mu\text{N}/\text{particle}$]) is calculated from the individual values of $F_{em,i}$ at the electromagnetic force increment i and the ΔSCP_i at the very same increment. The electric current is first converted into the tensile force $F_{em,i}$ by applying the

calibration function (e.g. equation C.3). Then the mean pull off force F_m is calculated as:

$$F_m = \sum_{i=1}^n \frac{(F_{em,i} \times \Delta SCP_i)}{100} \quad (C.4)$$

C.5 Calculating surface adhesion from the mean pull off force

So far the calibration resulted in a mean pull off force. The mean pull off force (F_m) is a vertically upwards directed averaged force needed to attract the particles from a surface (as presented in the simplified concept in Figure C.1). In the context of the material property “surface adhesion” the mean pull off force F_m plays an important role. However, F_m alone is not sufficient to describe surface adhesion as it depends strongly on the design of the measuring method.

For example, it is intuitive to assume that particles which are fully covered by EPS are much more difficult to separate from the surrounding EPS, which would inevitably result in a higher pull off force. Or, the particles in use are larger, hypothetically having a larger deadweight and additionally the area of contact between them and the adhesive surface increases as well. In case of a “material property: adhesion” these differences in testing must not lead to any differences in the results.

Figure C.24 illustrates the impact of the area of contact between particles and an adhesive surface. Even though the particle characteristics are identical, the particle on the top image has a smaller area of contact ($A_{c,1}$) and the pull off force to retrieve the particle from the surface is consequently lower. In fact the pull off force can be expressed as a function of the contact area between the particle and the adhesive material.

It therefore makes sense to scale the force which must exceed the adhesive force to retrieve a particle from the surface with the contact area to obtain the surface adhesion A_s :

$$A_s = \frac{F_{ad}}{A_c} \quad (C.5)$$

which is in line with the definition used by Ohashi and Harada (1994). Here, F_{ad} in [$\mu\text{N}/\text{particle}$] is the mean pull off force due to adhesion (F_{ad}) of a single ferromagnetic particle (will be further defined below). The area of contact is the lateral surface area of a sphere, where h is the depth of penetration of the sphere into the adhesive surface:

$$A_c = 2\pi r \cdot h \quad (C.6)$$

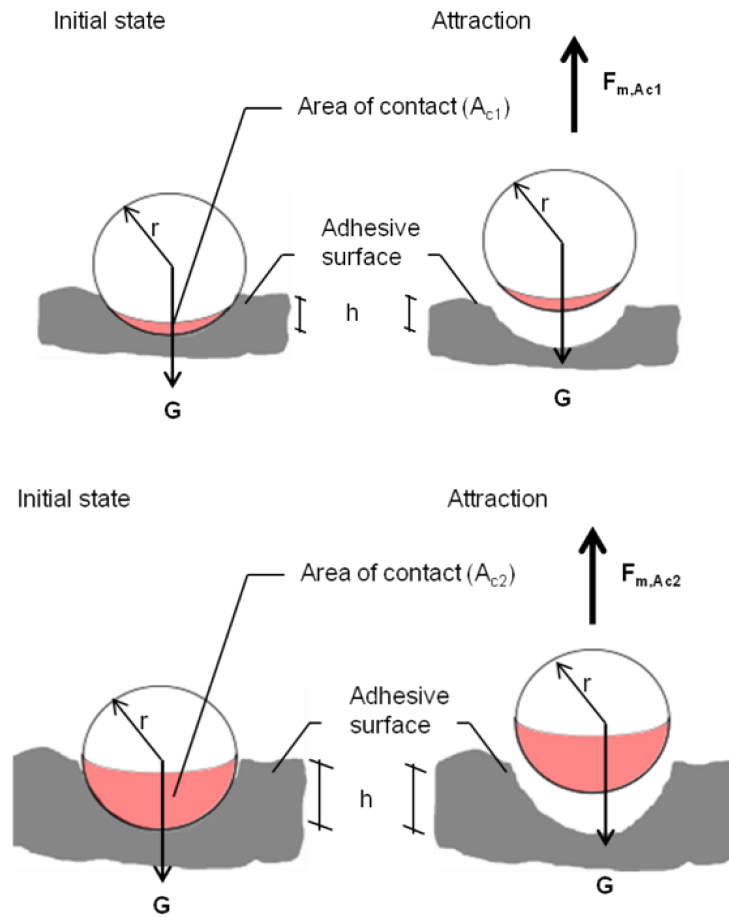


Figure C.24 A refined model of the impact of surface adhesion on the pull off force. *Top*: A ferromagnetic particle which is only partly in contact with the adhesive surface needs a lower pull off force to be retrieved by the electromagnet as opposed to *Bottom*: Where the particle penetrates deeper into the surface. The pink area is the area of contact (A_c).

Adhesion, as defined above, is consequently depending on the depth of penetration and the sphere's radius:

$$A_s = \frac{F_{ad}}{2\pi r \cdot h} \quad (\text{C.7})$$

It is important to mention that the weight of the ferromagnetic particles must be taken into account for calculating the F_{ad} . In measurements on non-adhesive (glass) surfaces it is demonstrated that a non-negligible force is needed to retrieve particles only due to their deadweight. When retrieving the FP from an adhesive surface the exerted force must overcome the adhesion forces as well as the deadweight.

Consequently, the mean pull off force due to adhesion is the difference between the force needed for an adhesive surface (F_m) and a non adhesive reference surface ($F_{m,0}$). F_{ad} can

be written as:

$$F_{ad} = F_m - F_{m,0} \quad (\text{C.8})$$

The full adhesion equation then reads as:

$$A_s = \frac{F_m - F_{m,0}}{2\pi r h} \quad (\text{C.9})$$

or

$$A_s = \varsigma \cdot (F_m - F_{m,0}) \quad (\text{C.10})$$

where $\varsigma = 1/2\pi r h$ is the reciprocal lateral area of a sphere for a known ratio of r to h . Here ς is defined for an ideally spherical object. In reality, the particles are not spherical (see e.g. Figure C.12), furthermore (Zafar et al., 2014) showed that the micro roughness of such particles has an influence on adhesion. On the other hand, the determination of the exact value of ς is currently not possible but reasonable assumptions can be made (see next section). For future research it is strongly recommended to further elucidate the impact of the particle geometries and probably also the surface chemistry.

Determination of the area of contact between a spherical particle and an adhesive surface

The area of contact (A_c) can be calculated from the depth of penetration of a spherical particle into an adhesive surface (see Equation C.6). ς describes the reciprocal value of the area of contact and is partly responsible for the surface adhesion force (see Equation C.10). This value is highly sensitive and therefore deserves special attention. For example, Figure C.25 illustrates the ratio between depth of penetration and particle diameter (h/d [%]) and ς . The graph demonstrates a source of great uncertainty in the lower region of h/d ($< 20\%$) as ς changes significantly with small changes in depth of penetration (e.g. $h/d = 10 \rightarrow \varsigma = 41 \text{ mm}^{-2}$ and $h/d = 8 \rightarrow \varsigma = 51 \text{ mm}^{-2}$). While ς is more insensitive at higher values of h/d (e.g. $h/d = 30 \rightarrow \varsigma = 14 \text{ mm}^{-2}$ and $h/d = 40 \rightarrow \varsigma = 10 \text{ mm}^{-2}$).

Determination of the depth of penetration

There are essentially two ways tested to determine the area of contact. None of these methods will give a precise value but an approximation that will be used in this study. It is strongly encouraged to go into deeper detail on this specific aspect as it may have a major impact on the results of this method. A simple way and probably the most efficient to reduce uncertainties related to the heterogeneity of particle geometries is to purchase particles which are generally well defined in their properties (primarily geometry but equally important are the

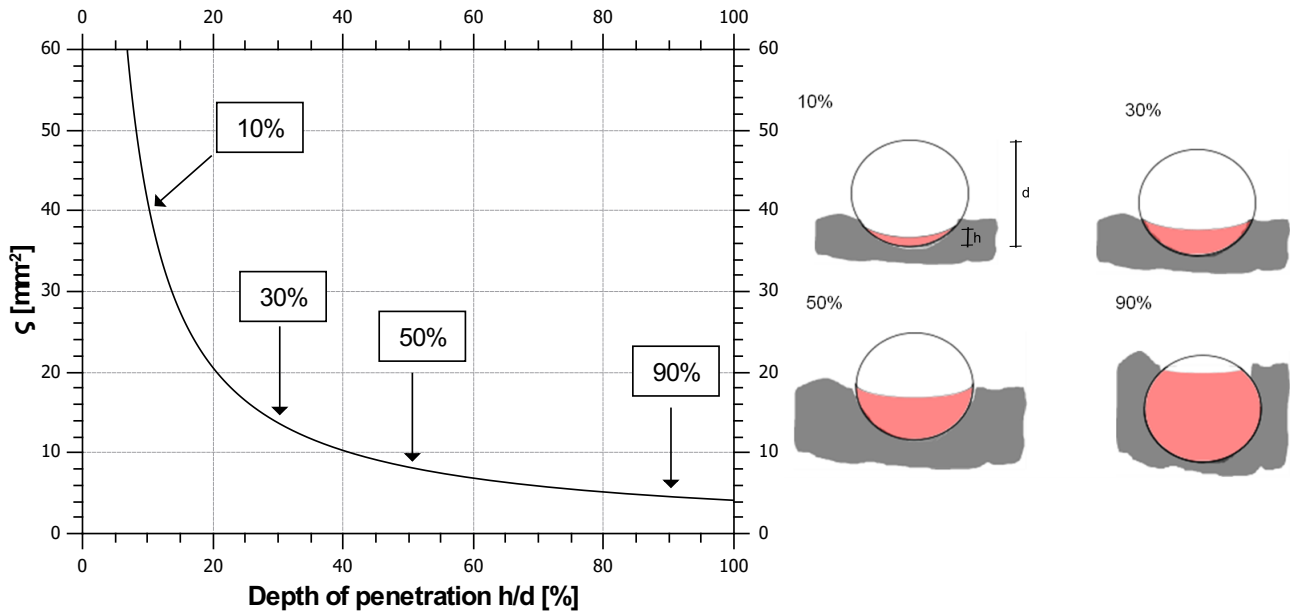


Figure C.25 Graph showing the values of the reciprocal area of contact (ς) for different depths of penetration. Especially at lower values of h/d the values of ς increase drastically, underlining the high sensitivity of surface adhesion calculations from the area of contact.

magnetic properties as discussed in Section C.3.2).

Analysis of side view images

An analysis of side view pictures (see Figure C.26), with particles that have been spread out on a silicone surface, yields that the particles have sunk into the silicone by approximately 30% (on average) of their diameter (i.e. with a r/h ratio of 1.65 ($= h/d = 30\%$), $n > 70$, $SD = 0.6$) which seems to be a reasonable proxy. The pictures have been analyzed using the software GIMP as follows: The horizontal extent of the particles (d [px]) and the visible vertical extent (a [px]) have been measured using GIMP's measuring tool. Assuming spherical particles the depth of penetration h and the dimensionless ratio between r and h is determined by solving $r/h = d/(2 \cdot (d-a))$.

Using the PARTRAC[®] particles, applying the ratio $r/h = 1.65$ (i.e. $h/d = 30\%$) (with $r_{mean} = 0.139$ mm) the depth of penetration is $h_{mean} = 0.084$ mm and the area of contact is $A_c = 0.073$ mm², accordingly. This yields $\varsigma = 13.63$

Analysis of surface adhesion forces

The theory behind the analysis of the surface adhesion forces is that these forces are immanent to the material. By testing one specific material, Equation C.10 must consequently always yield one specific surface adhesion value, irrespective of the depth of penetration of the particles. In other words, a decreasing ς (a greater depth of penetration) must be balanced by an increasing pull off force due to adhesion: $F_{ad} = F_m - F_{m,0}$ (a greater force is

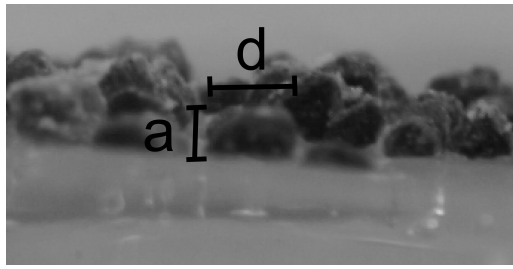


Figure C.26 Determination of the r/h value for particles spread on a silicone surface by image analysis.

needed to retrieve the particles). In the following this theory is used to estimate the depth of penetration of particles spread on a surrogate EPS from surface adhesion measurements.

Different samples have been prepared in petri dishes by mixing a Xanthan Gum (XG) solution as a surrogate EPS (1 wt.% powder dissolved in water) to fine sand (ratio: 6 g sediment and 1.5 g XG solution). Particles are spread on the surface and adhesion measurements are conducted after one minute (as in the original procedure), 70, 80, 140 and 1080 minutes (18 hours) on separate samples. During the incubation time the particles got more and more embedded into the XG.

This is most obvious for the sample where the particles were incubated for 18 hours (see Figure C.27 *Left*). In contrast to the picture of the sample directly after addition, no particles are visible after 18 hours of incubation. In other words, the particles surface is fully covered so that it can be assumed that $h/d = 1$. The 18 hour sample is taken as a reference and ς is now determined by solving equation C.10 for $h/d = 1$ and a manually measured $A_{s,100} = 4.26 \text{ N/m}^2$ ⁴.

As outlined above, a surface adhesion of 4.26 N/m^2 must also be valid for the other measurements such that Equation C.9 is solved for the depth of penetration ($F_{ad} = F_m - F_{m,0}$ is known from the measurements). The results are illustrated in Figure C.27 *Right*. As expected, the graph shows that the depth of penetration increases with time of incubation as a consequence of increasing F_{ad} . It is remarkable that the depth of penetration directly after adding the particles ($h/d = 33\%$) is surprisingly similar to the results from the analysis of side view pictures ($h/d = 30\%$).

The similarity of results from both methods presented here, creates confidence in assuming a $h/d = 30\%$ for the determination of surface adhesion in the following parts of this thesis. This assumption is indicated by the indices *s* for surface measurements and *30* for the depth of penetration in the notation of surface adhesion ($\rightarrow A_{s,30}$). Nevertheless, for applying different materials and particles in future projects it is strongly recommended to reassess

⁴As with ongoing incubation time the particles get more and more difficult to be captured by the camera the Image Processing could not be applied. Instead the manual observation from the original procedure (after Larson et al., 2009) was applied

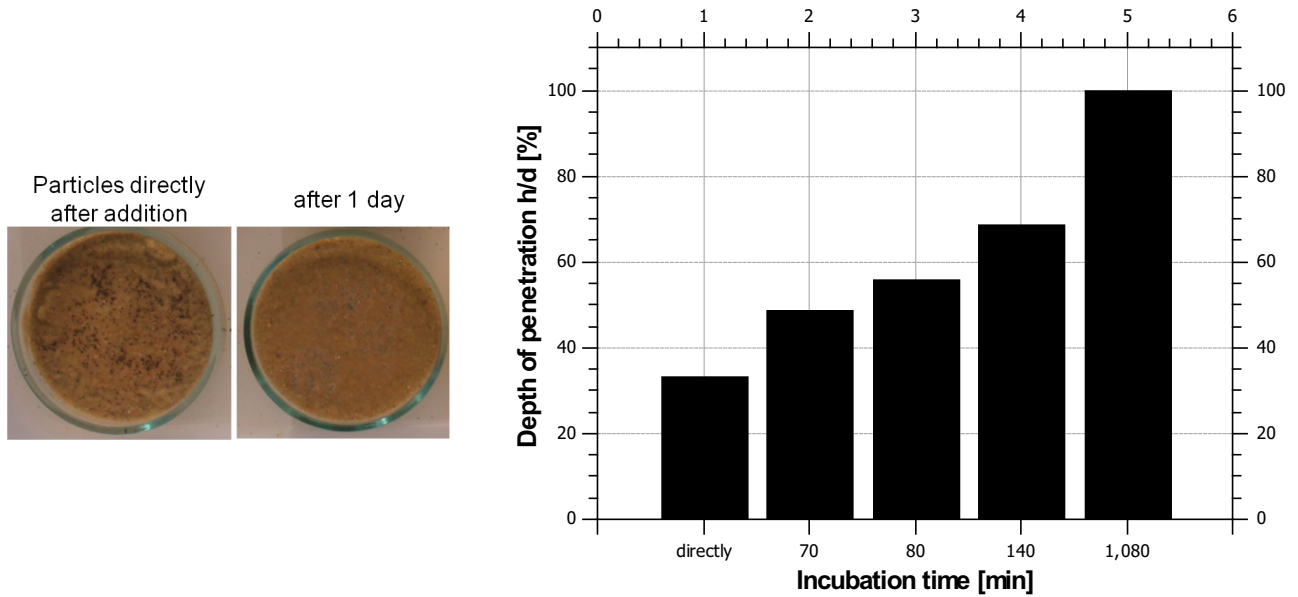


Figure C.27 Ferromagnetic particles left on an adhesive surface for different periods of time before measuring the pull off force to determine the h/d ratio. *Left*: top view image of particles directly after addition and after 1 day. *Right*: Bar graph plot of the calculated h/d values for different incubation times assuming that the surface adhesion is constant. The h/d increase indicates that the particles sunk into the adhesive surface over the time.

the area of contact individually.

C.6 Evaluating the performance of the MagPI-IP

Surface adhesion measurements using the MagPI-IP method are conducted on different surfaces to test the performance of the method (data acquisition by Ries, 2016). Therefore the following surfaces are tested: a) a blank surface (“BLANK”) and b) glass beads (“GB”) that are used in the experiments, to evaluate differences and determine the reference (non-adhesive) mean pull off force $F_{m,0}$. And c) an EPS surrogate (Xanthan gum “XG” at different concentration: $C = 3, 6, 9 \text{ g/l}$) and d) two biofilms of different ages (“BIO16” after 16 days of growth and “BIO48” after 48 days of growth).

Except for the biofilms, all surfaces of the test materials are flattened to exclude effects of height variations on the distance between the electromagnet and the surface. All tests are conducted under water by applying the procedure described above. PARTRAC[®] ferromagnetic particles ($d = 200 \dots 355 \mu\text{m}$) are used. The measurements are repeated on random spots on the test materials. For the data evaluation the mean pull off force of n measurements is averaged ($\overline{F_m}$ or $\overline{F_{m,0}}$, see Table C.1). Additionally the coefficient of variation (“CV”) for $\overline{F_m}$ or $\overline{F_{m,0}}$, the averaged net mean pull off force due to adhesion ($\overline{F_{ad}}$) and the averaged surface adhesion ($\overline{A_{s,30}}$) is analyzed.

Table C.1 Summary of results of surface adhesion measurements on different surfaces and random positions.

Name	n	$\overline{F_m}$ or $\overline{F_{m,0}}$	CV ($\overline{F_m}$ or $\overline{F_{m,0}}$)	$\overline{F_{ad}}$	$\overline{A_{s,30}}$
	–	$\mu\text{N}/\text{particle}$	%	$\mu\text{N}/\text{particle}$	N/m^2
BLANK	15	0.14	4.4	-	-
GB	12	0.15	8.9	-	-
XG3	15	0.22	9.7	0.08	1.02
XG6	10	0.26	9.5	0.12	1.53
XG9	5	0.41	7.6	0.27	3.67
BIO16	20	0.23	14.0	0.09	1.21
BIO48	10	0.39	14.4	0.25	3.28

C.6.1 Determination of the reference force on non adhesive surfaces

In the measurements where ferromagnetic particles are detached from a blank surface and a glass beads surface the influence of the particles weight is examined. Both measurements on non-adhesive surfaces reveal a relatively high averaged pull off force (BLANK: $\overline{F_{m,0}} = 0.14 \mu\text{N}/\text{particle}$ and GB: $\overline{F_{m,0}} = 0.15 \mu\text{N}/\text{particle}$) compared to the adhesive surfaces (e.g. XG3: $\overline{F_m} = 0.22 \mu\text{N}/\text{particle}$), indicating that a reference force needs to be taken into account to evaluate the surface adhesion forces (as has been done in Equation C.8). Table C.1 further demonstrates that the coefficient of variation (CV) is 4.4 and 8.9% respectively, which can probably be explained by the uncertainties in the calibration procedure (see Section C.3.2) where the CV is in a similar range.

While the $\overline{F_{m,0}}$ of both materials are well comparable, a detailed look at the individual measurements illustrates considerable differences (see Figures C.28 and C.29). From these plots, the skewness and the kurtosis is determined which can be used to quantify deviations from a normal distribution. The results of individual measurements on the blank surface are almost normally distributed (averaged skewness of all individual measurements is $\overline{Sk} = 1.0$ and kurtosis is $\overline{Ku} = 3.6$), which should be expected for non-adhesive measurements.

On the other hand the results on the GB surface have an average skewness of $\overline{Sk} = 4.1$ and an averaged kurtosis of $\overline{Ku} = 38.4$, which indicate that a) at fewer increments of F_{em} much more particles are retrieved and b) there are more extreme outliers, where only a few FP are retrieved at higher increments. Figure C.29 is a generic plot of an individual measurement which confirms the statistical data. Especially important and representative for the measurements on glass beads surfaces is that FP might get physically trapped between the beads and are only attracted by applying much higher tensile forces (see the arrow pointing at an extreme outlier in Figure C.29).

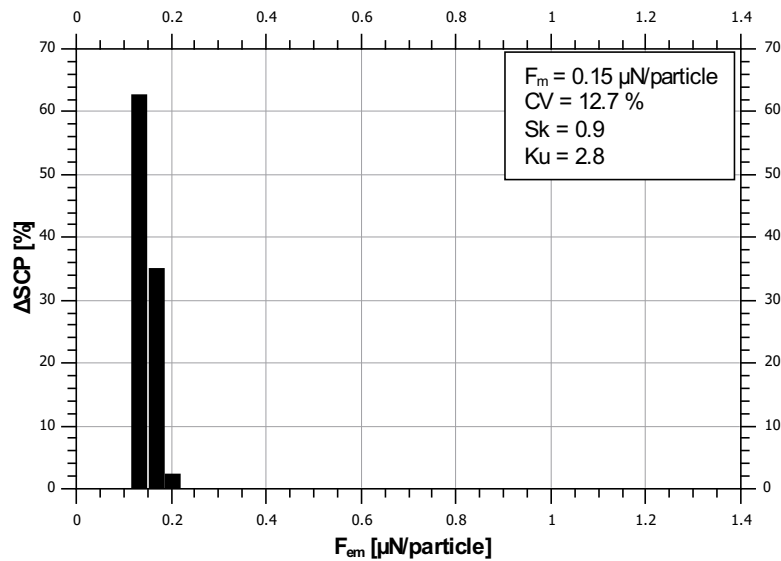


Figure C.28 Example of an individual measurement on a flat glass slide without adhesion (denoted as “BLANK”). The bar graph shows the percental decrease of SCP plotted against the applied tensile force F_{em} . All the particles are retrieved at a few increments of F_{em} concentrated in the lower range. The box in the upper right corner presents some statistical values of this individual measurement, which might also be useful for a deeper analysis of adhesion forces.

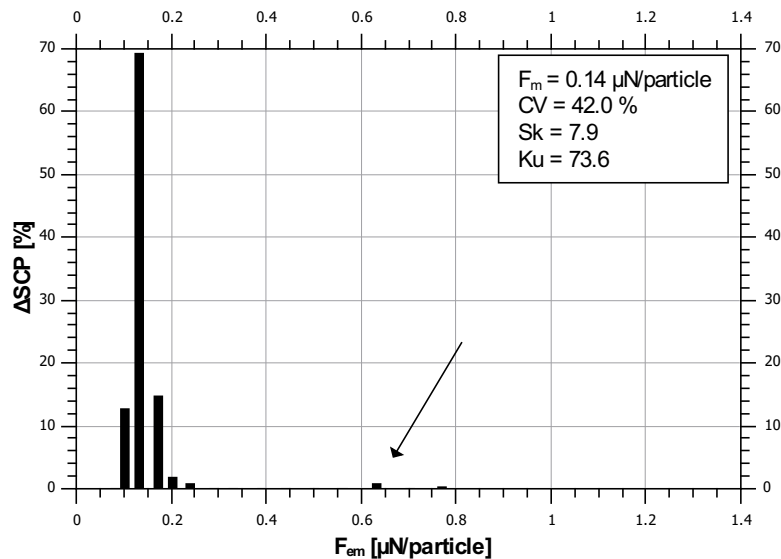


Figure C.29 Example of an individual measurement on glass beads without adhesion (denoted as “GB”). The bar graph shows the percental decrease of SCP plotted against the applied tensile force F_{em} . Most of the particles are retrieved at a few increments of F_{em} concentrated in the lower range. Still, some particles are retrieved at higher F_{em} (see arrow), indicative for a physical trapping. The box in the upper right corner presents some statistical values of this individual measurement, which might also be useful for a deeper analysis of adhesion forces.

This brief analysis already indicates the great potential of the novel method to evaluate data on a quasi particle scale. The reference force should be equal to $F_{m,0} = 0.14 \mu\text{N}$ determined for the glass surface (BLANK) as these data are less prone to outliers. Unfortunately, the detailed analysis here was conducted at a very late stage of the project as the priority was to measure surface adhesion in the experiments and develop this novel method simultaneously. Therefore in the experiments a reference value of $F_{m,0} = 0.16 \mu\text{N}$ is applied, which was evaluated in a smaller study before this detailed study was conducted.

C.6.2 Adhesion forces measured on a surrogate EPS surface

Xanthan Gum (XG, Sigma Aldrich, G1253-100G) is used as a model material because it can be assumed that it behaves more heterogeneous than natural biofilms. XG is commercially available as a food additive and rheology modifier to modify the viscosity of food products. It is secreted by the bacterium *Xanthomonas campestris* and was previously tested by Tolhurst et al. (2002) and Black et al. (2001) as an EPS surrogate to investigate erosion characteristics at different concentrations. Preparation of the Xanthan Gum is relatively straightforward and therefore it is well suited as a model material to compare different measuring methods at different laboratories. Here, the Xanthan gum is mixed in tap water at three concentrations ($C_{XG} = 3, 6$ and 9 g/l), then heated (to approximately 90°C), stirred again and mixed with glass beads. The surface is flattened prior to the measurements. Please see also Appendix B.1. It is expected that the surface adhesion measurements at the individual concentrations are highly reproducible, as the mixing was done with great care. Furthermore, it is expected that with increasing concentrations, surface adhesion ($A_{s,30}$) increases likewise.

In fact, $A_{s,30}$ increases with concentration of XG in a non linear way (see Figure C.30).

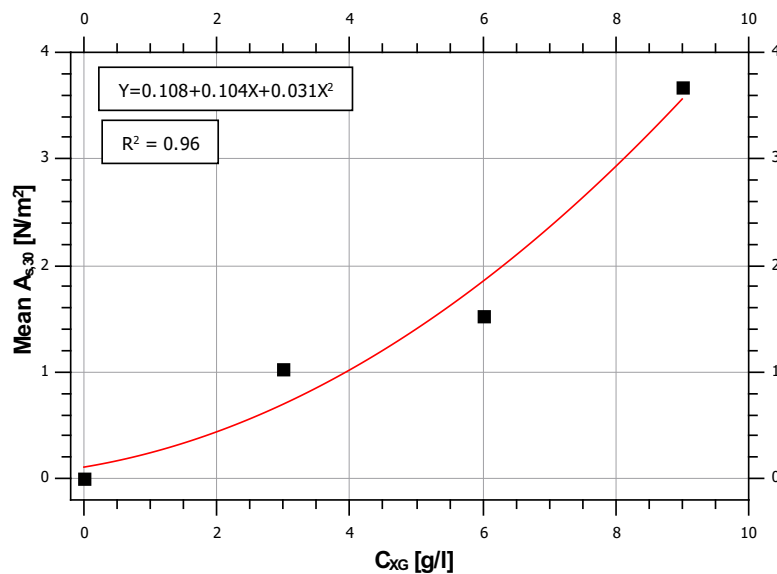


Figure C.30 Surface adhesion of an EPS surrogate (Xanthan gum) at different concentrations. Solid red line: best fit (polynomial regression).

A doubling of the concentration from $C_{XG} = 3 \text{ g/l}$ to $C_{XG} = 6 \text{ g/l}$ results in a factor of 1.5 increase in $\overline{A_{s,30}}$ and a threefold increase (from $C_{XG} = 3 \text{ g/l}$ to $C_{XG} = 9 \text{ g/l}$) results in a more than three fold increase in $\overline{A_{s,30}}$. This trend is well in line with the results on stability of XG - sediment mixtures reported by Black et al. (2001) using the CSM (Cohesive Strength Meter) device which employs a vertical water jet to erode sediments. A similar, yet more linear, trend was also shown by Tolhurst et al. (2002) using the same device but probably with a different setup as the stability differs significantly from the data of Black et al. (2001).

It can be further derived from the data that by applying the MagPI-IP method a clear difference between non-adhesive and adhesive surfaces can be measured. Furthermore, the measurements on a surrogate material (here: XG) is highly reproducible ($CV (\overline{F_m}/\overline{F_{m,0}})$ below 10 %, see Table C.1).

C.6.3 Adhesion forces measured on a biofilm surface

Briefly, the biofilms are cultivated on glass beads that are filled and compacted into cartridges. These cartridges are placed in a small flume where natural river water (River Enz, sampled in March 2015) is circulated (water exchange rate approximately 1/hour). Water temperature is not controlled in these experiments, i.e. it is assumed to be similar to the ambient temperature (approximately 20 °C) and light is applied in a 8/16 h day/night cycle with a light intensity of $50 \mu\text{mol}/\text{m}^2\text{s}$. Measurements are taken on one sample after 16 (BIO16) and 48 (BIO48) days of cultivation. In one month of cultivation the surface adhesion increased impressively by a factor of 2.7 (BIO16: $A_{s,30} = 1.21 \text{ N}/\text{m}^2$; BIO48: $A_{s,30} = 3.28 \text{ N}/\text{m}^2$). This sharp increase is well in line with observations from the experiments which will be discussed in Part D. The surface adhesion force of the young biofilm is comparable to that of the XG with the lowest Concentration (BIO16: $A_{s,30} = 1.21 \text{ N}/\text{m}^2$; XG3 $A_{s,30} = 1.02 \text{ N}/\text{m}^2$) and the same is true for the matured biofilm and the XG with the highest concentration (BIO48: $A_{s,30} = 3.28 \text{ N}/\text{m}^2$; XG9 $A_{s,30} = 3.67 \text{ N}/\text{m}^2$). However, the CV of the biofilm samples is slightly higher than of the XG samples. This possibly indicates, that the biofilm is slightly more heterogeneous than the surrogate material, which was presumed beforehand. Still, as the differences are relatively small (Biofilm: $CV (\overline{F_m}/\overline{F_{m,0}}) \approx 14 \%$; surrogate: $< 10 \%$) more measurements need to be taken to prove this hypothesis.

C.6.4 Comparison to other methods reported in literature

Table C.2 summarizes some of the results of direct and indirect measurements of adhesion from literature. It is the same table as already presented in Section A.5.3, but with the additional information of this study.

Regarding the direct measurements, the data reported by Ohashi and Harada (1996) have the closest agreement to the data of this study. The differences between the directly determined adhesion forces may have a couple of reasons (see discussion in Section A.5.3). It is highly recommended to conduct bench mark tests (as discussed above) on surrogate

Table C.2 Updated overview on different methods to measure biofilm-adhesion forces and results from literature (updated from Böl et al., 2013).

Parameter	Range	Magnitude	Unit	Reference
MagPI-IP				
Surface adhesion	0.0 ... 3.67	10^0	N/m ²	<i>This study</i>
Centrifugation device				
Adhesion strength	0.0 ... 4.9	10^1	N/m ²	Ohashi and Harada (1994)
Tensile strength	0.0 ... (> 8.0)	10^0	N/m ²	Ohashi and Harada (1996)
Micromanipulation				
Adhesive strength	0.6 ... 2.0	10^{-1}	Nm/m ²	Chen et al. (1998)
Adhesive strength	0.0 ... 1.0	10^0	Nm/m ²	Chen et al. (2005)
Microjet impingement				
Adhesive strength	0.2 ... 6.4	10^2	N/m ²	Kreth et al. (2004)
Atomic force microscopy				
Adhesion pressure	1.9 ... 33	10^1	N/m ²	Lau et al. (2009)
MagPI				
Surface adhesion	0.2 ... 1.5	10^1	mTesla	Larson et al. (2009)
Model application				
Adhesion coefficient	0.0 ... 2.5	10^0	N/m ²	Righetti and Lucarelli (2007)
Adhesion coefficient	2.0 ... 11.0	10^0	N/m ²	Righetti and Lucarelli (2010)
Adhesive strength	0.4 ... 4.5	10^0	N/m ²	Dade et al. (1990)
Adhesion coefficient	1.5 ... 3.0	10^0	N/m ²	Fang et al. (2014)

materials in order to compare between different methods.

The table further demonstrates that the overall best agreement to the MagPI-IP data is with the values calculated from the theoretical models of Righetti and Lucarelli (2007, 2010); Dade et al. (1990) and Fang et al. (2014). As the model described by Righetti and Lucarelli (2007) will be combined with the surface adhesion measurements to investigate the feasibility of using physics-based models on predicting biostabilization, this close agreement is highly encouraging.

C.7 Limitations/uncertainties and needs for further development

Even though, the modifications applied to the original system improve the quality of data acquisition significantly and produce more confidence in the results, a number of uncertainties and limitations persist. The major limitations and uncertainties can be roughly divided into four categories and are presented below.

Limitations in the calibration procedure

The potentially highest source of uncertainties is related to the magnetic particle properties. The particles in use are highly heterogeneous in shape, size, and magnetic properties. It is generally recommended to concentrate further investigations on particle properties and test different particles, probably with a narrower particle size distribution.

Limitations due to the image processing

The quality of the image processing and subsequent evaluation of the results strongly depends on the quality of the captured images. Specifically, a poor contrast between the FP and the biofilm can hinder the evaluation of the pictures. Particles on biofilms that have a dark color can hardly be distinguished by the MATLAB[®] program. Changes in light during the measuring process are also problematic (Ries, 2016). These changes may result in an incorrect identification of FP or the background.

Generally it would be desirable that the area where the particles are spread on is photographed from above to have an unbiased view on the surface of the FP. However, due to practical reasons this is impossible as the electromagnet is already located above the particles. Therefore, the images are captured from the side with a camera angle of approximately 20°.

Limitations due to the measuring procedure

Filaments and highly heterogeneous biofilm topographies generally prevent measurements on certain spots of the biofilm as the particles get trapped. Consequently, the measurements are not completely unbiased. In the later experiments the filaments were cut using scissors to allow MagPI-IP measurements on more spots.

Limitations in the calculation of surface adhesion

In Section C.5 it is demonstrated that the area of contact (A_c) between FP and the adhesive surface influences both, the pull off force and the surface adhesion forces. Even though it has been demonstrated that a depth of penetration of 30% is a reasonable assumption, a deeper analysis of the A_c is recommended for future investigations, as the A_c might also change with different materials.

Part D

TEMPORAL DEVELOPMENT OF SURFACE ADHESION AND STABILITY

It is generally accepted that adhesion forces between EPS and sediments play a role in biostabilization processes. Surprisingly little data can be found on adhesion forces and studies investigating both, adhesion characteristics and critical bed shear stress are literally non-existing. In this part the method to determine surface adhesion forces as described in the previous Part C is applied in three experiments to monitor the development of $A_{s,30}$ over time. The specific objectives of this part are to a) evaluate the feasibility of the advanced method, b) characterize surface adhesion over time considering the different environmental conditions and seasonality effects and c) correlate the results to the stability measurements by regression analysis to draw first conclusions about the role of adhesion in biostabilization processes. It is important to give a short introduction on the possible interrelationship between surface adhesion and erosion threshold for the reader to understand the analyses conducted in this and the following part (Part E).

D.1 Preliminary considerations on the interrelationship between surface adhesion and erosion threshold

According to the information given in Part A sediment particles may be glued together by adhesion forces to form a coherent surface layer (see Figure D.1 *Left*). In the event of erosion individual aggregates are detached (see Figure D.1 *Right*) when considering a crust like erosion as described in Part B¹.

The forces that initially hold the aggregates in place are the submerged weight force and additionally the adhesion forces at the boundary of the aggregates. In Figure D.1 *Right*, this boundary is depicted with a red line. Apparently, the adhesion forces that need to be

¹The carpet-like erosion is much more complex (see Part A), and in this thesis there are some strong indications that surface adhesion measurements are unlikely to be useful in this context. Therefore, only the crust-like erosion is described here.

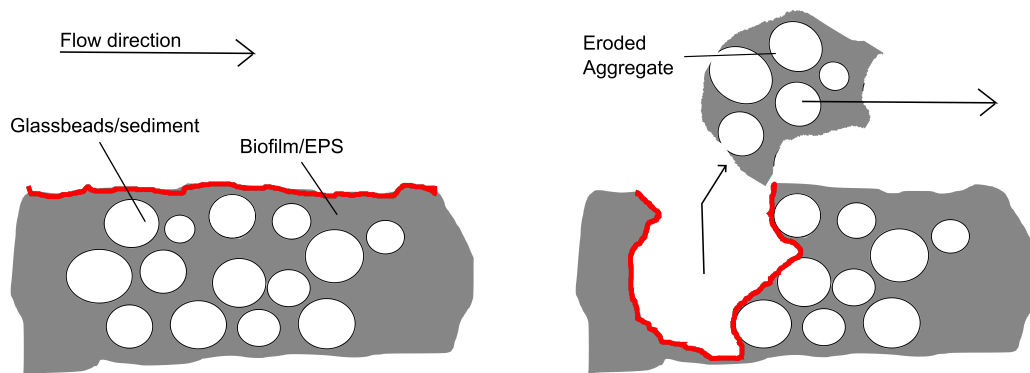


Figure D.1 A comparison between measured surface adhesion and adhesion responsible for resisting the attacking forces in the event of erosion. *Left*: Intact biofilm- sediment matrix. The red line indicates that the adhesion measurements conducted in this thesis only account for the surface of the coherent layer. *Right*: A biofilm-sediment aggregate is detached by the erosive forces of the fluid. The red line indicates the area at which the adhesion forces counteract the attacking forces prior to erosion.

exceeded by the erosive forces are distributed over the depth of the biofilm.

On the other hand, the MagPI-IP measurements are conducted on the surface and consequently the adhesion forces are termed “surface adhesion” (the red line in Figure D.1 *Left*). The crucial question one asks is how the measured surface adhesion can account for the adhesion over depth.

By conducting a regression analysis between erosion threshold and surface adhesion it is implicitly assumed that either the surface adhesion forces exactly resemble or are at least related to the adhesion forces over depth. The first is hypothetically possible as the thickness of the biofilm is relatively small (the eroded aggregates in this study have equivalent diameters of maximal 1.2 mm) and it could be possible that the material properties of the EPS do not change considerably over this small distance. However, the latter hypothesis seems to be more realistic considering the limited current state of research. To the authors’ knowledge only one study has been published in which the adhesion forces of biofilms over depth have been investigated, which is the study of Ohashi and Harada (1994). Their results suggest a similar functional relationship of adhesion over depth for biofilms at different ages (see Part A).

It must be fairly mentioned that understanding biostabilization would greatly benefit from measuring the adhesion forces over depth and conducting the here presented analyses. Moreover, the here developed MagPI-IP device could easily be used for this purpose, by cutting the biofilm horizontally in slices and measuring surface adhesion on each slice. However, one significant downside of this method would be the vast number of measurements that need to be conducted. Focusing on the development of growing biofilms under different environmental conditions, these fundamental investigations are out of the time frame of the project.

Another reason for investigating the relation between the surface adhesion and erosion threshold is that the here described method could be applied by engineers in the field for a better prediction of the erosion threshold, provided a reasonable correlation is found. This is hardly feasible for the more detailed investigations over the depth of the biofilm which would therefore limit the applicability of the proposed method. Still, it is strongly recommended for future investigations to conduct fundamental studies on this aspect.

As far as this Section is concerned, it is assumed that the surface adhesion forces resemble a proxy for the averaged adhesion over depth. In fact in Part E it will be demonstrated that the measured surface adhesion underestimates only slightly the effective adhesion calculated from application of a model.

D.2 The experimental setup

In the following the setup for biofilm cultivation, surface adhesion and stability measurements are described and an overview on the experimental programs of the here discussed three long term experiments (in March 2014 (Mar14), July 2014 (Jul14) and March 2015 (Mar15)) is given. The experimental program of the Mar15 experiment differs from the standard procedure applied in the two other experiments. Furthermore, in Mar15, an additional installation was set into the erosion flume to decrease the impact of roughness changes that occur in the transition between the initially smooth bed of the erosion flume and the rough surface of the biofilm (as discussed in Section B.1.3). The changes and impacts on the results are indicated in the text below.

D.2.1 The setup for biofilm cultivation

This section is a modified version of Thom et al. (2016)

The setup for biofilm cultivation is identical to the setup for the first set of experiments in Part B. The setup is described in detail in Section B.1.1 and in Schmidt et al. (2015). The key facts are repeated here briefly.

The biofilm is cultivated by circulating river water (containing a natural community of advected microbes) in six identical straight flumes over artificial sediments (glass beads, $d = 0.1 \dots 0.2 \text{ mm}$). The flumes geometries are identical ($l \times w \times h = 3.00 \times 0.15 \times 0.15 \text{ m}^3$) and biofilm growth is promoted in the rear 1.5 m of the flumes to ensure fully turbulent conditions (the first 1.5 m are the inlet flow section). While the temperature is held at a constant level ($15 \dots 15.3 \text{ }^\circ\text{C}$), the flow velocity and light intensity can be adjusted in each flume individually to simulate different environmental conditions (an overview on the boundary conditions applied in the experiments and the notations used in the following text is given in Table D.1).

Furthermore, the flumes are placed in containers to avoid unwanted contamination.

Table D.1 Boundary conditions applied in the experiments and the specific notations used in the following text

Notations used in the text	Light intensity (LI) [$\mu\text{mol}/\text{m}^2\text{s}$]	τ_b (Q) [N/m^2]	Temperature [$^{\circ}\text{C}$]
Low/None	0	0.02	15
Medium	50	0.04	15
High	100	0.08	15
Highest	-	0.10	15

During the cultivation period several measurements on different aspects (biological/chemical analysis, erosion, surface adhesion, aggregate/floc geometries, settling velocity and floc density) are conducted. For this reason, the sediment on which the biofilm grows, is filled (and compacted) into removable PVC cartridges ($l \times w \times h = 88 \times 58 \times 18 \text{ mm}^3$).

D.2.2 Erosion measurements in the SETEG flume

To determine the stability (i.e. the critical bed shear stress $\tau_{c,bio}$) of the biofilm-sediment matrix, the sample cartridges are placed in a straight erosion flume in such way, that the flume bed is on one level with the surface of the sample. The discharge (i.e. the bed shear stress τ_b) is then increased incrementally and bed failure is documented. For a more comprehensive description of the setup for erosion measurements please see Section B.1.3.

Modifications made to the SETEG flume in Mar15

As already discussed in Part B, a downside of the SETEG flume so far was that the roughness of the flume bed differs from the roughness of the biofilm surface and the transition between both elements is abrupt, which might cause two potential inaccuracies: 1) Fully turbulent conditions cannot be ensured over the sample and 2) the abrupt transition may result in unwanted edge effects like a local increase in bed shear stress and scour development. To solve this issue, extensive investigations on the biofilm roughness are conducted (see Part F), and sandpaper was fitted onto the flume bed with a similar roughness as investigated for a matured biofilm. This method is first applied in the Mar15 experiment (for further details please see Section F.3).

D.2.3 Surface adhesion measurements

Surface adhesion measurements are conducted using the newly modified MagPI-IP system as described in Part C. A quick summary on the concept is provided below.

Briefly, the MagPI-IP system consists of an electro-magnet, an automated power supply, a camera, a PC and image processing software. To determine the surface adhesion forces ferromagnetic particles ($d = 200 \dots 350 \text{ m}$, manufactured by PARTRAC[®], UK) are spread on a biofilm surface and attracted by the electromagnet (positioned 4 mm above them) at increasing magnetic forces. The particles are retracted directly after their addition, as this ensures reproducible measurements (Larson et al., 2009). This means that particles are not overgrown by the biofilm but are in contact with the sticky surface by a smaller part of their surface. To determine the surface adhesion $A_{s,30}$ in the here described experiments equation C.10 is solved by determination of the mean net pull off force (F_{ad}) from the tensile force on one particle (via calibration) and the reference force $F_{m,0} = 0.16 \mu\text{N}/\text{particle}$. It is assumed that on average the ferromagnetic particles depth of penetration into the adhesive surface is 30% of their mean diameter ($d_{mean} = 0.2775 \text{ mm}$) which yields a $\zeta = 13.64 \text{ }^1/\text{mm}^2$.

D.3 The experimental program of the conducted experiments

The experimental program of cultivation

Table D.2 gives an overview on the specific study objectives of each experiment as well as applied boundary conditions and abbreviated identifiers (ID). The notations used in this table relate to their definitions in Table D.1. An example illustrates the meaning of the IDs: In the March 2014 experiment biofilms in flumes 3 and 6 were cultivated in darkness (Light intensity = None). The IDs of the two flumes read as *Mar14LNA* and *Mar14LNB* - the abbreviation **Mar14** stands for experiment conducted in March 2014. The first letter after the year stands for the study objective **L**ight intensity, the second letter denotes the level of the light intensity **N**one (see Table D.1) and the third is the numbering of the Replicates, e.g. replicate **A** or replicate **B**. The same procedure is applied for the experiments where the bed shear stress is varied, abbreviated with **Q** (i.e. discharge) for reasons of readability. The experimental program of Mar15* experiments differs from this procedure as the boundary conditions changed during the course of the experiment in each flume (indicated by the *).

Table D.2 can be summarized as follows:

Mar14

In Mar14 the primary objective is to investigate the impact of different light intensities (Darkness, medium and high light intensity) on biostabilization (while the bed shear stress is at a constantly low level). The total duration of the experiment is 7 weeks.

Jul14

The study objective of Jul14 is on the impact of hydrodynamics. Three levels of bed shear stress are applied during cultivation: Low, medium and high. The light intensity is constantly

Table D.2 Detailed overview on experiments (Mar14, Jul14, Mar15*), their study objectives and applied boundary conditions. Abbreviations used: L - light intensity, Q - discharge (i.e. the applied τ_b during cultivation), N - none, L - low, M - medium, H - High, H+ - highest, A - replicate A, B - replicate B, C -replicate C. The * in Mar15: the flow velocity is changed during the experiments. The hydrodynamic conditions during the main sampling phase are used as an abbreviation.

Name	Study objectives	Flumenr.	ID	Light intensity	discharge Q
March 2014	Light intensity	1	Mar14LMA	Medium	Low
		2	Mar14LHA	High	Low
		3	Mar14LNA	None	Low
		4	Mar14LMB	Medium	Low
		5	Mar14LHB	High	Low
		6	Mar14LNB	None	Low
July 2014	Hydrodynamics	1	Jul14QHA	Medium	High
		2	Jul14QHB	Medium	High
		3	Jul14QHC	Medium	High
		4	Jul14QLA	Medium	Low
		5	Jul14QLB	Medium	Low
		6	Jul14QLC	Medium	Low
March 2015	Hydrodynamics	1	Mar15QH+A*	Medium	Highest
		2	Mar15QHA*	Medium	High
		3	Mar15QLA*	Medium	Low
		4	Mar15QH+B*	Medium	Highest
		5	Mar15QLB*	Medium	Low
		6	Mar15QHB*	Medium	High

set to medium. The total duration of the experiment is 9 weeks.

Mar15

The Mar15 experiment is different in that the flow velocities are adjusted during the course of the experiments. The objective of the Mar15 experiment is to investigate the response of biofilms cultivated under defined boundary conditions to abrupt changes in flow velocities (e.g. to simulate a storm event or low flow after a period of temperate growth). Therefore, the biofilms are cultivated under the same conditions (light intensity is medium, $\tau_b = \text{low}$) in the first two weeks (with no measurements). Consequently, all biofilms have the same starting conditions. Hereafter three flumes are exposed to high flow velocities whereas the remaining three flumes are unchanged. These conditions can be regarded as the initial conditions. After one week, the flow velocity was adjusted again to different flow velocities (low, high and

highest). A detailed experimental program of Mar15 is illustrated in the Appendix C.1.

The experimental program of SETEG measurements

The experimental programs are briefly summarized:

Mar14

At the end of week 1 one sample from each flume was eroded, hereafter 2 samples from each flume are eroded each week (a total of 41 samples, as one sample was destroyed unintentionally).

Jul14

One sample is eroded every 3 to 5 days (starting from week 3). Due to several unexpected events (erosion at the beginning of the experiments due to setting the flow velocity too high in one flume and a power cut affecting 3 flumes for several hours) the total number of samples eroded is 43.

Mar15

Erosion measurements started in week 7 with one sample per flume on a weekly basis. The last measurements were conducted on day 75 (after starting the experiment) with a temporal gap of 2 weeks. A total of 24 measurements were conducted.

The experimental program of MagPI-IP measurements

The cartridges are transferred from the flumes to a water filled box. Then the MagPI-IP device is positioned and measurements are conducted. Over the time, the adhesion is measured on different biofilm samples (not continuously on one and the same sample). The reason for this procedure is that the erosion as well as the biological analysis is destructive to the samples and the number of samples for each flume is limited. Therefore, the measurements on the different samples provide only a quasi-continuous monitoring over time as different biofilms were tested.

Mar14

Each week (until week 5) surface adhesion is measured twice (with a temporal gap of 3 to 4 days). In each flume 3 cartridges are sampled and for each cartridge 3 replicate measurements are conducted on random spots. In the first 5 weeks a total of 540 measurements are conducted. After week 5 (until the end of the experiment) measurements are conducted more irregularly.

Jul14

The experimental program from Mar14 was optimized to have longer periods of surface adhesion measurements on one specific sample. The longest measurement on one sample

is two weeks (or 4 sampling days). On average, 4 cartridges per flume are sampled with 3 replicate measurements each on random spots. More than 250 cartridges are sampled, which results in ≈ 750 measurements.

Mar15

The sampling strategy differs significantly, because of the specific study objective. The first measurements are conducted in week 6 with 3 cartridges on the first sampling day and 3 on the second sampling day of week 6. Thereafter, each week alternately 3 cartridges and 1 cartridge are used for adhesion measurements but also for destructive measurements. On each cartridge 5 replicate measurements are conducted. This yields > 650 measurements. The electromagnet in use for this experiment (see Section A.1.2) is also different from the electromagnet applied in experiments Mar14 and Jul14 (see Section A.1.3), as the latter was destroyed after Jul14 by accidentally overheating. The calibration applied here gives comparable results for both electromagnets and as a consequence, the results are also well comparable.

Evaluation of the data

The surface adhesion data is processed in two different ways: 1) In Section D.4.1, where the characterization of the surface adhesion is in the focus, all results are evaluated. The surface adhesion is averaged for each sampling day and flume. And 2) Section D.4.3 discusses the correlation between critical bed shear stress and surface adhesion. Here, only the adhesion data from the samples that are eroded at the same day are averaged.

Generally, some measurements had a bad quality of images due to unfavorable light conditions. Those measurements were discarded prior to the evaluation. This results in unequal numbers of replicates/samples and therefore the standard error (SE) which considers the number of samples was chosen to represent the deviations.

D.4 Evaluation of the experiments

In this section the surface adhesion and erosion threshold measurements are evaluated.

D.4.1 Characterization of the temporal development of surface adhesion

Figures D.2, D.3 and D.4 are generic plots of the temporal development of mean surface adhesion forces ($\bar{A}_{s,30}$, standard error \ddagger) evaluated in the experiments Jul14, Mar14 and Mar15 respectively. The complete results can be found in the Appendix C.3.

Analyzing all results, it is striking that a) the developments of $\bar{A}_{s,30}$ are similar in the respective experiments and b) the surface adhesion forces have a characteristic development over time. The latter is most obvious in the Jul14 experiment (see Figure D.2). In the first weeks,

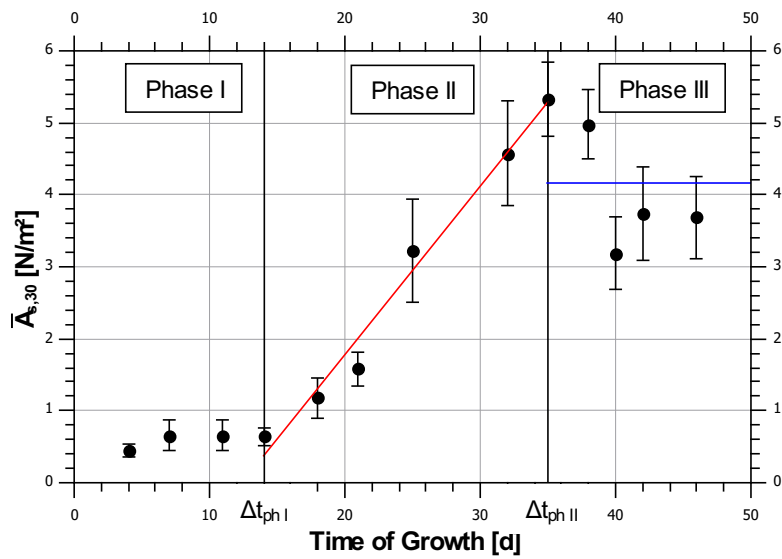


Figure D.2 Generic plot of the development of mean surface adhesion forces (The \bullet symbol: $\bar{A}_{s,30}$, standard error \ddagger) in the Jul14 experiment. Data from Jul14QLC. In this experiment, the development can be divided into three distinct phases. The red line is the linear regression in Phase II. The blue line is the averaged $\bar{A}_{s,30}$ in Phase III. The vertical black lines illustrate the beginning or end of the different phases.

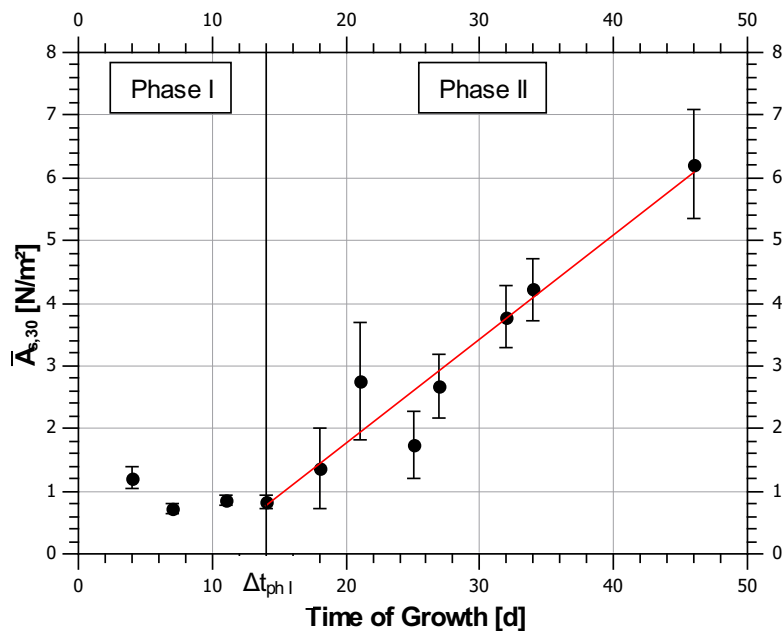


Figure D.3 Generic plot of the development of mean surface adhesion forces (The \bullet symbol: $\bar{A}_{s,30}$, standard error \ddagger) in the Mar14 experiment. Data from Mar14LHA. In this experiment, the development can be divided into two distinct phases. The red line is the linear regression in Phase II. Phase III is absent in this experiment. The vertical black lines illustrate the beginning or end of the different phases.

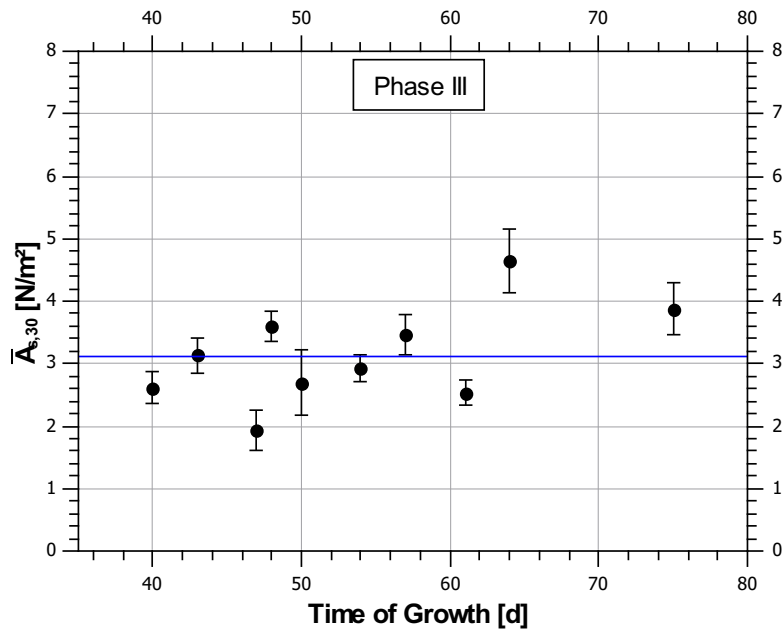


Figure D.4 Generic plot of the development of mean surface adhesion forces (The ● symbol: $\bar{A}_{s,30}$, standard error ‡) in the Mar15* experiment. Data from Mar15QHA. Measurements are first conducted on day 40 of biofilm growth. Therefore the data presented only corresponds to Phase III. The vertical black lines illustrate the beginning or end of the different phases.

the $\bar{A}_{s,30}$ is nearly constant and hardly exceeds 1.0 N/m^2 (e.g. from the beginning of the experiments to day 14 in Figure D.2). This is then followed by an increase of $\bar{A}_{s,30}$ (e.g. from day 14 to day 35 in Figure D.2) until it fluctuates around a mean value (e.g. after day 35 until the end of the experiment in Figure D.2). In Mar15 the surface adhesion measurements only started after 40 days which could imply that the biofilm was already “matured” and the data can only be represented as fluctuations around a certain mean value (see Figure D.4). In the Mar14 experiment (see Figure D.3) only the initial phase of constantly low adhesion and the following increase is visible, which could imply that the “matured” stage was not reached during the duration of the experiment.

Consequently the data on $\bar{A}_{s,30}$ can be subdivided into three distinct phases. In the following an interpretation of these phases is suggested relating to the commonly accepted theory on biofilm development (see also Figure A.3 and Vasudevan, 2014). Furthermore, a parameterization is suggested which is helpful in comparing the data of different experiments and applied environmental conditions. According to the definition and description given by Lüdecke et al. (2014) the phases can be described as follows:

Initial lag-phase: No or slow surface adhesion (Phase I)

Phase I describes the formation of a conditioning film on the abiotic sediment for further growth. Suspended microbes settle onto the sediment (as described in Chapter B) where they secrete a thin layer of EPS to attach to the sediment. Once the microbes resist the fluid shear more EPS is secreted to promote growth of the biofilm. After Lüdecke et al. (2014) the

adhesion kinetics in this phase are low and nearly constant (Lüdecke et al., 2014 studied the substratum coverage of *E.coli* on different materials, as a proxy for adhesion). In classical theory, this phase typically lasts some minutes or hours. The data, the classical theory was developed on, was derived from small scale batch experiments mostly on monospecies biofilms. The meaning of the term conditioning film in the context of this study is slightly different but still strikes the core of the definition. Here, a conditioning film is the necessary condition for further and much more advanced biofilm growth but without relevant impact on the erosion threshold (as will be demonstrated in below). In the experiments the biofilm is largely transparent, suggesting a bacterial biofilm. Phase I can be characterized by two parameters: The total duration of this phase Δt_{phI} (starting at day 0) and $\bar{A}_{s,30,I} \lesssim 1.0 \text{ N/m}^2$, where $\bar{A}_{s,30,I}$ is the surface adhesion in Phase I.

Fast adhesion phase (Phase II)

Phase II is the growth phase. In this phase the biofilm accumulates EPS. This phase is characterized by a quick increase of mean surface adhesion. For example, in Figure D.2, $\bar{A}_{s,30}$ increases from 0.6 to 5.3 N/m^2 in 3 weeks time ($\Delta t_{phII} = 21 \text{ d}$), which corresponds to a nearly 9 fold increase. In the present study, the value of $\bar{A}_{s,30}$ can be expressed as a function of time of growth applying a linear regression:

$$\bar{A}_{s,30}(t) = r \cdot t + b \quad (\text{D.1})$$

where r is the adhesion rate (or the daily increment) in $\text{N/m}^2\text{d}$, t is the time of growth in Phase II and b is the absolute term derived from the regression. The absolute term b may be used to determine the value $A_{s,30,I}$:

$$A_{s,30,I} = r \cdot \Delta t_{phI} + b \quad (\text{D.2})$$

Phase of saturation III

The phase of saturation is characterized by a fluctuating surface adhesion around a mean value. Phase III is here termed the “mechanically matured” phase. In the classic theory, the biofilm reaches a state of dynamic equilibrium between detachment/dispersal and growth. This phase can be parameterized by the starting day (or $\Delta t_{phI} + \Delta t_{phII}$), an averaged surface adhesion (averaged $\bar{A}_{s,30} = \bar{A}_{s,30,III}$) and the standard error (SE).

The full parameterization reads as:

$$\bar{A}_{s,30}(t) = \begin{cases} \bar{A}_{s,30,I} = \text{const.} & , t \leq \Delta t_{phI} \\ r \cdot t + b & , \Delta t_{phI} < t \leq (\Delta t_{phI} + \Delta t_{phII}) \\ \bar{A}_{s,30,III}(\pm SE) & , t > (\Delta t_{phI} + \Delta t_{phII}) \end{cases} \quad (\text{D.3})$$

Evaluation of the complete dataset

Table D.3 summarizes the parameters from equation D.3 for all available data on surface adhesion.

Table D.3 Summary of results on surface adhesion and erosion threshold development over time for the experiments Jul14, Mar14 and Mar15*. Note: $\bar{A}_{s,30,I}$ is calculated from equation D.2 where possible.

ID	Phase I		Phase II			Phase III				
	Δt_{phI} [d]	$\bar{A}_{s,30,I}$ [N/m ²]	Δt_{phII} [d]	r [%]	b [N/m ²]	R^2	$\bar{A}_{s,30,III}$ [N/m ²]	SE $A_{s,30}$	$\bar{\tau}_{c,bio}$ [N/m ²]	SE $\tau_{c,bio}$
Jul14QHA	18	0.56	21	17	-2.5	0.87	4.24	0.69	1.40	0.06
Jul14QHB	14	1.32	19	28	-2.6	0.86	6.75	0.15	1.02	0.10
Jul14QHC	11	0.24	17	24	-2.4	0.71	5.37	0.37	1.13	0.13
Jul14QLA	14	1.12	18	28	-2.8	0.98	4.73	0.43	0.91	0.08
Jul14QLB	14	0.26	11	44	-5.9	0.93	4.94	0.20	0.97	0.09
Jul14QLC	14	0.32	21	23	-2.9	0.98	4.18	0.41	1.01	0.08
Mar14LNA	end	-	-	-	-	-	-	-	-	-
Mar14LNB	end	-	-	-	-	-	-	-	-	-
Mar14LMA	14	1.44	end	17	-0.94	0.89	-	-	-	-
Mar14LMB	14	0.24	end	21	-2.7	0.81	-	-	-	-
Mar14LHA	14	0.78	end	17	-1.6	0.93	-	-	-	-
Mar14LHB	21	1.01	end	21	-3.4	0.92	-	-	-	-
Mar15QH+A*	-	-	-	-	-	-	2.21	0.14	1.00	0.05
Mar15QH+B*	-	-	-	-	-	-	3.37	0.26	1.36	0.01
Mar15QHA*	-	-	-	-	-	-	3.14	0.25	1.37	0.11
Mar15QHB*	-	-	-	-	-	-	3.40	0.29	1.51	0.17
Mar15QLA*	-	-	-	-	-	-	1.55	0.10	0.81	0.07
Mar15QLB*	-	-	-	-	-	-	4.32	0.43	1.58	0.22

In principle, the development of surface adhesion forces is surprisingly well in line with the evaluation of the temporal development of the critical bed shear stress in Part B. Phase I is available in all experiments where the measurements started at day 0. The duration of that phase is on average approximately 2 weeks which can also be confirmed by observations. As discussed in Part B the first visible (i.e. non transparent) biofilm developed just after

these 2 initial weeks.

The fast adhesion phase (Phase II) lasts on average 18 days. The daily increment of surface adhesion forces, further denoted as the adhesion rate (r), ranges between 17 and 44 %. In experiment Jul14 the average adhesion rate is higher for biofilms cultivated under low flow velocities ($\bar{r} = 32.7 \text{ N/m}^2\text{d}$) than under high flow velocities ($\bar{r} = 23 \text{ N/m}^2\text{d}$), possibly to be explained by enhanced growth under lower flow velocities. This is well in line with the findings from erosional studies in Chapter B where a higher flow velocity leads to a delayed development in growth and stabilization. Regarding the applied light intensities, it is striking that in principle biofilms cultivated under darkness conditions have surface adhesion forces $\lesssim 1.0 \text{ N/m}^2$. This means that no relevant adhesion could be measured and the biofilm rested in the lag-phase until the end of the experiment. Again, this mirrors the observations made in Part B, where no biostabilization effect was visible for biofilms under darkness conditions.

Comparing the adhesion rate from experiments under similar boundary conditions but at different seasons (i.e. spring: Mar14LMA, Mar14LMB and summer: Jul14QLA, Jul14QLB, Jul14QLC) the summer experiments had considerably higher adhesion rates (averaged $r = 31.7$) than the spring biofilms (averaged $r = 19$). This is in contrast to the development of biostabilization as discussed in Part B where $\tau_{c,bio}$ is higher in spring than in summer. Still, the data underline that seasonality plays an important role also for the development of surface adhesion as underlined by two more observations: 1. In the course of the experiment Mar14, the saturation phase III was not reached (i.e. the biofilms in spring can be classified as “still developing” even after ≈ 7 weeks) and 2. the averaged surface adhesion in phase III of Mar15 is considerably lower than in Jul14. These interpretations should be treated with great care as the number of experiments is still very limited. Furthermore, the variability of the results (especially Jul14) from replicate flumes is unexpectedly high and certainly more experiments are needed to confirm the interpretations.

D.4.2 The development of stability divided in phases

The concept of surface adhesion phases is applied on the measured erosion thresholds with the aim to better understand the biostabilization process. Following this idea Figures D.5, D.6 and D.7 show the temporal development of the erosion threshold from one flume as representative for each experiment. The complete results can be found in the Appendix (C.2).

In Phase I (lasting ≈ 2 weeks) the stability of the sediments is almost without exception equal to the stability of non-biostabilized sediments. This indicates that surface adhesion values below $A_{s,30} \approx 1.0 \text{ N/m}^2$ do not result in any biostabilization effect. Hereafter, the erosion threshold increases with time in almost all experiments in the fast adhesion phase (Phase II). In the saturation phase (Phase III) the stability is subjected to strong fluctuations (see e.g. Figure D.6). Applying the concept of phases to characterize the development of the erosion

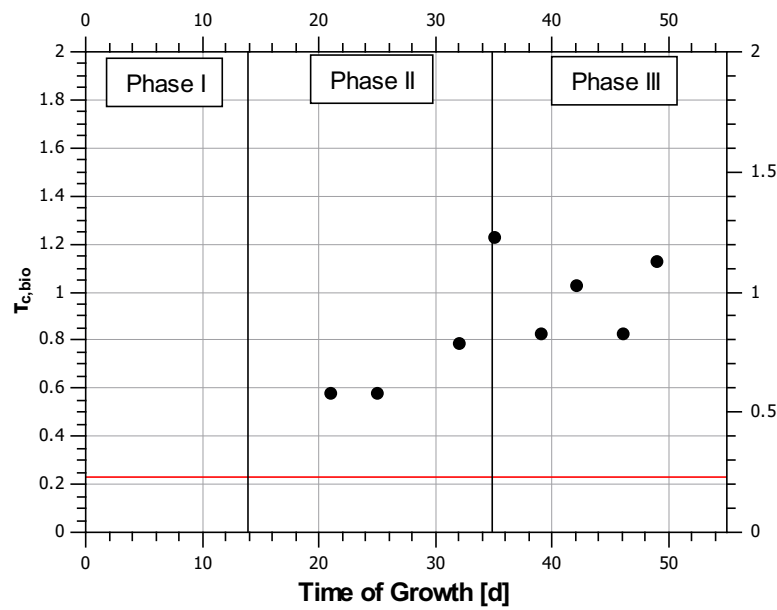


Figure D.5 Temporal development of $\tau_{c,bio}$ as typical for the Jul14 experiment. Data from Jul14QLC. Additionally the surface adhesion phases are illustrated, where the vertical black lines illustrate the beginning or end of the different phases. The solid red line is the abiotic sediment stability (i.e. the τ_c of the initial non-biostabilized sediments).

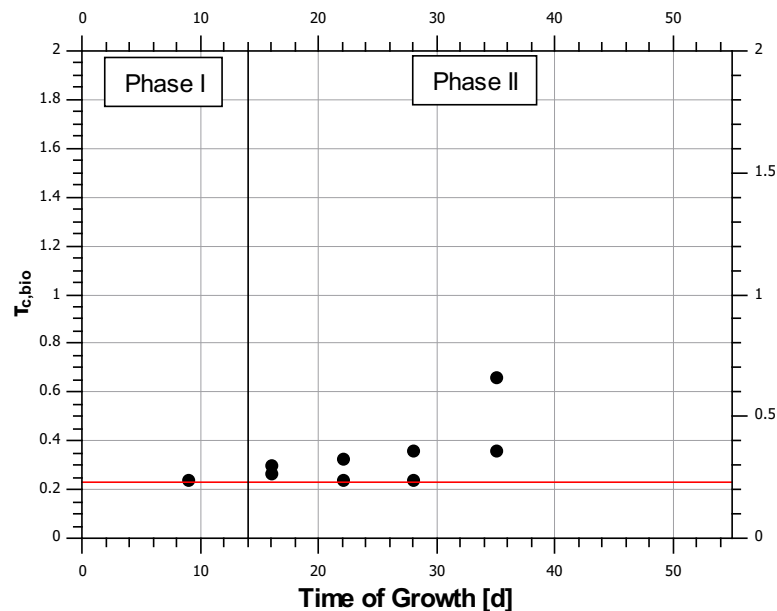


Figure D.6 Temporal development of $\tau_{c,bio}$ as typical for the Mar14 experiment. Data from Mar14LHA. Additionally the surface adhesion phases are illustrated, where the vertical black lines illustrate the beginning or end of the different phases. The solid red line is the abiotic sediment stability (i.e. the τ_c of the initial non-biostabilized sediments).

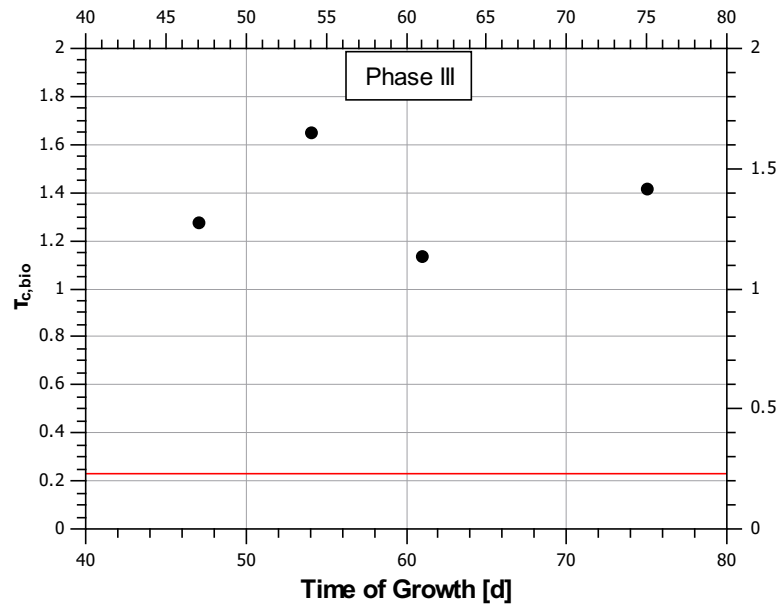


Figure D.7 Temporal development of $\tau_{c,bio}$ as typical for the Mar15* experiment. Data from Mar15QHA*. Additionally the surface adhesion phases are illustrated, where the vertical black lines illustrate the beginning or end of the different phases. The solid red line is the abiotic sediment stability (i.e. the τ_c of the initial non-biostabilized sediments).

threshold is especially beneficial when interpreting data in the mechanically matured stage of biofilms (Phase III). Data from Jul14 (see Table D.3) illustrates that the averaged $\tau_{c,bio}$ is higher for biofilms cultivated under higher flow velocities compared to biofilms cultivated under low flow velocities (under high flow velocities: BI = 5.1, under low flow velocities BI = 4.2) confirming the results of Pereira et al. (2002) and Graba et al. (2013).

D.4.3 The correlation between critical bed shear stress and surface adhesion

A correlation between the critical bed shear stress and surface adhesion may provide indications for an existing functional relationship. Supported by the information from the previous paragraphs, it is hypothesized that the erosion threshold increases with surface adhesion. By plotting all data from Mar14, Jul14 and Mar15 into one graph (see Appendix C.3.1), however, it is demonstrated that such a simple relationship cannot be found due to the large scattering of the data. Instead the data is plotted into three different graphs, each representing the correlation at the three distinct phases (see Figures D.8, D.9 and D.10). Please note, that the data of $A_{s,30}$ presented here, is the averaged surface adhesion measured on the same samples that are eroded to determine the erosion threshold, thus the data potentially deviates from the results in Section D.4.1.

Phase I

The results presented in Figure D.8 clearly demonstrate that samples with surface adhesion forces in phase I (i.e. $A_{s,30} \lesssim 1.0 \text{ N/m}^2$) have a negligible effect on biostabilization. The biostabilization index ranges from 0.75 to 1.5. As expected, biofilms at early stages (\approx first two weeks) do not contribute to enhanced biostabilization. The same applies to biofilms cultivated under darkness conditions. By application of the MagPI-IP, non-biostabilized sediments can be clearly differentiated from biostabilized sediments.

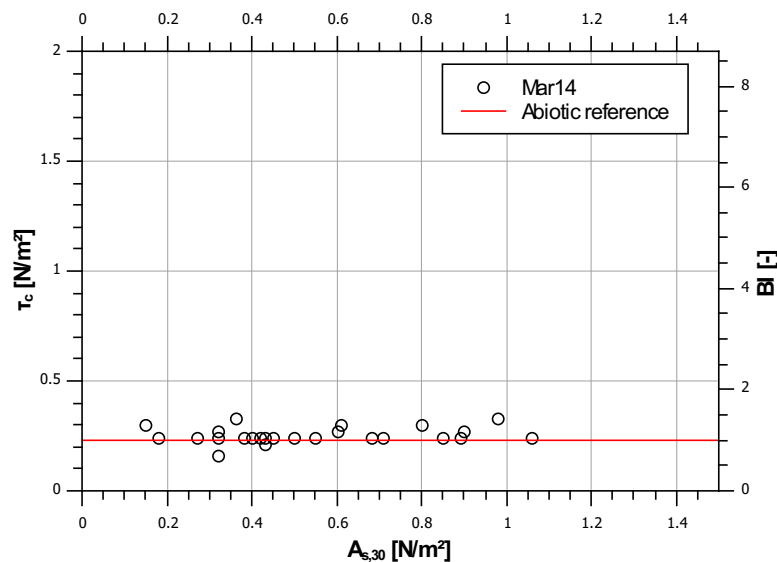


Figure D.8 The interrelationship between erosion threshold and surface adhesion in Phase I as measured in experiment Mar14.

Phase II

The data in phase II (Figure D.9) suggests a positive linear correlation of $A_{s,30}$ and $\tau_{c,bio}$. The erosion threshold increases with surface adhesion. The biostabilization effect of elevated surface adhesion values is much smaller than expected. In both experiments a six fold increase of $A_{s,30}$ results only in a factor 1.3 increase of $\tau_{c,bio}$ (the dashed and solid black lines in Figure D.9).

Furthermore, the graph illustrates readily that surface adhesion forces alone cannot predict biostabilization effects, as the proposed linear regression from the Mar14 experiment deviates from the regression of the Jul14 experiment indicating that additional factors might play a role in biostabilization processes.

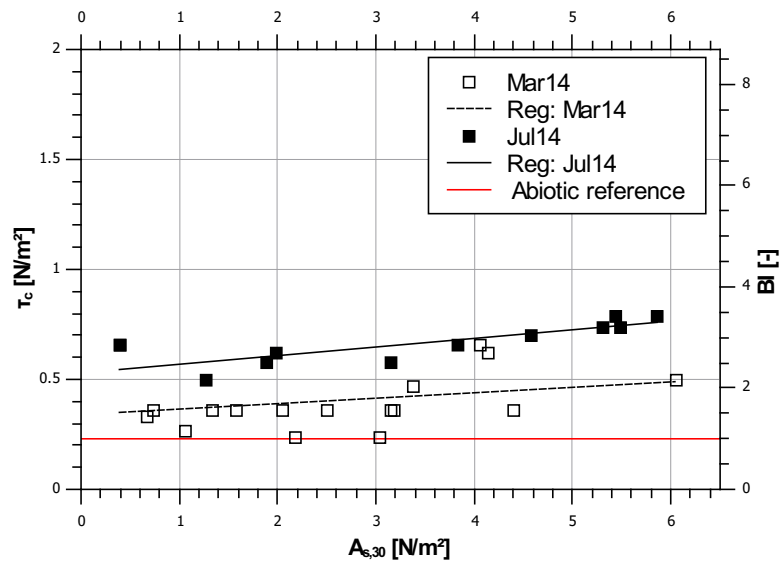


Figure D.9 The correlation between erosion threshold and surface adhesion in Phase II as measured in experiments Mar14 and Jul14. Additionally the plot shows the linear regression curves for each experiment.

Phase III

The erosion threshold in the mechanically matured phase III is characterized by a biostabilization index $\gtrsim 3.5$, that is mostly higher than the stability in phase II (see Figure D.10). In both experiments the data is highly scattered and no correlation can be found. It is also noteworthy that a large part of the erosion thresholds have related surface adhesion forces that are well in the range of the data from phase II.

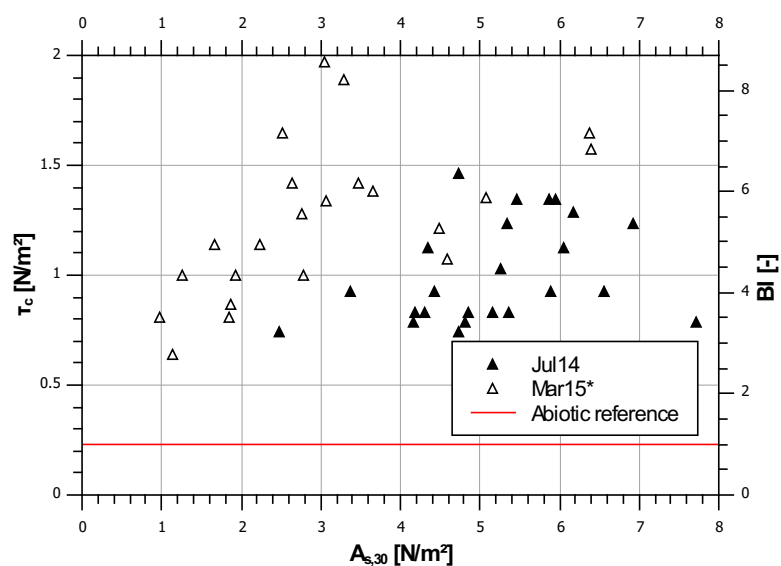


Figure D.10 The interrelationship between erosion threshold and surface adhesion in Phase III as measured in experiments Jul14 and Mar15*.

D.5 Hypotheses on the role of surface adhesion for biostabilization

The results of surface adhesion measurements in relation to the stability and the temporal development of surface adhesion forces allow a deeper insight into the role of adhesion in biostabilization processes. In general, the trend of surface adhesion forces is well in line with the observations on stability, both in the experiments presented here and in Section B. As these datasets are the first of their kind (to the best of the authors' knowledge), much more experimental work is needed to confirm the following hypotheses. Still, based on the results in the previous section the following conceptual model on the role of a developing adhesion in biostabilization processes is put forward:

In the experiments river water containing advected microbes is circulated over the initially abiotic sediment. These microbes settle to the sediment surface where they produce a conditioning film. This means that they produce EPS to attach to the sediment and promote further growth. During this phase, which, in the here conducted experiments, lasts approximately 2 weeks, the surface adhesion forces are low and probably only small parts of the sediment surface is covered by the EPS. In any case the impact of the low-adhesive EPS on sediment stability is negligible.

This changes abruptly in Phase II. Depending on the applied boundary conditions adhesion rates between 17 and 44 % suggest fast developing biofilms. At the same time the first biostabilization effects (i.e. an increase in $\tau_{c,bio}$) are visible and can be correlated to surface adhesion. The glue-like effect of the EPS (as well as its quantity) is sufficient to connect sediments to form larger aggregates. These aggregates are, compared to the single sediment grains, more difficult to erode because of their increased size. On the other hand, the increased size is at the expense of a drastically reduced bulk density of these aggregates. As more and more EPS is produced, the EPS to sediment ratio increases and, as the EPS has a density of around 1.0 t/m^3 , the bulk density of the aggregates decreases. This effect could explain why the enhancements in biostabilization are comparably low (factor 1.3) while at the same time the surface adhesion force increases are high (factor 6).

From another point of view one could speculate that the adhesion forces balance the loss in stability due to a decreasing weight of the aggregates mediated by a reduction of bulk density. After all, biofilms in Phase II experience a biostabilization effect of factor 1...3.5 compared to the initial abiotic sediment. In accordance to the USDA classification and using a standard fine sand as a reference ($d = 0.15 \text{ mm}$, $\rho_s = 2.65 \text{ t/m}^3$) the enhancements of a $BI = 3.5$ translated into an increase in grain size, would mean a new sediment size of $d = 1.0 \text{ mm}$. A $BI = 3.5$ would have the same effect as increasing the diameter of sand grains by a factor of 6.7, or in other words from fine sand to the lower boundary of very

coarse sand.

The adhesion rate (r) and the corresponding lower critical bed shear stress in Mar14 indicate that besides surface adhesion other factors play an important role. It is possible, that in Mar14 less EPS is produced and as a consequence, the grains are not sticking together as in Jul14.

In Phase III no further enhancements in surface adhesion are measured, the $A_{s,30}$ and probably also the $\tau_{c,bio}$ fluctuate around a constant mean. Potentially these fluctuations of the erosion threshold can be explained by the increasing heterogeneity of the biofilm surface. While in phase II the surface roughness is still low and evenly distributed over the biofilm surface, distinct biofilm spots that are exposed to the fluid develop with time and are clearly visible in phase III (see Chapter F). In this matured stage no correlation is found between surface adhesion and erosion threshold as the data scattered widely. However, the “matured” biofilm is more stable ($BI > 3.5$) than the biofilm in phase II. This might also be related to a structural change. In later stages of biofilm development so called biofilm mats (or carpets as described in Chapter B) are frequently found which generally have a higher stability as compared to the crust-like biofilms (see also Figure B.8). In contrast to the aggregate like erosion of the crust, these mats oscillate in the flow (with increasing τ_{bed}) until they suddenly fail (Vignaga et al., 2013). The results in this study suggest that surface adhesion forces in phase II (where the erosion mechanism is clearly aggregate like) might be useful in predicting biostabilization effects, on the other hand the erosion mechanism of biofilm mats might be completely independent of the surface adhesion.

The results presented in this study are strictly limited to the experimental conditions applied. The fits between $A_{s,30}$ and $\tau_{c,bio}$ in phase II must therefore not be considered as a general approach to predict biostabilization. As described above, a number of other factors influence the biostabilization effect (with the bulk density and floc size as probably the most influential ones). While it is certainly impossible to unravel the phenomena of biostabilization in the context of this study an attempt to model biostabilization with the help of a physics-based model is made in the following Part E.

Part E

APPLICATION OF A THEORETICAL MODEL TO PREDICT BIOSTABILIZATION

The aim of this part is to evaluate the feasibility of using surface adhesion measurements for predicting the biostabilization potential by application of a physics-based model. The findings from the previous part indicate some striking similarities between surface adhesion and biostabilization development over time. This is also true for the trends reported from biofilms cultivated under different environmental boundary conditions and at different seasons. On the other hand it is clear that the results reported in Part D are only valid for the specific experiments that are discussed and it has been demonstrated that a simple regression analysis between surface adhesion and erosion threshold is not sufficient to predict biostabilization.

Consequently, in this part, a physics-based model (after Righetti & Lucarelli, 2007) is applied, considering 1) the eroded floc size (D), 2) the eroded floc bulk density (ρ_b) and 3) an effective adhesion between eroded flocs (A_{eff}). As suggested by Righetti and Lucarelli (2007) only the adhesion forces are considered and the cohesion forces are neglected. Therefore, the individual flocs are held together only by adhesion (EPS-sediment) as illustrated in the definition sketch (the red linkages in Figure E.1).

For further details on the model please see Section A.6.3 and Part A. The calculated effective adhesion is then correlated to the surface adhesion measurements to elucidate the potential of the MagPI-IP measurements to predict biostabilization. In conducting this analysis further methods had to be developed to evaluate 1) the eroded floc size and 2) the bulk density of flocs (presented in Section E.1). After all, the data of one experiment (Jul14) is evaluated in this part, consequently the results presented must be regarded as the first step into the application of a physics based model. Still, in this part important information about experimental procedures and the relevance of individual parameters is proposed serving as a basis for further investigations.

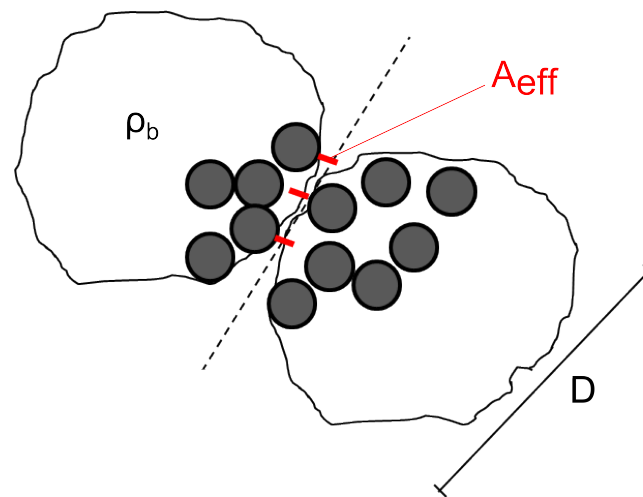


Figure E.1 Definition sketch of important parameters considered in the physics-based model of Righetti and Lucarelli (2007). Illustrated are two flocs that stick together by the effective adhesion forces (A_{eff}). The flocs properties are considered by their diameter D and the floc bulk density ρ_b . The grey circles are the initial abiotic sediment hold together by the biofilm to form the flocs.

E.1 Additional methods for the quantification of floc geometry and bulk density

In addition to the methods used in Chapter D (Surface adhesion measurements using the MagPI-IP, erosion threshold in the SETEG flume) a floc size and a bulk density analysis are performed in the Jul14 experiment. This is necessary as the model applied here is based on momentum balance considerations of eroded flocs extending the original work of Shields (1936) and the developments hereafter. The analysis is based on the experiments already discussed in Section D.4.3. The total experimental data is slightly reduced as at 5 points in time no floc data were available in the flumes where the erosion measurements are conducted on.

E.1.1 Floc size analysis

To determine the sizes of eroded biofilm aggregates (or flocs) a combination of a smaller erosion chamber, a specifically constructed settling column and a camera system is used. Biofilm samples in cartridges are eroded in the erosion chamber which has the advantage that all eroded aggregates are kept inside the small volume of the device and thus can be relatively easy transferred into the settling column. The camera system then captures the settling of the flocs in the column and the raw images are further processed with a MATLAB[®] software.

A number of studies have been conducted with the objectives to 1) develop a working system for the evaluation of floc (settling) characteristics (Santolamazza, 2013; Ziegler, 2013) and b) evaluation of floc settling velocities with regard to different applied boundary conditions

during growth (Githua, 2014; Sengottuvel, 2015). From the relatively huge datasets only the geometrical properties are of interest in this study and the setup is described accordingly in the following.

Floc generation with an erosion chamber

Sample cartridges from the experimental flumes are transferred and placed in the so called Gust chamber (after Gust, 1990). The Gust chamber is a round shaped microcosm ($d = 18.0\text{ cm}$) with a stirring disc that can be rotated at different speeds (see Figure E.2). In operational mode, the Gust chamber is filled with water and the stirring disc, which is in contact with the water initiates a rotation of the water body around its vertical axis. The centrifugal forces which are induced are balanced by a pump whose outlet is located in the center of the microcosm. To insert a biofilm sample the lid (with the stirring disc) is removed and the cartridge is placed in a specially constructed frame. This frame houses an additional reservoir below the cartridge in which the eroded flocs are collected. Then water is carefully filled into the chamber and the rotational speed is increased in increments of 10 rpm every 2 minutes.

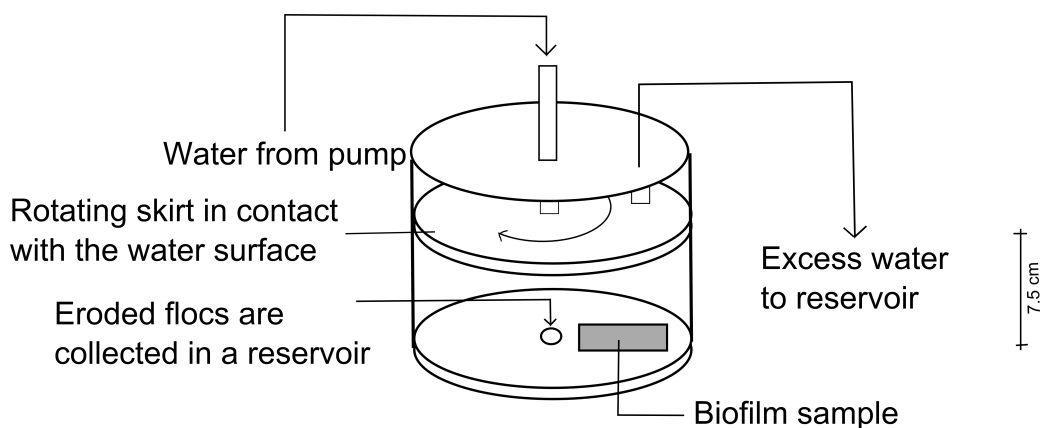


Figure E.2 Schematic drawing of the Gust chamber (Gust, 1990) used for the collection of eroded flocs. After inserting the biofilm sample the “skirt” is adjusted to the correct height (in contact with the water) and rotated. Every two minutes the revolutions per minute (rpm) of the skirt are increased by 10. The pump flow rate is adjusted according to Gust (1990). This process is stopped when the biofilm-sediment matrix is eroded.

Settling column and camera system

After erosion the flocs are collected from the reservoir using a pipette or spatula and transferred into the settling column (see Figure E.3). The settling column ($l \times w \times h = 34 \times 4 \times 330\text{ mm}$, see Figure E.3 *Left* and *Right*) consists of two sheets of a special glass mounted on a metallic frame. A void between the sheets is filled with water to allow settling of the flocs. The flocs are inserted through an open top.

At terminal fall velocity (18 cm from top) a camera (uEye UI-2250-M) is positioned recording the movement of the flocs at 8 fps (frames per second) and with a resolution of $1600 \times 1200\text{ px}$ (see Figure E.3 *Left*). To improve the contrast between the flocs and the background an ad-

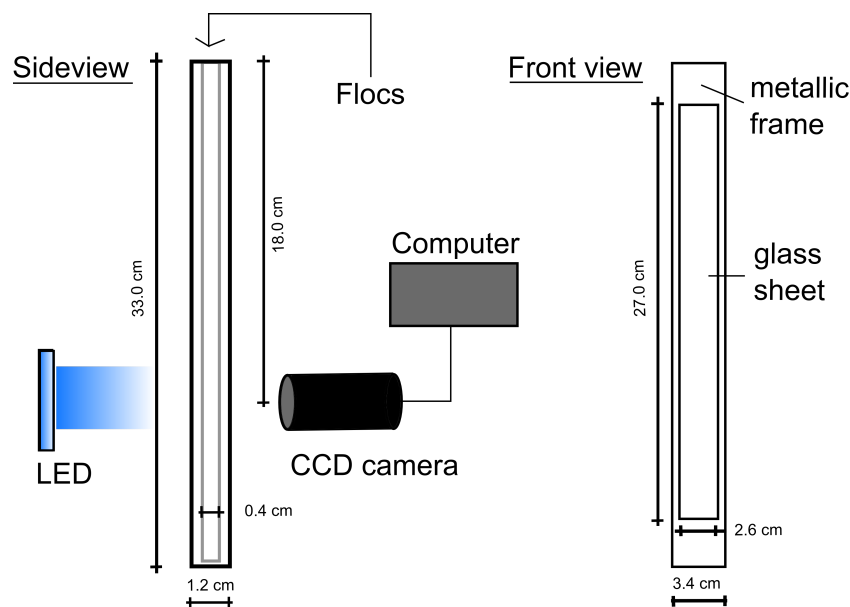


Figure E.3 The settling column and camera system to investigate floc geometries and settling velocity. *Left:* Side view of the settling column with CCD camera. The flocs are inserted through an open top. *Right:* Front view of the settling column.

ditional backlight LED producing diffuse light is fixed behind the column. The design of the column is optimized especially in regard to the optical qualities and its length, to allow capturing the flocs movement at terminal fall velocity. A movement of the flocs in the camera axis is impeded by the distance between the glass sheets (4 mm). This is especially important for the geometrical evaluation of the flocs. Flocs which are further away from the camera appear smaller on the images. The calibration of the camera (from pixels to millimeter), only applies for a given distance and consequently, flocs which deviate from that distance will be either too small or too large. A drawback of this method is that the narrow width of the settling column also limits the maximum size of eroded flocs to be inserted.

Image Processing for floc geometry measures

The MATLAB[®] code for the image processing of the captured pictures named “Flocula-Mazza” was developed by Santolamazza (2013). Its primary function is to determine the floc settling velocities and floc geometries. In this thesis only the floc geometries are analyzed and a brief summary of the processing is given focusing on this particular aspect.

The pictures captured by the camera are loaded into the program and transformed into binary (black and white) images using the adaptive method for thresholding. Similar to the image processing from Part C the adaptive method uses a reference image. Taking a background image (i.e. without flocs) as a reference image the background information are subtracted from the following pictures, and ideally only the flocs are visible on the binary image. In the next step, all visible flocs from all pictures are geometrically characterized (e.g. position of the centroid, length of major axis/minor axis and convex hull, see Figure E.4 *Left*). Those information are already given in SI units as the pixel-millimeter relation was deter-

mined a priori via calibration.

To follow the path of the settling flocs, the geometrical characteristics of two subsequent images are analyzed and based on tolerance values (defined by the operator) the program finds pairs of flocs with the same characteristics (see Figure E.4 *Right*).

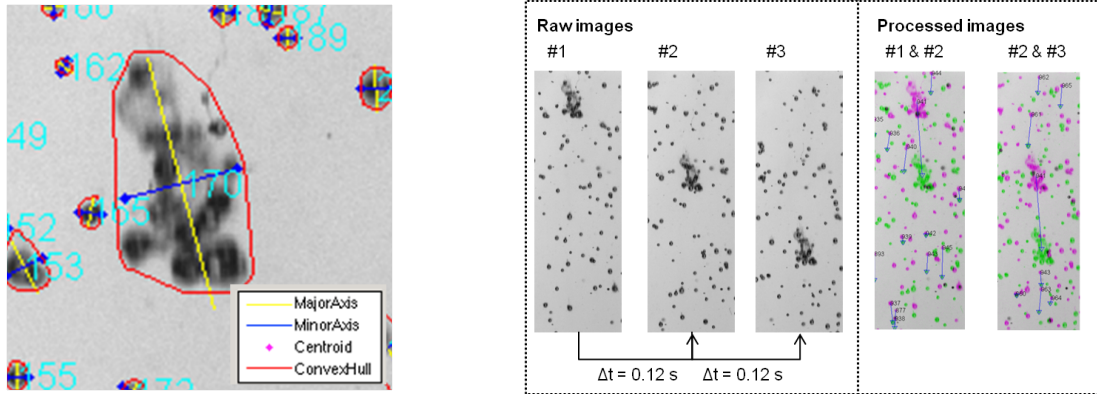


Figure E.4 Example of processing the images of settling flocs (screenshots). *Left*: All flocs on one image are characterized by their geometry (length of major/minor axis, length of convex hull, position of centroid). *Right*: Subsequent images are analyzed using the geometrical information to find matching pairs. To calculate the settling velocity the centroid movement from the first image (see processed images: the pink floc) to the second image (the green floc) is evaluated and divided by the time span between capturing the images.

Once these pairs are found, the movement can be calculated from comparing the position of their centroids in two subsequent images and the time interval between 2 subsequent images (for more details please see Santolamazza, 2013). All information on the recognized flocs (geometrical as well as velocities) are then saved for further analysis.

Evaluation of floc data

Characterization of the floc diameter

One of the biggest challenges in investigating biostabilized floc properties is that their shape differs considerably from spherical particles which influences their settling behavior. Consequently a number of different shape factors have been investigated (see e.g. Dietrich, 1982). In contrast to Righetti and Lucarelli (2007) who used the mean Feret diameter¹ as a proxy, the more commonly used spherical-equivalent diameter (d_f in [mm]) is calculated (see e.g. Keyvani & Strom, 2013) in this study. The spherical-equivalent diameter is the diameter of a circular particle of the same surface area as the irregularly shaped floc and calculated as:

$$d_f = \sqrt{\frac{4 \cdot A}{\pi}} \quad (\text{E.1})$$

where A in [mm²] is the surface area of the floc.

¹The Feret or caliper diameter is the distance between edges of an object along a specified axis.

Peak analysis

Biostabilized sediments are eroded in a wide range of floc sizes. A rough distinction can be made between micro- and macroaggregates. While Microaggregates consist of primary particles, macroaggregates are composed of microaggregates. In their original publication Righetti and Lucarelli (2007) used the size of macroaggregates as a characteristic diameter. To determine the characteristic diameter Righetti and Lucarelli (2007) applied a “lognormal high pass filter” to the measured floc diameter distribution and calculated the D_{50} . Unfortunately, no further information was given on the characteristics of the filter and consequently an alternative procedure is applied aiming at a similar output.

Figure E.5 is a typical histogram of the equivalent diameter distribution from one experiment.

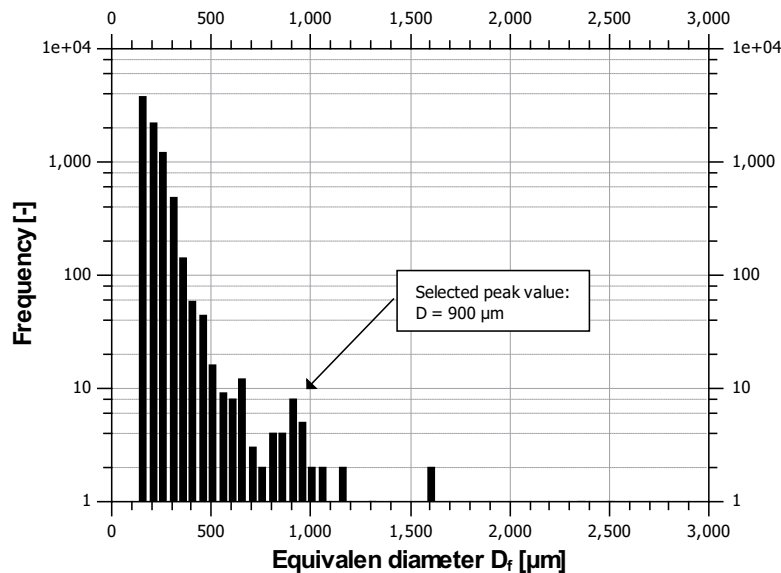


Figure E.5 Example of histogram plot showing the distribution of spherical-equivalent diameters from one eroded biofilm sample. From these plots the macroaggregate diameters D are determined manually by analysing the displayed peaks. The arrow indicates the selected peak.

Similar to the histograms in Righetti and Lucarelli (2007) it shows a bimodal distribution with a peak in the larger size range of particles (see arrow). This peak indicates the size of a macroaggregate and is used as a proxy for the floc diameter D . All other datasets on floc size distribution are evaluated in the same manual way. It is noteworthy, that the here applied procedure involves considerable uncertainties: In some datasets it is particularly difficult to determine distinct second peaks. In this regard, the procedure proposed by (Righetti & Lucarelli, 2007) may lead to more unambiguous results. On the other hand, it has to be generally clarified which aggregate sizes play the most important role in biostabilization processes, suggesting more detailed investigations on the geometrical characteristics of the aggregates. However, in the context of this study the above described procedure is used yielding similar floc sizes as reported in Righetti and Lucarelli (2007) and their follow up publication (Righetti & Lucarelli, 2010).

Experimental program for floc analysis

The flocs are analyzed each week for each flume starting from week three until week 7. It is important to note that the floc size analysis is conducted on biofilm samples which are different to those that are eroded. This is because two different devices are used for the two types of measurements: 1) the SETEG flume, which is currently not equipped with a method to determine eroded floc sizes but is a useful device for measuring the erosion threshold and 2) the Gust chamber which keeps the eroded flocs in place for subsequent floc size analysis. Still, the samples for floc size analysis which is later related to the erosion threshold are cultivated in the same flumes and thus experienced the same environmental boundary conditions. However, even biofilms which are cultivated under the same conditions partly vary in their structure and growth patterns (see Part B), an influence of the aforementioned limitation on the results cannot be fully excluded.

E.1.2 Bulk density analysis

The bulk density of eroded flocs (ρ_b in $[\text{kg}/\text{m}^3]$) is determined by the use of a pycnometer, assuming that the flocs are an enclosed space. Flocs are collected from each experimental run and the weight of the flocs (m_1 in [g]) is obtained by a laboratory scale. Then the weight of the water-filled pycnometer (m_2 in [g]) is obtained in the same way, as well as the fluid temperature (the density of water depends on its temperature). In the last step, the weight of the pycnometer filled with water and the biofilm flocs is measured (m_3 in [g]). Following the ASTM D 85402 standard (modified for bulk density, after ASTM, 2002) the density can be determined as shown in equation E.2:

$$\rho_b = \frac{m_1 \cdot \rho_{w,t}}{m_1 + m_2 - m_3} \quad (\text{E.2})$$

where $\rho_{w,t}$ is the density of the water at the test temperature.

Experimental program for floc bulk density measurements

Measurements on bulk density are performed every 3 to 4 days (starting in week 3, with 3 to 6 replicates each) and averaged irrespective of applied boundary conditions for each day (no clear trend between different environmental conditions is observed). Additionally, data from day 61 of the Mar15 experiment is evaluated to represent a more reliable estimate (here: $n = 14$) of matured biofilm bulk density.

E.2 Application of the modified Shields approach with measured surface adhesion and floc property values

Eroded floc diameter

Figures E.6 and E.7 show the measured equivalent diameters (D) for eroded flocs over time of growth. For better visualization the data is plotted into these two separate graphs, Figure E.6 for biofilms cultivated under low and Figure E.7 for biofilms cultivated under high flow velocities.

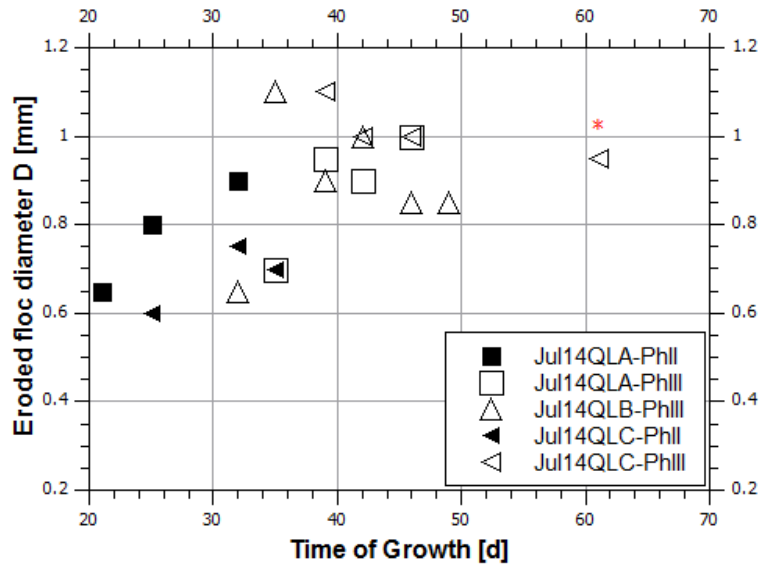


Figure E.6 Temporal development of eroded floc diameters D for biofilms cultivated under low flow velocities. The graph differentiates between different flumes and phases. All data, except of data for day 61 (marked with *), is used in the modified Shields model.

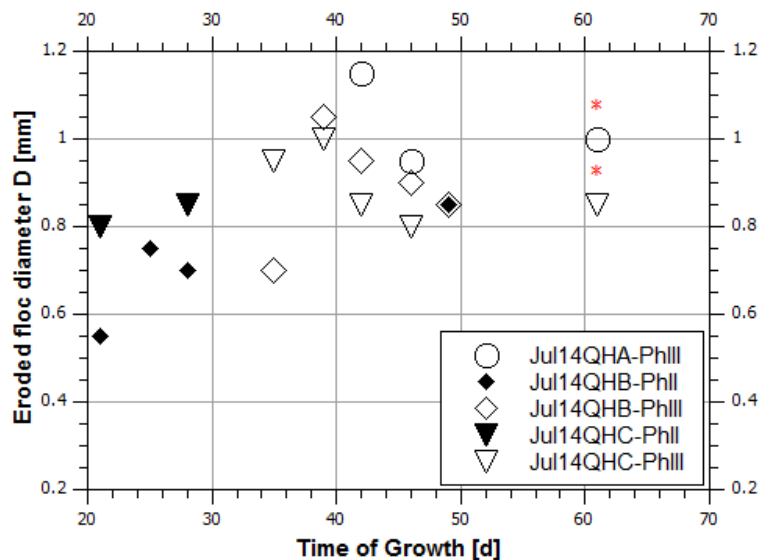


Figure E.7 Temporal development of eroded floc diameters D for biofilms cultivated under high flow velocities. The graph differentiates between different flumes and phases. All data, except of data for day 61 (marked with *), is used in the modified Shields model.

Floc sizes range between $D = 0.55 \dots 1.18$ mm, which corresponds to a factor of ≈ 2.1 . In Phase II (between days 21 \dots 35) a slight tendency of floc sizes to increase with time is ob-

served. In contrast, floc sizes in Phase III tend to fluctuate around $D = 0.95$ mm, further supported by the data of day 61 (these data have not been used in the model as no erosion thresholds are determined at that day). As already mentioned above, the floc sizes are well in range with the data of Righetti and Lucarelli (2007) ($D = 0.581 \dots 0.890$ mm) and Righetti and Lucarelli (2010) ($D = 0.565 \dots 0.853$ mm).

Eroded floc bulk density

Between days 21 and 46 the averaged bulk density decreases from 1.81 to 1.56 t/m^3 (see Figure E.8) corresponding to a decreasing relative density (after e.g. Van Rijn, 1984: $\Delta = (\rho_b - \rho)/\rho$) by 70%. Measurements conducted on day 61 (the \bullet symbol, labeled Jul14) indicate that the bulk density is no further decreased and probably reaches a steady state. However, additional averaged data from a later experiment (the \bullet symbol, labeled Mar15) with a higher number of measurements conducted suggest lower bulk densities. This indicates that densities might differ significantly between experimental runs (more on this issue in Section E.4).

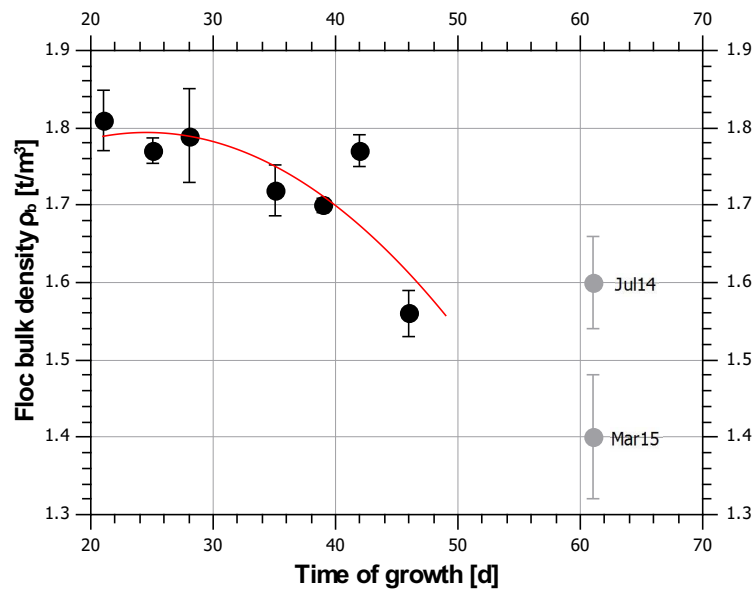


Figure E.8 Temporal development of measured floc bulk density in the Jul14 experiment. The bulk density is represented as an average value (\pm SD). The red line is the calculated best fit between days 21 and 46, which will be used in the modified Shields model. The \bullet symbols stand for measurements conducted on day 61 in Jul14 and additional data from Mar15.

Unfortunately, no measured values of the bulk density are available at the specific days 32 and 49 where large erosion measurements were conducted. Therefore, a polynomial regression (solid red line in Figure E.8) is fitted to the data based on the measurements between days 21 and 46. Equation E.3 ($R^2 = 0.67$) is used in the following to relate the bulk density to the remainder data:

$$\rho_b = 1.55572 + 0.01942t - 0.0004t^2 \quad (\text{E.3})$$

Please note that the data for day 49 is extrapolated. However, due to the regression the density is equal to the density measured three days before (day 49 (regression) and day 46 (measured): $\rho_b = 1.56 \text{ t/m}^3$). Consequently, this extrapolation should not yield any unrealistic results.

At this point it seems necessary to emphasize that the here presented regression curve cannot be applied for the evaluation of other experiments. The bulk density depends on e.g. the ratio between volume biofilm and volume sediments. Both factors may strongly depend on the investigated biofilms and the sediment size used in the experiments. Still, the trend of decreasing bulk density is well in line with the observations made by Droppo et al. (1997) who reported that the floc density reduction is associated with a porosity increase and generally comes along with increasing floc sizes. Even though the measurements on floc size and bulk density are conducted separately, it is also observed that the floc size increases with time.

Erosion threshold and surface adhesion measurements

For a description of the results on erosion threshold and surface adhesion measurements in Jul14 the reader is kindly referred to Part D. A detailed representation of the results is further to be found in the Appendix C.2 for erosion threshold and C.3 for surface adhesion forces. Moreover Table E.1 below summarizes all relevant data for the here applied model.

Application of the modified Shields approach

As expected, the application of the traditional Shields approach (not considering adhesion effects) to the data of Jul14 underestimates the critical Shields parameter significantly as illustrated in Figure E.9. The differences between the curve and the measured values can be explained by the additional glue like effects underlining the importance of a more comprehensive understanding of the involved forces and the need for adjusting the curve.

Before going into detail, the modified Shields approach (after Righetti & Lucarelli, 2007) is briefly recalled (for more details please see Section A.6.3). The general form is:

$$\Theta_C = \frac{\tau_{c,bio}}{(\rho_b - \rho)gD} = \Theta_{C0} + \overset{0}{\cancel{\Theta_{CC}}} + \Theta_{CA} \quad (\text{E.4})$$

where Θ_{C0} being the traditional critical Shields parameter, here derived by the Brownlie equation: $\Theta_{C0}(D^*) = 0.22 \cdot D^{*-0.9} + 0.06 \cdot e^{-17.77 \cdot D^{*-0.9}}$ with the macroaggregate/floc dimensionless characteristic diameter $D^* = D \cdot ([g \cdot \Delta] / \nu^2)^{\frac{1}{3}}$ (e.g. after Van Rijn, 1984). D is the floc diameter as explained above. The term Θ_{CC} accounting for cohesion effects is neglected as this thesis focuses solely on adhesion effects. This has also been done by Righetti and Lucarelli (2007, 2010) and is a valid approach as the model is dimensionally consistent.

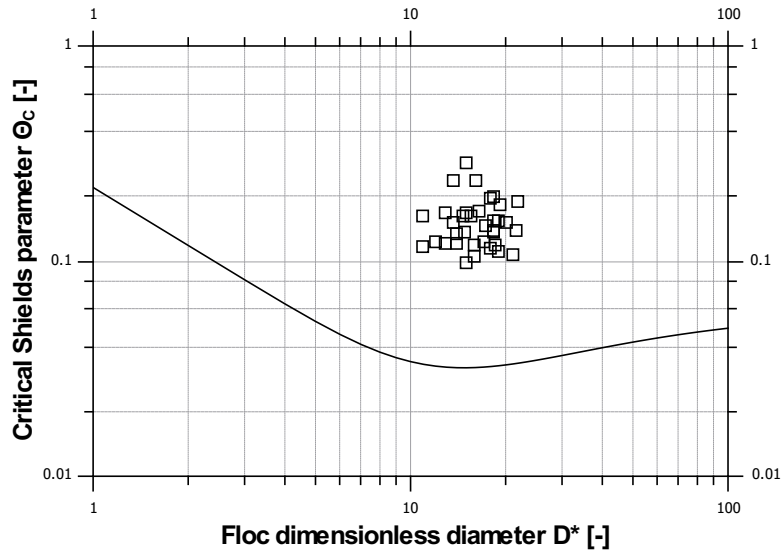


Figure E.9 Comparison between the traditional Shields parameter (curve, calculated by applying the Brownlie equation) and experimental results of Jul14 (The □ symbols).

Θ_{CA} is the critical mobility parameter accounting for adhesion effects between contiguous flocs:

$$\Theta_{CA} = \frac{\Theta_{C0}(D^*)}{\alpha_3} \frac{A_{eff}}{(\rho_s - \rho)gD} \quad (E.5)$$

As one can see, Θ_{CA} is a function of the traditional Shields parameter (Θ_{C0}), the floc shape parameter α_3 (here defined as $\alpha_3 = \pi/6$ for spherical flocs), the denominator $(\rho_b - \rho)gD$ and the adhesion coefficient A_{eff} in N/m^2 . As described in Righetti and Lucarelli (2010), the adhesion coefficient refers to the contribution of adhesive forces between contiguous flocs. Consequently, the A_{eff} is an effective adhesion, containing all effects related to adhesion forces and the resulting binding force between flocs. These additional effects have not been defined by Righetti and Lucarelli (2007) probably as no measurements on adhesion were available in their studies.

Consequently, in this study the modified Shields approach is applied to calculate the adhesion coefficient (or effective adhesion) A_{eff} . Hereafter the calculated A_{eff} is compared with the measured surface adhesion forces. Table E.1 is a summary of the measured values and calculated results, additionally containing information about the particle Reynolds numbers $Re^*(D)/Re^*(d)$ and the ratio between adhesive forces and submerged particle weight F_A/F'_G . The results will be described below and discussed in the next section.

Classification of adhesion effects after Dade et al. (1992)

After Dade et al. (1990, 1992) the term F_A/F'_G is the ratio between adhesive forces and submerged particle weight. When the ratio is less than unity ($F_A/F'_G < 1.0$) the biofilm sediment

Table E.1 Measured input parameters for the modified Shields equation, calculated results and additional info (Jul14). Parameters not listed: $\alpha_3 = \pi/6$, $\rho = 0.9982 \text{ t/m}^3$, $\nu = 1.004 \times 10^{-6} \text{ m}^2/\text{s}$, primary particle diameter $d = 150 \mu\text{m}$. Observed erosion processes (“E.p.”): (A) aggregate-like, (C) carpet-like. Co-existence possible. Additional influences: (B) bubble entrainment and (2A) a second layer.

Measured			Calculated						Info	
Time of Growth	$\overline{A_{s,30}}$	$\tau_{c,bio}$	D	ρ_b	A_{eff}	$Re^*(D)$	$Re^*(d)$	F_A/F'_G	Ph.	E.p.
[d]	[N/m ²]	[N/m ²]	[mm]	[t/m ³]	[N/m ²]	[-]	[-]	[-]	[-]	[-]
21	4.57	0.70	0.55	1.79	8.82	15	40	6.8	II	A
21	0.39	0.66	0.80	1.79	7.55	20	38	0.6	II	A
21	1.97	0.62	0.65	1.79	7.43	16	37	2.9	II	A
25	1.27	0.50	0.55	1.79	5.67	12	33	1.9	II	A,2A
25	3.14	0.58	0.75	1.79	6.43	18	36	4.7	II	A,2A
25	5.48	0.74	0.80	1.79	8.92	22	41	8.1	II	A,2A
25	5.30	0.74	0.70	1.79	9.34	19	41	7.9	II	A,2A
25	1.87	0.58	0.60	1.79	6.86	14	36	2.8	II	A,2A
28	3.83	0.66	0.70	1.79	7.96	18	38	5.7	II	A,C,2A
32	5.86	0.79	0.90	1.77	9.21	25	42	8.7	II	C,A,2A
32	5.43	0.79	0.75	1.77	9.96	21	42	8.1	II	C,A,2A,B
32	4.86	0.83	0.65	1.77	10.98	19	43	7.2	III	C,A,2A
35	5.36	0.83	0.95	1.75	9.77	27	43	8.0	III	A,C,2A
35	4.81	0.79	0.70	1.75	10.20	20	42	7.1	III	C,2A
35	6.06	1.13	1.10	1.75	13.45	37	50	9.0	III	C,2A
35	6.93	1.23	0.70	1.75	17.50	25	53	10.3	III	C,2A,B
39	5.94	1.35	0.95	1.71	18.26	35	55	8.8	III	C,A,2A
39	4.35	1.13	1.05	1.71	14.08	35	50	6.5	III	C,A,2A,B
39	6.17	1.29	1.00	1.71	17.01	36	54	9.2	III	C,2A
39	3.37	0.93	0.95	1.71	11.51	29	46	5.0	III	C,A,2A
39	4.42	0.93	0.90	1.71	11.79	27	46	6.6	III	C,2A
39	5.16	0.83	1.10	1.71	9.11	32	43	7.7	III	C,2A,B
42	4.74	1.46	1.15	1.67	18.89	44	57	7.0	III	C,2A
42	5.33	1.23	0.95	1.67	16.70	33	53	7.9	III	C,A,2A
42	5.46	1.35	0.85	1.67	19.08	31	55	8.1	III	C,2A
42	2.48	0.74	0.90	1.67	9.01	24	41	3.7	III	C,2A
42	4.73	0.74	1.00	1.67	8.50	27	41	7.0	III	C,2A
42	5.25	1.03	1.00	1.67	13.02	32	48	7.8	III	C,2A
46	6.56	0.93	0.90	1.61	12.32	27	46	9.7	III	C,A,2A
46	4.17	0.79	0.80	1.61	10.42	22	42	6.2	III	C,2A
46	5.89	0.93	1.00	1.61	11.84	30	46	8.7	III	C,A
46	4.29	0.83	0.85	1.61	10.99	24	43	6.4	III	C,A,2A
46	4.19	0.83	1.00	1.61	10.32	29	43	6.2	III	C,A
49	7.71	0.79	0.85	1.56	10.50	24	42	11.4	III	C,B,2A
49	5.88	1.35	0.85	1.56	19.63	31	55	8.7	III	C

matrix is weakly adhesive² and the erosion resistance is primarily due to a combination of particle interaction and gravity. On the other hand, when F_A/F'_G exceeds 1.0 the additional stability is dominated by adhesive effects (strongly adhesive). The values of F_A/F'_G from Jul14 are shown in Table E.1. The ratio can be calculated from the measured data as follows:

$$\frac{F_A}{F'_G} = \frac{A_{s,30} \cdot A_{fp}}{F_{m,0}} \quad (\text{E.6})$$

where A_{fp} is the surface area of one ferromagnetic particle: $A_{fp} = \pi \cdot d^2$ with an averaged $d = 275 \mu\text{m}$. As described in Part C $F_{m,0}$ is the averaged submerged weight force of one ferromagnetic particle ($F_{m,0} = 0.16 \mu\text{N}/\text{particle}$). Fortunately, $F_{m,0} = 0.16 \mu\text{N}$ is equivalent to the submerged weight force of a mineral particle (with density $\rho_s = 2.65 \text{ t/m}^3$) only slightly larger than the glass beads used in the experiments ($d = 266 \mu\text{m}$) such that F_A/F'_G can be used to classify the effect of adhesion on sediments used in this thesis.

In the present study no biostabilization effects are observed when $A_{s,30} \lesssim 1.0$ (see Part D) which translates into a ratio F_A/F'_G of ≈ 1.5 . Assuming the same stickiness between sediment-biofilm and ferromagnetic particle-biofilm, this means that the adhesive force on the surface needs to be 50 % higher than the submerged weight of the sediment to induce a biostabilization effect. Consequently $F_A/F'_G \approx 1.5$ can be defined as the threshold between an increased and no stabilization effect, which might be an interesting information for future research.

As can be seen from Table E.1 values of F_A/F'_G range between 1.9 (assuming that the surface adhesion measurement displayed in the second row is an outlier) and 11.4 (on average = 6.9). This is surprisingly well in line with the calculated values reported by Dade et al. (1990) (= 0.9 . . . 11.4) and indicates that the biofilms in this study form strongly adhesive sediments. On average the impact of surface adhesion exceeds the gravitational force (due to submerged weight) by 590%, emphasizing the importance of biofilm stabilization processes to be considered in erosional studies.

The particle Reynolds number

For a description of the particle Reynolds number and its impact on the erosion threshold please see Part A. The particle Reynolds number Re^* is calculated here either as a function of the aggregate diameter:

$$Re^*(D) = \frac{u^* D}{\nu} \quad (\text{E.7})$$

²In their original publication Dade et al. (1992) used the term weakly “cohesive” as they focused on cohesive muds, rather than the impact of biofilms. In the present study this phrase is translated into weakly “adhesive”.

or as a function of the average abiotic sediment diameter (with $d = 150 \mu\text{m}$):

$$Re^*(d) = \frac{u^*d}{\nu} \quad (\text{E.8})$$

with u^* in [m/s] being the shear velocity defined as $u^* = \sqrt{\tau_c/\rho}$. Both ranges of $Re^*(D)$ and $Re^*(d)$ are presented in Table E.1 and indicate that the surface can be considered as neither hydraulically rough nor smooth instead as transitional ($5 < Re^* < 70$). This means that the bed shear stress is caused by both viscous shear as well as pressure forces by turbulence impact. The biofilm roughness elements are exposed partly to the turbulent zone of the boundary layer and therefore influence the resistance of the near bed hydraulics.

However, as will be demonstrated in the next part, it is highly doubtful that the biofilm surface roughness can be characterized by either sediment (d) or aggregate (D) diameters. While using the abiotic particle diameter or the aggregate diameter as a reference for Re^* it is assumed that the bed is composed of well-sorted particles of the respective sizes (Wiberg & Smith, 1987). In fact, the biofilm topography is heterogeneous (this will be demonstrated in Part F) and may be better described as a microscale landscapes (with peaks and valleys as suggested by Battin et al., 2007). Therefore it is hypothesized that the particle Reynolds numbers are between the evaluated values of $Re^*(d)$ and $Re^*(D)$ or even reach values > 70 such that the bed can be categorized as hydraulically rough.

Comparing the calculated effective adhesion with the measured surface adhesion

Figure E.10 illustrates the relation between the physically measured $A_{s,30}$ and the calculated A_{eff} . Additionally a linear regression is conducted (the red lines in Figure E.10) on all values (see label “Reg. Phase II + III”), on the values of data from Phase II (“Reg. Phase II”) and from Phase III (“Reg. Phase III”).

Two things are to be noticed. Firstly, a general trend is observed that A_{eff} increases with surface adhesion. On the other hand the data scatters considerably where the measured values of $A_{s,30}$ are high. Considering all phases (Reg. Phase II + III) the linear regression is very weakly correlated ($R^2 = 0.32$, see also Table E.2 for an overview). Secondly, it is striking that both results, the calculated effective adhesion and the measured surface adhesion are largely in the same order of magnitude ($10^0 \dots 10^1$) as was already indicated by comparison of surface adhesion measurements on surrogate materials to values from the studies of Righetti and Lucarelli (2007, 2010) (see Table C.2). All regression equations (see table E.2) have a constant term greater than zero. As such the calculated data is always higher than the measured data.

In principle, this regression analysis yields similar results as the regression analysis between the erosion threshold and surface adhesion in the previous part. For example, scattering of data has also been observed for Phase III-biofilms and has been related to heterogeneities

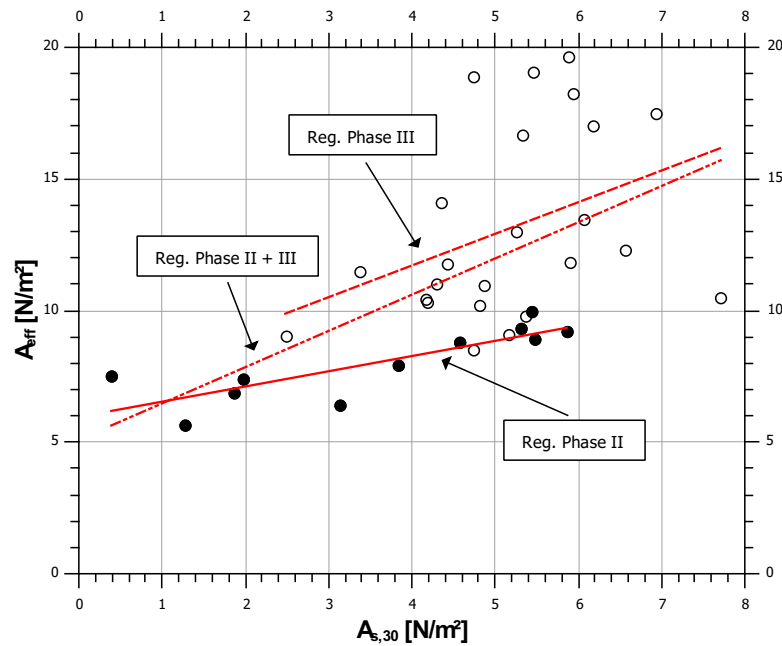


Figure E.10 The correlation between calculated effective adhesion and measured surface adhesion in Jul14. The ● symbols are data from Phase II. The ○ symbols are data from Phase III. The red lines are the linear regression curves for each individual and both phases.

Table E.2 Parameters, quality and valid range of the linear fits ($A_{eff} = aA_{s,30} + b$) between the calculated effective adhesion and the measured surface adhesion in Jul14

Rank	Description	R^2	Coefficient a	Coefficient b	n	valid range ($A_{s,30}$)
[–]	[–]	[–]	[–]	[–]	[–]	N/m^2
1	Phase II	0.68	0.58	6.00	11	1 ... 5.9
2	Phase II + III	0.32	1.38	5.10	35	1 ... 7.7
3	Phase III	0.15	1.20	6.90	24	2.5 ... 7.7

of the biofilm and its structure. In Phase II the simple statistical correlation between surface adhesion and erosion threshold was much stronger.

Likewise, in this analysis the data from phase II has the strongest correlation ($R^2 = 0.68$). The linear fit has a slope of ≈ 0.6 and a constant term of ≈ 6.0 . To increase the effective adhesion by $1 N/m^2$ a nearly 3 fold increase of measured surface adhesion is necessary. The weakest correlation is determined for the mechanically matured biofilm in Phase III ($R^2 = 0.15$).

In the following the correlation in phase II is further evaluated. The regression equation ($R^2 = 0.68$) is:

$$A_{eff} = \begin{cases} 0 & A_{s,30} < 1.0 \text{ N/m}^2 \\ 0.5775 \cdot A_{s,30} + 5.9604 & A_{s,30} \geq 1.0 \text{ N/m}^2 \end{cases} \quad (\text{E.9})$$

In the previous part it has been demonstrated that first biostabilization effects are observed when the surface adhesion is higher than unity. Consequently, the threshold for increased biostabilization is ($A_{s,30} = 1.0 \text{ N/m}^2$). The constant term in Equation E.9 illustrates that the effective adhesion is generally higher than the measured surface adhesion or in other words, the measured surface adhesion underestimates the adhesion forces between flocs.

In fact, (Ohashi & Harada, 1994) reported that the adhesion strength increased with the depth of the biofilm. In one example, the strength of adhesion at a depth of 2 mm is in the order of 10^1 higher than at the biofilm surface. As the effective adhesion can be thought of as an averaged adhesion over the contact area it is possible that it ranges between the here measured surface adhesion (order of magnitude 10^0) and the measured values in 2 mm depth by Ohashi and Harada (1994) (10^1). Consequently a constant term of ≈ 6 seems reasonable. Even more important is that the data provided by Ohashi and Harada (1994) indicates that the development of adhesion over depth of the biofilm was similar for the tested biofilms at different ages, perhaps indicative for a functional relationship between surface adhesion and adhesion over depth. As already outlined in Section D.1 it is strongly suggested to conduct fundamental studies on the development of adhesion over depth in future work as the data in literature is extremely scarce.

A second issue concerning the parameterization of A_{eff} is the discontinuity in the early phase of biofilm growth. From the previous chapter it is known that biofilms with a $A_{s,30} \lesssim 1.0$ do not contribute to biostabilization. This is taken into account by Equation E.9. As a consequence, there is a sudden increase in A_{eff} and also in predicted biostabilization. This phenomenon may be explained by the comparably low sensitivity of the SETEG flume to detect smaller changes in stability. For example the applied increments of bed shear stress are too large, or more likely, the biofilm has not developed on the whole surface and patches which are non-stabilized dominate the erosion process. It might also be possible, that although a biofilm developed on the top few μm of the biofilm the quantity of EPS in higher depths is too little. The abruptly initiated biostabilization effect could also be the result of micro-algae growth at the start of phase II producing much higher quantities of EPS.

The slope of the linear regression is relatively small (≈ 0.6), which means that smaller enhancements of surface adhesion will only have a minor effect on the effective adhesion between contiguous flocs and consequently also on the biostabilization predicted by the

model. Consequently, the question here arises if adhesion forces should be considered at all to predict the biostabilization effect by the model or if measuring the floc diameter and the bulk density alone is sufficient. In other words, it is of interest how sensitive the predicted erosion threshold responds to a variation of measured parameters. To answer this question the model is applied (considering the surface adhesion) and evaluated for a variety of realistic values (from this thesis) and for each parameter separately in the following section.

E.3 The impact of individual parameters on the predicted erosion threshold

The response of the model to realistic changes in $A_{s,30}$, ρ_b and D^* is interesting as it might explain the individual contribution of each parameter to biostabilization. As mentioned above, the effective adhesion is not particularly sensitive to changes in the measured surface adhesion. Therefore it might be possible, that for example, the bulk density is more important and the effects of surface adhesion can be neglected in future analyses (which would have practical implications for setting up experiments). In fact some earlier work on muddy sediments considers bulk density for prediction of the erosion threshold (e.g. Jepsen et al., 1997). To test the response of the model (the critical Shields parameter) three cases are investigated: (A) - variation of surface adhesion, (B) - variation of bulk density and (C) variation of floc diameter. All values are in the range of measured values from this study. An exception is $\rho_b = 1.1 \text{ t/m}^3$, which is additionally investigated because it was used in the study of Righetti and Lucarelli (2007).

CASE A: Variation of surface adhesion

Figure E.11 shows the critical Shields parameter Θ_C as the result of the model by a variation of the floc diameter D and the surface adhesion. The bulk density ($\rho_b = 1.4 \text{ t/m}^3$), as well as all other parameters (ν, ρ, α_3) are kept constant.

The critical Shields parameter Θ_C increases with increasing surface adhesion for a specific D^* while the differences between $A_{s,30} = 1.0, 3.0$ and 6.0 N/m^2 are small. Comparing the lowest adhesion measured in phase II ($A_{s,30} = 1.0 \text{ N/m}^2$) and the highest (6.0) the difference is $\Delta\Theta_c = 0.07$. However, there is a remarkable difference between the critical Shields parameter in phase II ($A_{s,30} \geq 1.0$) compared to phase I ($A_{s,30} < 1.0$), represented by the “traditional” Shields curve for abiotic sediments, namely $\Delta\Theta_c \geq 0.17$ at $D^* = 10$. Following this analysis it seems to be more important to have knowledge on whether adhesion forces exist than what their quantitative values are. If adhesion forces exist they may drastically impact the erosion threshold.

Another conclusion that can be drawn from Figure E.11 is that all curves (including the “traditional”) converge asymptotically to $\Theta_C \cong 0.06$ with increasing D^* , which means that the

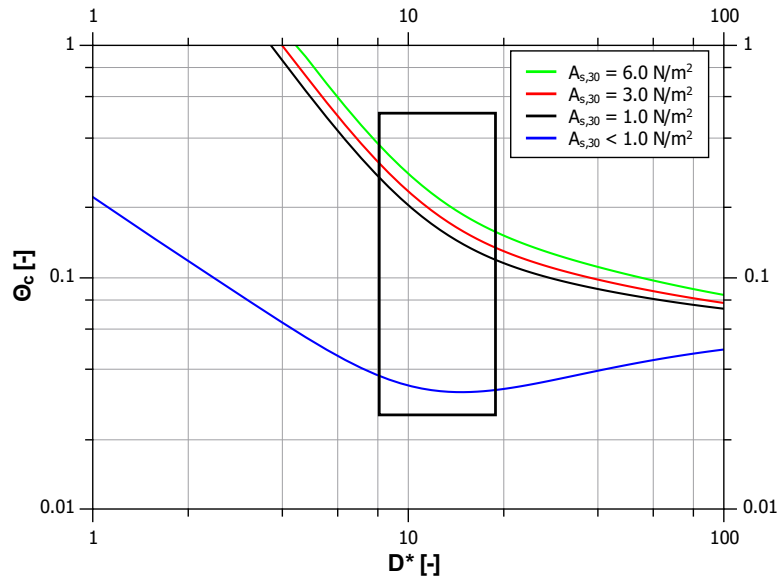


Figure E.11 The critical Shields parameter at different values of surface adhesion. The black box indicates the range of D^* corresponding to floc diameters between $D = 0.6 \dots 1.2$ mm. $\rho_b = \text{const.} = 1.4 \text{ t/m}^3$

effect of the adhesion is reduced to zero for greater sediment size classes. This makes sense as the weight force increases with aggregate diameter (the bulk density is constant in this example) up to a point where it dominates over the adhesion forces. In this example, this critical diameter would be comparable to very coarse gravel of ≈ 57 mm, but with a bulk density of 1.4 t/m^3 . The critical diameter decreases with increasing bulk density (not shown), e.g. for a density of 2.65 t/m^3 it becomes ≈ 40 mm, which still seems to be unrealistically large. In fact in this example the ratio F_A/F'_G for $A_{s,30} = 6.0$ would be $\ll 1$ which illustrates that adhesion forces should not have any impact at all. Moreover, Fang et al. (2014) reported a critical diameter of $0.1 \dots 0.2$ mm from their experiments. Consequently, the model needs improvement for the size range ($D^* > 20$).

Towards finer D^* the impact of adhesion is increased as it diverges significantly from the abiotic curve. At a floc size comparable to the size of cohesive sediments ($d = 0.063$ mm) the critical Shields parameter is greater than 10 (for $A_{s,30} = 6.0 \text{ N/m}^2$). Based on this model, this indicates that for cohesive sediments which are often also composed of organic material a significant impact on their stability (besides the cohesive forces) could originate from adhesion. Still, the size range investigated in this study is non-cohesive and therefore this statement should be handled with great caution.

CASE B: Variation of bulk density

Figure E.12 shows the critical Shields parameter as a function of D^* (by variation of the floc diameter) and bulk density with a constant surface adhesion of 3.0 N/m^2 .

The critical Shields parameter increases with a decrease of the bulk density. The increases

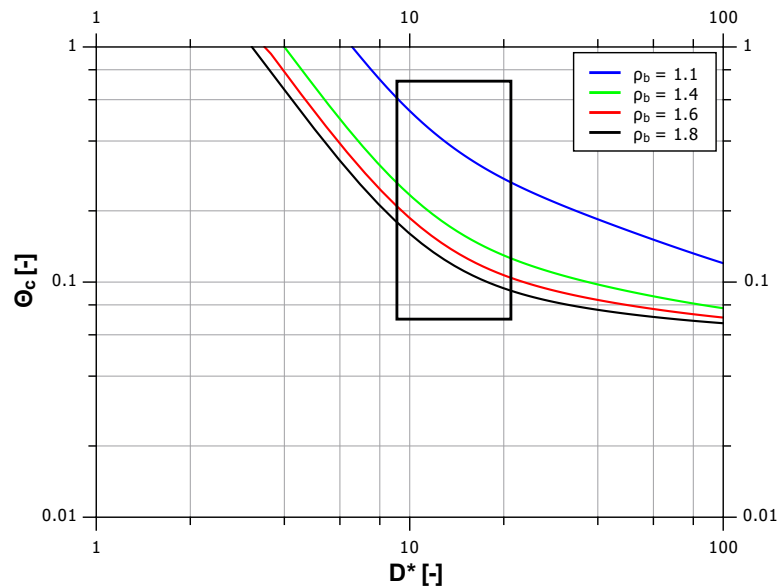


Figure E.12 The critical Shields parameter at different values of aggregate bulk density. The black box indicates the range of D^* corresponding to floc diameters between $D = 0.6 \dots 1.2$ mm. $A_{s,30} = \text{const.} = 3.0 \text{ N/m}^2$

of Θ_c is especially high when the bulk density approaches the density of water (see the blue curve: $\rho_b = 1.1 \text{ t/m}^3$, in other words, measurements on bulk density for flocs having a bulk density similar to water must be conducted extremely carefully, as they will affect the critical Shields parameter significantly.

The bulk densities measured in the Jul14 experiment are generally higher than 1.1 t/m^3 . Still, their impact on the critical Shields parameter suggests that accurate measurements of the bulk density are necessarily to be conducted in biostabilization research. At $D^* = 10$ the difference between a bulk density of 1.4 and 1.8 (which is similar to the measured range) is identical to the difference reported for the lowest and highest surface adhesion in Phase II ($\Delta\Theta_c = 0.07$). As these differences are in the same range (but with opposite impact) it may be hypothesized that the additional adhesion forces balance the losses in stability mediated by the reduced bulk density. Following this line of thought the additional stabilization effect due to adhesion can be regarded as the “net biostabilization”

CASE C: Variation of floc diameters

The model is most sensitive to changes of the floc diameter (the black box in Figures E.11 and E.12). As an example, at a surface adhesion of 3.0 N/m^2 and a bulk density of 1.4 t/m^3 the difference of the critical Shields parameter at $D = 0.5$ mm and $D = 1.2$ mm amounts to $\Delta\Theta_c = 0.19$. This value is more than 2 times greater than reported for the sensitivity of bulk density and surface adhesion. For smaller aggregates the difference even increases, while for larger it decreases.

E.4 Experimental limitations and recommendations for further research

For the first time, a mechanical model to predict the erosion threshold of biostabilized sediments is applied by also considering “real” measured surface adhesion forces. The results of this section provide a framework for further experiments by inclusion of material properties (such as the adhesion) in physics-based models. It is of no doubt that much more experimental work is needed on the way to a reliable model than has been presented here. The following limitations/uncertainties and future recommendations are important for achieving this goal and shall inform further research on biostabilization:

Limitations due to data scarcity

The most obvious limitation is the limited number of samples and the corresponding data on which the model relies. The analysis is based on 35 samples, while the regression in Phase II is based on a mere of 11 samples. This implies that the results must be treated with caution. The most important outcome of the conducted analysis is the recommendation for parameters which need to be measured and the limitation of applicability of the modified Shields equation. The limited data does not permit to restate the existing or even develop a more precise model on biostabilization. This is especially true as it has been demonstrated that natural biofilms are highly heterogeneous with strong effects on the erosion threshold (e.g. in Part B) and consequently much more data is needed to account for these heterogeneities.

Uncertainties in the determination of bulk density

It has been demonstrated that the bulk density is of equal importance as the adhesion. Measurements on bulk density are conducted with the help of a pycnometer at different ages of the biofilm and then a curve is fitted to calculate the bulk density for the missing measuring points. A decreasing floc bulk density over time indicates that the ratio volume of EPS to the volume of sediments increases.

Generally a reliable determination of bulk densities for biofilm-flocs is difficult and therefore many researchers have used Stokes law to estimate the density of flocs. For example, Droppo et al. (1997) used a settling column and analysis of data similar to the one used for this thesis to calculate the bulk density. Nevertheless, they also admit that the application of Stokes law is not ideal for this kind of evaluation primarily because of the obvious differences of floc geometries from impermeable spherical particles.

On the other hand the pycnometer analysis is also strongly affected by measuring uncertainties. Due to the necessary transfer of the fragile flocs to the device, the samples are easily destroyed. Furthermore, minor differences in weight (by e.g. evaporation of the wet surface

of flocs) may have a huge impact on the bulk density. Last but not least, different flocs may have completely different densities (e.g. surface flocs with lots of EPS vs. subsurface flocs with a higher volume of particles), consequently it makes sense to collect a number of flocs to determine an averaged density (as was done here). Figure E.8 also indicates a huge variability especially for the young biofilms. Consequently it is recommended to measure the bulk density in a huge number of replicates directly on the flocs that are eroded and used for floc analysis.

Limitations in the determination of floc geometries

Generally it is recommended to conduct the analysis of both bulk density and floc geometries as well as the measurement of the erosion threshold on the same samples as deviations of these parameters between different samples cannot be fully excluded. Furthermore, large flocs or “carpets” could not be investigated due to the geometry of the settling column. The latter might not be important for this study as in Part D it was already indicated that for carpet-like biofilms the chosen approach is not feasible. Moreover, for aggregate like erosion processes the results in Figures E.6 and E.7 show that the eroded floc diameter is well below the available width of the settling column and therefore the results are reliable. Still, the eroded floc diameter plays the most important role in the modified Shields equation and therefore the data acquisition in future experiments can be optimized.

Limitations in adhesion measurements

Adhesion is measured on the surface of the biofilms. Even though it is demonstrated that the effective adhesion and the measured surface adhesion is largely in the same order of magnitude and the differences between these two values can be plausibly explained, it is admitted that ideally the adhesion shall be measured over the whole depth of the biofilm as already suggested in Part D.

Uncertainties in erosion measurements

In the Jul14 experiment (as well as in all other experiments that were conducted before Jul14) the samples are placed in the SETEG flume such that the surface of the biofilm is on one level with the flume bed. The flume bed is made of glass and therefore not representing the roughness of the biofilm surface. Therefore, there is an abrupt transition between the smooth glass and the rough biofilm which may lead to unwanted perturbations influencing the erosion mechanism. Moreover, the flow over the sample to be eroded is not fully developed in terms of turbulence. Solving this issue means, that first the roughness of growing biofilms needs to be investigated to subsequently adopt the roughness to the flume bed which will be demonstrated in the following Part. Because a detailed investigation of the topography could only be conducted in the Jul14 experiment (at first a method needed to be developed for continuous monitoring of the topography), the implementation of a roughness in the SETEG flume could only be realized in the very last experiment (Mar15).

E.5 Concluding remarks

A physics-based model to predict biostabilization is applied that considers an effective adhesion between contiguous flocs as an additional stabilization mechanism. A conducted regression analysis in which the calculated effective adhesion is related to “real” measured surface adhesion yields a reasonably good correlation coefficient ($R^2 = 0.68$) for young biofilms. For mechanically matured biofilms (Phase III) and for a combination of both the regression indicates that the model is unable to predict biostabilization from real measurements. As already suggested in the previous part, matured biofilms (Phase III) may be structurally different from young biofilms in that they erode as a coherent mat - a mechanism that is not considered in the modified Shields equation. Because the surface adhesion values fluctuate around a mean value it is further expected that adhesion forces might not play an important role in the stabilization mechanism of these mats as they cannot explain the differences in erosion thresholds. This is well in line with the model proposed by (Vignaga et al., 2013) which relates primarily the horizontal length scale of oscillating biofilms to their stability (see also Part A) and no binding mechanisms.

Figure E.13 illustrates the correlation between measured and predicted critical shear stress by application of the linear regression between A_{eff} and $A_{s,30}$ (Equation E.9).

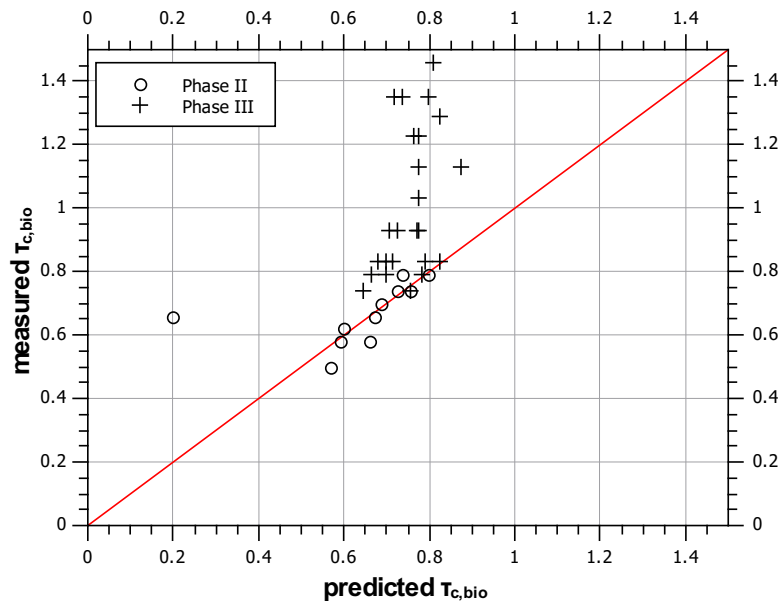


Figure E.13 Graph comparing the measured and predicted erosion threshold by using the parameterization of the modified Shields equation based on the measured surface adhesion values. The symbols indicate the experimental data from Phases II and III. Data which is below the red line are overestimated by the model and data above the red line is underestimated.

Not surprisingly, all except of one (most probably due to an erroneous measurement) erosion thresholds of Phase II-biofilms are predictable. It is striking that nearly all values of Phase-III biofilms are located above the predicted curve (the red line). This is interesting as

it means that the predicted critical shear stress from data of Phase II may be regarded as a lower boundary threshold for Phase III biofilms.

The application of physics-based models in biostabilization research is still in its infancy and the model proposed by Righetti and Lucarelli (2007) possibly needs further improvements. The first remark is related to the consideration of cohesion forces in that model. In the evaluation of their results Righetti and Lucarelli (2007) and Righetti and Lucarelli (2010) neglected the cohesion forces as they showed that their impact was much less than the impact of adhesion forces. However, they only investigated the cohesion between the sediments that are found in the aggregates but not the cohesion between EPS-EPS, which might also impact the binding between aggregates. As long as it is not clarified where the aggregates break apart in the event of erosion (between sediment-EPS, EPS-EPS or both) it is suggested to include an additional term for this cohesive effect.

The second remark concerns the effective adhesion or adhesion coefficient (after Righetti & Lucarelli, 2007). This parameter describes the “mechanical contribution to floc stability due to the production of biologically-mediated linkages between contiguous flocs” (Righetti & Lucarelli, 2010). In fact the effective adhesion can be low even though the measured adhesion is high. This would be the case when for example a highly adhesive EPS binds two aggregates together but only over a small area. These two aggregates could still be separated easily from each other. While the same effect would be achieved if a low adhesive EPS covers the whole surface of the aggregate (i.e. has a large area of contact). The effective adhesion could thus be refined as the product of the material property and the fraction of the surface area covered by a biofilm (e.g. α_A in [–], following the notation of Chen et al., 2005). Even though introducing another unknown into the modified Shields equation seems not to be very appealing, it might help in further elucidating the role of the physically measured adhesion forces in biostabilization.

To improve the model it is further useful to learn more about the eroded floc geometries. Firstly, in this study and in the studies of Righetti and Lucarelli (2007, 2010) it is assumed that the eroded flocs are nearly spherical (particle shape factor $\alpha_3 = \pi/6$) which is hardly the case for biostabilized sediments. Secondly, the characteristic aggregate diameter seems to play the most important role in the model (compared to the bulk density and adhesion), still its definition is not clear. The specific problem is that the sizes of eroded aggregates are widely distributed such that a deeper analysis of floc geometries seems very useful to define a diameter that is characteristic for the erosion threshold. It would be certainly interesting to link the measured adhesion forces to floc geometries as these forces are partly responsible for the aggregation processes of flocs.

A last aspect concerns the lift forces due to bubble entrainment which have not been in the

focus of this study. Biofilms may produce gas bubbles as e.g. a product of photosynthesis (see Part B). These gas bubbles may be located on top or below the surface creating an additional lifting force. Only very few studies have investigated the effect of these bubbles on stability (e.g. Mendoza-Lera et al., 2015; Sutherland et al., 1998). Amos et al. (2003) proposed to include the lift force per unit area (F_1) by addition to the surface bed strength in their experiments. However, according to the observations made during the erosion process bubble entrainment mostly affected Phase-III biofilms (see Table E.1) and therefore this effect hardly influenced the results in this part.

Figure E.14 is a conceptual model summarizing the most important mechanical impacts on biostabilization based on the findings of this thesis and the literature review.

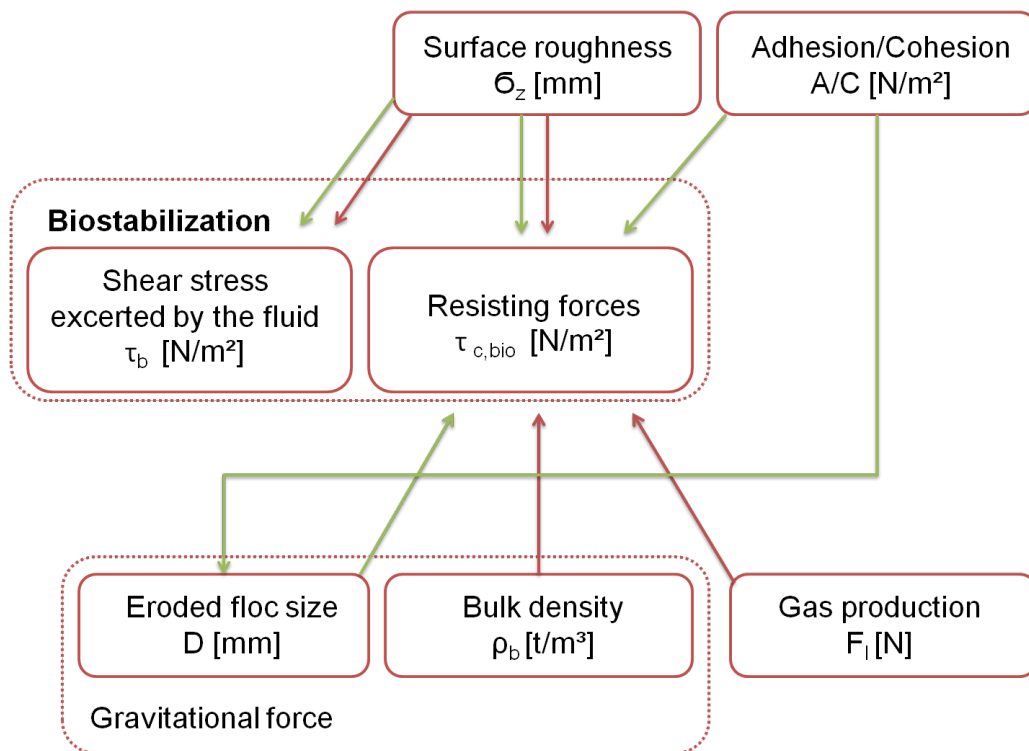


Figure E.14 Conceptual model of the most important mechanical impacts on biostabilization. Green arrows indicate an expected positive (increasing) impact on the stability (when the value of the parameter is increased) compared to sediments without biofilm, red arrows indicate an expected negative (decreasing) impact.

The surface roughness changes mediated by the growth of a biofilm may have an increasing or decreasing effect on both the fluid force (either the surface is roughened or smoothed, depending on the abiotic sediment size) and on the resisting forces of the biofilm-sediment matrix (either parts are exposed to the fluid or not). Knowledge on the surface roughness is further important for modifying the erosion flume in such way that there is a smooth transition between the flume bed and the biofilm. These aspects will be discussed in more detail in the final part.

Part F

CONTINUOUS SURVEY OF BIOFILM TOPOGRAPHY

Parts of the following section are from Thom et al. (2014)

A growing biofilm may change the roughness of sediments significantly which is of particular interest to this study as the roughness influences the bed shear stress, and thereby also impacts the erosion threshold. Specifically, in this study the information on biofilm topography is used to modify the inlet flow section of the straight erosion flume to account for biofilm roughness. Moreover, the change in surface roughness is monitored over time and quantitative values are given. It is pointed out that the traditional ways of roughness characterization, for example by determination of a characteristic grain diameter D_{50} or D_{84} is not applicable for biofilms as the surface topography is no longer shaped by sediments, but may be better described as a “microbial landscape” (Battin et al., 2007) with distinctive features like elevations, valleys, forests and crusts on a small scale (see also qualitative contour lines in Figure F.1).

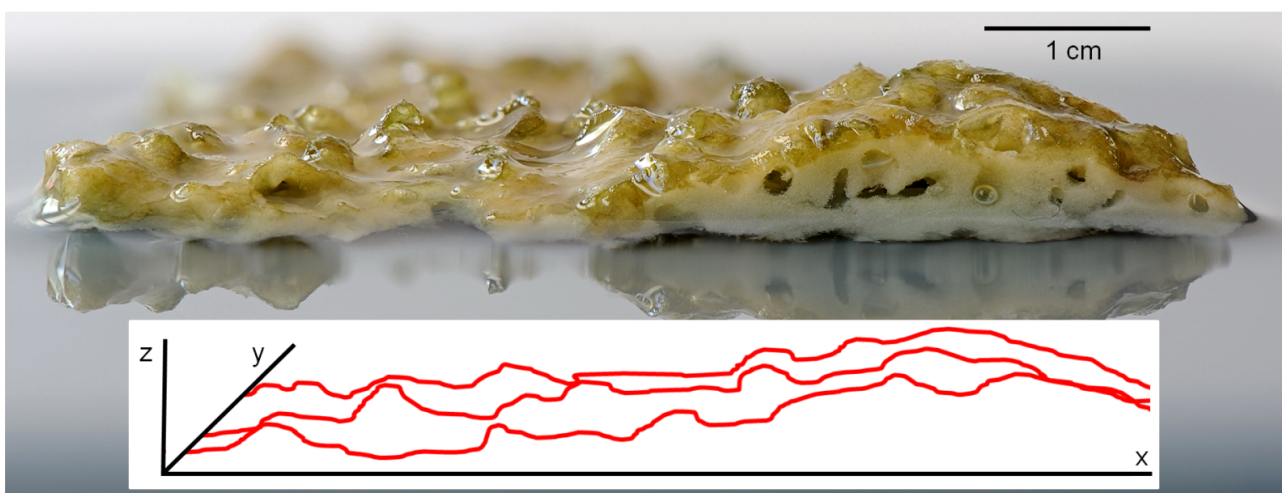


Figure F.1 Side view image of a biofilm from one of the experiments (photograph by Bojan Skodic). Contour lines (red) represent the biofilm topography qualitatively.

Moreover, nutrient availability (and thus growth) is influenced by the hydraulic conditions near the surface of the biofilm, which in turn are depending on the roughness characteristics of the investigated topography shaping the boundary layer flows (Nikora, 2010). In order to understand the mechanisms that form these landscapes a reliable method to measure topography is needed.

By adapting and modifying a method commonly used in terrestrial surveys (laser triangulation) investigations on biofilm topography are carried out. The special challenge in this study is that topographical changes need to be monitored over time to characterize the growth and roughness of young developing biofilms. To obtain unbiased results, the surveys are conducted on submerged biofilms as a desiccation could result in unwanted changes of the topography. Yet another requirement is that biofilm topography must be measured at a high resolution to monitor even slight changes of topography (both spatial and temporal).

Additionally, two methods are proposed for further research on biofilm topography to 1) analyze the spatial distribution of roughness elements and 2) to monitor submerged biofilm topography over larger areas.

F.1 Setup for topographical measurements and calibration

To measure the topographical development of biofilm grown under different abiotic conditions a method based on laser triangulation is developed. In this section the setup of the measuring device is described along with information on post-processing of data and a calibration procedure to account for the effects of underwater measurements.

The setup

The topography scanner (see Figure F.2 *Left*) consists of a laser triangulation distance sensor (Pepperl + Fuchs VDM18-300/32/105/122, Germany; with a vertical resolution of 0.2 mm) mounted on a traverse (ISEL, Germany). The traverse provides high resolution horizontal (X and Y) movement of the sensor while its height is fixed. Consequently, only vertical distances to the (biofilm-) surface are measured (2.5D). This means that topographical features only visible from an angle cannot be detected. The movement of the traverse and the distance measurements are synchronized by a microcontroller (Arduino Mega) which also transforms the analog output of the sensor to digital values.

The basic principle of laser scanning is based on triangulation. A laser spot is projected on the surface and a sensor (detector) monitors the position of the laser spot (see Figure F.3). The position of the laser spot on the sensor can then be transformed into a height via calibration.

The development of biofilm topography is surveyed by removing the cartridges from the

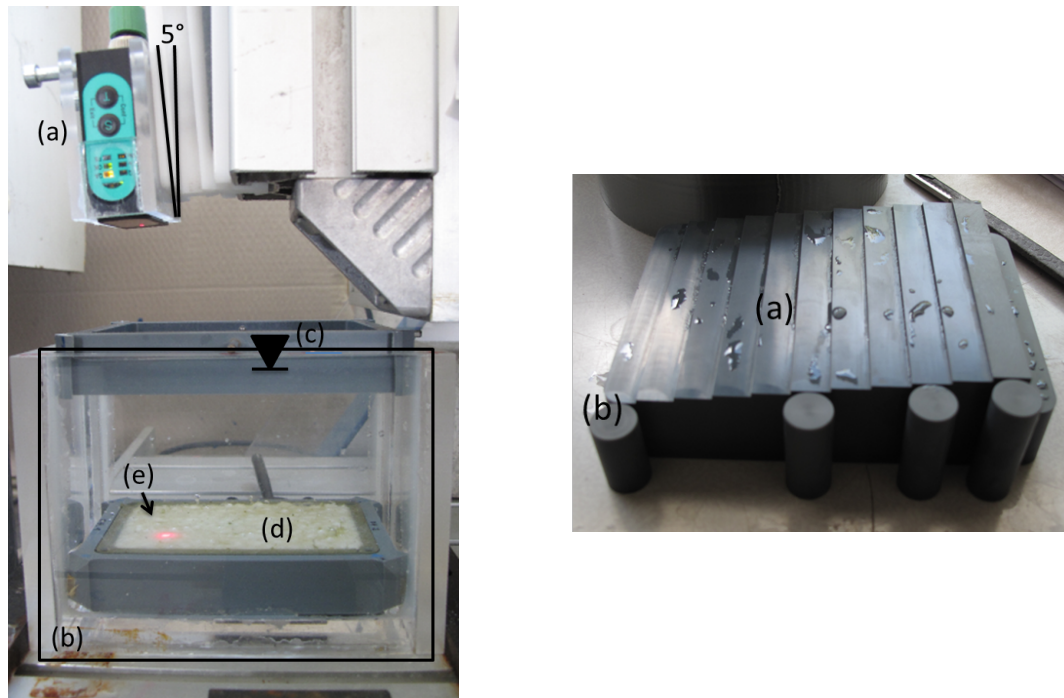


Figure F.2 The developed measuring device for surveillance of submerged biofilm topography and an exactly milled stairway for calibration. *Left*: Side view of the setup for measuring topography. (a) sensor (b) water filled tank (c) frame with glass plate and direct contact to the water surface (d) cartridge containing biofilm sample (e) laser spot. *Right*: Tools used for underwater calibration (a) PVC milled stairway (b) PVC rods, both with defined heights.

flumes and placing them into a small water-filled (clear tap water) tank at a fixed position (see Figure F.2 *Left*). This tank is then placed below the sensor of the scanner. Minor changes of water depth (e.g. by surface waves) produce considerable deviations from the real topography (due to optical refractions, see next page). To fix this problem a frame with a glass plate, is placed in direct contact with the water surface.

The size of the projected laser spot determines the minimal horizontal resolution. In a feasibility study Thesenvitz (2014) investigated (amongst others) the resolution and the impacts of transparency. It is shown that the sensor can detect semi- or non-transparent media, which makes the method largely suitable for biofilm research, but may in some cases also result in inaccuracies (e.g. with transparent filaments lying flat on the surface, see also Barton et al., 2010). For example, objects or elevations which are smaller than half the spot size (here: $0.5 \times d_{spot,min} = 0.75 \text{ mm}$) may not be detected accurately (Löffler-Mang, 2012). If the projected laserspot is on different heights at the same time, the sensor reports the height of the object where the largest part of the laser spot is projected on (revealed by measurements on a PVC stairway, see Figure F.2 *Right*).

This is an important aspect as biofilm surfaces are highly heterogeneous even on the microscale. Still, for the purpose of investigating the impact of biofilm roughness on hydraulics the method provides reasonable results (Thesenvitz, 2014). The total number of measurements is 115 measuring points in x direction and 89 in y direction yielding a total of 10235 measurements on a biofilm surface of the size $A = 88 \times 58 \text{ mm}^2$ (i.e. the size of 1 cartridge).

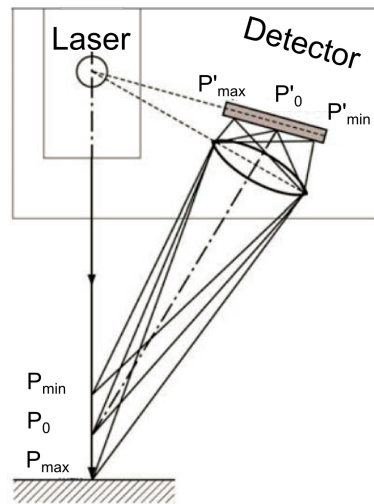


Figure F.3 The basic principle of laser triangulation modified after Löffler-Mang (2012). A laser spot is projected on a surface at different heights (P_{min} , P_0 , P_{max} , where P_{min} , P_{max} is the working range of the sensor). A sensor determines the position of the reflected laser on a detector (P'_{min} , P'_0 , P'_{max}). Knowing the relative positions of the laser and the detector and after conducting a calibration the exact height of the surface can be calculated via triangulation.

Postprocessing of data from under water measurements

In the system two major uncertainties are identified which are related to under water measurements: 1) the recommended two point calibration and linear interpolation may result in errors due to the optical properties of the different phases (diffraction between air-glass-water). An underwater calibration procedure is described below. And 2) in an idealized setup the horizontal movement of the sensor is parallel to the glass plate and parallel to the surface where the measurements are taken. In the presented setup, where measurements are taken on a sub millimeter scale, this requirement cannot be fulfilled. For example a skewness of the cartridge due to its construction or due to sediment grains trapped below one edge is very likely. To address these two problems the raw data is processed in two steps. In the first step the skewness is identified and the data is transformed to a horizontal reference level. In the second step the transformed values are related to heights by calibration.

Transformation

The surface of the cartridge walls should be perfectly horizontal. A measured skewness of these walls is corrected by performing a linear axis transformation. This results in a horizontal reference level equivalent to the initial biofilm-free surface because the sediment which exceeded the height of the cartridges is removed prior to the experiments.

Calibration

While the minimum and maximum height is defined by the initial two point calibration of the sensor, it remains unclear whether the recommended linear calibration applies for all interjacent heights. A CNC milled PVC stairway (see Figure F.2 *Right*, with a tolerance of

0.01 mm) with 1 mm steps is used for calibration.

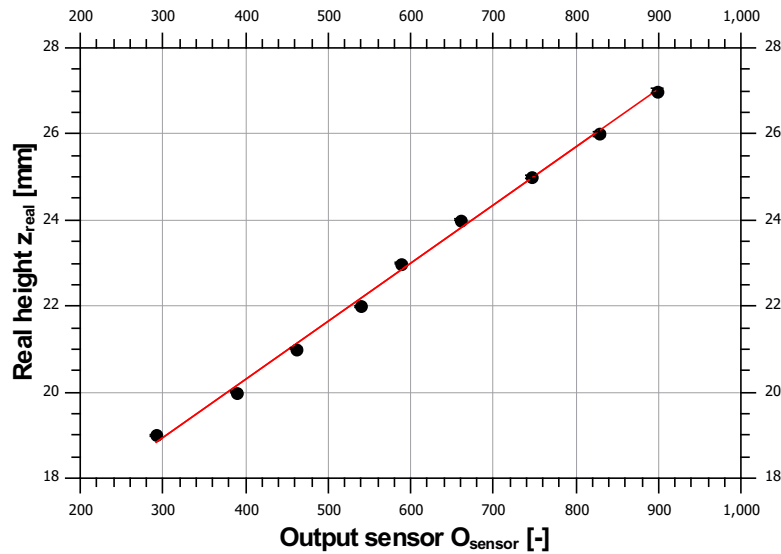


Figure F.4 Graph comparing the real heights of the submerged milled stairway with the digital output of the laser triangulation sensor. The linear regression ($R^2 = 0.9972$, $SD < 0.05$ mm) is used to calibrate the device to measure the underwater topography of growing biofilms.

After axis transformation the measured heights are compared to the real heights yielding a linear calibration equation by curve fitting ($R^2 = 0.9972$, see Figure F.4 and Equation F.1) with a maximum deviation of ≈ 0.2 mm from the actual height. Equations of higher order further reduce the deviation. In addition, a low standard deviation of three independent measurements ($SD < 0.05$ mm) confirms that the setup is applicable for high resolution measurements under water. The linear regression equation is as follows ($R^2 = 0.9972$):

$$z_{real} = 0.0135 \cdot O_{sensor} + 14.895 \quad (F.1)$$

with z_{real} the known heights of the milled stairway and O_{sensor} the digital output of the sensor.

F.1.1 The experimental program of biofilm topography measurements

Detailed topographical measurements are conducted in the experiment Jul14. Measurements are conducted each week on one and the same cartridge for 9 weeks. That way biofilm growth is monitored in 4 flumes (Jul14QLA, Jul14QLC, Jul14QHC and Jul14QHA). The experimental boundary conditions can be found in table D.2. Briefly two different flow velocities are applied: low and high. Even though all elevations are in the vertical measuring range of the sensor, the laser scanner was not able to detect all elevations at later stages of biofilm development probably due to a bad contrast between the laser spot and the brown biofilm surface. This results in a reduction of data up to 40 % in the Jul14QHC experiment. In contrast Jul14QHA is not affected at all. All results with data reduced by more than 15% are marked with an asterisk (*) and should therefore be treated with caution (for more details

please see Table F.1).

F.2 Evaluation of the temporal changes of biofilm topography

Growth patterns

The elevations at distinct spots are best visualized by a digital elevation model (DEM). Figure F.5 illustrates the development of the DEMs of two representative flumes (Jul14QLC, Jul14QHA). As a reference level (i.e. $z = 0$ mm) the height of the cartridge walls is chosen as this height represents the surface of the initial abiotic sediment.

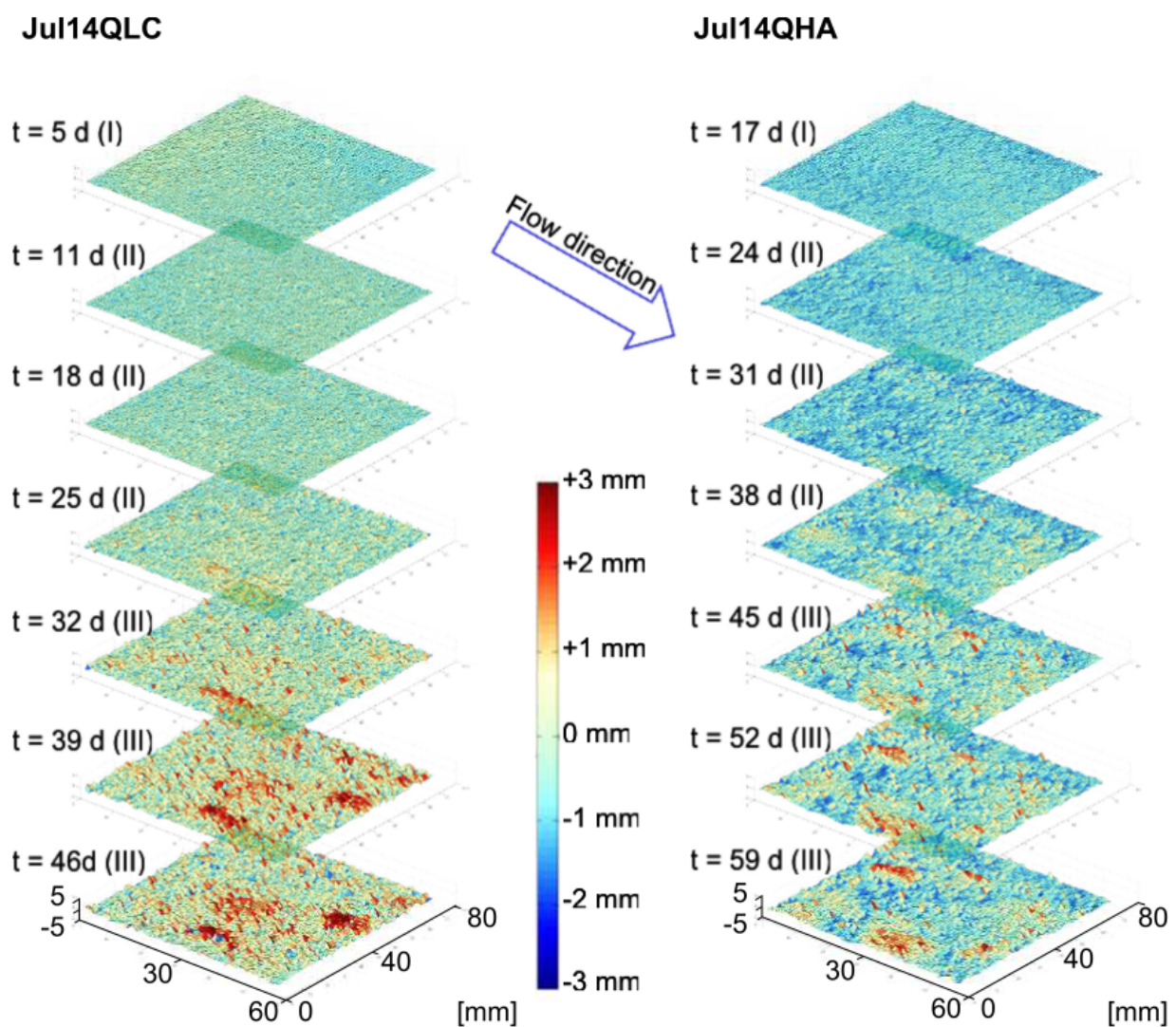


Figure F.5 Development of biofilm topography over time of growth in Jul14QLC (*Left*) and Jul14QHA (*Right*). Only topographies with minor deviations from the achievable total point densities (i.e. $< 15\%$) are illustrated. Roman numerals in brackets denote the phase at the respective age of the biofilm (as defined in Part D) and t is the time of growth at which the respective measurements were conducted.

Therefore, the DEMs at early stages of biofilm development should start at $z \approx 0$ (see Figure F.5 *Left*: JUL14QLC). In contrast, Figure F.5 *Right* (Jul14QLA) illustrates that the surface at

start of the measurements is lower which is explained by an initial handling error resulting in an erosion of the upper 0.77 mm of the whole surface.

Still, a similar trend is observed for both developments and all other measurements, irrespective of the applied boundary conditions: First variations of the initially smooth surface (i.e. the glass beads) are visible after 3 to 4 weeks, which very roughly corresponds to the shift from phase I to phase II mentioned in Section D and indicated by the roman numerals in brackets. The differences in elevations are nearly homogeneously distributed. After 1 month (Jul14QLC) or 5 weeks (Jul14QHA) smaller areas of concentrated height increases are visible. For example at day 32 in the lower corner (Jul14QLC) where the surface is elevated to approximately 3 mm. Interestingly these spots further grow in height while the rest of the surface remains largely unaffected. The surface topography can thus be regarded as heterogeneous. This development is also well in line with the mechanical maturity of biofilms (phase III). Table F.1 summarizes the results.

Statistics

To characterize biofilm growth quantitatively, the averaged elevations (\bar{z} as a proxy for growth) as well as the standard deviations of elevations (σ_z as a proxy for surface roughness) are analyzed (see Table F.1). Further statistical moments (skewness, kurtosis) are also analyzed and demonstrate that the data is almost normally distributed ($2.74 < Ku < 5.44$ (slightly peaked), $-0.55 < Sk < 0.79$).

Statistical moments have been used in a number of studies to characterize bedforms (e.g. Aberle et al., 2010) and roughness (e.g. Nikora et al., 1998). Aberle and Nikora (2006) demonstrated that σ_z is equivalently useful as a roughness descriptor as the traditional approaches. Other papers even demonstrate a superiority over the traditional approaches (summarized in Aberle & Nikora, 2006). For the evaluation of biofilm topography both \bar{z} and σ_z are especially useful parameters to characterize growth and roughness development.

Figure F.6 illustrates the development of roughness and averaged bed elevations over time. Both, \bar{z} and σ_z follow a clear trend: In the first 2 to 3 weeks, the bed remains unaffected. Then, simultaneously, both, mean elevation and roughness increase. In the coming ≈ 20 days the mean bed elevation increases by approximately 1...1.5 mm while the roughness increases by 0.6...1.2 mm. This is followed by a phase of no further increases. Mean bed elevation as well as roughness is stable over time indicating that biofilm growth has hit the limit. In principle, the surface topography changes follow a similar development as already evaluated for the surface adhesion forces and the erosion threshold.

Table F.1 Details of the topographical survey of four biofilm surfaces in Jul14. Deviation from total count - the percentage of measurements which are defective (* denotes measurements with more than 15% deviation). \bar{z} - the average height of elevations (the reference level ($z = 0$) is the abiotic sediment surface). σ_z - standard deviation of bed elevations as a proxy for biofilm roughness. K_u - Kurtosis. S_k - skewness.

ID	Time of Growth	deviation from total count	\bar{z}	σ_z	Kurtosis K_u	Skewness S_k	
[-]	[d]	[%]	[mm]	[mm]	[-]	[-]	
Jul14QLA	4		-0.39	0.26	5.43	0.33	
	11	0.7	-0.28	0.28	4.05	-0.44	
	18	0.6	-0.27	0.34	4.15	-0.10	
	25	0.5	-0.08	0.46	4.32	0.42	
	32	0.9	0.41	0.78	3.44	0.55	
	39	7.5	0.75	0.98	2.93	0.41	
	*	46	23.6	1.01	1.19	2.95	0.43
*	53	34.1	1.05	1.26	3.34	0.60	
*	59	36.4	1.01	1.22	3.00	0.44	
Jul14QLC	5		-0.35	0.28	4.16	0.18	
	11	0.6	-0.34	0.22	5.44	-0.55	
	18	0.6	-0.33	0.29	4.47	-0.15	
	25	0.6	-0.17	0.45	4.41	0.39	
	32	0.4	0.02	0.62	4.39	0.63	
	39	2.6	0.37	0.81	3.58	0.62	
	46	8.7	0.30	0.86	3.49	0.53	
	*	53	17.2	0.41	0.85	3.41	0.44
*	60	20.6	0.40	0.86	3.44	0.40	
Jul14QHC	4		-0.13	0.29	4.57	0.52	
	12	0.7	-0.21	0.26	4.47	0.20	
	19	0.6	-0.07	0.35	4.24	0.41	
	24	0.1	-0.06	0.56	3.67	0.53	
	31	3.2	0.25	0.79	3.18	0.38	
	*	38	22.2	0.47	0.91	3.25	0.20
	*	45	28.8	0.70	0.94	3.13	0.08
	*	52	34.0	0.62	1.02	3.29	0.10
*	60	39.6	0.84	1.06	3.25	0.09	
Jul14QHA	3		-0.77	0.18	4.95	0.17	
	10	0.2	-0.88	0.24	2.74	-0.10	
	17	0.2	-0.83	0.24	2.83	0.01	
	24	0.4	-0.84	0.29	2.89	-0.10	
	31	1.6	-0.87	0.42	3.45	0.30	
	38	2.0	-0.64	0.53	3.59	0.54	
	45	3.8	-0.45	0.67	4.01	0.78	
	52	5.4	-0.40	0.76	3.81	0.77	
	59	4.6	-0.35	0.81	3.66	0.79	

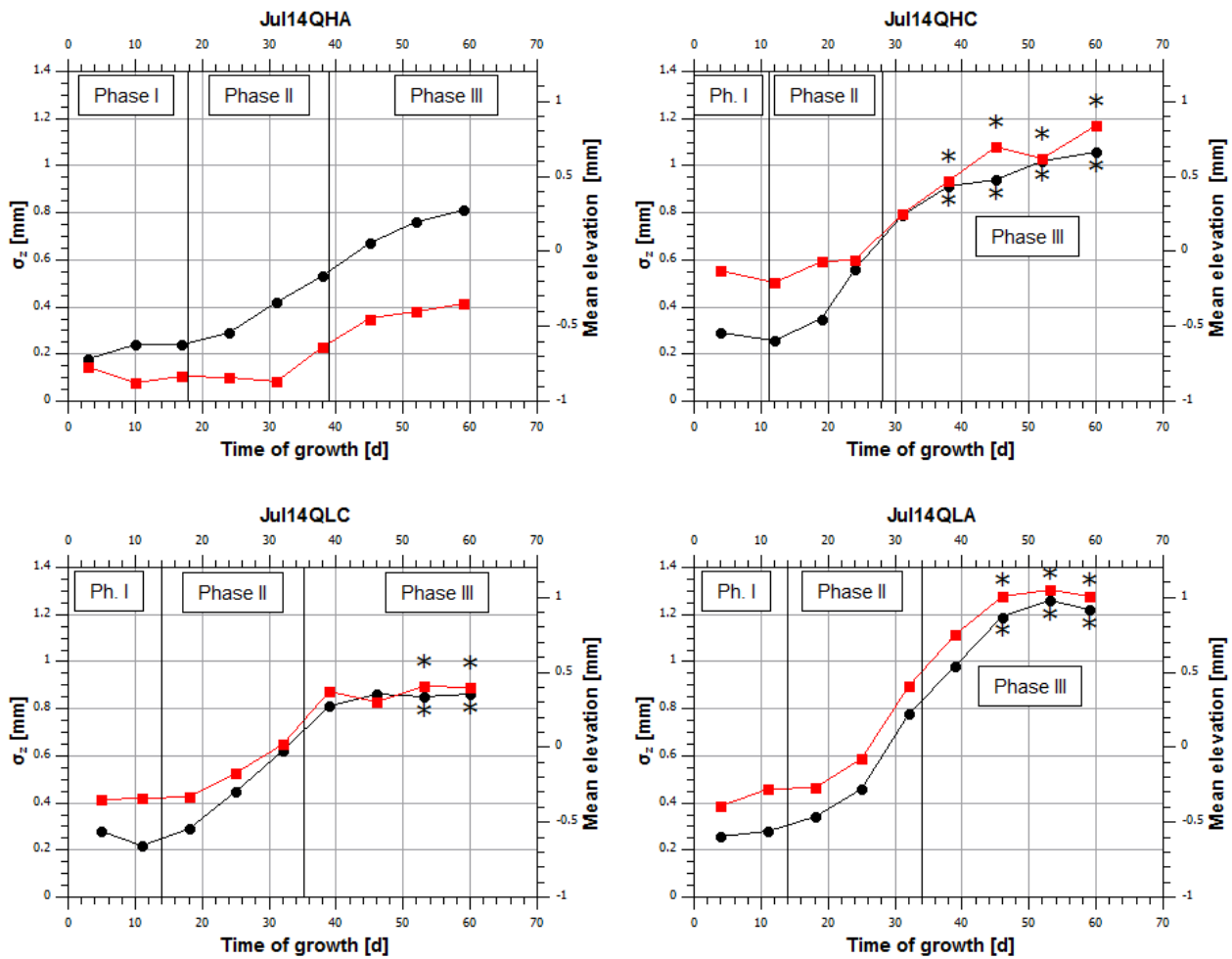


Figure F.6 Mean elevation and standard deviation of four different biofilm DEMs over time of growth. The ● symbols: standard deviation in z direction. The ■ symbols: mean elevation (values on the second vertical axis). The * labels denote results with more than 15 % defective measurements. The subdivision into the three phases is based on the evaluation of surface adhesion forces (from Part D) and is similar to the development of \bar{z} and σ_z .

Averaged over all biofilms (also including information from the *-data), the increase in growth (\bar{z}) is 0.86 mm and the increase in roughness (σ_z) is 0.74 mm (corresponding to an averaged factor of 4 between the initial surface and the matured biofilm surface). No considerable trends can be reported relating the topographical development to the applied environmental boundary conditions (low and high flow velocity), as such it is suggested that the differences in flow velocity are too low to impact the biofilm topography.

It is noteworthy, that even though σ_z is a reasonable integral measure of bed-roughness height, it contains no information about the spatial distribution of roughness elements (a potentially useful approach for consideration of the spatial distribution is presented in Section F.4). The data collected here is useful for adapting the bed of the erosion flume with elements that are of similar roughness.

F.3 Modified roughness in the erosion flume

For the purpose of implementing a uniform roughness in the inlet section of the erosion flume that represents the roughness of the biofilm to be eroded, sandpapers of different grit sizes are surveyed following the procedure described above. Table F.2 summarizes the results and gives a recommendation on what sandpaper to be used to represent biofilm at different ages. It must be noted, that these recommendations arise from the measurements conducted in this study. Depending on the initial roughness, biofilm growth might also result in a smoother surface, as was for example demonstrated by Barton et al. (2010).

Table F.2 Sandpaper with different grit sizes to represent biofilm roughness.

ISO/FEPA Grit designation [–]	σ_z [mm]	Equivalent to biofilm roughness measured in weeks [weeks]
P120	0.41	2 ... 3
P60	0.60	3 ... 4
P40	0.94	> 5
P30	0.96	> 5

The erosion flume is modified in the very last experiment (Mar15*). In this experiment only matured biofilms are investigated, therefore sandpaper P40 is selected and glued to a metal plate (with a length of 1.3 m) with a hole at the end, which is then fitted into the flume such that the biofilm sample can be raised on one level with the flume bed (see Figure F.7).

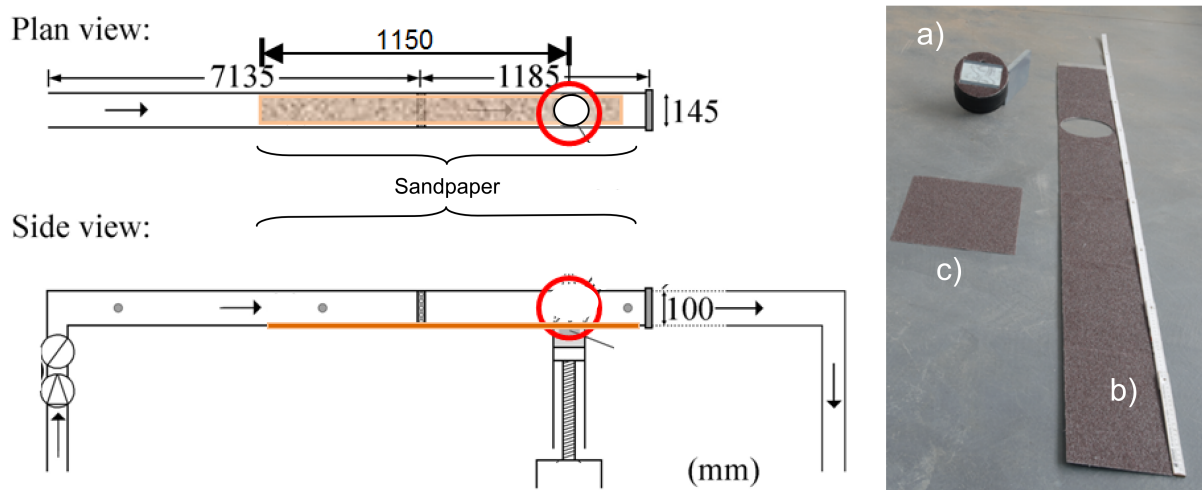


Figure F.7 Implementation of a sandpaper roughness in the erosion flume to adapt the inlet section with a biofilm similar roughness. *Left:* The red circles are the position of the biofilm sample to be eroded. *Right:* a) the roughness of the adapter for biofilm-sediment cartridges is modified with the same sandpaper which is b) glued to a metal plate and inserted into the erosion flume. c) a piece of sandpaper P40.

As a consequence of this modification, the original calibration curve (discharge Q versus bed shear stress τ_b) for the smooth flume bed needed to be updated to account for the changes in τ_b mediated by the increased roughness. Consequently, Laser Doppler Anemometry (LDA) measurements are conducted to investigate the new relationship between Q and τ_b . Averaging the shear stress (after Reynolds decomposition) in the bottom 20 mm for discharges between $4^{1/s}$ and $16^{1/s}$ yields a factor of ≈ 1.5 higher bed shear stress as compared to the smooth bed calibration curve.

Even though, this modification is especially useful in the context of erosion measurements, the erosion threshold of the MAR15 experiment is no longer comparable to the other experimental results, for two reasons: 1) While it would be theoretically conceivable to scale up the erosion thresholds from previous experiments and for matured biofilms by a factor derived from roughness investigations as mentioned above, no information on the impact of the roughness changes on τ_b is available for growing biofilms, 2) eliminating the unwanted perturbations mentioned above and establishing fully turbulent conditions certainly has an impact on the erodibility, which unfortunately could not be quantified. Consequently, the erosion thresholds of Mar15* have been discussed separately in this thesis.

F.3.1 Comparison of hydraulics between a smooth and a sandpaper bed

To quantify the impact of adapted roughness, LDA measurements (velocity in flow direction u and Reynolds stress) are conducted at the center of the sediment core at different heights above the bed (the red circle in Figure F.7). Additional measurements are conducted off-center to account for possible deviations (e.g. due to random edge effects) but confirmed the results of center measurements. Figure F.8 and Figure F.9 show the velocity (in flow direction) and shear stress profiles at different discharges and over depth. The red lines and symbols represent the results over the smooth and the black lines and symbols over the rough (modified) surface.

As expected, the velocity in the near-bed region is higher (\approx factor 1...2) for the smooth surface as compared to the rough surface. The opposite applies for the shear stress in Figure F.9. Due to the rough surface, turbulence is enhanced close to the bed and consequently also the shear stress is increased. The resulting shear stress is calculated as:

$$\tau = -\rho \overline{u'_s \cdot v'_n} \quad (\text{F.2})$$

where, $\overline{u'_s}$ and $\overline{v'_n}$ are the time averaged velocity fluctuations (after Reynolds decomposition, in longitudinal and normal directions) from the mean velocity multiplied with the fluid density ρ . To calculate the bed shear stress (τ_b) the shear stress τ in the lower centimeters is averaged (where the τ is nearly constant over depth).

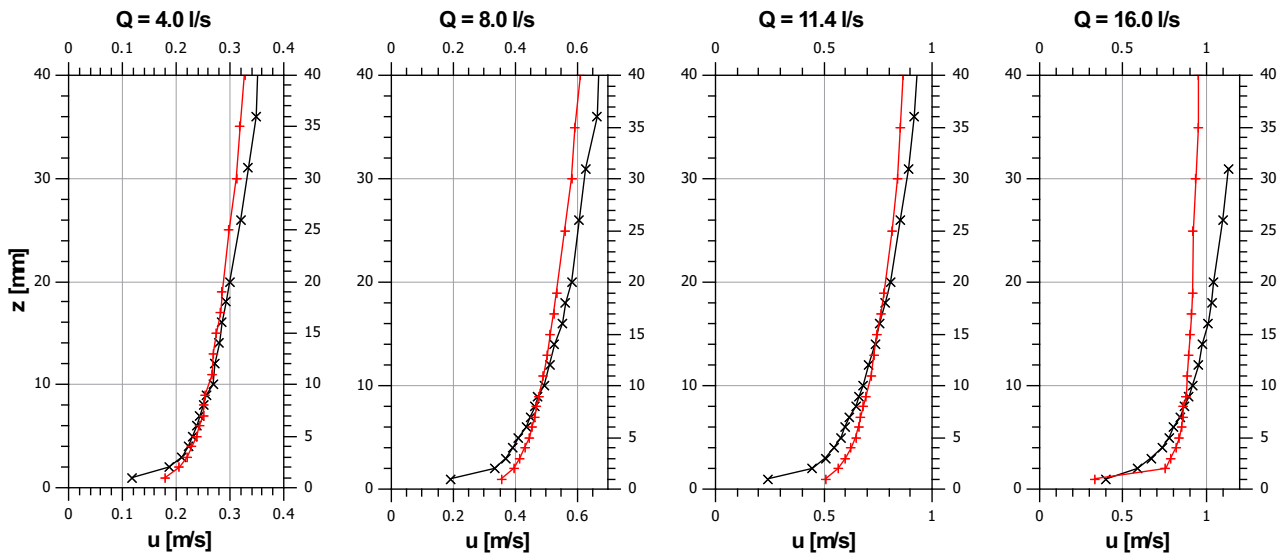


Figure F.8 Velocity distribution in flow direction over depth in the erosion flume (reference level is the bottom of the flume $z = 0$) at different discharges. The Symbols: “+” indicate the results of the smooth initial bed and the “x” symbols are the results of the modified (rough sandpaper) bed. Please note the different scaling on the horizontal axis.

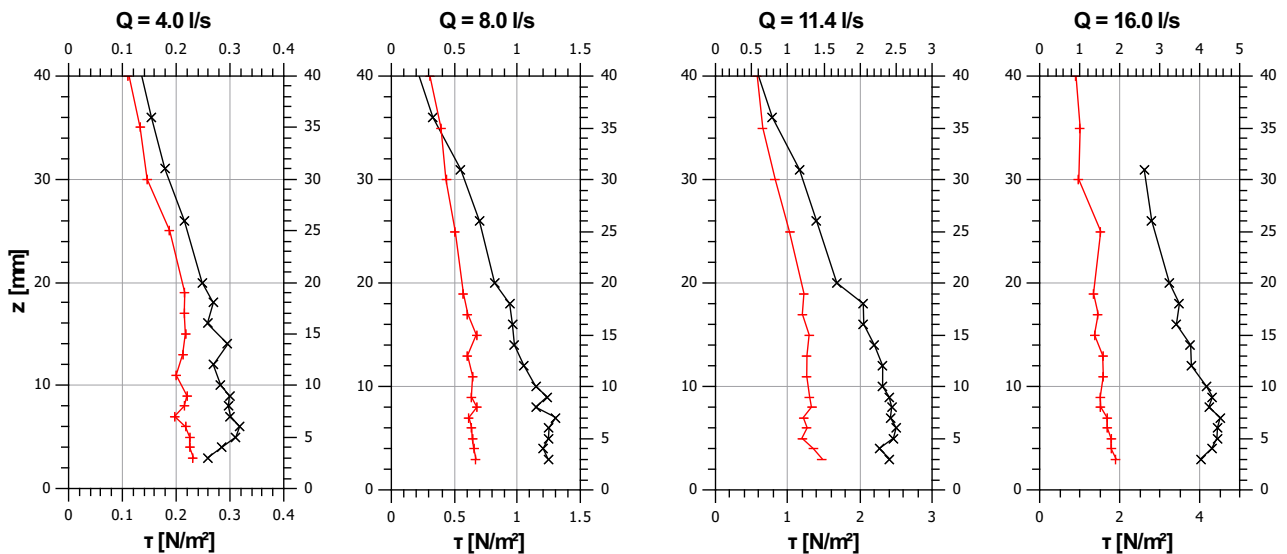


Figure F.9 Shear stress distribution in flow direction over depth in the erosion flume (reference level is the bottom of the flume $z = 0$) at different discharges. The Symbols: “+” indicate the results of the smooth initial bed and the “x” symbols are the results of the modified (rough sandpaper) bed. Please note the different scaling on the horizontal axis.

Figure F.10 provides the original as well as the updated (sandpaper) calibration curve for the erosion flume for discharges between 4.0 and 16.0 l/s. The effects of the roughened surface are clearly visible. Compared to the original calibration the bed shear stress is increased by a factor of 1.5.

Even though the measurements are not conducted over a biofilm surface but over the rough

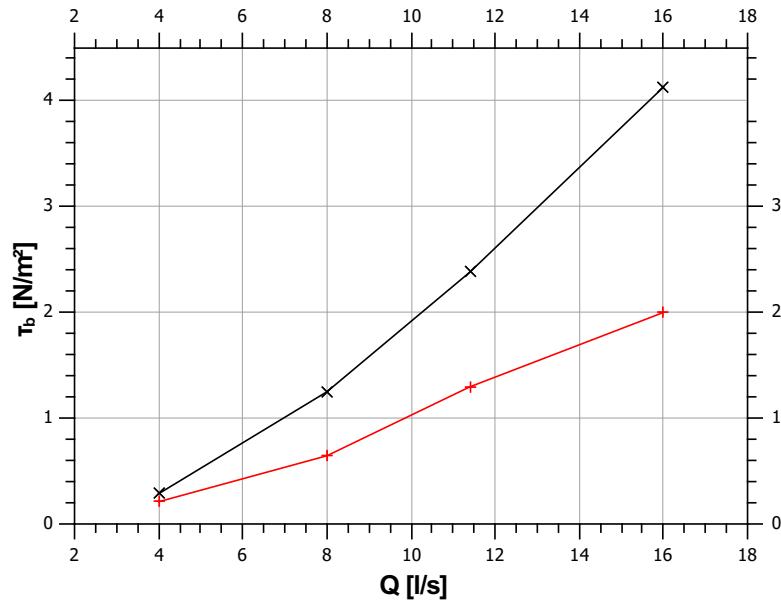


Figure F.10 Updated and original calibration curve (Q versus τ_b) for the erosion flume over a rough and a smooth bed. The Symbols: “+” indicate the results from the smooth initial bed and the “x” symbols are the results from the modified (rough sandpaper) bed.

surface of a sandpaper of equivalent roughness the results indicate a significant impact on bed shear stress that should be considered in future studies. A drawback of this method is that it does not account for the spatial distribution of roughness elements. In contrast to a natural biofilm the roughness elements of the sandpaper are homogeneously distributed over the surface. Furthermore, the presented procedure is very time consuming¹. Consequently, in the following section two methods are presented that have been tested and are found to be promising approaches for further research.

F.4 Proposed further investigations on biofilm roughness

Second order structure function

The topography of biofilm surfaces is heterogeneous. As shown above, the roughness elements develop on distinct spots. A comparison between a sandpaper surface and a natural (age: 45 days) biofilm topography, as illustrated in Figure F.11 underlines this finding. Both surfaces have the same $\sigma_z = 0.94$ but the difference in their appearance are striking.

Table F.3 presents the results of a simple statistical analysis, where all elevations, independent from their spatial position in the DEM, are analyzed.

Both datasets (biofilm and sandpaper) show a skewness close to zero and a kurtosis close to three, i.e. both distributions of elevations are nearly symmetrical and normally peaked (see also Figure F.12).

¹One measurement over an area of $\approx 51 \text{ cm}^2$ (one biofilm sample) takes approximately 4.5 hours

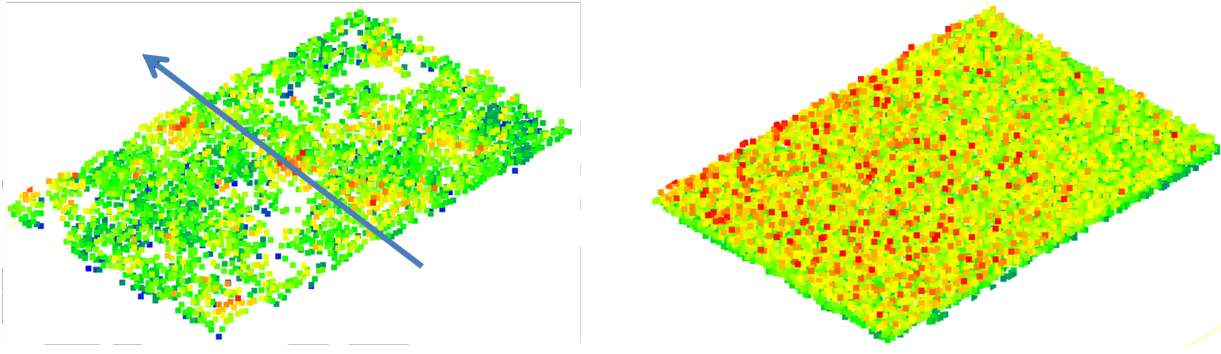


Figure F.11 Comparison between a biofilm and a sandpaper topography. *Left:* DEM of a biofilm, the arrow indicates the direction of flow during the cultivation phase. *Right:* DEM of a P40 sandpaper.

Table F.3 Statistical moments of elevations, measured on a generic biofilm surface and a sandpaper. Count denotes the number of elevations that have been analyzed. $\Delta_{Min,Max}$ is the difference between the lowest and highest elevation and σ_z , Ku and Sk are the statistical moments, as described above

ID	Count	$\Delta_{Min,Max}$	Standard deviation σ_z	Kurtosis Ku	Skewness Sk
[–]	[–]	[mm]	[mm]	[–]	[–]
Biofilm	3736	6.15	0.94	3.13	0.08
Sandpaper	10664	4.99	0.94	2.88	0.41

Still, referring to the appearance of both surfaces (see Figure F.11) it seems obvious that the spatial distribution of elevations is different between the biofilm and the sandpaper. While obviously the peaks on the sandpaper DEM are homogeneously distributed, the peaks in the biofilm DEM appear more randomly on the first sight. Nevertheless, it would be of great interest if one can quantify the spatial distribution of surface elevations to potentially investigate regularities related to e.g. the environmental conditions of cultivation (e.g. flow direction and -velocity). One such method is the so called random field approach in which the roughness is described as a random field of bed elevations $Z(x, y, t)$ (Nikora et al., 1998). Here, x and y are the coordinates in flow direction and transverse to the flow direction, respectively and t is the time. For example, Aberle and Nikora (2006) made use of the second order structure function (see Equation F.3) to investigate the roughness development of armored gravel beds:

$$D_{G2}(l_x, l_y) = \frac{1}{(N-n)(M-m)} \cdot \sum_{i=1}^{N-n} \sum_{j=1}^{M-m} \{|z(x_i + n\delta x, y_j + m\delta y) - z(x_i, y_j)|\}^2 \quad (\text{F.3})$$

where, $l_x = n\delta x$, $l_y = m\delta y$ are the spatial lags (or distances) between bed elevations in x and y direction, respectively. δx , δy are the measuring intervals (here: $\delta x = \delta y \approx 0.75$ mm). N and M are the total number of measuring points in x and y direction. In simple words, the second order structure function illustrates the spatial correlation between two bed elevations

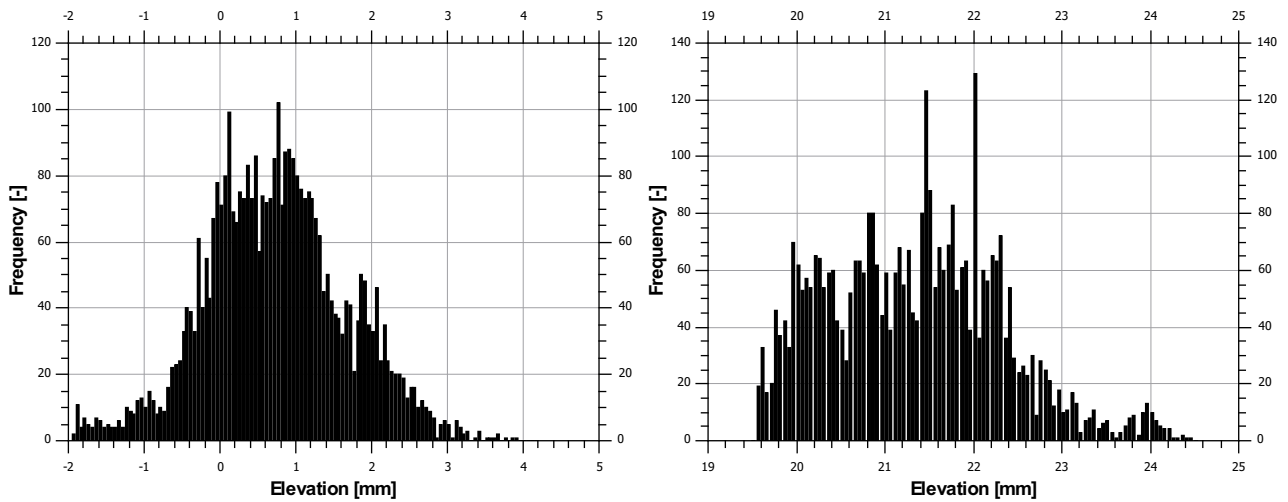


Figure F.12 Histograms of elevations measured on a generic biofilm surface and a sandpaper. *Left:* Histogram of the Biofilm DEM; *Right:* Histogram of the P40 sandpaper DEM. Please note that the absolute values of elevations are different as the initial height of the two surfaces differed (bin size = 0.05 mm).

at distances l_x and l_y where the distances are increased in every step of calculation. The results can be used to determine a characteristic length scale (or distance) at which the bed elevations are no longer correlated. This means, that all elevations with a maximum distance equal to the characteristic length scale are related and may be used to describe the field of elevations. Following the hypothesis, that the surface topography of biofilms is not random, but depending on e.g. parameters like the flow velocity/direction would mean that the results of the structure function (e.g. the characteristic length scale) are somehow related to these parameters.

Unfortunately though, the obtained bed elevations in the Jul14 experiment do not allow drawing such conclusions which is likely to be related to the relatively small extent of the measuring area (one cartridge = 6×8 cm) in which only few peaks and valleys can be found or an insufficient resolution of the measurements. Still, a comparison between structure functions obtained from the sandpaper and the biofilm topography gives a hint on the differences between both surfaces in longitudinal and transverse direction (illustrated in Figure F.13).

Figure F.13 shows the results of the second order structure function for both, the biofilm surface (*Left*) as well as the sandpaper surface (*Right*). There is a remarkable difference between both surfaces. While the values of D_{G2} are nearly constant for the sandpaper over all spatial lags, the values of D_{G2} first increase with lag distance to reach a plateau (also called “sill”) at lag distances greater than ≈ 7 mm for the biofilm topography. This indicates that elevations with lags < 7 mm are correlated while no such correlation can be found for the sandpaper topography as all roughness elements are homogeneously distributed over the measuring area.

An important conclusion to be drawn from the geostatistical analysis is thus, that in contrast

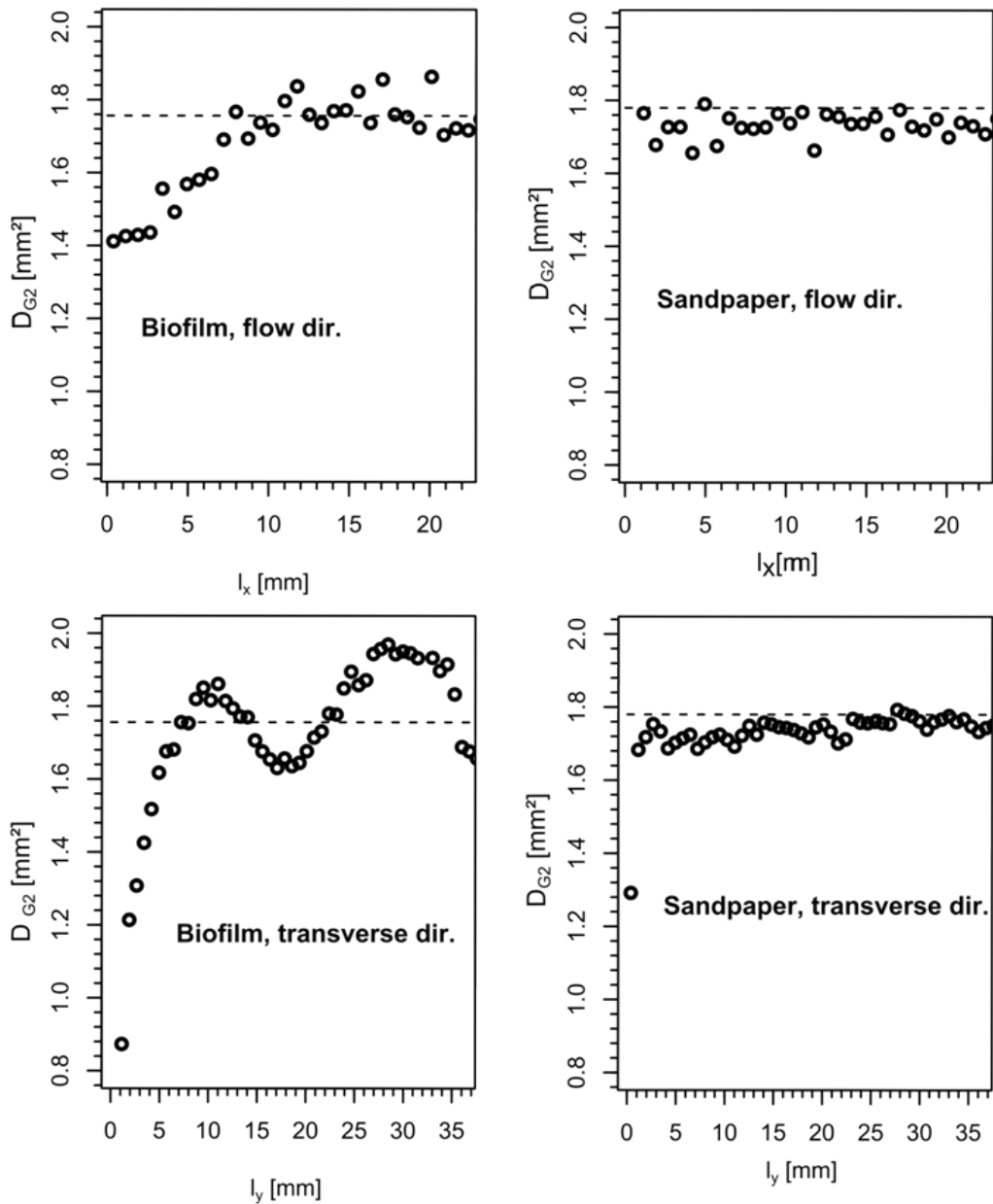


Figure F.13 Second-order structure functions for a sandpaper and a biofilm topography in flow and transverse direction. *Left:* The biofilm surface. *Right:* The sandpaper surface. The horizontal dashed lines are the corresponding values of $2\sigma_z^2$ indicating the “sill”. Second order structure functions are calculated by using the “R” library “geoR”.

to the sandpaper the elevation data of the biofilm surface contains evidence that the biofilm surface has distinct topographical features (i.e. peaks, valleys) which surely also have an impact on the near bed hydraulics. For future research it is recommended that the high potential of this geostatistical analysis is applied on data of biofilm topographies. An important prerequisite for a successful application would be a reliable method to determine biofilm elevations on larger areas as can be potentially done by using the so called Structure from Motion procedure (SfM).

Structure from motion (SfM)

Structure from Motion (SfM) is a photogrammetric method that analyzes photographs from

a specific object at different angles and distances to create a 3 dimensional representation of the object. In contrast to stereo photogrammetry where traditionally two cameras capture an object at defined angles and thus can reconstruct the object by triangulation, the position of the cameras must first be calculated by a software (based on feature recognition). The images that can be processed are largely scale invariant and even photographs from different cameras combined produce surprisingly good results. A drawback of this method is that the models need to be calibrated to account for true geometries. However, a number of advantages easily outcompete this limitation.

- Compared to commercial solutions of stereo photogrammetry, SFM can be extremely low cost. Almost every camera can be used and software exists which is free for non-commercial use (e.g. VisualSFM)
- The acquisition of the data lasts only a few seconds (as compared to the laser scanning where the biofilm surface is scanned for 4.5 hours. This also allows the topographical measuring of larger surface areas. On the contrary, post processing of data can take hours, largely depending on the number of images to be processed
- Additionally SFM provides color information (which cannot be obtained by laser scanning) useful for the identification of e.g. biofilm spots and blank surfaces

Furthermore, the use of SFM allows investigations of topography(-changes) even during running experiments in the hydraulic laboratory as was investigated by Ziegler (2013) and Lorenz (2016). In their studies a specially designed frame was used with 5 fixed cameras that have been synchronized (see also Noack et al., 2016a for a first evaluation of feasibility). Consequently, SfM and the developed method is especially interesting for continuous monitoring of growing biofilm topography as drainage of water during the experiments might harm the biofilm.

Part G

SUMMARY, CONCLUSIONS & OUTLOOK

The stability of sediments exposed to the fluid forces is a key research topic in hydraulic engineering and also has considerable implications for the ecological functioning of aquatic systems. While several abiotic properties of the mineral grains influence the stability (geometry, density) it is nowadays increasingly recognized that biology can influence the sediment stability likewise. In this context, biofilms which are the study objective of this thesis play an important role. Biofilms, comprising e.g. bacteria, microalgae and their secreted substances, grow in-between and on top of surficial sediments and act like a natural glue. Even though these glueing effects can lead to considerable sediment stabilization, a prediction of this “biostabilization” potential is impeded so far due to a lack of a proper understanding of the underlying mechanics.

This thesis aims at improving the knowledge on biostabilization mechanics needed to pave the way for developing a universally applicable model to predict the stabilization effect of biofilms. In this regard, physics-based models, which predict the incipient motion of biostabilized sediments from mechanical considerations analogous to the erosion of non-cohesive sediments (e.g. the Shields approach) have a high potential to reach this goal. However, physics-based models are still in their infancy, as appropriate instruments to measure the additional forces involved in biostabilization (adhesion and cohesion) are not readily available up to now. Consequently, the present thesis enters uncharted territory in testing a physics-based model with the results from an advanced method to measure surface adhesion forces. Much of this work has been devoted to develop this advanced method and the experimental protocols with the authors' hope that the here presented information will help in developing improved models in the near future. There is no doubt that there remains much more to be discovered in biostabilization mechanics as can be covered by the present thesis. In this context, the thesis raises new questions and hypotheses which are worthwhile to be investigated in future research for a better understanding of biostabilization. The most urgent questions include: What is the role of EPS-EPS cohesion in biostabilization? How are the adhesion forces distributed over the depth of the biofilm?

The study objectives of this dissertation are evaluated in the following and the key findings are summarized:

Study the impact of environmental conditions on biostabilization

The information on the impact of environmental conditions obtained by the physical experiments add to knowledge on biostabilization by two aspects: 1. Data is provided and discussed by studying the impact of single environmental conditions and their effect on biostabilization 2. Design, experimental programs and orientation values for applied conditions are reported, useful in setting up future experiments:

Constructing a sophisticated flume setup consisting of six flumes with adjustable light-, hydrodynamic and temperature conditions proved successful to investigate biostabilization under different environmental conditions. Particularly, the consideration of biofilm heterogeneities by providing a large number of replicates is an important aspect to generate reliable results and it is recommended to follow this concept in future research. Cultivating biofilms on glass beads and subsequent biostabilization measurements largely confirmed the findings from in-situ studies indicating that the presented setup is helpful for more fundamental biostabilization research.

However, great care must be taken by transferring the results to natural environments as all experiments have been conducted under idealized conditions and thus, differences to natural systems are inevitable. For example, in a river, the water is exchanged continuously, and the same applies to the advected microbes. On the other hand, the water circulated in the flumes is sampled at one point in time and thus the microbial community is not exchanged, hypothetically resulting in more pronounced seasonal effects.

The most profound differences in biostabilization have been observed for biofilms which developed from water sampled at different seasons. It is found that the sediment stability is highest in spring (up to ten times higher compared to abiotic sediments), followed by summer. In late autumn only little stability enhancements are detected compared to the case without a biofilm. Biofilms cultivated in complete darkness did not contribute to biostabilization, while biofilms cultivated under medium and high light intensities stabilized the sediment. In contrast to the expectations, there is surprisingly little difference in biostabilization between biofilms cultivated under different hydrodynamic conditions ($\tau_b = 0.02, 0.04$ and 0.08 N/m^2) and between medium and high light intensities ($LI = 50$ and $100 \mu\text{mol/m}^2\text{s}$). In the reported range, the biofilms can be described as largely unaffected by changes of the hydrodynamic forcing in absolute values, while minor differences exist in their temporal development: under higher forcing the development of biostabilization is delayed. For future experiments it is suggested to apply more contrasting conditions to allow drawing more precise inference from the impact of environmental conditions on the biostabilization effect.

Systematic research in the laboratory is essential to understand basic mechanisms. For example, two different modes of erosion are observed: A carpet-like erosion and a crust-like erosion. These modes of erosion seemingly influenced the stabilization potential to different degrees (the carpet-like biofilms are more stable but developed later) and therefore deserve separate and focused analysis.

Develop advanced methods and experimental programs to measure important parameters

Even though frequently considered as the key mechanical effect in pertinent literature on biostabilization, adhesion forces in established engineering units (i.e. N/m^2), have not been measured and related to biostabilization before. The value of developing a suitable method to measure these forces is not to be underestimated as this opens up completely new opportunities in research (not only restricted to biostabilization):

The MagPI (first published by Larson et al., 2009), consisting of an electromagnet attracting magnetic particles from biofilm surfaces, is a promising approach to estimate the surface adhesion, yet the results cannot be readily used in mechanical models due to two reasons. First, the proposed calibration only considers the magnetic forces of the electromagnet as a proxy for surface adhesion, not a mechanical force. Furthermore, the magnetic properties of the attracted particles were not considered, which *inter alia* impedes a comparison of the measurements between different laboratories, where different particles are used. Second, the determination of when particles are recaptured by the electromagnet is of major importance but often prone to uncertainties, especially when an averaged adhesion shall be measured. Consequently the method is improved (here called MagPI-IP) by developing a calibration procedure to determine the mechanical force needed to attract a particle which is in contact with a sticky surface. And additionally the system is partly automated with a camera capturing images of the particles below the electromagnet and subsequent image processing to determine when particles are attracted. The performance of the advanced system is tested on surrogate materials with different degrees of stickiness and it is found that the device is sensitive enough to measure even slight differences in adhesion. Applied in the experiments, surface adhesion values ranging between 0 and $\approx 7 \text{ N}/\text{m}^2$ are measured. However, the novel system is also limited as the image processing requires a good contrast between particles and biofilm surface which is not always guaranteed. To further improve the system it is recommended to focus on the characteristics of the particles and find alternative particles which are geometrically more homogeneous.

A second method which is developed in the course of the dissertation is a system based on laser triangulation to measure the topographical development of submerged biofilms. The fact that the biofilms are submerged during the measurements is important for a continuous survey as biofilms can be easily destroyed when they are exposed to the air. It is demon-

strated that the data can be used to determine the roughness of developing biofilms. In one experiment the roughness (expressed as the standard deviation of elevations, σ_z) remains constantly low during the first two weeks of growth ($\sigma_z \approx 0.25$ mm) then increases up to a value of $\sigma_z \approx 1.2$ mm to reach a plateau hereafter. Additional investigations on hydrodynamics indicate that biofilm growth can have a considerable impact on near bed hydrodynamics; the bed shear stress over a sandpaper with a similar roughness as a matured biofilm is 50% higher than over a glass surface. For this reason further research on the roughness of biofilms in combination with hydrodynamic measurements are strongly recommended.

Provide data from robust measurements on mechanical properties

Besides measuring the critical bed shear stress of biofilm-sediment samples, the MagPI-IP method is applied in three experiments to investigate the temporal development of surface adhesion forces to better understand the forces involved and the development of biostabilization.

The temporal development of the data showed some strong similarities to the development of the erosion measurements also in the context of environmental conditions and indicates a possible relationship between both values: In the first two weeks of biofilm cultivation and under darkness conditions the stability of the samples is comparable to the stability of the initial abiotic sediment (i.e. the stability is low). Similarly, the measured surface adhesion is low on these samples, not exceeding ≈ 1.0 N/m². In the coming weeks the stability mostly increases, which is also reflected by the measured surface adhesion values (increasing from ≈ 1.0 N/m² to ≈ 7.0 N/m²). After approximately one month of cultivation the stability largely scattered while the surface adhesion values fluctuated around a constant value.

Even though the similarities are striking, it is important to note that the quantity of surface adhesion alone cannot be used to predict the biostabilization effect. This is demonstrated by applying a modified Shields approach, which also considers adhesion forces based on dimensional analysis, combined with measured values of surface adhesion. The results indicate that adhesion forces might be responsible for the increase of stability mediated by young biofilms that are eroded in aggregates. In this regard, further measurements on adhesion forces over the depth of the biofilm could provide highly significant insights and conducting these measurements should be straightforward with the help of the MagPI-IP system. However, other parameters, especially the geometry and the bulk density of the eroded aggregates seem to be of equal or even higher importance. Even though no final proof can be given, the findings of this thesis indicate that adhesion forces might play a decisive role in biostabilization and thereby encourages more fundamental investigations on biofilm mechanics for a better understanding of biostabilization mechanisms.

References

- Aberle, J., & Nikora, V. (2006). Statistical properties of armored gravel bed surfaces. Water Resources Research, *42*(11). doi: 10.1029/2005WR004674
- Aberle, J., Nikora, V., Henning, M., Ettmer, B., & Hentschel, B. (2010). Statistical characterization of bed roughness due to bed forms: A field study in the Elbe River at Aken, Germany. Water Resources Research, *46*(3). doi: 10.1029/2008WR007406
- Aberle, J., Nikora, V., & Walters, R. (2004). Effects of bed material properties on cohesive sediment erosion. Marine Geology, *207*(1-4), 83–93. doi: 10.1016/j.margeo.2004.03.012
- Ahimou, F., Semmens, M. J., Novak, P. J., & Haugstad, G. (2007). Biofilm Cohesiveness Measurement Using a Novel Atomic Force Microscopy Methodology. Applied and Environmental Microbiology, *73*(9), 2897–2904. doi: 10.1128/AEM.02388-06
- Amos, C. L., Bergamasco, A., Umgiesser, G., Cappucci, S., Cloutier, D., DeNat, L., ... Cristante, S. (2004). The stability of tidal flats in Venice Lagoon-the results of in-situ measurements using two benthic, annular flumes. Journal of Marine Systems, *51*(1-4), 211–241. doi: 10.1016/j.jmarsys.2004.05.013
- Amos, C. L., Droppo, I. G., Gomez, E. A., & Murphy, T. P. (2003). The stability of a remediated bed in Hamilton Harbour, Lake Ontario, Canada. Sedimentology, *50*(1), 149–168.
- Andalib, M., Jesse, Z., & Nakhla, G. (2010). Terminal settling velocity and drag coefficient of biofilm-coated particles at high Reynolds numbers. AIChE journal, *56*(10), 2598–2606.
- Anderson, A. M., Spears, B. M., Paterson, D. M., Lubarsky, H. V., Davidson, I., & Gerbersdorf, S. U. (2011). Magnetic particle induction and its importance in biofilm research. INTECH Open Access Publisher.
- Andrewartha, J., Perkins, K., Sargison, J., Osborn, J., Walker, G., Henderson, A., & Hallegraeff, G. (2010). Drag force and surface roughness measurements on freshwater biofouled surfaces. Biofouling, *26*(4), 487–496. doi: 10.1080/08927014.2010.482208
- ASTM. (2002). Standard Test Methods for Specific Gravity of Soil Solids by Water Pycnometer (Tech. Rep. No. D 854-02).
- Barton, A. F., Sargison, J. E., Osborn, J. E., Perkins, K., & Hallegraeff, G. (2010). Characterizing the roughness of freshwater biofilms using a photogrammetric methodology. Biofouling, *26*(4), 439–448. doi: 10.1080/08927011003699733
- Battin, T. J., Kaplan, L. A., Newbold, J. D., Cheng, X., & Hansen, C. (2003a). Effects of Current Velocity on the Nascent Architecture of Stream Microbial Biofilms. Applied and Environmental Microbiology, *69*(9), 5443–5452. doi: 10.1128/AEM.69.9.5443-5452.2003
- Battin, T. J., Kaplan, L. A., Newbold, J. D., & Hansen, C. M. (2003b). Contributions of microbial biofilms to ecosystem processes in stream mesocosms. Nature, *426*(6965), 439–442.

- Battin, T. J., & Sengschmitt, D. (1999). Linking Sediment Biofilms, Hydrodynamics, and River Bed Clogging: Evidence from a Large River. *Microbial Ecology*, *37*(3), 185–196. doi: 10.1007/s002489900142
- Battin, T. J., Sloan, W. T., Kjelleberg, S., Daims, H., Head, I. M., Curtis, T. P., & Eberl, L. (2007). Microbial landscapes: new paths to biofilm research. *Nature Reviews Microbiology*, *5*(1), 76–81.
- Berlamont, J., Ockenden, M., Toorman, E., & Winterwerp, J. (1993). The characterisation of cohesive sediment properties. *Coastal Engineering*, *21*, 105–128.
- Bierbaum, T. (2015). *Das Messprinzip von MagPI zur Bestimmung der Adhäsion von Biofilmen* (Bachelor thesis). University of Stuttgart: 1. Physics Institute.
- Billings, N., Birjiniuk, A., Samad, T. S., Doyle, P. S., & Ribbeck, K. (2015). Material properties of biofilms—a review of methods for understanding permeability and mechanics. *Reports on Progress in Physics*, *78*(3), 036601. doi: 10.1088/0034-4885/78/3/036601
- Black, K. S., Sun, H., Craig, G., Paterson, D. M., Watson, J., & Tolhurst, T. (2001). Incipient erosion of biostabilized sediments examined using particle-field optical holography. *Environmental science & technology*, *35*(11), 2275–2281.
- Black, K. S., Tolhurst, Paterson, D. M., & Hagerthey. (2002). Working with Natural Cohesive Sediments. *Journal of Hydraulic Engineering*, *128*(1), 2–8.
- Böl, M., Ehret, A. E., Bolea Albero, A., Hellriegel, J., & Krull, R. (2013). Recent advances in mechanical characterisation of biofilm and their significance for material modelling. *Critical Reviews in Biotechnology*, *33*(2), 145–171. doi: 10.3109/07388551.2012.679250
- Boudreau, B. P. (2012). The physics of bubbles in surficial, soft, cohesive sediments. *Marine and Petroleum Geology*, *38*(1), 1–18. doi: 10.1016/j.marpetgeo.2012.07.002
- Boudreau, B. P., Gardiner, B. S., & Johnson, B. D. (2001). Rate of growth of isolated bubbles in sediments with a diagenetic source of methane. *Limnology and Oceanography*, *46*(3), 616–622.
- Boulêtreau, S., Charcosset, J.-Y., Gamby, J., Lyautey, E., Mastrotrillo, S., Azémar, F., ... Garabetian, F. (2011). Rotating disk electrodes to assess river biofilm thickness and elasticity. *Water Research*, *45*(3), 1347–1357. doi: 10.1016/j.watres.2010.10.016
- Brown, J. H., Gillooly, J. F., Allen, A. P., Savage, V. M., & West, G. B. (2004). Toward a metabolic theory of ecology. *Ecology*, *85*(7), 1771–1789.
- Brownlie, W. (1981). *Prediction of flow depth and sediment discharge in open channels* (Tech. Rep. No. KH-R-43A). Pasadena: Calif. Inst. of Technol.
- Brunke, M., & Gonser, T. (1997). The ecological significance of exchange processes between rivers and groundwater. *Freshwater Biology*, *37*, 1–33.
- Bryers, & Characklis. (1981). Early fouling biofilm formation in a turbulent flow system: Overall kinetics. *Water Research*, *4*(15), 483–491.
- Buffington, J., & Montgomery, D. (1997). A systematic analysis of eight decades of incipient motion studies, with special reference to gravel-bedded rivers. *Water Resources*

Research, 33(8), 1993–2029.

- Characklis, W. G., & Cooksey, K. (1983). Biofilms and microbial fouling. Advances in applied microbiology, 29, 93–138.
- Chen, M. J., Zhang, Z., & Bott, T. (2005). Effects of operating conditions on the adhesive strength of *Pseudomonas fluorescens* biofilms in tubes. Colloids and Surfaces B: Biointerfaces, 43(2), 61–71. doi: 10.1016/j.colsurfb.2005.04.004
- Chen, M. J., Zhang, Z., & Bott, T. R. (1998). Direct measurement of the adhesive strength of biofilms in pipes by micromanipulation. Biotechnology Techniques, 12(12), 875–880.
- CoastalWiki. (2016). Biostabilization. Retrieved 2016-06-28, from <http://www.coastalwiki.org/wiki/Biostabilization>
- Costanza, R., d'Arge, R., De Groot, R., Faber, S., Grasso, M., Hannon, B., ... others (1997). The value of the world's ecosystem services and natural capital. Nature, 387.
- Cuthbertson, A. J. S., Ibikunle, O., McCarter, W. J., & Starrs, G. (2016). Monitoring and characterisation of sand-mud sedimentation processes. Ocean Dynamics, 66(6-7), 867–891. doi: 10.1007/s10236-016-0958-7
- Dade, W. B., Davis, J. D., Nichols, P. D., Nowell, A. R., Thistle, D., Trexler, M. B., & White, D. C. (1990). Effects of bacterial exopolymer adhesion on the entrainment of sand. Geomicrobiology Journal, 8(1), 1–16.
- Dade, W. B., Nowell, A. R. M., & Jumars, P. A. (1992). Predicting erosion resistance of muds. Marine geology, 105(1-4), 285–297.
- Dany, C. (2015). Charakterisierung ferromagnetischer Partikel und ihre Anwendung bei quantitativen Adhäsionsmessungen (Zulassungsarbeit). University of Stuttgart: 1. Physics Institute.
- De Brouwer, J. F. C., Bjelic, S., De Deckere, E., & Stal, L. J. (2000). Interplay between biology and sedimentology in a mudflat (Biezelingse Ham, Westerschelde, The Netherlands). Continental shelf research, 20(10), 1159–1177.
- De Brouwer, J. F. C., Ruddy, G. K., Jones, T. E. R., & Stal, L. J. (2002). Sorption of EPS to sediment particles and the effect on the rheology of sediment slurries. Biogeochemistry, 61(1), 57–71.
- Defew, E., Tolhurst, T. J., Paterson, D., & Hagerthey, S. (2003). Can the stability of intertidal sediments be predicted from proxy parameters? An in situ investigation. In D. Raffaelli, M. Solan, D. Paterson, A. Buck, & J. Pomfret (Eds.), Estuarine and Coastal Sciences Association (pp. 61–70).
- Deshpande, M. D., & Vaishnav, R. N. (1983). Wall stress distribution due to jet impingement. Journal of Engineering Mechanics, 109(2), 479–493.
- Dickhudt, P. J., Friedrichs, C. T., Schaffner, L. C., & Sanford, L. P. (2009). Spatial and temporal variation in cohesive sediment erodibility in the York River estuary, eastern USA: A biologically influenced equilibrium modified by seasonal deposition. Marine Geology, 267(3-4), 128–140. doi: 10.1016/j.margeo.2009.09.009
- Dietrich, W. (1982). Settling velocity of natural particles. Water Resources Research, 18(6).

- Droppo, I. G. (2001). Rethinking what constitutes suspended sediment. Hydrological Processes, 15(9), 1551–1564. doi: 10.1002/hyp.228
- Droppo, I. G. (2009). Biofilm structure and bed stability of five contrasting freshwater sediments. Marine and Freshwater Research, 60(7), 690–699. doi: 10.1071/MF08019
- Droppo, I. G., Lau, Y. L., & Mitchell, C. (2001). The effect of depositional history on contaminated bed sediment stability. Science of the Total Environment, 266(1), 7–13.
- Droppo, I. G., Leppard, G. G., Flannigan, D. T., & Liss, S. N. (1997). The freshwater floc: a functional relationship of water and organic and inorganic floc constituents affecting suspended sediment properties. Water, Air, and Soil Pollution, 99(1-4), 43–54.
- Droppo, I. G., Ross, N., Skafel, M., & Liss, S. N. (2007). Biostabilization of cohesive sediment beds in a freshwater wave-dominated environment. Limnology and Oceanography, 52(2), 577–589.
- Fang, H., Shang, Q., Chen, M., & He, G. (2014). Changes in the critical erosion velocity for sediment colonized by biofilm. Sedimentology, 61(3), 648–659. doi: 10.1111/sed.12065
- Flemming, H.-C. (2011). The perfect slime. Colloids and Surfaces B: Biointerfaces, 86(2), 251–259. doi: 10.1016/j.colsurfb.2011.04.025
- Flemming, H.-C., & Wingender, J. (2010). The biofilm matrix. Nature Reviews Microbiology, 8, 623–633. doi: 10.1038/nrmicro2415
- Friend, P., Ciavola, P., Cappucci, S., & Santos, R. (2003). Bio-dependent bed parameters as a proxy tool for sediment stability in mixed habitat intertidal areas. Continental Shelf Research, 23(17-19), 1899–1917. doi: 10.1016/j.csr.2002.12.001
- Gardel, M., Valentine, M., & Weitz, D. (2005). Microrheology. In Microscale Diagnostic Techniques (pp. 1–49). Springer Verlag.
- Gargaud, M., et al. (Eds.). (2011). Encyclopedia of Astrobiology. Berlin, Heidelberg: Springer Berlin Heidelberg.
- Garrett, T. R., Bhakoo, M., & Zhang, Z. (2008). Bacterial adhesion and biofilms on surfaces. Progress in Natural Science, 18(9), 1049–1056. doi: 10.1016/j.pnsc.2008.04.001
- Gerbersdorf, S. U., Bittner, R., Lubarsky, H., Manz, W., & Paterson, D. M. (2009). Microbial assemblages as ecosystem engineers of sediment stability. Journal of Soils and Sediments, 9(6), 640–652. doi: 10.1007/s11368-009-0142-5
- Gerbersdorf, S. U., Cimadoribus, C., Class, H., Engesser, K.-H., Helbich, S., Hollert, H., ... Wieprecht, S. (2015). Anthropogenic Trace Compounds (ATCs) in aquatic habitats - Research needs on sources, fate, detection and toxicity to ensure timely elimination strategies and risk management. Environment International, 79, 85–105. doi: 10.1016/j.envint.2015.03.011
- Gerbersdorf, S. U., Hollert, H., Brinkmann, M., Wieprecht, S., Schüttrumpf, H., & Manz, W. (2011). Anthropogenic pollutants affect ecosystem services of freshwater sediments: the need for a “triad plus x” approach. Journal of Soils and Sediments, 11(6), 1099–1114. doi: 10.1007/s11368-011-0373-0

- Gerbersdorf, S. U., Jancke, T., Westrich, B., & Paterson, D. M. (2007). Microbial stabilization of riverine sediments by extracellular polymeric substances. *Geobiology*, *0*(0), 57–69. doi: 10.1111/j.1472-4669.2007.00120.x
- Gerbersdorf, S. U., & Wieprecht, S. (2015). Biostabilization of cohesive sediments: revisiting the role of abiotic conditions, physiology and diversity of microbes, polymeric secretion, and biofilm architecture. *Geobiology*, *13*(1), 68–97. doi: 10.1111/gbi.12115
- Githua, T. K. (2014, November). *The Characterization of Biostabilized Floccs Applying Flocc Settling Column and Image Analysis* (Master thesis). Institute for Modelling Hydraulic and Environmental Systems - University of Stuttgart.
- Graba, M., Moulin, F. Y., Boulêtreau, S., Garabétian, F., Kettab, A., Eiff, O., ... Sauvage, S. (2010). Effect of near-bed turbulence on chronic detachment of epilithic biofilm: Experimental and modeling approaches. *Water Resources Research*, *46*(11). doi: 10.1029/2009WR008679
- Graba, M., Sauvage, S., Moulin, F. Y., Urrea, G., Sabater, S., & Sanchez-Pérez, J. M. (2013). Interaction between local hydrodynamics and algal community in epilithic biofilm. *Water Research*, *47*(7), 2153–2163. doi: 10.1016/j.watres.2013.01.011
- Grabowski, R. C., Droppo, I. G., & Wharton, G. (2011). Erodibility of cohesive sediment: The importance of sediment properties. *Earth-Science Reviews*, *105*(3-4), 101–120. doi: 10.1016/j.earscirev.2011.01.008
- Grant, J., & Gust, G. (1987). Prediction of coastal sediment stability from photopigment content of mats of purple sulphur bacteria. *Nature*, *330*, 244 – 246. doi: 10.1038/330244a0
- Guelon, T., Mathias, J.-D., & Stoodley, P. (2011). Advances in biofilm mechanics. In *Biofilm Highlights* (5th ed.). Springer Science & Business Media.
- Gust, G. (1990). *Method of generating precisely-defined wall shearing stresses* (Nos. 4,973,165).
- Heise, S., & Förstner, U. (2007). Risk assessment of contaminated sediments in river basins-theoretical considerations and pragmatic approach. *Journal of Environmental Monitoring*, *9*(9), 943–952. doi: 10.1039/b704071g
- Hjulstrom, F. (1939). Transportation of detritus by moving water: Part 1. Transportation. In *Recent Marine Sediments* (pp. 5–32).
- Horn, H., & Hempel, D. C. (1997). Growth and decay in an auto-/heterotrophic biofilm. *Water Research*, *31*(9), 2243–2252.
- Horne, A. J., & Goldman, C. R. (1994). *Limnology* (2nd ed.). New York: McGraw-Hill.
- Israelachvili, J. (2011). *Intermolecular and surface forces* (third ed.). Academic Press.
- Jepsen, R., McNeil, J., & Lick, W. (2000). Effects of gas generation on the density and erosion of sediments from the Grand River. *Journal of Great Lakes Research*, *26*(2), 209–219.
- Jepsen, R., Roberts, J., & Lick, W. (1997). Effects of bulk density on sediment erosion rates. In *The Interactions Between Sediments and Water* (pp. 21–31). Springer.

- Johnson, B. D., Boudreau, B. P., Gardiner, B. S., & Maass, R. (2002). Mechanical response of sediments to bubble growth. *Marine Geology*, *187*, 347–363.
- Jonsson, P. R., van Duren, L. A., Amielh, M., Asmus, R., Aspden, R. J., Daunys, D., ... Schaaff, E. (2006). Making water flow: a comparison of the hydrodynamic characteristics of 12 different benthic biological flumes. *Aquatic Ecology*, *40*(4), 409–438. doi: 10.1007/s10452-006-9049-z
- Jumars, P. A., & Nowell, A. R. M. (1984). Effects of benthos on sediment transport: Difficulties with functional grouping. *Continental Shelf Research*, *3*(2), 115–130.
- Keyvani, A., & Strom, K. (2013). A fully-automated image processing technique to improve measurement of suspended particles and flocs by removing out-of-focus objects. *Computers & Geosciences*, *52*, 189–198. doi: 10.1016/j.cageo.2012.08.018
- Kikillus, A. (2012). Messmethodik mittels magnetischer Mikropartikel zur Bestimmung der Adhäsion in Biofilmen - MagPI (Bachelor thesis). University of Stuttgart: 1. Physics Institute.
- Kornman, & de Deckere. (1998). Temporal variation in sediment erodibility and suspended sediment dynamics in the Dollard estuary. In Sedimentary processes in the intertidal zone.
- Kreth, J., Hagerman, E., Tam, K., Merritt, J., Wong, D. T. W., Wu, B. M., ... Qi, F. (2004). Quantitative analyses of *Streptococcus mutans* biofilms with quartz crystal microbalance, microjet impingement and confocal microscopy. *Biofilms*, *1*(04), 277–284.
- Lanuru, M. (2004). The spatial and temporal patterns of erodibility of an intertidal flat in the East Frisian Wadden Sea, Germany (PhD thesis). Christian-Albrechts-Universität zu Kiel.
- Larned, S. T., Nikora, V. I., & Biggs, B. J. (2004). Mass-transfer-limited nitrogen and phosphorus uptake by stream periphyton: A conceptual model and experimental evidence. *Limnology and Oceanography*, *49*(6), 1992–2000.
- Larned, S. T., Packman, A. I., Plew, D. R., & Vopel, K. (2011). Interactions between the mat-forming alga *Didymosphenia geminata* and its hydrodynamic environment. *Limnology & Oceanography: Fluids & Environments*, *1*(0), 4–22. doi: 10.1215/21573698-1152081
- Larson, F., Lubarsky, H., Gerbersdorf, S. U., & Paterson, D. M. (2009). Surface adhesion measurements in aquatic biofilms using magnetic particle induction: MagPI. *Limnology and Oceanography: Methods*, *7*(7), 490–497.
- Lau, P. C., Dutcher, J. R., Beveridge, T. J., & Lam, J. S. (2009). Absolute Quantitation of Bacterial Biofilm Adhesion and Viscoelasticity by Microbead Force Spectroscopy. *Biophysical Journal*, *96*(7), 2935–2948. doi: 10.1016/j.bpj.2008.12.3943
- Lee, K.-S., & Park, J.-I. (2008). An effective transplanting technique using shells for restoration of *Zostera marina* habitats. *Marine Pollution Bulletin*, *56*(5), 1015–1021. doi: 10.1016/j.marpolbul.2008.02.010
- Le Hir, P., Monbet, Y., & Orvain, F. (2007). Sediment erodability in sediment transport

- modelling: Can we account for biota effects? Continental Shelf Research, 27(8), 1116–1142. doi: 10.1016/j.csr.2005.11.016
- Lick, W., Jin, L., & Gailani, J. (2004). Initiation of movement of quartz particles. Journal of Hydraulic Engineering, 130(8), 755–761.
- Liu, Y., & Fang, H. H. P. (2003). Influences of Extracellular Polymeric Substances (EPS) on Flocculation, Settling, and Dewatering of Activated Sludge. Critical Reviews in Environmental Science and Technology, 33(3), 237–273. doi: 10.1080/10643380390814479
- Löffler-Mang, M. (2012). Optische Sensorik Lasertechnik, Experimente, Light Barriers. Vieweg and Teubner Verlag.
- Lorenz, R. (2016). Structure from Motion to investigate the bathymetry of rough surfaces in hydraulic laboratories (Bachelor thesis). University of Stuttgart: Institute for Modelling Hydraulic and Environmental Systems.
- Lubarsky, H. V., Gerbersdorf, S. U., Hubas, C., Behrens, S., Ricciardi, F., & Paterson, D. M. (2012). Impairment of the Bacterial Biofilm Stability by Triclosan. PLoS ONE, 7(4), e31183. doi: 10.1371/journal.pone.0031183
- Lubarsky, H. V., Hubas, C., Chocholek, M., Larson, F., Manz, W., Paterson, D. M., & Gerbersdorf, S. U. (2010). The Stabilisation Potential of Individual and Mixed Assemblages of Natural Bacteria and Microalgae. PLoS ONE, 5(11), e13794. doi: 10.1371/journal.pone.0013794
- Lucas, C. H., Widdows, J., & Wall, L. (2003). Relating spatial and temporal variability in sediment chlorophyll a and carbohydrate distribution with erodibility of a tidal flat. Estuaries, 26(4), 885–893. doi: 10.1007/BF02803347
- Lüdecke, C., Jandt, K. D., Siegismund, D., Kujau, M. J., Zang, E., Rettenmayr, M., ... Roth, M. (2014). Reproducible Biofilm Cultivation of Chemostat-Grown Escherichia coli and Investigation of Bacterial Adhesion on Biomaterials Using a Non-Constant-Depth Film Fermenter. PLoS ONE, 9(1), e84837. doi: 10.1371/journal.pone.0084837
- Madsen, K. N., Nilsson, P., & Sundbäck, K. (1993). The influence of benthic microalgae on the stability of a subtidal sediment. Journal of Experimental Marine Biology and Ecology, 170(2), 159–177. doi: 10.1016/0022-0981(93)90150-M
- Manzenrieder, H. (1983). Die biologische Verfestigung von Wattflächen aus der Sicht des Ingenieurs (Miteilungen Leichtweiss- Instituts Wasserbau, T.U. Braunschweig No. 79).
- Manzenrieder, H. (1985). Retardation of Initial Erosion under Biological Effects in Sandy Tidal Flats. In (pp. 455–466). 1985 Australasian Conference on Coastal and Ocean Engineering, Barton.
- Meadows, P. S., & Anderson, J. G. (1969). Micro-organisms attached to marine sand grains. Journal of the Marine Biological Association of the United Kingdom, 48(01), 161–175.
- Mendoza-Lera, C., Federlein, L. L., Knie, M., & Mutz, M. (2015). The algal lift: Buoyancy-mediated sediment transport. Water Resources Research, 52(1), 108–118. doi: 10.1002/2015WR017315

- Meysman, F., Middelburg, J., & Heip, C. (2006). Bioturbation: a fresh look at Darwin's last idea. Trends in Ecology & Evolution, 21(12), 688–695. doi: 10.1016/j.tree.2006.08.002
- Miedema, S. A. (2010). Constructing the Shields curve, a new theoretical approach and its applications. WODCON XIX, Beijing China.
- Miller, M. C., McCave, I. N., & Komar, P. (1977). Threshold of sediment motion under unidirectional currents. Sedimentology, 24(4), 507–527.
- Neumann, A. C., Gebelein, C. D., & Scoffin, T. P. (1970). The composition, structure and erodability of subtidal mats, Abaco, Bahamas. Journal of Sedimentary Research, 40(1).
- Newcomer, M. E., Hubbard, S. S., Fleckenstein, J. H., Maier, U., Schmidt, C., Thullner, M., ... Rubin, Y. (2016). Simulating bioclogging effects on dynamic riverbed permeability and infiltration. Water Resources Research, 52(4), 2883–2900. doi: 10.1002/2015WR018351
- Nikora, V. I. (2010). Hydrodynamics of aquatic ecosystems : An interface between ecology, biomechanics and environmental fluid mechanics. River Research and Applications, 26(4), 367–384. doi: 10.1002/rra.1291
- Nikora, V. I., Goring, D. G., & Biggs, B. J. (1998). On gravel-bed roughness characterization. Water Resources Research, 34(3), 517–527.
- Nikora, V. I., Goring, D. G., & Biggs, B. J. F. (1997). On stream periphyton turbulence interactions. New Zealand Journal of Marine and Freshwater Research, 31(4), 435–448. doi: 10.1080/00288330.1997.9516777
- Nikora, V. I., Goring, D. G., & Biggs, B. J. F. (2002). Some observations of the effects of micro-organisms growing on the bed of an open channel on the turbulence properties. Journal of Fluid Mechanics, 450. doi: 10.1017/S0022112001006486
- Noack, M., Gerbersdorf, S. U., Hillebrand, G., & Wieprecht, S. (2015). Combining Field and Laboratory Measurements to Determine the Erosion Risk of Cohesive Sediments Best. Water, 7, 5061–5077. doi: 10.3390/w7095061
- Noack, M., Ortlepp, J., & Wieprecht, S. (2016b). An Approach to Simulate Interstitial Habitat Conditions During the Incubation Phase of Gravel-Spawning Fish: Interstitial Habitat Conditions for Gravel-Spawning Fish. River Research and Applications. doi: 10.1002/rra.3012
- Noack, M., Schmid, G., Thom, M., & Wieprecht, S. (2016a). Testing “Structure-from-Motion” photogrammetry for high-resolution topographic surveys in hydraulic laboratories. Iowa City, USA.
- Noffke, N., Gerdes, G., Klenke, T., & Krumbein, W. E. (2001). Microbially Induced Sedimentary Structures-A New Category within the Classification of Primary Sedimentary Structures: Perspectives. Journal of Sedimentary Research, 71(5), 649–656.
- Ohashi, A., & Harada, H. (1994). Adhesion Strength of Biofilm Developed in an attached growth reactor. Water Science & Technology, 29(10–11), 281–288.

- Ohashi, A., & Harada, H. (1996). A novel concept for evaluation of biofilm adhesion strength by applying tensile force and shear force. Water Science and Technology, *34*(5–6), 201–211. doi: 10.1016/0273-1223(96)00647-6
- Okkerse, W., Ottengraf, S., & Osinga-Kuipers, B. (2000). Biofilm thickness variability investigated with a laser triangulation sensor. Biotechnol Bioeng, *70*, 619–629.
- Otto, K. (2008). Biophysical approaches to study the dynamic process of bacterial adhesion. Research in Microbiology, *159*(6), 415–422. doi: 10.1016/j.resmic.2008.04.007
- Owens, P. N., Batalla, R. J., Collins, A. J., Gomez, B., Hicks, D. M., Horowitz, A. J., ... Trustrum, N. A. (2005). Fine-grained sediment in river systems: environmental significance and management issues. River Research and Applications, *21*(7), 693–717. doi: 10.1002/rra.878
- Packman, A. (2013). Rivers: Building bacterial bridges. Nature Geoscience, *6*(9), 682–683.
- Pal, A., & Paul, A. (2008). Microbial extracellular polymeric substances: central elements in heavy metal bioremediation. Indian J. Microbiol., *48*, 49–64.
- Palacio, M. L. B., & Bhushan, B. (2012). Bioadhesion: a review of concepts and applications. Philosophical Transactions of the Royal Society A: Mathematical, Physical and Engineering Sciences, *370*(1967), 2321–2347. doi: 10.1098/rsta.2011.0483
- Paola, C. (2001). Modelling Stream braiding over a range of scales. New Zealand Hydrological Society.
- Parchure, T., & Mehta, A. (1985). Erosion of soft cohesive sediment deposits. Journal of Hydraulic Engineering, *111*(10).
- Paterson, D. M. (1989). Short-term changes in the erodibility of intertidal cohesive sediments related to the migratory behavior of epipellic diatoms. Limnology and Oceanography, *34*(1), 223–234.
- Paterson, D. M., & Daborn, G. R. (1991). Sediment stabilisation by biological action: significance for coastal engineering. Developments in coastal engineering, 111–119.
- Pereira, M. O., Kuehn, M., Wuertz, S., Neu, T., & Melo, L. F. (2002). Effect of flow regime on the architecture of pseudomonas fluorescens biofilm. Biotechnology and Bioengineering, *78*(2), 164–171. doi: 10.1002/bit.10189
- Piqué, G., Vericat, D., Sabater, S., & Batalla, R. J. (2016). Effects of biofilm on river-bed scour. Science of The Total Environment. doi: 10.1016/j.scitotenv.2016.08.009
- Postma, H. (1967). Sediment transport and sedimentation in the estuarine environment. Estuaries, *83*, 158–179.
- Proia, L., Cassió, F., Pascoal, C., Tlili, A., & Romaní, A. M. (2012). The Use of Attached Microbial Communities to Assess Ecological Risks of Pollutants in River Ecosystems: The Role of Heterotrophs. In H. Guasch, A. Ginebreda, & A. Geiszinger (Eds.), Emerging and Priority Pollutants in Rivers (Vol. 19, pp. 55–83). Berlin, Heidelberg: Springer Berlin Heidelberg.
- Raudkivi, A. J. (1982). Grundlagen des Sedimenttransports. Berlin, Heidelberg: Springer Berlin Heidelberg.

- Rice, S. P., Lancaster, J., & Kemp, P. (2010). Experimentation at the interface of fluvial geomorphology, stream ecology and hydraulic engineering and the development of an effective, interdisciplinary river science. Earth Surface Processes and Landforms, *35*(1), 64–77. doi: 10.1002/esp.1838
- Ries, D. (2016). Das MagPI-IP System: Eine Versuchsreihe zu teilautomatisierten Adhäsionsmessungen auf Biofilmen und Datenanalyse mittels MATLAB (Diploma thesis). Institute for Modelling Hydraulic and Environmental Systems - University of Stuttgart.
- Riethmüller, R., Hakvoort, J., Heineke, M., Heymann, K., Kühn, H., & Witte, G. (1998). Relating erosion threshold to tidal flat surface color. In Sedimentary Processes in the Intertidal Zone, (Vol. 139, pp. 283–293).
- Riethmüller, R., Heineke, M., Kühn, H., & Keuker-Rüdiger, R. (2000). Chlorophyll a concentration as an index of sediment surface stabilisation by microphytobenthos? Continental Shelf Research, *20*(10), 1351–1372.
- Righetti, M., & Lucarelli, C. (2007). May the Shields theory be extended to cohesive and adhesive benthic sediments? Journal of Geophysical Research, *112*(C5). doi: 10.1029/2006JC003669
- Righetti, M., & Lucarelli, C. (2010, May). Resuspension phenomena of benthic sediments: The role of cohesion and biological adhesion. River Research and Applications, *26*(4), 404–413. doi: 10.1002/rra.1296
- Roeselers, G., Zippel, B., Staal, M., Van Loosdrecht, M., & Muyzer, G. (2006). On the reproducibility of microcosm experiments - different community composition in parallel phototrophic biofilm microcosms: Reproducibility of microcosm experiments. FEMS Microbiology Ecology, *58*(2), 169–178. doi: 10.1111/j.1574-6941.2006.00172.x
- Roulund, A., Sumer, B. M., Fredsøe, J., & Michelsen, J. (2005). Numerical and experimental investigation of flow and scour around a circular pile. Journal of Fluid Mechanics, *534*, 351–401. doi: 10.1017/S0022112005004507
- Santolamazza, D. P. (2013). Flocculation and Erosion analysis using Image Processing and EPS analysis (Master thesis). Institute for Modelling Hydraulic and Environmental Systems - University of Stuttgart.
- Schlichting, H., & Gersten, K. (2006). Grenzschicht-theorie. Springer-Verlag.
- Schmidt, H., Thom, M., King, L., Wieprecht, S., & Gerbersdorf, S. U. (2016). The effect of seasonality upon the development of lotic biofilms and microbial biostabilisation. Freshwater Biology. doi: 10.1111/fwb.12760
- Schmidt, H., Thom, M., Matthies, K., Behrens, S., Obst, U., Wieprecht, S., & Gerbersdorf, S. U. (2015). A multi-disciplinarily designed mesocosm to address the complex flow-sediment-ecology tripartite relationship on the microscale. Environmental Sciences Europe, *27*(1). doi: 10.1186/s12302-014-0037-y
- Schultz, M. P., & Swain, G. W. (1999). The Effect of Biofilms on Turbulent Boundary Layers. J. Fluids Eng, *121*(1), 44–51.

- Schultz, M. P., Walker, J. M., Steppe, C. N., & Flack, K. A. (2015). Impact of diatomaceous biofilms on the frictional drag of fouling-release coatings. Biofouling, 31(9-10), 759–773. doi: 10.1080/08927014.2015.1108407
- Schüttrumpf, H., Brinkmann, M., Cofalla, C., Frings, R. M., Gerbersdorf, S. U., Hecker, M., ... others (2011). A new approach to investigate the interactions between sediment transport and ecotoxicological processes during flood events. Environmental Sciences Europe, 23(1), 1–5.
- Sengottuvel, D. (2015). Biofilms exposed to abrupt changes in flow conditions: Differences in floc properties and their settling behaviour (Master thesis). Institute for Modelling Hydraulic and Environmental Systems - University of Stuttgart.
- Shang, Q., Fang, H., Zhao, H., He, G., & Cui, Z. (2014). Biofilm effects on size gradation, drag coefficient and settling velocity of sediment particles. International Journal of Sediment Research, 29(4), 471–480. doi: 10.1016/S1001-6279(14)60060-3
- Shen, Y., Monroy, G. L., Derlon, N., Janjaroen, D., Huang, C., Morgenroth, E., ... Nguyen, T. H. (2015). Role of Biofilm Roughness and Hydrodynamic Conditions in *Legionella pneumophila* Adhesion to and Detachment from Simulated Drinking Water Biofilms. Environmental Science & Technology, 49(7), 4274–4282. doi: 10.1021/es505842v
- Shields, A. (1936). Application of similarity principles and turbulence research to bed-load movement (translated by W. P. Ott and J. C. van Uchelen). Pasadena: Calif. Inst. of Technol.
- Singer, G., Besemer, K., Hödl, I., Chlup, A., Hochedlinger, G., Stadler, P., & Battin, T. J. (2006). Microcosm design and evaluation to study stream microbial biofilms. Limnology and Oceanography: Methods, 4(11), 436–447.
- Southard, J. (2006). 12.090 Introduction to Fluid Motions, Sediment Transport, and Current-Generated Sedimentary Structures. Retrieved from <http://ocw.mit.edu>
- Spears, B. M., Saunders, J. E., Davidson, I., & Paterson, D. M. (2008). Microalgal sediment biostabilisation along a salinity gradient in the Eden Estuary, Scotland: unravelling a paradox. Marine and Freshwater Research, 59(4), 313–321. doi: 10.1071/MF07164
- Stal, L. J. (2010). Microphytobenthos as a biogeomorphological force in intertidal sediment stabilization. Ecological Engineering, 36(2), 236–245. doi: 10.1016/j.ecoleng.2008.12.032
- Stewart, P. (2012). Mini-review: convection around biofilms. Biofouling The Journal of Bioadhesion and Biofilm Research, 28(2), 187–198.
- Stoodley, P., Cargo, R., Rupp, C. J., Wilson, S., & Klapper, I. (2002). Biofilm material properties as related to shear-induced deformation and detachment phenomena. Journal of Industrial Microbiology and Biotechnology, 29(6), 361–367. doi: 10.1038/sj.jim.7000282
- Stoodley, P., Dodds, I., Boyle, J. D., & Lappin-Scott, H. M. (1998). Influence of hydrodynamics and nutrients on biofilm structure. Journal of applied microbiology, 85(S1).
- Sutherland, T., Amos, C., & Grant, J. (1998). The effect of buoyant biofilms on the erodibility

- of sublittoral sediments of a temperate microtidal estuary. Limnol Ocranogr, 43(2), 225–235.
- Thesenvitz, C. (2014). Investigations on biofilm topography at hydraulic relevant scales (Master thesis). Institute for Modelling Hydraulic and Environmental Systems - University of Stuttgart.
- Thom, M., Schmidt, H., Gerbersdorf, S. U., & Wieprecht, S. (2015a). Seasonal Biostabilization and Erosion Behavior of Fluvial Biofilms Under Different Hydrodynamic and Light Conditions. International Journal of Sediment Research, 30, 273–284.
- Thom, M., Schmidt, H., Wieprecht, S., & Gerbersdorf, S. U. (2012). Physikalische Modellversuche zur Untersuchung des Einflusses von Biofilm auf die Sohlenstabilität. Wasserwirtschaft, 102(6), 32–36.
- Thom, M., Schmidt, H., Wieprecht, S., & Gerbersdorf, S. U. (2015b). Biostabilization of fluvial sediments: An improved device to address an old problem. In E-proceedings of the 36th IAHR World Congress. The Hague, Netherlands.
- Thom, M., Schmidt, H., Wieprecht, S., & Gerbersdorf, S. U. (2016). The role of surface adhesion in biostabilization processes. Stuttgart.
- Thom, M., Thesenvitz, C., Wieprecht, S., & Gerbersdorf, S. U. (2014). Continues Survey of Biofilm Topography using a Laserscanning Method. Ecohydraulics conference, Trondheim, Norway.
- Thomas, R. E., Johnson, M. F., Frostick, L. E., Parsons, D. R., Bouma, T. J., Dijkstra, J. T., ... Vousdoukas, M. I. (2014). Physical modelling of water, fauna and flora: knowledge gaps, avenues for future research and infrastructural needs. Journal of Hydraulic Research, 52(3), 311–325. doi: 10.1080/00221686.2013.876453
- Tipler, P. A., & Mosca, G. (2015). Physik (J. Wagner, Ed.). Berlin, Heidelberg: Springer Berlin Heidelberg.
- Tolhurst, T. J., Black, K. S., Shayler, S., Mather, S., Black, I., Baker, K., & Paterson, D. M. (1999). Measuring the in situ Erosion Shear Stress of Intertidal Sediments with the Cohesive Strength Meter (CSM). Estuarine, Coastal and Shelf Science, 39(2), 281–294.
- Tolhurst, T. J., Consalvey, M., & Paterson, D. M. (2008). Changes in cohesive sediment properties associated with the growth of a diatom biofilm. Hydrobiologia, 596(1), 225–239. doi: 10.1007/s10750-007-9099-9
- Tolhurst, T. J., Gust, G., & Paterson, D. M. (2002). The influence of an extracellular polymeric substance (EPS) on cohesive sediment stability. Proceedings in Marine Science, 5, 409–425.
- Tourney, J., & Ngwenya, B. T. (2014). The role of bacterial extracellular polymeric substances in geomicrobiology. Chemical Geology, 386, 115–132. doi: 10.1016/j.chemgeo.2014.08.011
- Tran-Cong, S., Gay, M., & Michaelides, E. E. (2004). Drag coefficients of irregularly shaped particles. Powder Technology, 139(1), 21–32. doi: 10.1016/j.powtec.2003.10.002

- Ubertini, M., Lefebvre, S., Rakotomalala, C., & Orvain, F. (2015). Impact of sediment grain-size and biofilm age on epipelagic microphytobenthos resuspension. Journal of Experimental Marine Biology and Ecology, *467*, 52–64. doi: 10.1016/j.jembe.2015.02.007
- Van Rijn, L. C. (1984). Sediment transport, part 1: bed load transport. Journal of hydraulic engineering, *110*(10), 1431–1456.
- Vasudevan, R. (2014). Biofilms: Microbial Cities of Scientific Significance. Journal of Microbiology & Experimentation, *1*(3).
- Vignaga, E. (2012). The effect of biofilm colonization on the stability of non-cohesive sediments (PhD thesis). University of Glasgow.
- Vignaga, E., Haynes, H., & Sloan, W. (2012). Quantifying the tensile strength of microbial mats grown over noncohesive sediments. Biotechnology and Bioengineering, *109*(5), 1155–1164. doi: 10.1002/bit.24401
- Vignaga, E., Sloan, D. M., Luo, X., Haynes, H., Phoenix, V. R., & Sloan, W. T. (2013). Erosion of biofilm-bound fluvial sediments. Nature Geoscience, *6*(9), 770–774. doi: 10.1038/ngeo1891
- Villanueva, V. D., Font, J., Schwartz, T., & Romání, A. M. (2011). Biofilm formation at warming temperature: acceleration of microbial colonization and microbial interactive effects. Biofouling, *27*(1), 59–71. doi: 10.1080/08927014.2010.538841
- Walker, J. M., Sargison, J. E., & Henderson, A. D. (2013). Turbulent boundary-layer structure of flows over freshwater biofilms. Experiments in Fluids, *54*(12). doi: 10.1007/s00348-013-1628-x
- Wäsche, S., Horn, H., & Hempel, D. C. (2000). Mass transfer phenomena in biofilm systems. Water science and technology, *41*(4-5), 357–360.
- Webb, J. (1969). Biologically significant properties of submerged marine sands. Proceedings of the royal society, *174*(1036). doi: 10.1098/rspb.1969.0098
- Wiberg, P., & Smith, J. (1987). Calculations of the Critical Shear Stress for Motion of Uniform and Heterogeneous Sediments. Water Resources Research, *23*(8), 1471–1480.
- Widdows, J., Brinsley, M. D., Salkeld, P. N., & Lucas, C. H. (2000). Influence of biota on spatial and temporal variation in sediment erodability and material flux on a tidal flat (Westerschelde, The Netherlands). Marine Ecology Progress Series, *194*, 23–37.
- Witt, O., & Westrich, B. (2003). Quantification of erosion rates for undisturbed contaminated cohesive sediment cores by image analysis. In The Interactions between Sediments and Water (pp. 271–276). Springer.
- Wu, W., & Wang, S. S. (1999). Movable bed roughness in alluvial rivers. Journal of Hydraulic Engineering, *125*(12), 1309–1312.
- Yallop, M. L., de Winder, B., Paterson, D. M., & Stal, L. J. (1994). Comparative structure, primary production and biogenic stabilization of cohesive and non-cohesive marine sediments inhabited by microphytobenthos. Estuarine, Coastal and Shelf Science, *39*(6), 565–582.

- Yallop, M. L., Paterson, D., & Wellsbury, P. (2000). Interrelationships between Rates of Microbial Production, Exopolymer Production, Microbial Biomass, and Sediment Stability in Biofilms of Intertidal Sediments. Microbial Ecology, 39(2), 116–127. doi: 10.1007/s002489900186
- You, Z.-J. (2004). Discussion of “Initiation of Movement of Quartz Particles”. Journal of Hydraulic Engineering, 130(8), 755–761.
- Zafar, U., Hare, C., Hassanpour, A., & Ghadiri, M. (2014). Drop test: A new method to measure the particle adhesion force. Powder Technology, 264, 236–241. doi: 10.1016/j.powtec.2014.04.022
- Ziegler, T. (2013). Validierung eines Kamerasystems zur Bestimmung des Absinkverhaltens biologisch stabilisierter Sedimente (Bachelor thesis). Institute for Modelling Hydraulic and Environmental Systems - University of Stuttgart.

Appendix A

Additional materials: MagPI-IP

A.1 Hardware

A.1.1 Circuit diagram of the “filter” and control board

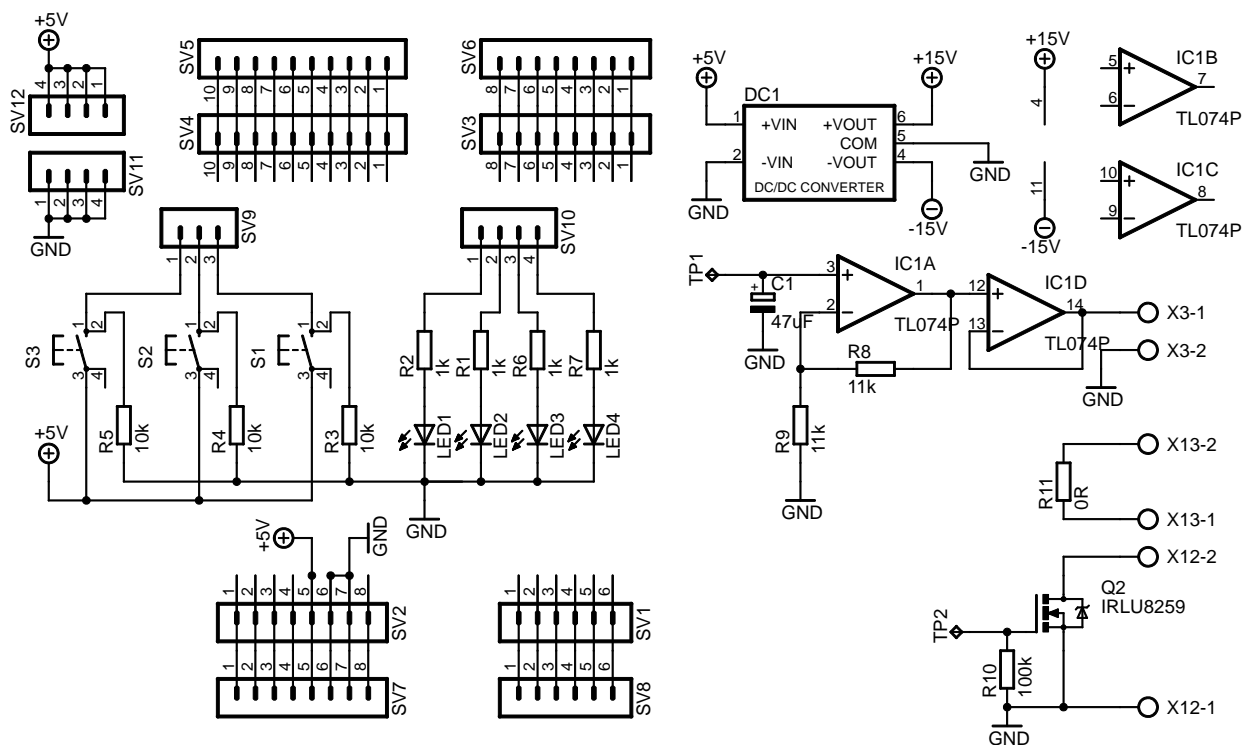


Figure A.1 Circuit diagram of the “filter” for smoothing the PWM signal to control the increase of electric current. Additionally, buttons (S1... S3) and LEDs (LED1... LED4) are implemented for starting/stopping the measuring routine and checking the current status. The “filter” is designed and produced by Steffen Hägele.

A.1.2 Datasheet electromagnet: Ersatz1000



Figure A.2 Image of the Electromagnet “Ersatz1000” (from Bierbaum, 2015)

Core-material	Mu-metal
Diameter of the core	8 mm
Length of the core	150 mm
Number of windings	1000
Diameter of the wire	0.52 mm

Table A.1 General information on materials: “Ersatz1000” (from Bierbaum, 2015)

Calibration curve ($F_{em} = f(I)$)

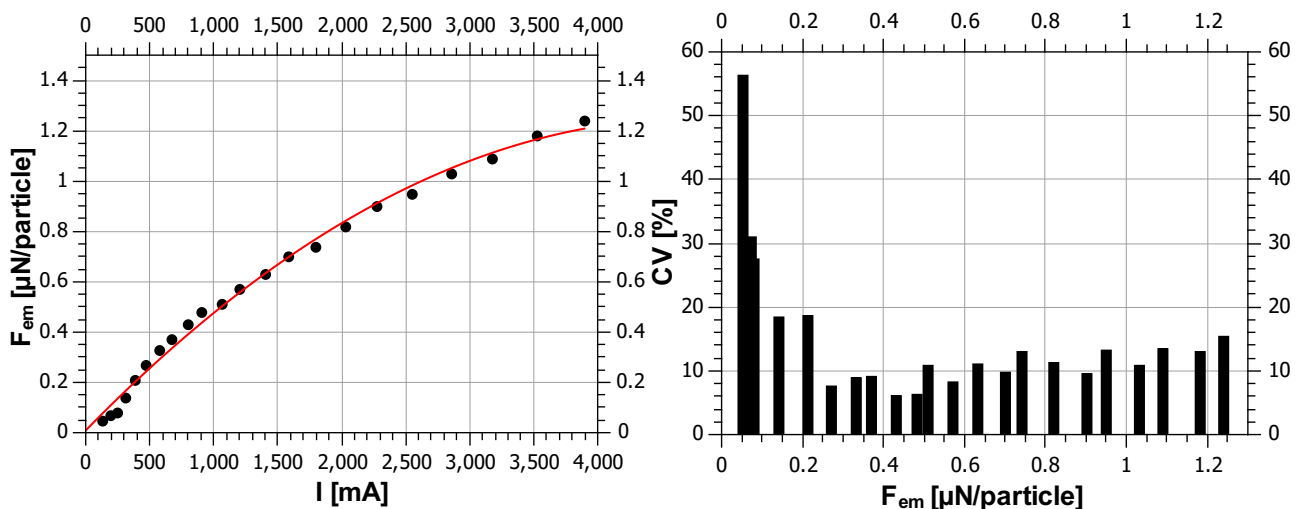


Figure A.3 Mechanical characteristics of the electromagnet “Ersatz1000” as determined in the calibration procedure (FP: PARTRAC[®] 200... 350 μ m, distance to particles: 4mm). *Left:* Calibration curve illustrating the relation between the tensile force exerted by the electromagnet on one particle and the applied electric current. The \bullet symbols are the averaged values of six measurements and the red line is the fitted quadratic regression. *Right:* The coefficients of variation for tensile forces on a single particle at the applied increments of electric current. Six measurements are conducted and the standard deviation at each increment is divided by the mean value to obtain the CV as a measure for precision of the calibration procedure.

Polynomial regression ($R^2 = 0.994$, $n = 6$)

$$F_{em} = 8.819 \times 10^{-3} + 5.216 \times 10^{-4}I - 5.488 \times 10^{-8}I^2 \quad (\text{A.1})$$

A.1.3 Datasheet electromagnet: Original1000

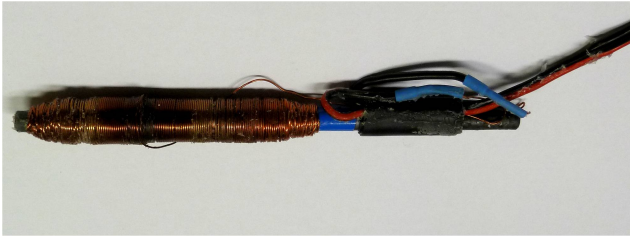


Figure A.4 Image of the Electromagnet “Original1000” (from Bierbaum, 2015)

Core-material	Mu-metal
Diameter of the core	7 mm
Length of the core	150 mm
Number of windings	1000
Diameter of the wire	0.52 mm

Table A.2 General information on materials: “Original1000” (from Bierbaum, 2015)

Calibration curve ($F_{em} = f(I)$)

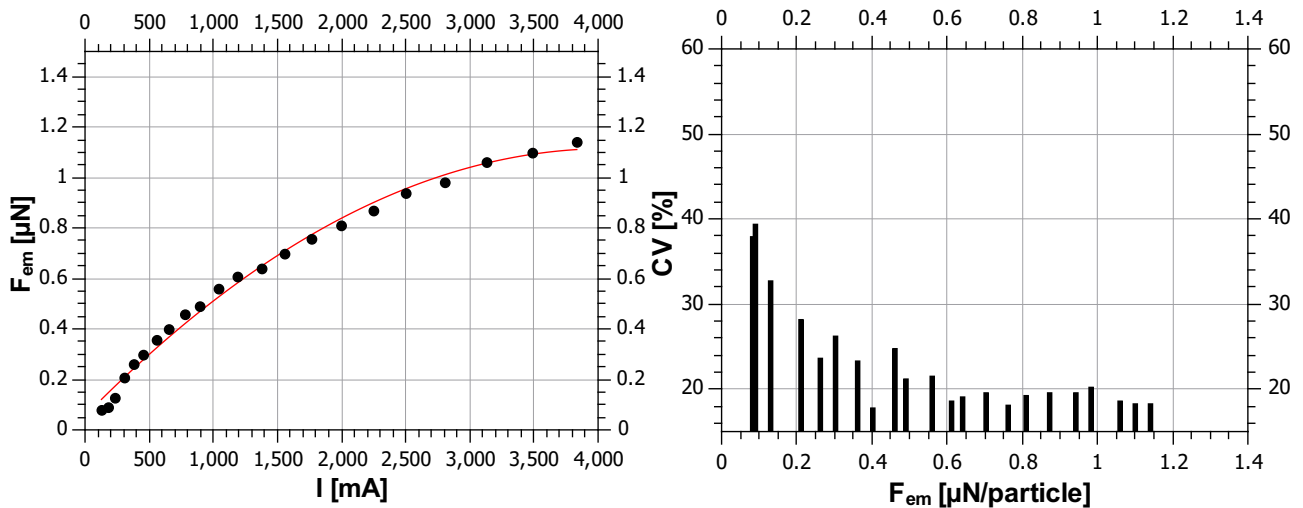


Figure A.5 Mechanical characteristics of the electromagnet “Original1000” as determined in the calibration procedure (FP: PARTRAC[®] 200 . . . 350 μ m, distance to particles: 4mm). *Left:* Calibration curve illustrating the relation between the tensile force exerted by the electromagnet on one particle and the applied electric current. The • symbols are the averaged values of eight measurements and the red line is the fitted quadratic regression. *Right:* The coefficients of variation for tensile forces on a single particle at the applied increments of electric current. Eight measurements are conducted and the standard deviation at each increment is divided by the mean value to obtain the CV as a measure for precision of the calibration procedure.

Polynomial regression ($R^2 = 0.993, n = 8$)

$$F_{em} = 5.538 \times 10^{-2} + 5.190 \times 10^{-4}I - 6.354 \times 10^{-8}I^2 \quad (\text{A.2})$$

A.1.4 Datasheet electromagnet: Ersatz1500



Figure A.6 Image of the Electromagnet “Original1500” (equivalent to the “Ersatz1500”) (from Bierbaum, 2015)

Core-material	Mu-metal
Diameter of the core	8 mm
Length of the core	150 mm
Number of windings	1500
Diameter of the wire	0.52 mm

Table A.3 General information on materials: “Ersatz1500” (from Bierbaum, 2015)

Calibration curve ($F_{em} = f(I)$)

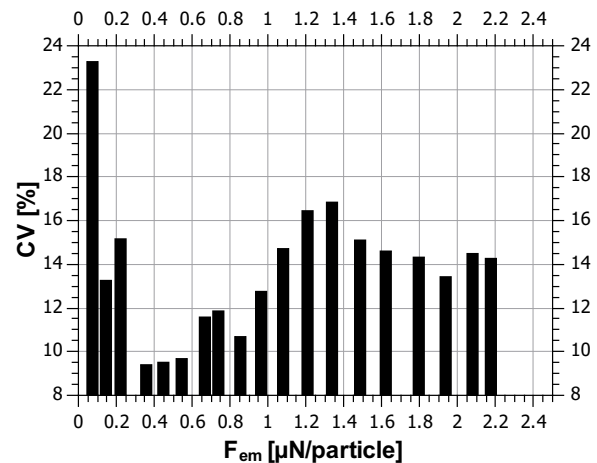
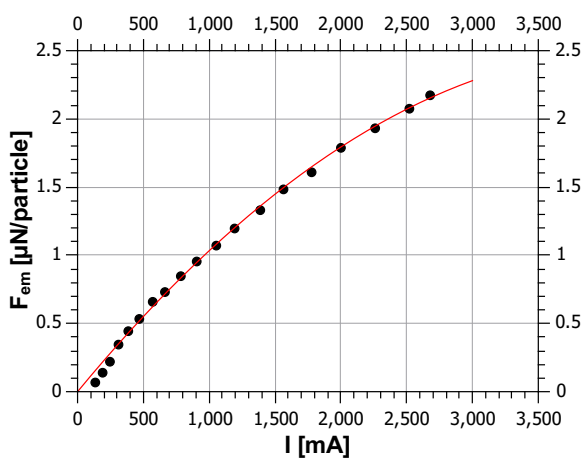


Figure A.7 Mechanical characteristics of the electromagnet “Ersatz1500” as determined in the calibration procedure (FP: PARTRAC[®] 200... 350 μm, distance to particles: 4mm). *Left:* Calibration curve illustrating the relation between the tensile force exerted by the electromagnet on one particle and the applied electric current. The • symbols are the averaged values of six measurements and the red line is the fitted quadratic regression. *Right:* The coefficients of variation for tensile forces on a single particle at the applied increments of electric current. Six measurements are conducted and the standard deviation at each increment is divided by the mean value to obtain the CV as a measure for precision of the calibration procedure.

Polynomial regression ($R^2 = 0.997, n = 6$)

$$F_{em} = 1.170 \times 10^{-3}I - 1.367 \times 10^{-7}I^2 \quad (\text{A.3})$$

A.2 Flow charts illustrating the basic procedures of measuring surface adhesion forces with the MagPI-IP

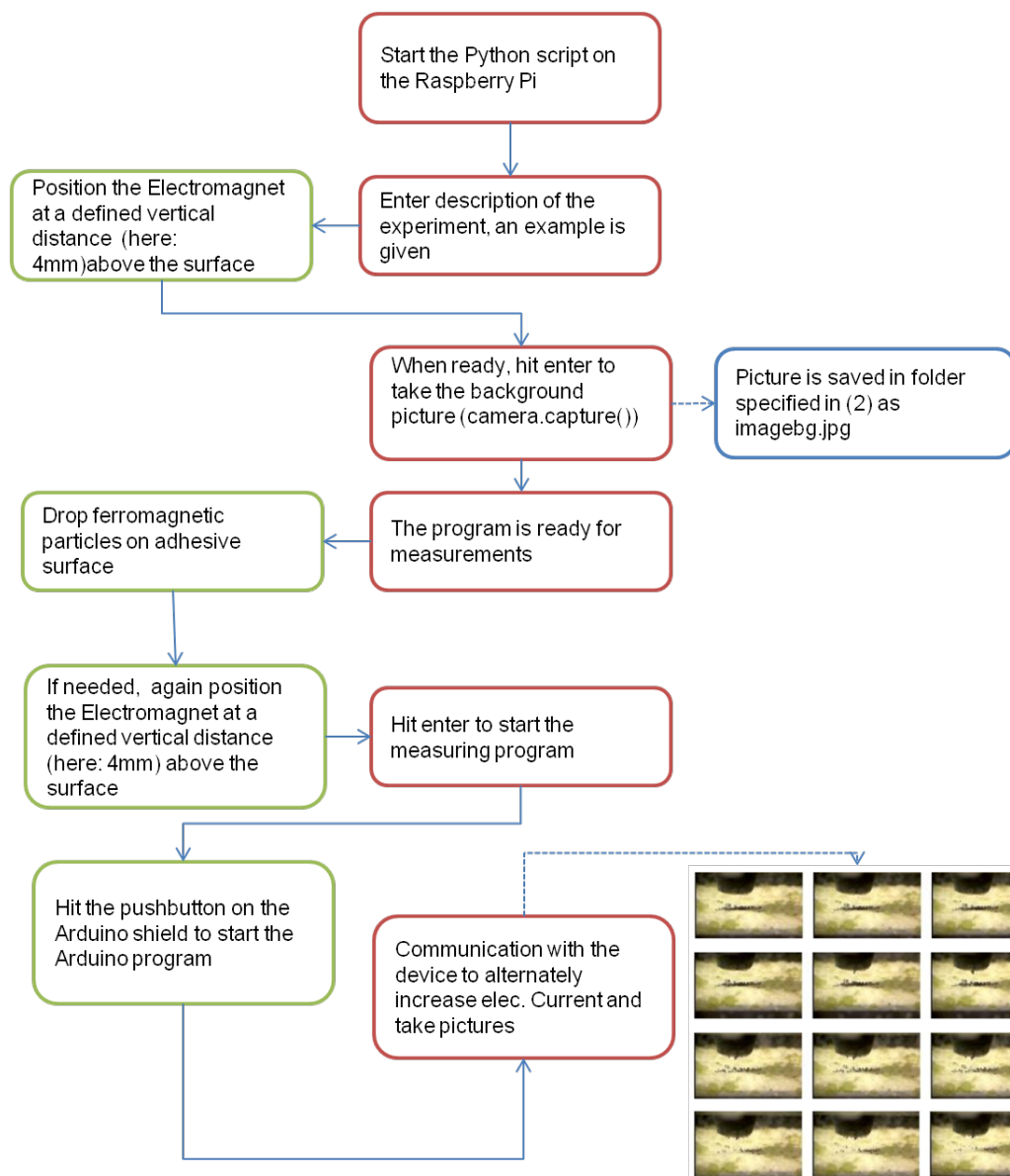


Figure A.8 Flow chart of the general procedure to control the MagPI-IP and conduct measurements. Green boxes: The operator is requested to physically intervene in the process. Red boxes: The operator is requested to communicate with the software. Blue boxes: Additional information.

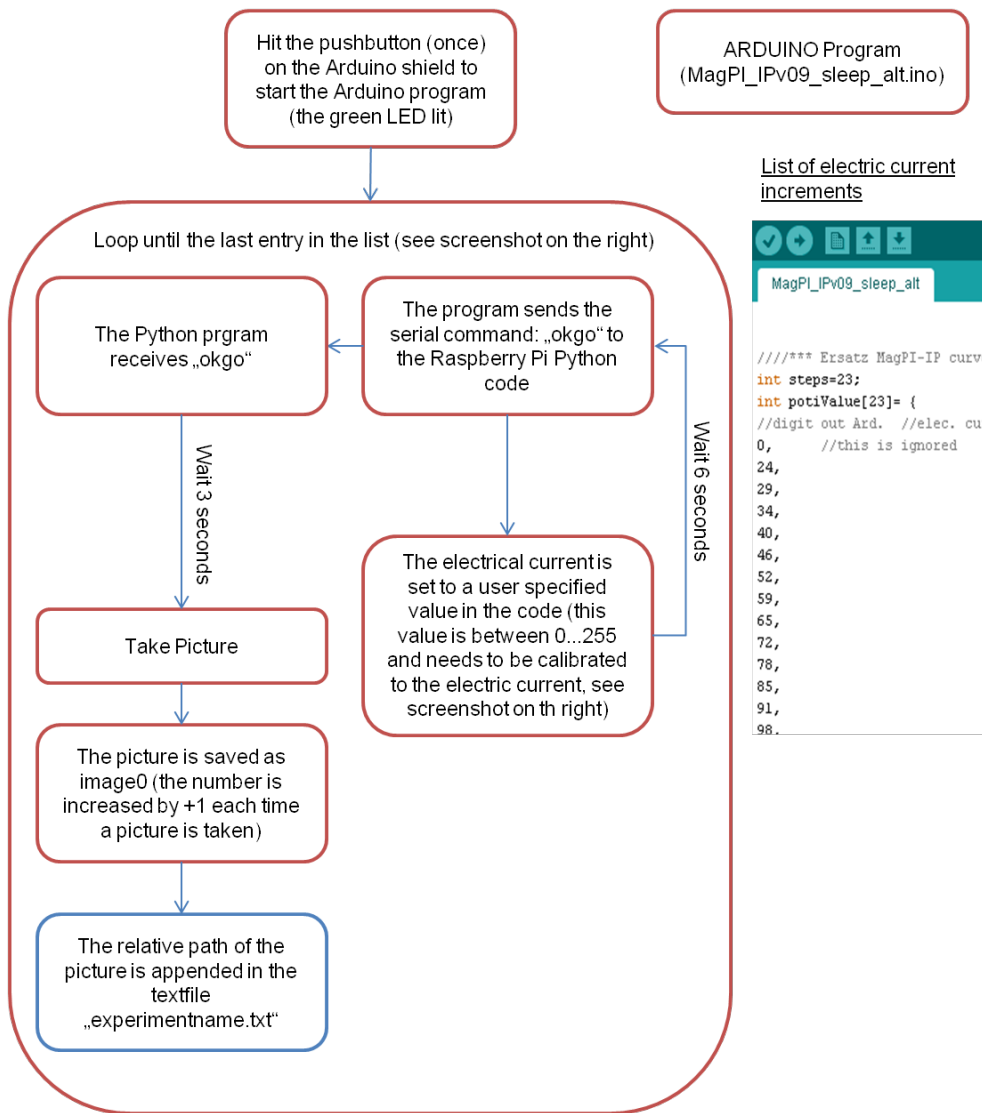


Figure A.9 The basic functioning principle of the Arduino software to control the changes in electric current and communication with the Raspberry PI to take pictures.

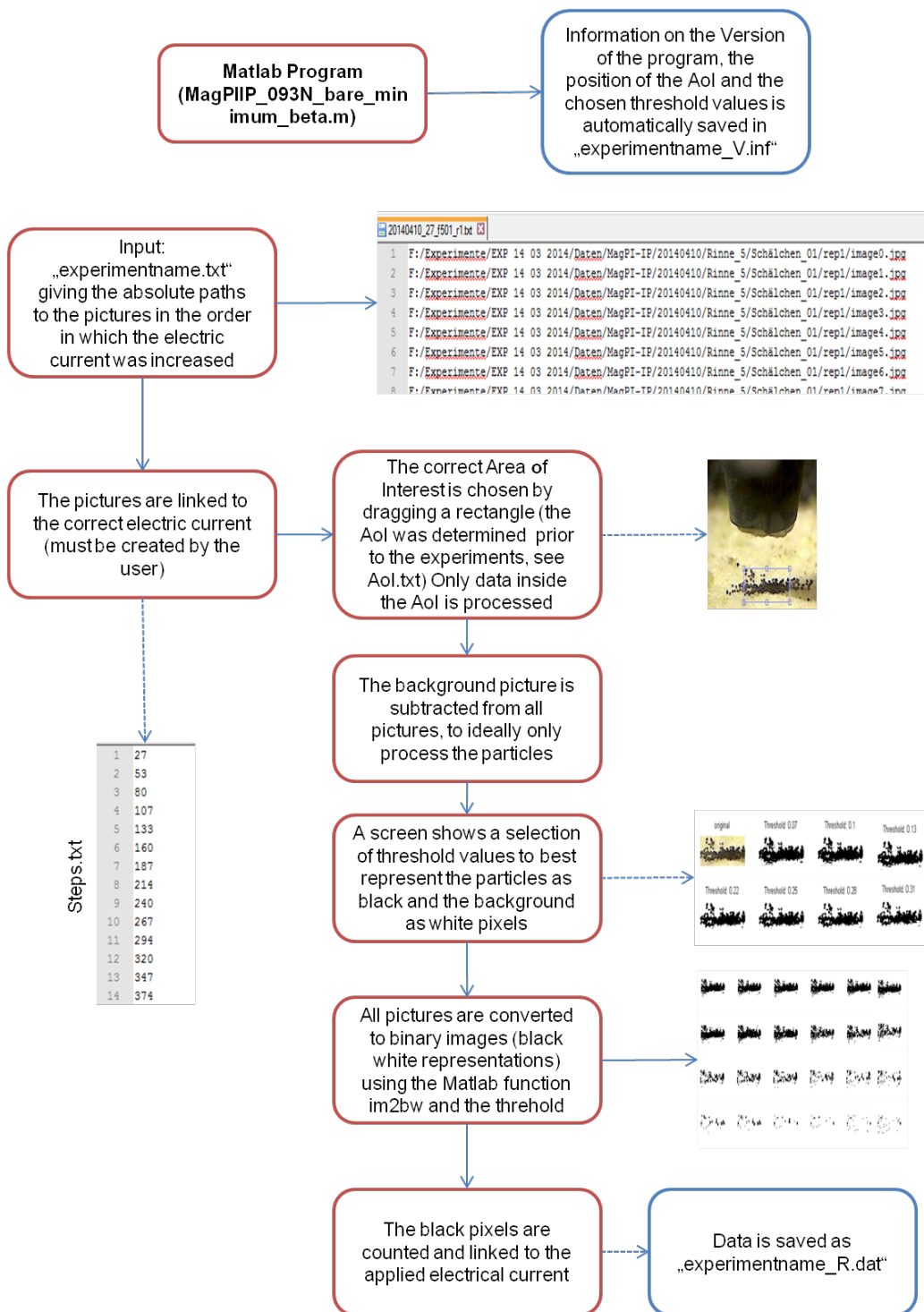


Figure A.10 The basic functioning principle of the MATLAB[®] code to process images (part 1). Input files and determination of ferromagnetic particles.

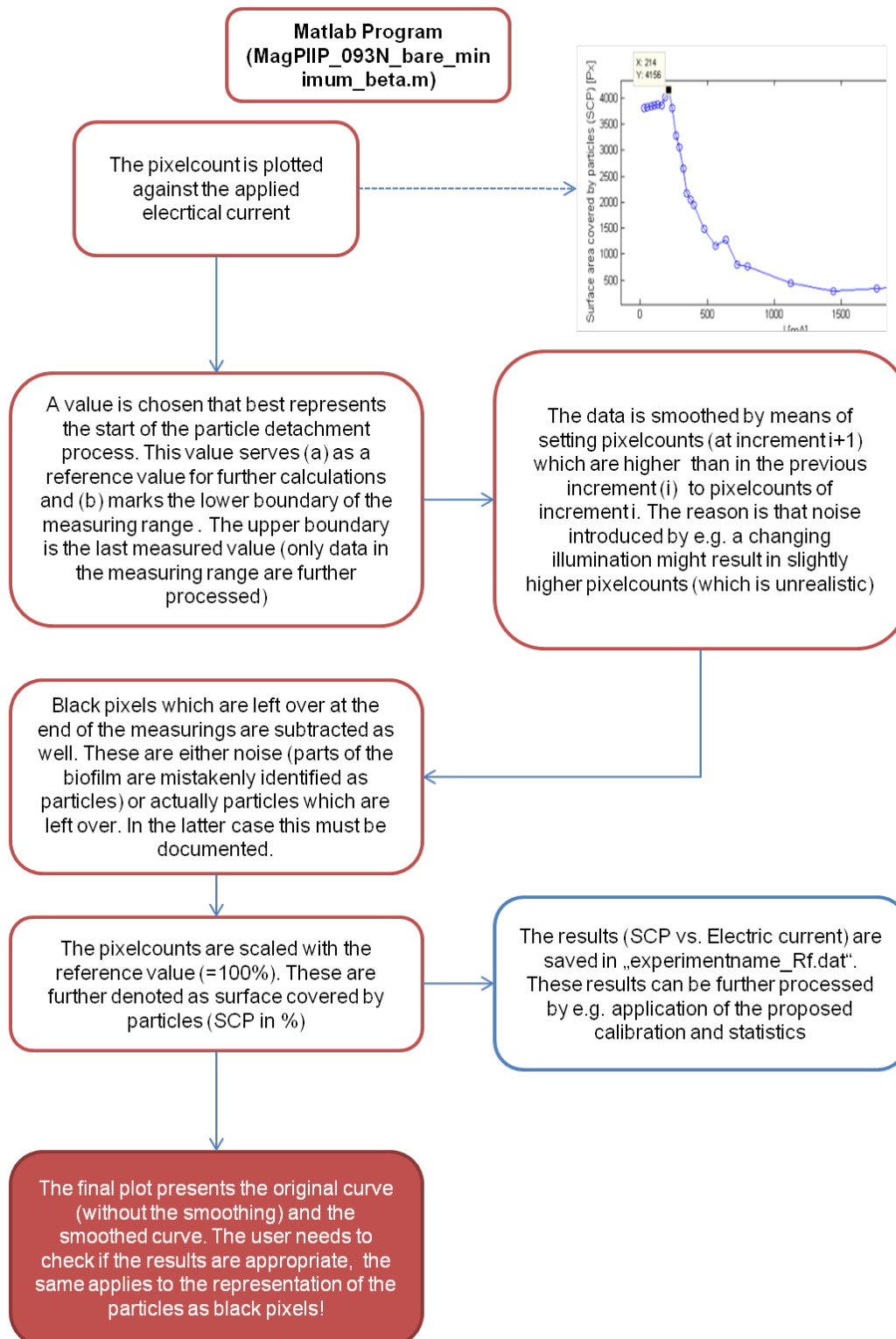


Figure A.11 The basic functioning principle of the MATLAB[®] code to process images (part 2). Processing of data (*inter alia* “filtering” and “subtraction”), visualization and output in text files.

For the MATLAB® code to work, additionally the following files need to be edited:

Table A.4 Input files needed to define important parameters for the MATLAB® image processing code.

File Name	Description	Content: example
Aol.txt	Defines the Area of Interest	365.997 284.1773 136.5305 63.9478
greythresh.txt	Defines the lowest black and white threshold	0.005
steps.txt	Contains a list of electric currents that are applied during one measurement (increasing order)	0 20 40 60

Appendix B

Additional methods

B.1 Preparation of EPS surrogates

Xanthan Gum (XG, from *Xanthomonas campestris*, Sigma Aldrich, G1253-100G)

- pour mass of XG powder in 200 ml tap water until the desired concentration is reached
- heat slowly in microwave to $\approx 100^\circ\text{C}$, stir in between
- mix 50 ml of the surrogate with 140 g sediment (here: glass beads $d \approx 100 \dots 200 \mu\text{m}$)
- fill mixture into petri-dish (placed in a small box), make sure there are no air bubbles
- after 10 mins: fill up the box with water
- after one hour: conduct measurements

B.2 Erosion evaluation form

CASE: SEDIMENT Tau crit << Biofilm Tau crit

Sediment Cartridge nr.:		First date of growth:	
Date of Erosion:		Bearbeiter-Erosion:	

History

Date	Environment: (Light regime, Rivername)

General Information on Sediment:

Size (μm):		Material:		Nr. of Layers:	
-------------------------	--	-----------	--	----------------	--

Information on Layers and Stability:**

LAYER 1 (Biofilm Surface):**

Color (%-Area):	White	Bright-Green	Dark-Green	Bright-Brown	Dark-Brown
Structure (%-Area):	Like Carpet	Sheets	Like Wool	Like Sediment	
Flat	Rough	Filaments (few)	Filaments (many)	Above Cart Height (mm):	Cracks* Bubbles
Description:	Discharge Q	Info (sudden detachment, single grains)			
Random Erosion					
Continuesly eroding					
Last Area eroded					

LAYER 2:**

Color (%-Area):	White	Bright-Green	Dark-Green	Bright-Brown	Dark-Brown
Structure (%-Area):	Flat	Rough	Sheets	Like Sediment	Misc: Bubbles Cracks*:
Description:	Discharge Q	Reason:			
Random Failure (max. 1 Sheet):		Unterspülung	Ohne	Versatz	
Continuesly Failing (>2 Sheets):		Unterspülung	Ohne	Versatz	
Definite total failing:		Unterspülung	Ohne	Versatz	
Failure coupled with failure of Layer 1(%-Area)		Info:			

LAYER 3:**

Color (%-Area):	White	Bright-Green	Dark-Green	Bright-Brown	Dark-Brown
Structure (%-Area):	Flat	Rough	Sheets	Like Sediment	Misc: Bubbles Cracks*:
Description:	Discharge Q	Reason:			
Random Failure (max. 1 Sheet):		Unterspülung	Ohne	Versatz	
Continuesly Failing (>2 Sheets):		Unterspülung	Ohne	Versatz	
Definite total failing:		Unterspülung	Ohne	Versatz	
Failure coupled with failure of Layer 2(%-Area)		Info:			

ADDITIONAL:

Description:	Discharge Q	Info
Kolkbildung bis Sediment		
Sediment looks like rocks? (normal=Yes)		

- *few= 1-8 sheets; medium= 8- 15; many >> 15
- ** not influenced by side effects, A layer is influenced by Biofilm (Definition)

Figure B.1 Developed form to note all relevant processes of erosion.

Appendix C

Additional data

C.1 Tabular overview on all conducted experiments

Table C.1 Overview on the experiments: Mar13, May13, Jul13, Aug13, Nov13, their study objectives and applied boundary conditions. Quantitative values for the notations of the boundary conditions can be found in Table D.1

Name	Study objectives	Flumenr.	ID	Light intensity	τ_b
March 2013	Hydrodynamics	1	Mar13QLA	Medium	Low
		2	Mar13QLB	Medium	Low
		3	Mar13QMA	Medium	Medium
		4	Mar13QMB	Medium	Medium
		5	Mar13QHA	Medium	High
		6	Mar13QHB	Medium	High
May 2013	Hydrodynamics	1	May13QHA	Medium	High
		2	May13QMA	Medium	Medium
		3	May13QLA	Medium	Low
		4	May13QLB	Medium	Low
		5	May13QMB	Medium	Medium
		6	May13QHB	Medium	High
July 2013	Light intensity	1	Jul13LNA	None	Medium
		2	Jul13LMA	Medium	Medium
		3	Jul13LHA	High	Medium
		4	Jul13LNB	None	Medium
		5	Jul13LMB	Medium	Medium
		6	Jul13LHB	High	Medium
August 2013	Light intensity	1	Aug13LHA	High	Medium
		2	Aug13LMA	Medium	Medium
		3	Aug13LNA	None	Medium
		4	Aug13LHB	High	Medium
		5	Aug13LMB	Medium	Medium
		6	Aug13LNB	None	Medium
November 2013	Hydrodynamics	1	Nov13QMA	Medium	Medium
		2	Nov13QLA	Medium	Low
		3	Nov13QHA	Medium	High
		4	Nov13QHB	Medium	High
		5	Nov13QLB	Medium	Low
		6	Nov13QMB	Medium	Medium

Table C.2 Overview on the experiments: Mar14, Jul14, Mar15*, their study objectives and applied boundary conditions. March15: the flow velocity is changed during the experiments (see Table C.3 for details). Quantitative values for the notations of the boundary conditions can be found in Table D.1

Name	Study objectives	Flumenr.	ID	Light intensity	τ_b
March 2014	Light intensity	1	Mar14LMA	Medium	Low
		2	Mar14LHA	High	Low
		3	Mar14LNA	None	Low
		4	Mar14LMB	Medium	Low
		5	Mar14LHB	High	Low
		6	Mar14LNB	None	Low
July 2014	Hydrodynamics	1	Jul14QHA	Medium	High
		2	Jul14QHB	Medium	High
		3	Jul14QHC	Medium	High
		4	Jul14QLA	Medium	Low
		5	Jul14QLB	Medium	Low
		6	Jul14QLC	Medium	Low
March 2015*	Hydrodynamics*	1	Mar15QH+A*	Medium	Highest
		2	Mar15QHA*	Medium	High
		3	Mar15QLA*	Medium	Low
		4	Mar15QH+B*	Medium	Highest
		5	Mar15QLB*	Medium	Low
		6	Mar15QHB*	Medium	High

Table C.3 Detailed experimental program of Mar15*

Flumenr.	weeks 1...2	week 3	weeks 4...11
1	QL	QL	QH+
2	QL	QL	QH
3	QL	QL	QL
4	QL	QH	QH+
5	QL	QH	QH
6	QL	QH	QL

C.2 Complete overview on erosion data

March 2013

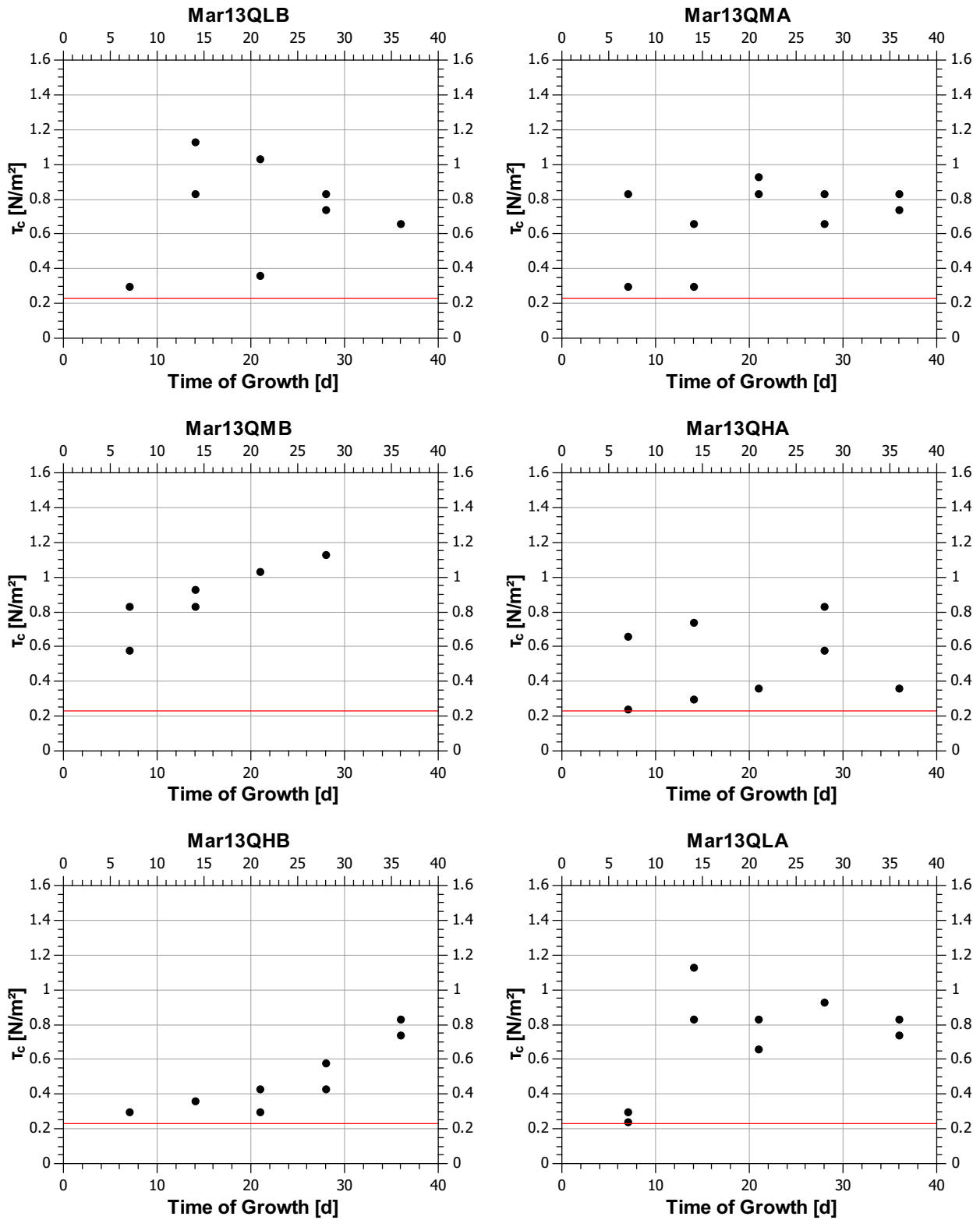


Figure C.1 Mar13: Critical bed shear stress versus time of growth. The solid red line denotes the non-biostabilized sediment stability. Each • symbol represents one erosion measurement.

May 2013

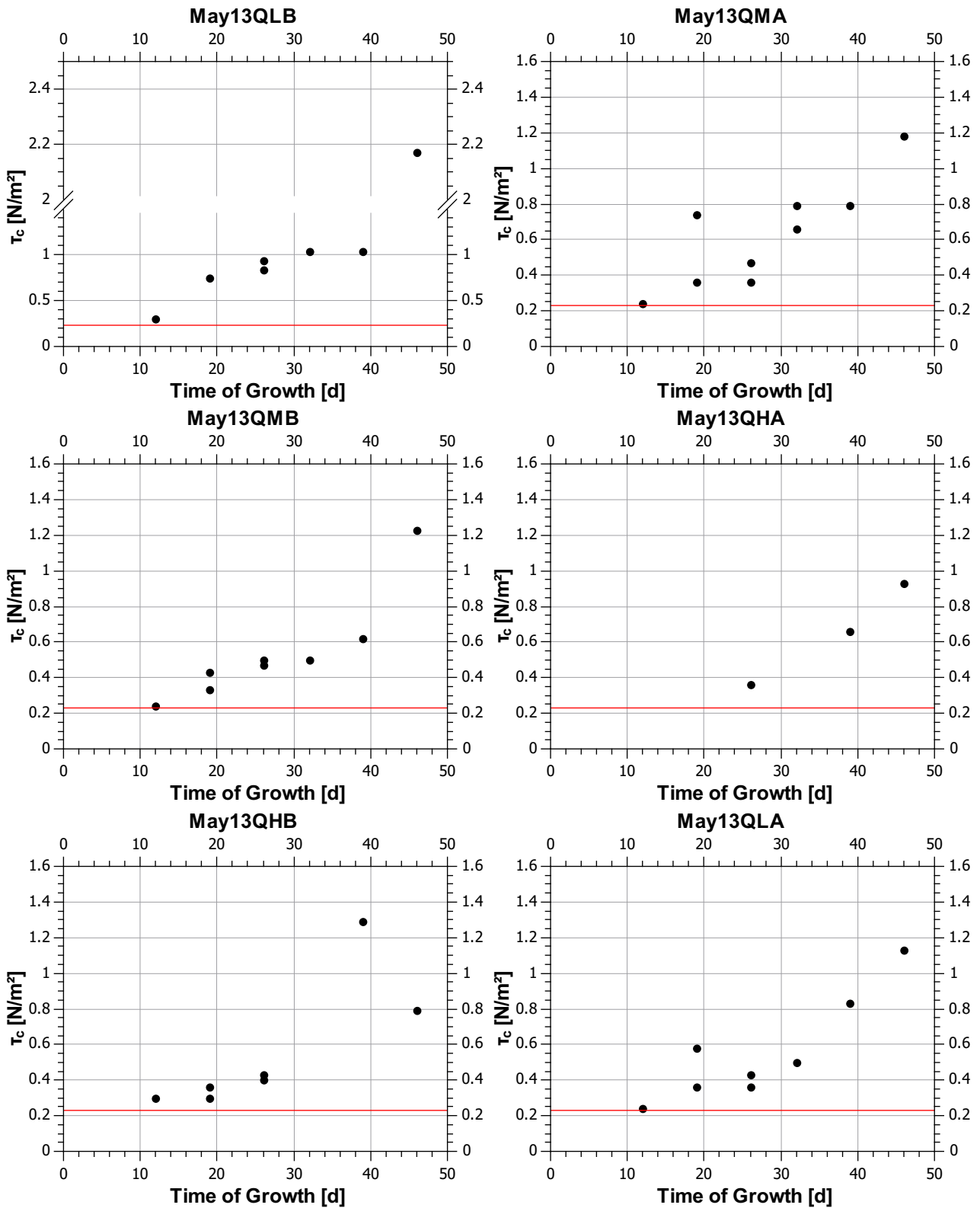


Figure C.2 May13: Critical bed shear stress versus time of growth. The solid red line denotes the non-biostabilized sediment stability. Each • symbol represents one erosion measurement.

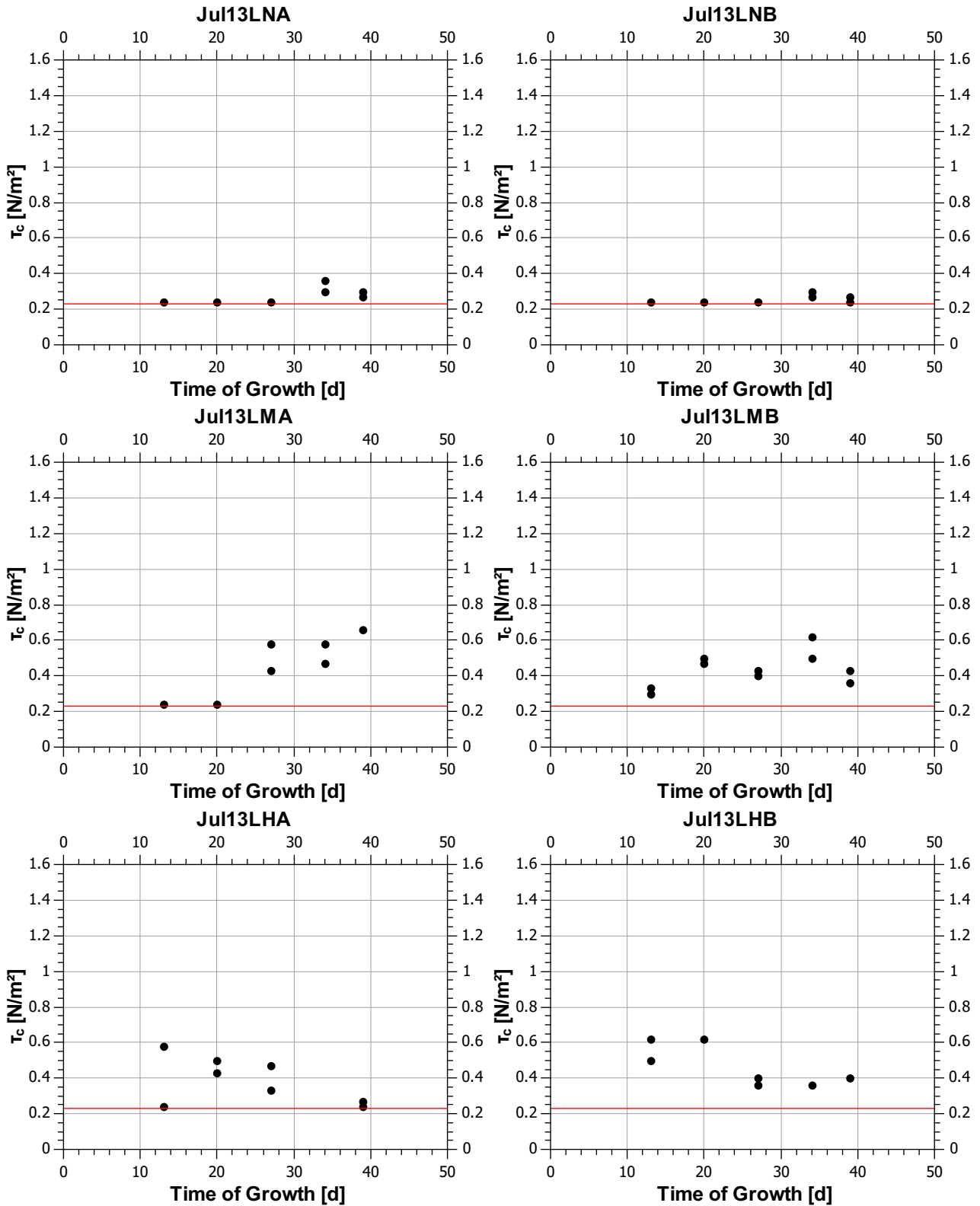


Figure C.3 Jul13: Critical bed shear stress versus time of growth. The solid red line denotes the non-biostabilized sediment stability. Each • symbol represents one erosion measurement.

August 2013

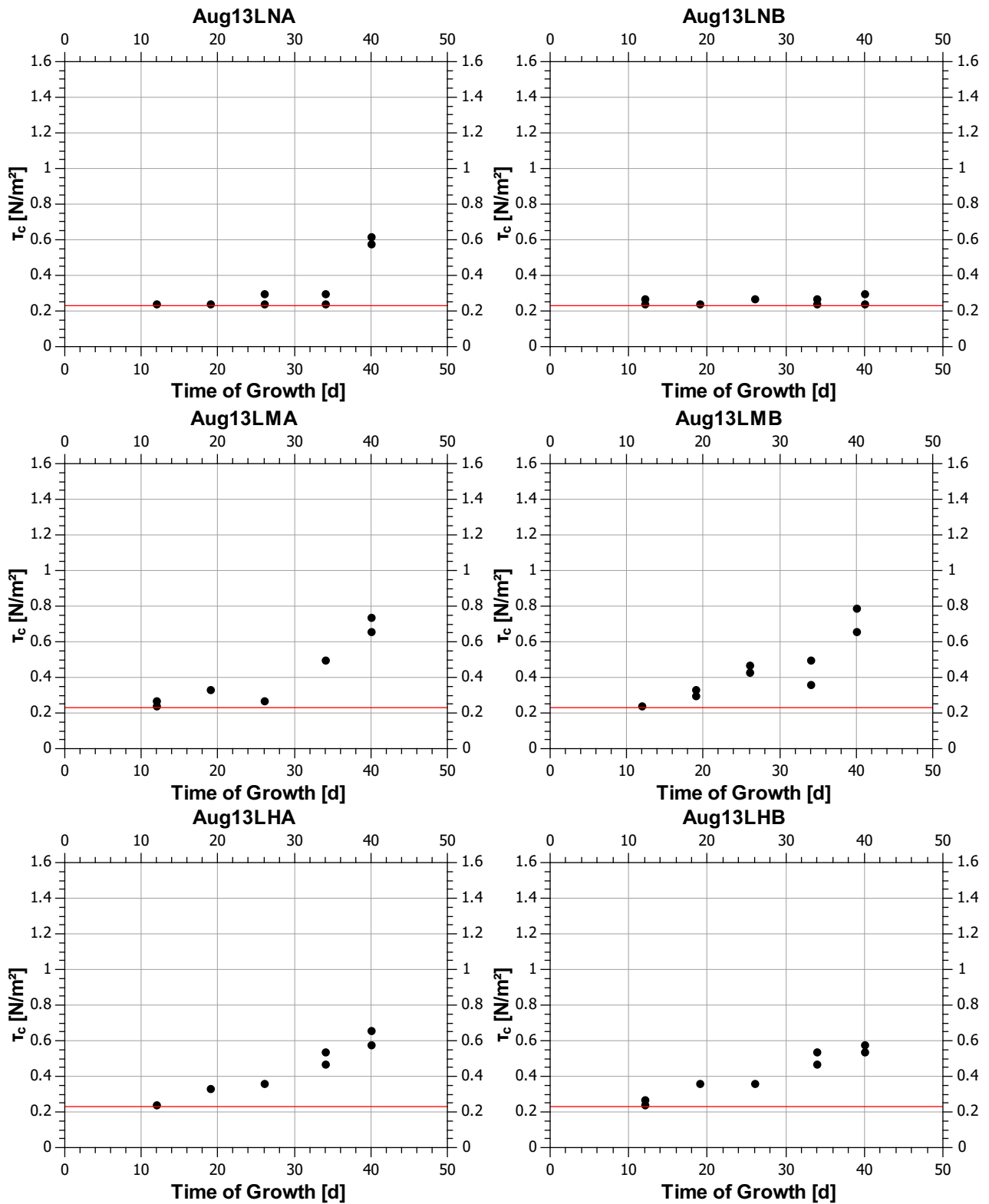


Figure C.4 Aug13: Critical bed shear stress versus time of growth. The solid red line denotes the non-biostabilized sediment stability. Each • symbol represents one erosion measurement.

November 2013

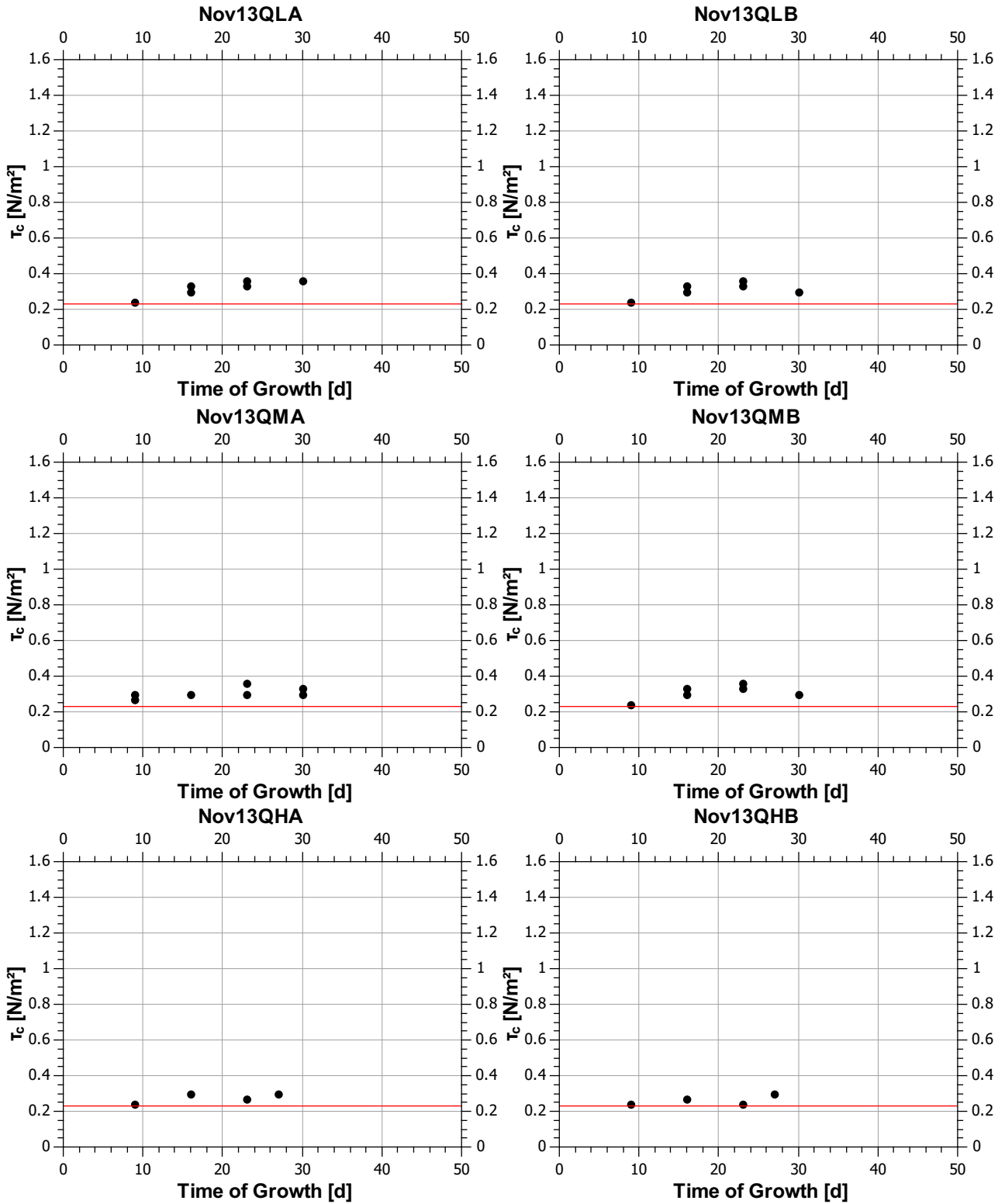


Figure C.5 Nov13: Critical bed shear stress versus time of growth. The solid red line denotes the non-biostabilized sediment stability. Each • symbol represents one erosion measurement.

March 2014

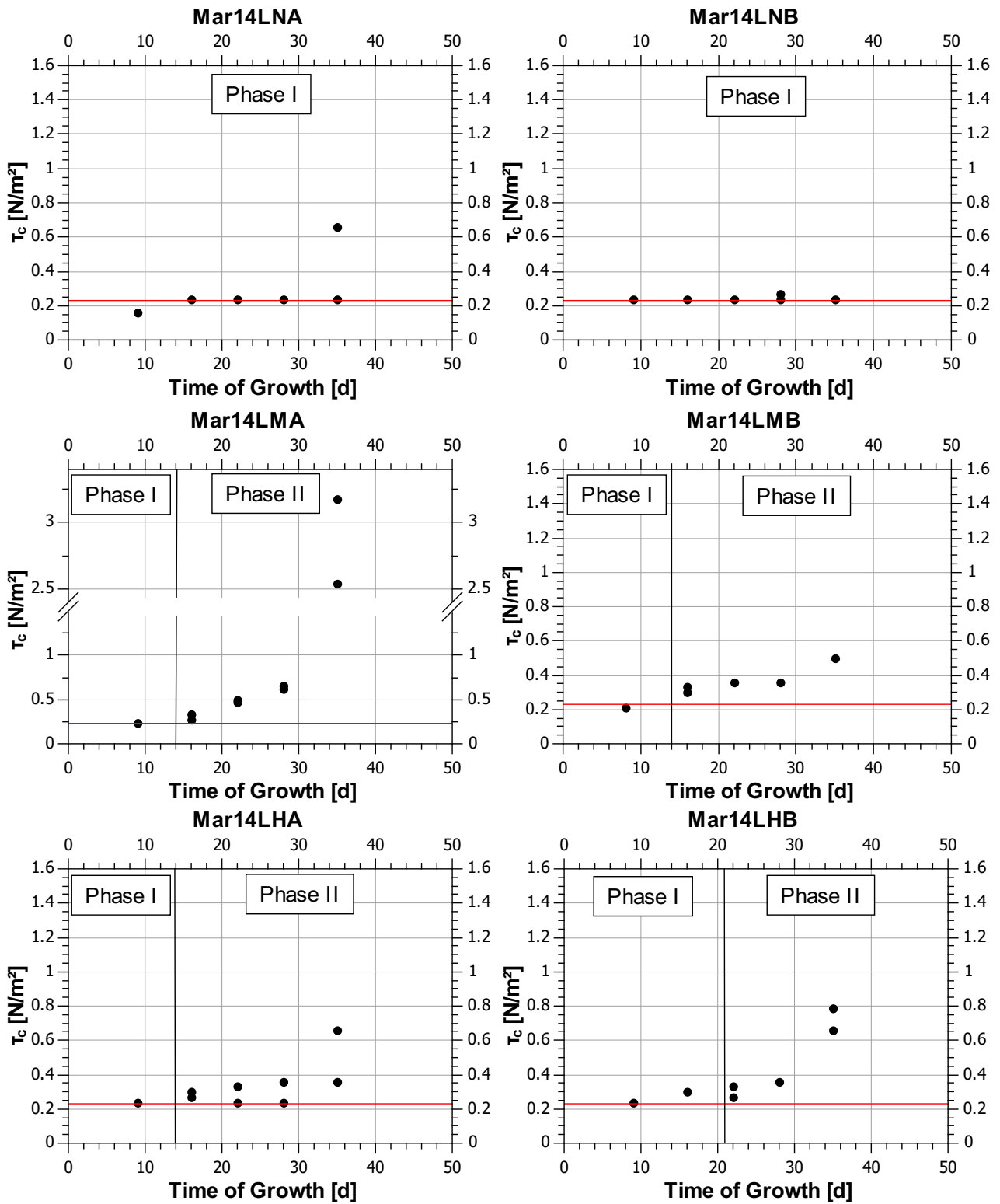


Figure C.6 Mar13: Critical bed shear stress versus time of growth. The solid red line denotes the non-biostabilized sediment stability. Each \bullet symbol represents one erosion measurement. Additionally the different phases determined by the evaluation of surface adhesion measurements are illustrated.

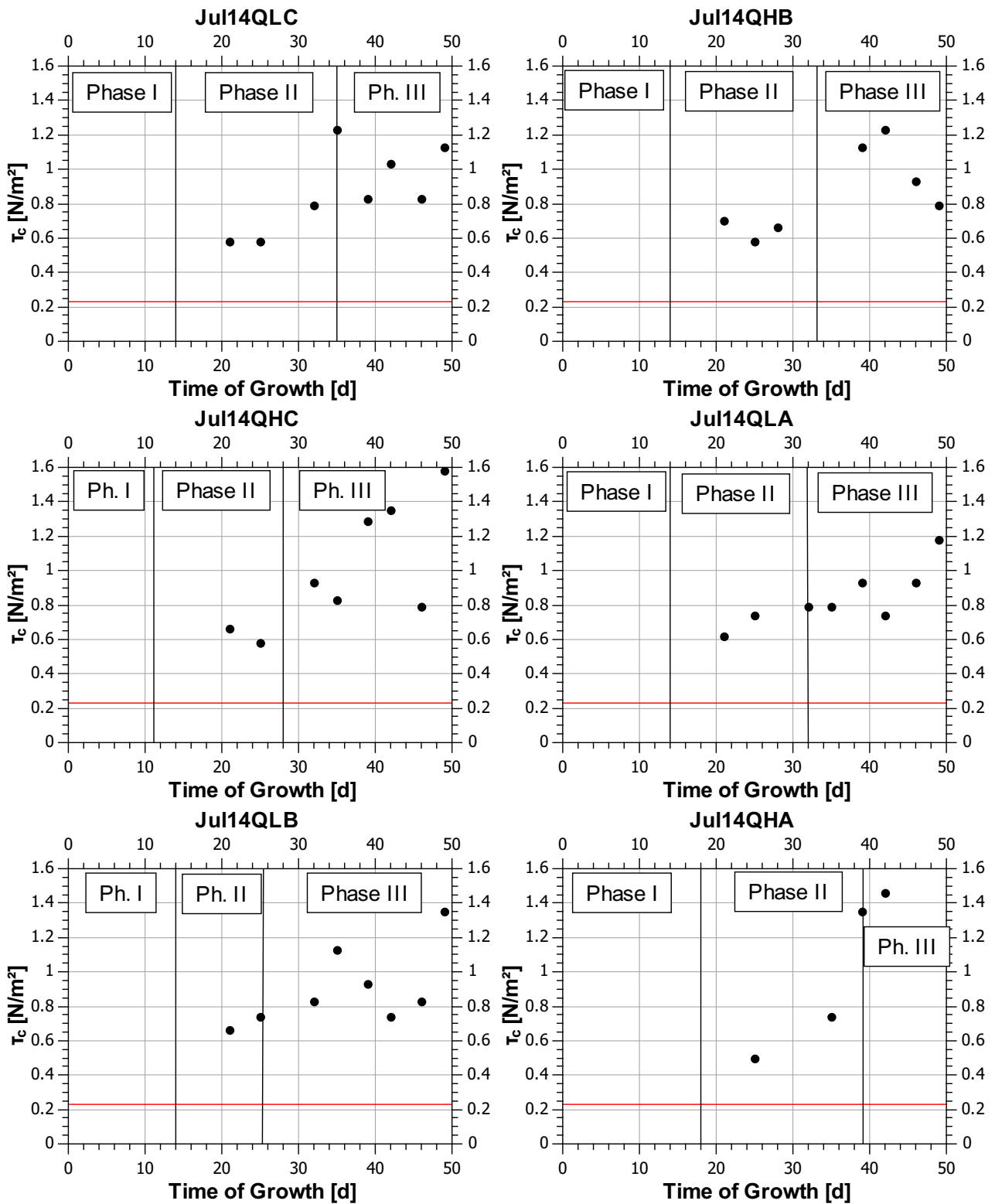


Figure C.7 Jul14: Critical bed shear stress versus time of growth. The solid red line denotes the non-biostabilized sediment stability. Each • symbol represents one erosion measurement. Additionally the different phases determined by the evaluation of surface adhesion measurements are illustrated.

March 2015*

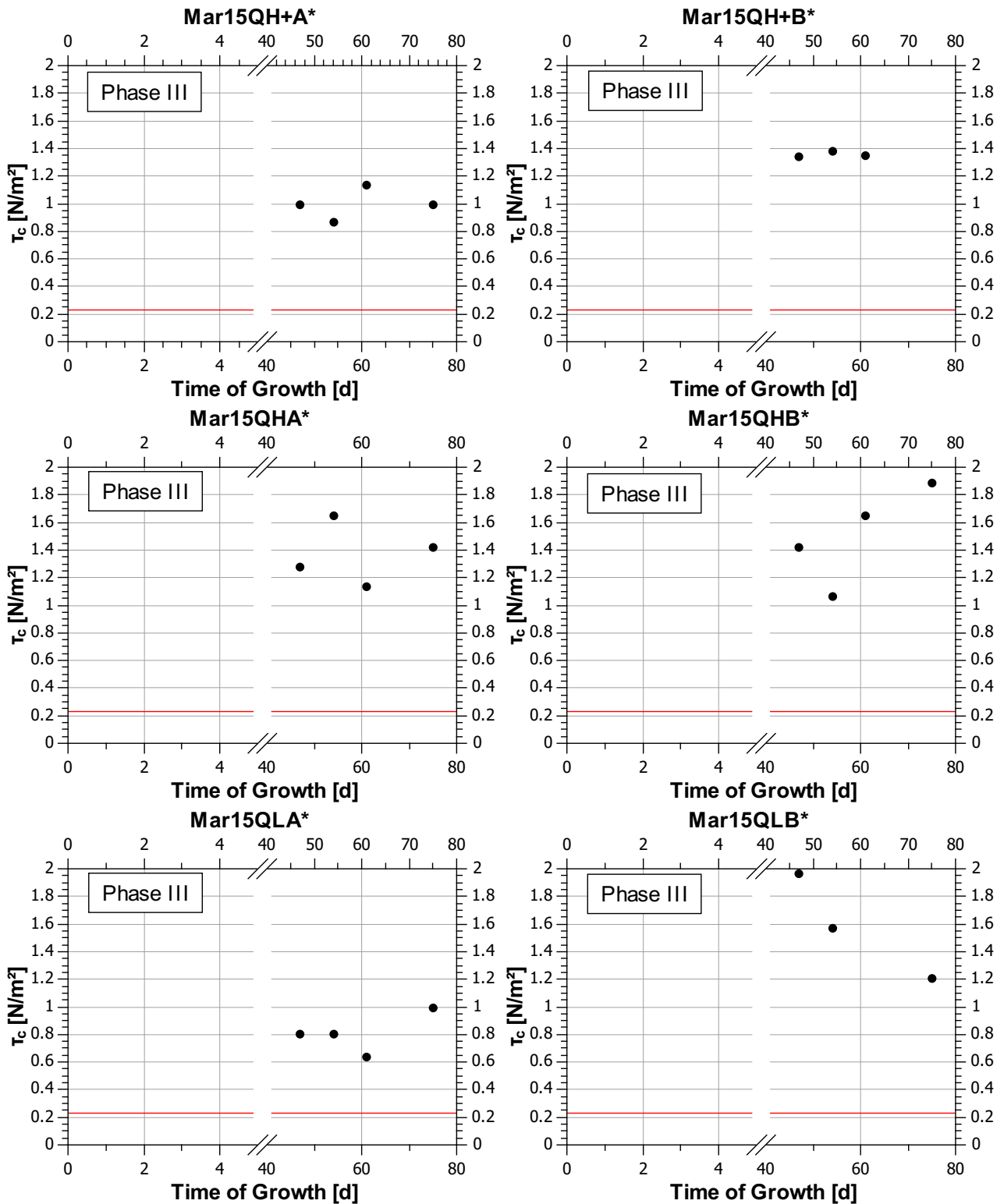


Figure C.8 Mar15*: Critical bed shear stress versus time of growth. The solid red line denotes the non-biostabilized sediment stability. Each • symbol represents one erosion measurement. All measurements conducted on mechanically matured biofilms (Ph. III). Please note that in this experiment the roughness of the flume bed is modified to account for the biofilm roughness (see Part F). The results of Mar15 are not directly comparable to the results of the other experiments.

C.3 Complete overview on surface adhesion data

March 2014

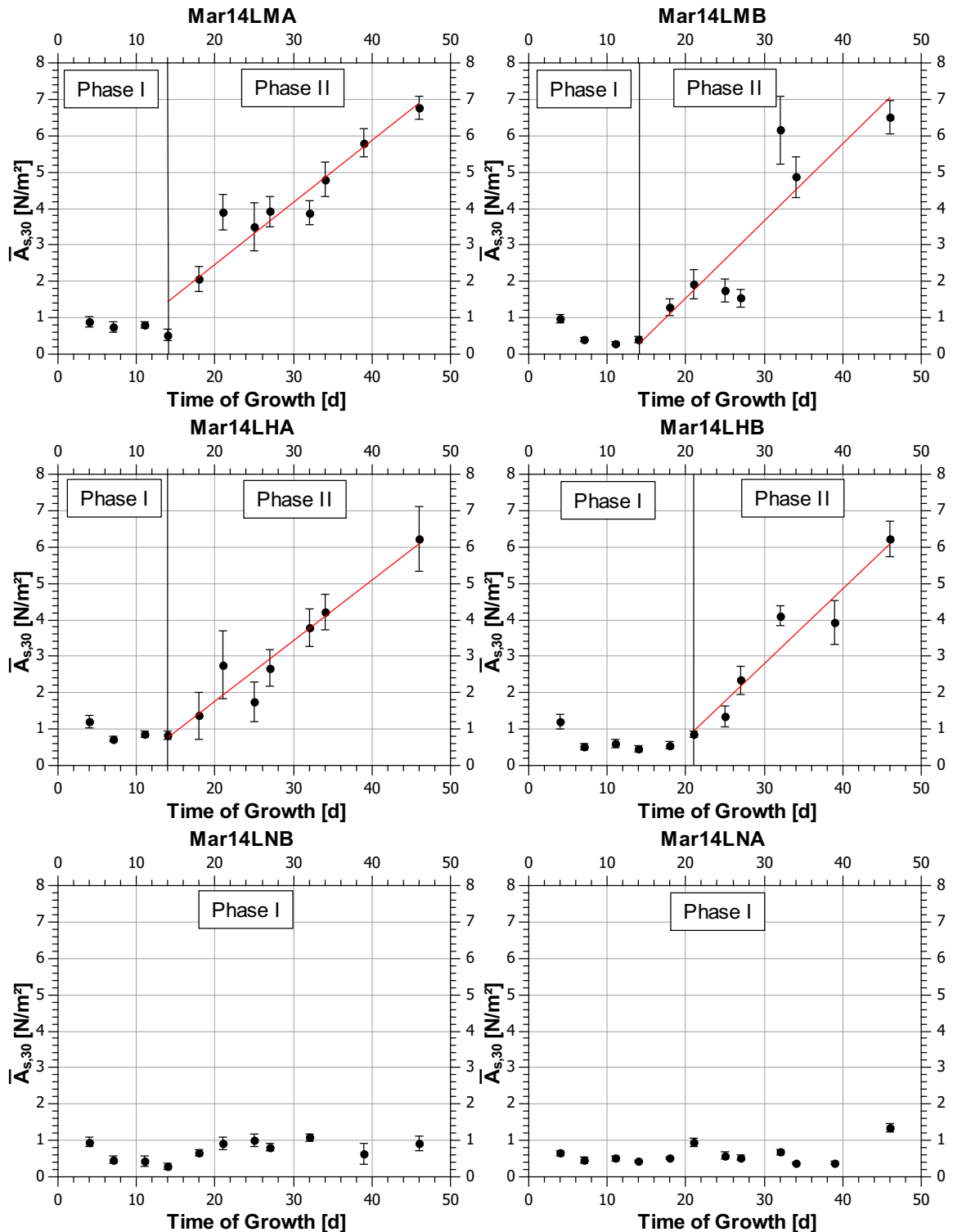


Figure C.9 Mar14: Surface adhesion versus time of growth. The • symbols represent the averaged surface adhesion (\pm standard error). The data is subdivided into phases with characteristic development (see Part D). The solid red line denotes a linear regression in Phase II

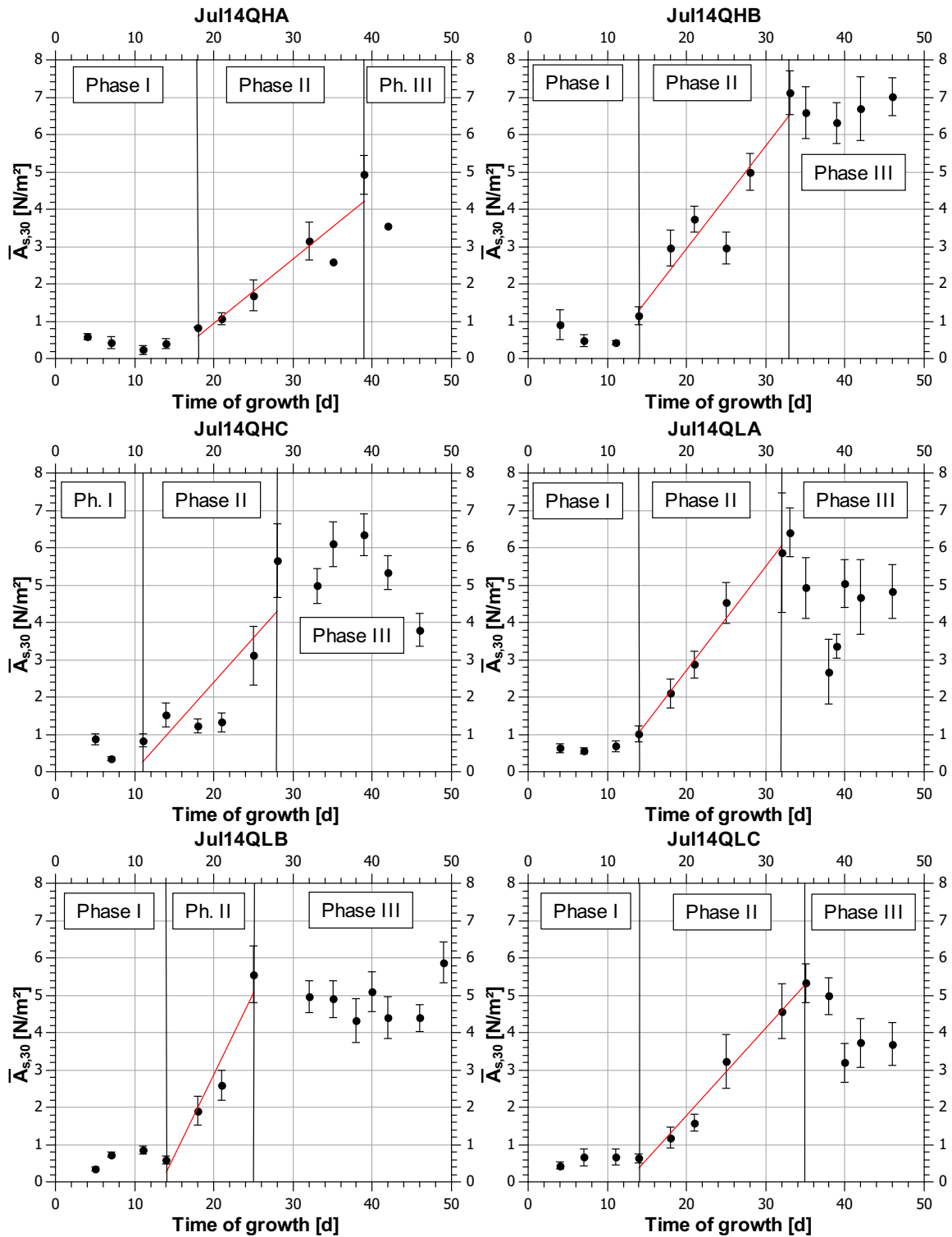


Figure C.10 Jul14: Surface adhesion versus time of growth. The • symbols represent the averaged surface adhesion (\pm standard error). The data is subdivided into phases with characteristic development (see Part D). The solid red line denotes a linear regression in Phase II

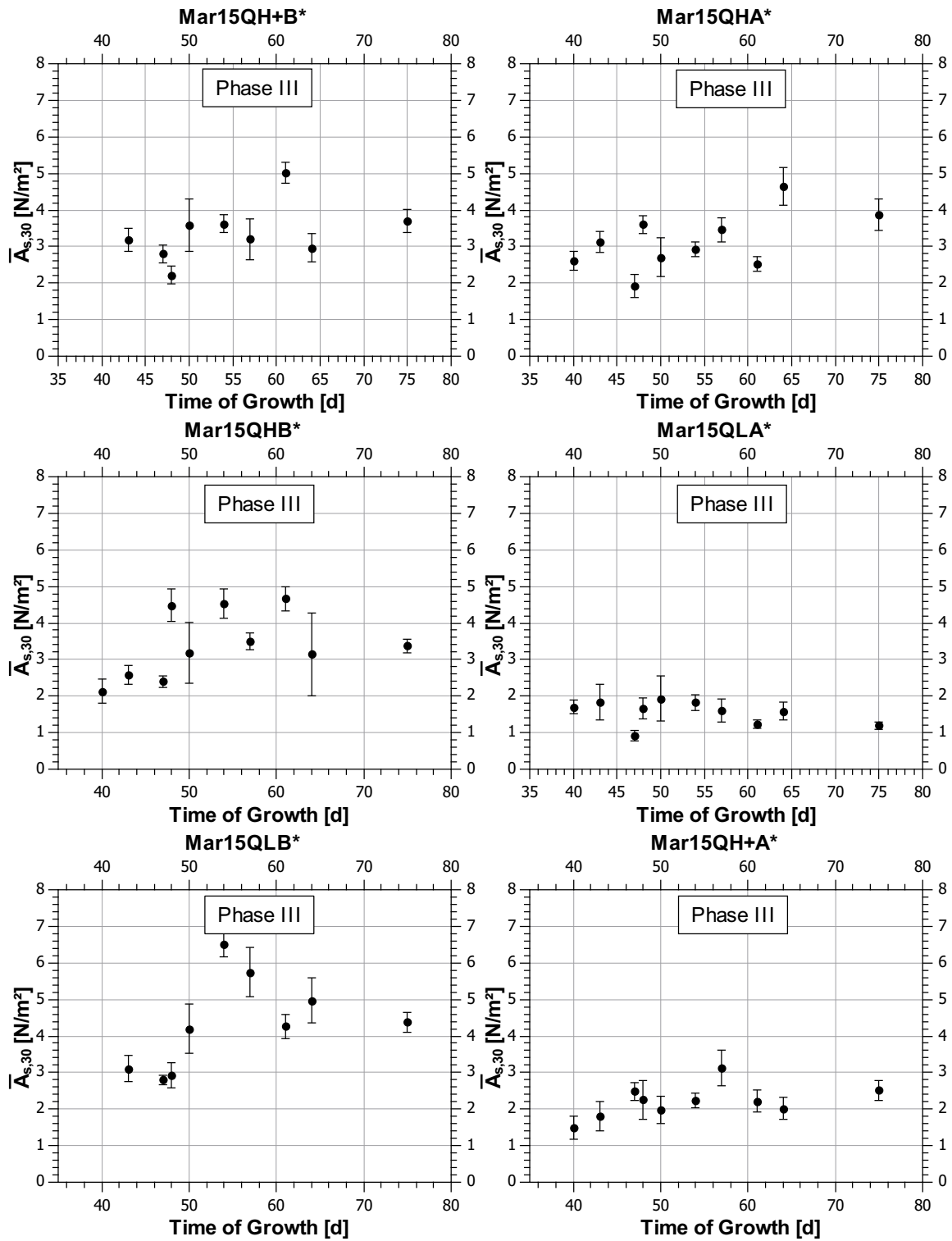


Figure C.11 Mar15: Surface adhesion versus time of growth. The • symbols represent the averaged surface adhesion (\pm standard error). The data is subdivided into phases with characteristic development (see Part D).

C.3.1 Relation between critical bed shear stress and surface adhesion

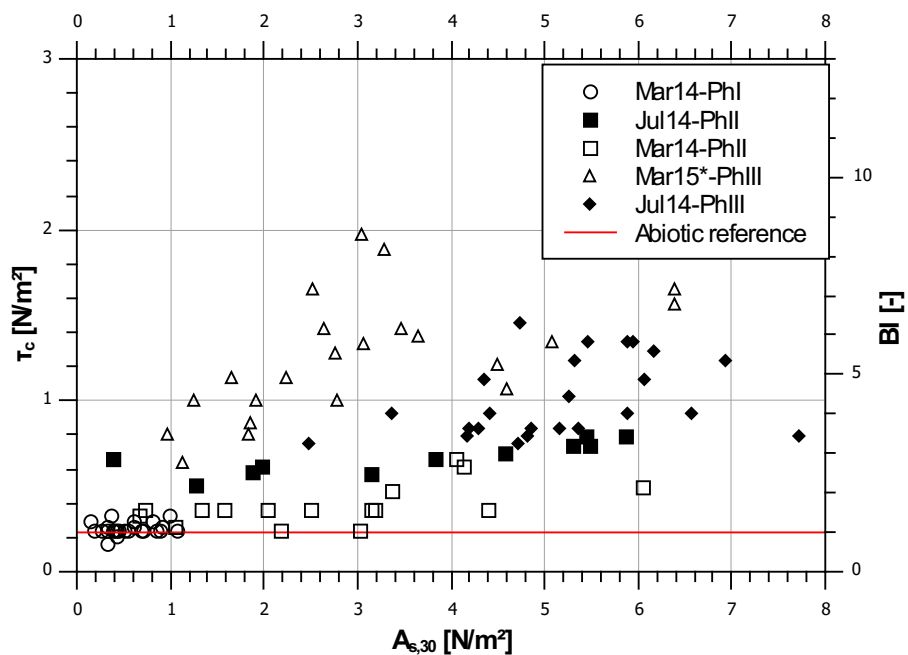
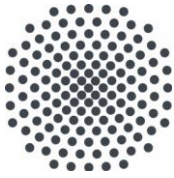


Figure C.12 All experiments of the second set: Critical bed shear stress versus surface adhesion. The solid red line denotes the non-biostabilized sediment stability



Institut für Wasser- und Umweltsystemmodellierung Universität Stuttgart

Pfaffenwaldring 61
70569 Stuttgart (Vaihingen)
Telefon (0711) 685 - 60156
Telefax (0711) 685 - 51073
E-Mail: iws@iws.uni-stuttgart.de
<http://www.iws.uni-stuttgart.de>

Direktoren

Prof. Dr. rer. nat. Dr.-Ing. András Bárdossy
Prof. Dr.-Ing. Rainer Helmig
Prof. Dr.-Ing. Wolfgang Nowak
Prof. Dr.-Ing. Silke Wieprecht

Vorstand (Stand 1.5.2019)

Prof. Dr. rer. nat. Dr.-Ing. A. Bárdossy
Prof. Dr.-Ing. R. Helmig
Prof. Dr.-Ing. W. Nowak
Prof. Dr.-Ing. S. Wieprecht
Prof. Dr. J.A. Sander Huisman
Jürgen Braun, PhD
apl. Prof. Dr.-Ing. H. Class
PD Dr.-Ing. Claus Haslauer
Stefan Haun, PhD
PD Dr.-Ing. habil. Sergey Oladyskin
Dr. rer. nat. J. Seidel
Dr.-Ing. K. Terheiden

Emeriti

Prof. Dr.-Ing. habil. Dr.-Ing. E.h. Jürgen Giesecke
Prof. Dr.h.c. Dr.-Ing. E.h. Helmut Kobus, PhD

Lehrstuhl für Wasserbau und Wassermengenwirtschaft

Leiterin: Prof. Dr.-Ing. Silke Wieprecht
Stellv.: Dr.-Ing. Kristina Terheiden
Versuchsanstalt für Wasserbau
Leiter: Stefan Haun, PhD

Lehrstuhl für Hydromechanik und Hydrosystemmodellierung

Leiter: Prof. Dr.-Ing. Rainer Helmig
Stellv.: apl. Prof. Dr.-Ing. Holger Class

Lehrstuhl für Hydrologie und Geohydrologie

Leiter: Prof. Dr. rer. nat. Dr.-Ing. András Bárdossy
Stellv.: Dr. rer. nat. Jochen Seidel
Hydrogeophysik der Vadosen Zone
(mit Forschungszentrum Jülich)
Leiter: Prof. Dr. J.A. Sander Huisman

Lehrstuhl für Stochastische Simulation und Sicherheitsforschung für Hydrosysteme

Leiter: Prof. Dr.-Ing. Wolfgang Nowak
Stellv.: PD Dr.-Ing. habil. Sergey Oladyskin

VEGAS, Versuchseinrichtung zur Grundwasser- und Altlastensanierung

Leiter: Jürgen Braun, PhD
PD Dr.-Ing. Claus Haslauer

Verzeichnis der Mitteilungshefte

- 1 Röhnisch, Arthur: *Die Bemühungen um eine Wasserbauliche Versuchsanstalt an der Technischen Hochschule Stuttgart*, und Fattah Abouleid, Abdel: *Beitrag zur Berechnung einer in lockeren Sand gerammten, zweifach verankerten Spundwand*, 1963
- 2 Marotz, Günter: *Beitrag zur Frage der Standfestigkeit von dichten Asphaltbelägen im Großwasserbau*, 1964
- 3 Gurr, Siegfried: *Beitrag zur Berechnung zusammengesetzter ebener Flächentragwerke unter besonderer Berücksichtigung ebener Stauwände, mit Hilfe von Randwert- und Lastwertmatrizen*, 1965
- 4 Plica, Peter: *Ein Beitrag zur Anwendung von Schalenkonstruktionen im Stahlwasserbau*, und Petrikat, Kurt: *Möglichkeiten und Grenzen des wasserbaulichen Versuchswesens*, 1966

- 5 Plate, Erich: *Beitrag zur Bestimmung der Windgeschwindigkeitsverteilung in der durch eine Wand gestörten bodennahen Luftschicht*, und
Röhnisch, Arthur; Marotz, Günter: *Neue Baustoffe und Bauausführungen für den Schutz der Böschungen und der Sohle von Kanälen, Flüssen und Häfen; Gestehungskosten und jeweilige Vorteile*, sowie
Unny, T.E.: *Schwingungsuntersuchungen am Kegelstrahlschieber*, 1967
- 6 Seiler, Erich: *Die Ermittlung des Anlagenwertes der bundeseigenen Binnenschiffahrtsstraßen und Talsperren und des Anteils der Binnenschifffahrt an diesem Wert*, 1967
- 7 *Sonderheft anlässlich des 65. Geburtstages von Prof. Arthur Röhnisch mit Beiträgen von*
Benk, Dieter; Breitling, J.; Gurr, Siegfried; Haberhauer, Robert; Honekamp, Hermann; Kuz, Klaus Dieter; Marotz, Günter; Mayer-Vorfelder, Hans-Jörg; Miller, Rudolf; Plate, Erich J.; Radomski, Helge; Schwarz, Helmut; Vollmer, Ernst; Wildenhahn, Eberhard; 1967
- 8 Jumikis, Alfred: *Beitrag zur experimentellen Untersuchung des Wassernachschubs in einem gefrierenden Boden und die Beurteilung der Ergebnisse*, 1968
- 9 Marotz, Günter: *Technische Grundlagen einer Wasserspeicherung im natürlichen Untergrund*, 1968
- 10 Radomski, Helge: *Untersuchungen über den Einfluß der Querschnittsform wellenförmiger Spundwände auf die statischen und rammtechnischen Eigenschaften*, 1968
- 11 Schwarz, Helmut: *Die Grenztragfähigkeit des Baugrundes bei Einwirkung vertikal gezogener Ankerplatten als zweidimensionales Bruchproblem*, 1969
- 12 Erbel, Klaus: *Ein Beitrag zur Untersuchung der Metamorphose von Mittelgebirgsschneedecken unter besonderer Berücksichtigung eines Verfahrens zur Bestimmung der thermischen Schneequalität*, 1969
- 13 Westhaus, Karl-Heinz: *Der Strukturwandel in der Binnenschifffahrt und sein Einfluß auf den Ausbau der Binnenschiffskanäle*, 1969
- 14 Mayer-Vorfelder, Hans-Jörg: *Ein Beitrag zur Berechnung des Erdwiderstandes unter Ansatz der logarithmischen Spirale als Gleitflächenfunktion*, 1970
- 15 Schulz, Manfred: *Berechnung des räumlichen Erddruckes auf die Wandung kreiszylindrischer Körper*, 1970
- 16 Mobasser, Manoutschehr: *Die Rippenstützmauer. Konstruktion und Grenzen ihrer Standsicherheit*, 1970
- 17 Benk, Dieter: *Ein Beitrag zum Betrieb und zur Bemessung von Hochwasserrückhaltebecken*, 1970
- 18 Gàl, Attila: *Bestimmung der mitschwingenden Wassermasse bei überströmten Fischbauchklappen mit kreiszylindrischem Staublech*, 1971, vergriffen
- 19 Kuz, Klaus Dieter: *Ein Beitrag zur Frage des Einsetzens von Kavitationserscheinungen in einer Düsenströmung bei Berücksichtigung der im Wasser gelösten Gase*, 1971, vergriffen
- 20 Schaak, Hartmut: *Verteilleitungen von Wasserkraftanlagen*, 1971
- 21 *Sonderheft zur Eröffnung der neuen Versuchsanstalt des Instituts für Wasserbau der Universität Stuttgart mit Beiträgen von* Brombach, Hansjörg; Dirksen, Wolfram; Gàl, Attila; Gerlach, Reinhard; Giesecke, Jürgen; Holthoff, Franz-Josef; Kuz, Klaus Dieter; Marotz, Günter; Minor, Hans-Erwin; Petrikat, Kurt; Röhnisch, Arthur; Rueff, Helge; Schwarz, Helmut; Vollmer, Ernst; Wildenhahn, Eberhard; 1972
- 22 Wang, Chung-su: *Ein Beitrag zur Berechnung der Schwingungen an Kegelstrahlschiebern*, 1972
- 23 Mayer-Vorfelder, Hans-Jörg: *Erdwiderstandsbeiwerte nach dem Ohde-Variationsverfahren*, 1972
- 24 Minor, Hans-Erwin: *Beitrag zur Bestimmung der Schwingungsanfachungsfunktionen überströmter Stauklappen*, 1972, vergriffen
- 25 Brombach, Hansjörg: *Untersuchung strömungsmechanischer Elemente (Fluidik) und die Möglichkeit der Anwendung von Wirbelkammerelementen im Wasserbau*, 1972, vergriffen
- 26 Wildenhahn, Eberhard: *Beitrag zur Berechnung von Horizontalfilterbrunnen*, 1972
- 27 Steinlein, Helmut: *Die Eliminierung der Schwebstoffe aus Flußwasser zum Zweck der*

- unterirdischen Wasserspeicherung, gezeigt am Beispiel der Iller, 1972*
- 28 Holthoff, Franz Josef: *Die Überwindung großer Hubhöhen in der Binnenschifffahrt durch Schwimmerhebwerke, 1973*
- 29 Röder, Karl: *Einwirkungen aus Baugrundbewegungen auf trog- und kastenförmige Konstruktionen des Wasser- und Tunnelbaues, 1973*
- 30 Kretschmer, Heinz: *Die Bemessung von Bogenstaumauern in Abhängigkeit von der Talform, 1973*
- 31 Honekamp, Hermann: *Beitrag zur Berechnung der Montage von Unterwasserpipelines, 1973*
- 32 Giesecke, Jürgen: *Die Wirbelkammertriode als neuartiges Steuerorgan im Wasserbau, und Brombach, Hansjörg: Entwicklung, Bauformen, Wirkungsweise und Steuereigenschaften von Wirbelkammerverstärkern, 1974*
- 33 Rueff, Helge: *Untersuchung der schwingungserregenden Kräfte an zwei hintereinander angeordneten Tiefschützen unter besonderer Berücksichtigung von Kavitation, 1974*
- 34 Röhnisch, Arthur: *Einpreßversuche mit Zementmörtel für Spannbeton - Vergleich der Ergebnisse von Modellversuchen mit Ausführungen in Hüllwellrohren, 1975*
- 35 *Sonderheft anlässlich des 65. Geburtstages von Prof. Dr.-Ing. Kurt Petrikat mit Beiträgen von: Brombach, Hansjörg; Erbel, Klaus; Flinspach, Dieter; Fischer jr., Richard; Gàl, Attila; Gerlach, Reinhard; Giesecke, Jürgen; Haberhauer, Robert; Hafner Edzard; Hausenblas, Bernhard; Horlacher, Hans-Burkhard; Hutarew, Andreas; Knoll, Manfred; Krummet, Ralph; Marotz, Günter; Merkle, Theodor; Miller, Christoph; Minor, Hans-Erwin; Neumayer, Hans; Rao, Syamala; Rath, Paul; Rueff, Helge; Ruppert, Jürgen; Schwarz, Wolfgang; Topal-Gökceli, Mehmet; Vollmer, Ernst; Wang, Chung-su; Weber, Hans-Georg; 1975*
- 36 Berger, Jochum: *Beitrag zur Berechnung des Spannungszustandes in rotationssymmetrisch belasteten Kugelschalen veränderlicher Wandstärke unter Gas- und Flüssigkeitsdruck durch Integration schwach singulärer Differentialgleichungen, 1975*
- 37 Dirksen, Wolfram: *Berechnung instationärer Abflussvorgänge in gestauten Gerinnen mittels Differenzenverfahren und die Anwendung auf Hochwasserrückhaltebecken, 1976*
- 38 Horlacher, Hans-Burkhard: *Berechnung instationärer Temperatur- und Wärmespannungsfelder in langen mehrschichtigen Hohlzylindern, 1976*
- 39 Hafner, Edzard: *Untersuchung der hydrodynamischen Kräfte auf Baukörper im Tiefwasserbereich des Meeres, 1977, ISBN 3-921694-39-6*
- 40 Ruppert, Jürgen: *Über den Axialwirbelkammerverstärker für den Einsatz im Wasserbau, 1977, ISBN 3-921694-40-X*
- 41 Hutarew, Andreas: *Beitrag zur Beeinflussbarkeit des Sauerstoffgehalts in Fließgewässern an Abstürzen und Wehren, 1977, ISBN 3-921694-41-8, vergriffen*
- 42 Miller, Christoph: *Ein Beitrag zur Bestimmung der schwingungserregenden Kräfte an unterströmten Wehren, 1977, ISBN 3-921694-42-6*
- 43 Schwarz, Wolfgang: *Druckstoßberechnung unter Berücksichtigung der Radial- und Längsverschiebungen der Rohrwandung, 1978, ISBN 3-921694-43-4*
- 44 Kinzelbach, Wolfgang: *Numerische Untersuchungen über den optimalen Einsatz variabler Kühlsysteme einer Kraftwerkskette am Beispiel Oberrhein, 1978, ISBN 3-921694-44-2*
- 45 Barczewski, Baldur: *Neue Meßmethoden für Wasser-Luftgemische und deren Anwendung auf zweiphasige Auftriebsstrahlen, 1979, ISBN 3-921694-45-0*
- 46 Neumayer, Hans: *Untersuchung der Strömungsvorgänge in radialen Wirbelkammerverstärkern, 1979, ISBN 3-921694-46-9*
- 47 Elalfy, Youssef-Elhassan: *Untersuchung der Strömungsvorgänge in Wirbelkammerdioden und -drosseln, 1979, ISBN 3-921694-47-7*
- 48 Brombach, Hansjörg: *Automatisierung der Bewirtschaftung von Wasserspeichern, 1981, ISBN 3-921694-48-5*
- 49 Geldner, Peter: *Deterministische und stochastische Methoden zur Bestimmung der Selbstdichtung von Gewässern, 1981, ISBN 3-921694-49-3, vergriffen*

- 50 Mehlhorn, Hans: *Temperaturveränderungen im Grundwasser durch Brauchwassereinleitungen*, 1982, ISBN 3-921694-50-7, vergriffen
- 51 Hafner, Edzard: *Rohrleitungen und Behälter im Meer*, 1983, ISBN 3-921694-51-5
- 52 Rinnert, Bernd: *Hydrodynamische Dispersion in porösen Medien: Einfluß von Dichteunterschieden auf die Vertikalvermischung in horizontaler Strömung*, 1983, ISBN 3-921694-52-3, vergriffen
- 53 Lindner, Wulf: *Steuerung von Grundwasserentnahmen unter Einhaltung ökologischer Kriterien*, 1983, ISBN 3-921694-53-1, vergriffen
- 54 Herr, Michael; Herzer, Jörg; Kinzelbach, Wolfgang; Kobus, Helmut; Rinnert, Bernd: *Methoden zur rechnerischen Erfassung und hydraulischen Sanierung von Grundwasserkontaminationen*, 1983, ISBN 3-921694-54-X
- 55 Schmitt, Paul: *Wege zur Automatisierung der Niederschlagsermittlung*, 1984, ISBN 3-921694-55-8, vergriffen
- 56 Müller, Peter: *Transport und selektive Sedimentation von Schwebstoffen bei gestautem Abfluß*, 1985, ISBN 3-921694-56-6
- 57 El-Qawasmeh, Fuad: *Möglichkeiten und Grenzen der Tropfbewässerung unter besonderer Berücksichtigung der Verstopfungsanfälligkeit der Tropfelemente*, 1985, ISBN 3-921694-57-4, vergriffen
- 58 Kirchenbaur, Klaus: *Mikroprozessorgesteuerte Erfassung instationärer Druckfelder am Beispiel seegangsbelasteter Baukörper*, 1985, ISBN 3-921694-58-2
- 59 Kobus, Helmut (Hrsg.): *Modellierung des großräumigen Wärme- und Schadstofftransports im Grundwasser*, Tätigkeitsbericht 1984/85 (DFG-Forschergruppe an den Universitäten Hohenheim, Karlsruhe und Stuttgart), 1985, ISBN 3-921694-59-0, vergriffen
- 60 Spitz, Karlheinz: *Dispersion in porösen Medien: Einfluß von Inhomogenitäten und Dichteunterschieden*, 1985, ISBN 3-921694-60-4, vergriffen
- 61 Kobus, Helmut: *An Introduction to Air-Water Flows in Hydraulics*, 1985, ISBN 3-921694-61-2
- 62 Kaleris, Vassilios: *Erfassung des Austausches von Oberflächen- und Grundwasser in horizontalebene Grundwassermodellen*, 1986, ISBN 3-921694-62-0
- 63 Herr, Michael: *Grundlagen der hydraulischen Sanierung verunreinigter Porengrundwasserleiter*, 1987, ISBN 3-921694-63-9
- 64 Marx, Walter: *Berechnung von Temperatur und Spannung in Massenbeton infolge Hydratation*, 1987, ISBN 3-921694-64-7
- 65 Koschitzky, Hans-Peter: *Dimensionierungskonzept für Sohlbelüfter in Schußrinnen zur Vermeidung von Kavitationsschäden*, 1987, ISBN 3-921694-65-5
- 66 Kobus, Helmut (Hrsg.): *Modellierung des großräumigen Wärme- und Schadstofftransports im Grundwasser*, Tätigkeitsbericht 1986/87 (DFG-Forschergruppe an den Universitäten Hohenheim, Karlsruhe und Stuttgart) 1987, ISBN 3-921694-66-3
- 67 Söll, Thomas: *Berechnungsverfahren zur Abschätzung anthropogener Temperaturanomalien im Grundwasser*, 1988, ISBN 3-921694-67-1
- 68 Dittrich, Andreas; Westrich, Bernd: *Bodenseeufererosion, Bestandsaufnahme und Bewertung*, 1988, ISBN 3-921694-68-X, vergriffen
- 69 Huwe, Bernd; van der Ploeg, Rienk R.: *Modelle zur Simulation des Stickstoffhaushaltes von Standorten mit unterschiedlicher landwirtschaftlicher Nutzung*, 1988, ISBN 3-921694-69-8, vergriffen
- 70 Stephan, Karl: *Integration elliptischer Funktionen*, 1988, ISBN 3-921694-70-1
- 71 Kobus, Helmut; Zilliox, Lothaire (Hrsg.): *Nitratbelastung des Grundwassers, Auswirkungen der Landwirtschaft auf die Grundwasser- und Rohwasserbeschaffenheit und Maßnahmen zum Schutz des Grundwassers*. Vorträge des deutsch-französischen Kolloquiums am 6. Oktober 1988, Universitäten Stuttgart und Louis Pasteur Strasbourg (Vorträge in deutsch oder französisch, Kurzfassungen zweisprachig), 1988, ISBN 3-921694-71-X

- 72 Soyeaux, Renald: *Unterströmung von Stauanlagen auf klüftigem Untergrund unter Berücksichtigung laminarer und turbulenter Fließzustände*, 1991, ISBN 3-921694-72-8
- 73 Kohane, Roberto: *Berechnungsmethoden für Hochwasserabfluß in Fließgewässern mit überströmten Vorländern*, 1991, ISBN 3-921694-73-6
- 74 Hassinger, Reinhard: *Beitrag zur Hydraulik und Bemessung von Blocksteinrampen in flexibler Bauweise*, 1991, ISBN 3-921694-74-4, vergriffen
- 75 Schäfer, Gerhard: *Einfluß von Schichtenstrukturen und lokalen Einlagerungen auf die Längsdispersion in Porengrundwasserleitern*, 1991, ISBN 3-921694-75-2
- 76 Giesecke, Jürgen: *Vorträge, Wasserwirtschaft in stark besiedelten Regionen; Umweltforschung mit Schwerpunkt Wasserwirtschaft*, 1991, ISBN 3-921694-76-0
- 77 Huwe, Bernd: *Deterministische und stochastische Ansätze zur Modellierung des Stickstoffhaushalts landwirtschaftlich genutzter Flächen auf unterschiedlichem Skalenniveau*, 1992, ISBN 3-921694-77-9, vergriffen
- 78 Rommel, Michael: *Verwendung von Klufdaten zur realitätsnahen Generierung von Kluftnetzen mit anschließender laminar-turbulenter Strömungsberechnung*, 1993, ISBN 3-92 1694-78-7
- 79 Marschall, Paul: *Die Ermittlung lokaler Stofffrachten im Grundwasser mit Hilfe von Einbohrloch-Meßverfahren*, 1993, ISBN 3-921694-79-5, vergriffen
- 80 Ptak, Thomas: *Stofftransport in heterogenen Porenaquiferen: Felduntersuchungen und stochastische Modellierung*, 1993, ISBN 3-921694-80-9, vergriffen
- 81 Haakh, Frieder: *Transientes Strömungsverhalten in Wirbelkammern*, 1993, ISBN 3-921694-81-7
- 82 Kobus, Helmut; Cirpka, Olaf; Barczewski, Baldur; Koschitzky, Hans-Peter: *Versuchseinrichtung zur Grundwasser- und Altlastensanierung VEGAS, Konzeption und Programmrahmen*, 1993, ISBN 3-921694-82-5
- 83 Zang, Weidong: *Optimaler Echtzeit-Betrieb eines Speichers mit aktueller Abflußregenerierung*, 1994, ISBN 3-921694-83-3, vergriffen
- 84 Franke, Hans-Jörg: *Stochastische Modellierung eines flächenhaften Stoffeintrages und Transports in Grundwasser am Beispiel der Pflanzenschutzmittelproblematik*, 1995, ISBN 3-921694-84-1
- 85 Lang, Ulrich: *Simulation regionaler Strömungs- und Transportvorgänge in Karstaquiferen mit Hilfe des Doppelkontinuum-Ansatzes: Methodenentwicklung und Parameteridentifikation*, 1995, ISBN 3-921694-85-X, vergriffen
- 86 Helmig, Rainer: *Einführung in die Numerischen Methoden der Hydromechanik*, 1996, ISBN 3-921694-86-8, vergriffen
- 87 Cirpka, Olaf: *CONTRACT: A Numerical Tool for Contaminant Transport and Chemical Transformations - Theory and Program Documentation -*, 1996, ISBN 3-921694-87-6
- 88 Haberlandt, Uwe: *Stochastische Synthese und Regionalisierung des Niederschlages für Schmutzfrachtberechnungen*, 1996, ISBN 3-921694-88-4
- 89 Croisé, Jean: *Extraktion von flüchtigen Chemikalien aus natürlichen Lockergesteinen mittels erzwungener Luftströmung*, 1996, ISBN 3-921694-89-2, vergriffen
- 90 Jorde, Klaus: *Ökologisch begründete, dynamische Mindestwasserregelungen bei Ausleitungskraftwerken*, 1997, ISBN 3-921694-90-6, vergriffen
- 91 Helmig, Rainer: *Gekoppelte Strömungs- und Transportprozesse im Untergrund - Ein Beitrag zur Hydrosystemmodellierung-*, 1998, ISBN 3-921694-91-4, vergriffen
- 92 Emmert, Martin: *Numerische Modellierung nichtisothermer Gas-Wasser Systeme in porösen Medien*, 1997, ISBN 3-921694-92-2
- 93 Kern, Ulrich: *Transport von Schweb- und Schadstoffen in staugeregelten Fließgewässern am Beispiel des Neckars*, 1997, ISBN 3-921694-93-0, vergriffen
- 94 Förster, Georg: *Druckstoßdämpfung durch große Luftblasen in Hochpunkten von Rohrleitungen* 1997, ISBN 3-921694-94-9

- 95 Cirpka, Olaf: *Numerische Methoden zur Simulation des reaktiven Mehrkomponententransports im Grundwasser*, 1997, ISBN 3-921694-95-7, vergriffen
- 96 Färber, Arne: *Wärmetransport in der ungesättigten Bodenzone: Entwicklung einer thermischen In-situ-Sanierungstechnologie*, 1997, ISBN 3-921694-96-5
- 97 Betz, Christoph: *Wasserdampfdestillation von Schadstoffen im porösen Medium: Entwicklung einer thermischen In-situ-Sanierungstechnologie*, 1998, SBN 3-921694-97-3
- 98 Xu, Yichun: *Numerical Modeling of Suspended Sediment Transport in Rivers*, 1998, ISBN 3-921694-98-1, vergriffen
- 99 Wüst, Wolfgang: *Geochemische Untersuchungen zur Sanierung CKW-kontaminierter Aquifere mit Fe(0)-Reaktionswänden*, 2000, ISBN 3-933761-02-2
- 100 Sheta, Hussam: *Simulation von Mehrphasenvorgängen in porösen Medien unter Einbeziehung von Hysterese-Effekten*, 2000, ISBN 3-933761-03-4
- 101 Ayros, Edwin: *Regionalisierung extremer Abflüsse auf der Grundlage statistischer Verfahren*, 2000, ISBN 3-933761-04-2, vergriffen
- 102 Huber, Ralf: *Compositional Multiphase Flow and Transport in Heterogeneous Porous Media*, 2000, ISBN 3-933761-05-0
- 103 Braun, Christopherus: *Ein Upscaling-Verfahren für Mehrphasenströmungen in porösen Medien*, 2000, ISBN 3-933761-06-9
- 104 Hofmann, Bernd: *Entwicklung eines rechnergestützten Managementsystems zur Beurteilung von Grundwasserschadensfällen*, 2000, ISBN 3-933761-07-7
- 105 Class, Holger: *Theorie und numerische Modellierung nichtisothermer Mehrphasenprozesse in NAPL-kontaminierten porösen Medien*, 2001, ISBN 3-933761-08-5
- 106 Schmidt, Reinhard: *Wasserdampf- und Heißluftinjektion zur thermischen Sanierung kontaminierter Standorte*, 2001, ISBN 3-933761-09-3
- 107 Josef, Reinhold: *Schadstoffextraktion mit hydraulischen Sanierungsverfahren unter Anwendung von grenzflächenaktiven Stoffen*, 2001, ISBN 3-933761-10-7
- 108 Schneider, Matthias: *Habitat- und Abflussmodellierung für Fließgewässer mit unscharfen Berechnungsansätzen*, 2001, ISBN 3-933761-11-5
- 109 Rathgeb, Andreas: *Hydrodynamische Bemessungsgrundlagen für Lockerdeckwerke an überströmbaren Erddämmen*, 2001, ISBN 3-933761-12-3
- 110 Lang, Stefan: *Parallele numerische Simulation instationärer Probleme mit adaptiven Methoden auf unstrukturierten Gittern*, 2001, ISBN 3-933761-13-1
- 111 Appt, Jochen; Stumpp Simone: *Die Bodensee-Messkampagne 2001, IWS/CWR Lake Constance Measurement Program 2001*, 2002, ISBN 3-933761-14-X
- 112 Heimerl, Stephan: *Systematische Beurteilung von Wasserkraftprojekten*, 2002, ISBN 3-933761-15-8, vergriffen
- 113 Iqbal, Amin: *On the Management and Salinity Control of Drip Irrigation*, 2002, ISBN 3-933761-16-6
- 114 Silberhorn-Hemminger, Annette: *Modellierung von Kluftaquifersystemen: Geostatistische Analyse und deterministisch-stochastische Kluftgenerierung*, 2002, ISBN 3-933761-17-4
- 115 Winkler, Angela: *Prozesse des Wärme- und Stofftransports bei der In-situ-Sanierung mit festen Wärmequellen*, 2003, ISBN 3-933761-18-2
- 116 Marx, Walter: *Wasserkraft, Bewässerung, Umwelt - Planungs- und Bewertungsschwerpunkte der Wasserbewirtschaftung*, 2003, ISBN 3-933761-19-0
- 117 Hinkelmann, Reinhard: *Efficient Numerical Methods and Information-Processing Techniques in Environment Water*, 2003, ISBN 3-933761-20-4
- 118 Samaniego-Eguiguren, Luis Eduardo: *Hydrological Consequences of Land Use / Land Cover and Climatic Changes in Mesoscale Catchments*, 2003, ISBN 3-933761-21-2
- 119 Neunhäuserer, Lina: *Diskretisierungsansätze zur Modellierung von Strömungs- und Transportprozessen in geklüftet-porösen Medien*, 2003, ISBN 3-933761-22-0
- 120 Paul, Maren: *Simulation of Two-Phase Flow in Heterogeneous Poros Media with Adaptive Methods*, 2003, ISBN 3-933761-23-9

- 121 Ehret, Uwe: *Rainfall and Flood Nowcasting in Small Catchments using Weather Radar*, 2003, ISBN 3-933761-24-7
- 122 Haag, Ingo: *Der Sauerstoffhaushalt staugeregelter Flüsse am Beispiel des Neckars - Analysen, Experimente, Simulationen -*, 2003, ISBN 3-933761-25-5
- 123 Appt, Jochen: *Analysis of Basin-Scale Internal Waves in Upper Lake Constance*, 2003, ISBN 3-933761-26-3
- 124 Hrsg.: Schrenk, Volker; Batereau, Katrin; Barczewski, Baldur; Weber, Karolin und Koschitzky, Hans-Peter: *Symposium Ressource Fläche und VEGAS - Statuskolloquium 2003, 30. September und 1. Oktober 2003*, 2003, ISBN 3-933761-27-1
- 125 Omar Khalil Ouda: *Optimisation of Agricultural Water Use: A Decision Support System for the Gaza Strip*, 2003, ISBN 3-933761-28-0
- 126 Batereau, Katrin: *Sensorbasierte Bodenluftmessung zur Vor-Ort-Erkundung von Schadensherden im Untergrund*, 2004, ISBN 3-933761-29-8
- 127 Witt, Oliver: *Erosionsstabilität von Gewässersedimenten mit Auswirkung auf den Stofftransport bei Hochwasser am Beispiel ausgewählter Stauhaltungen des Oberrheins*, 2004, ISBN 3-933761-30-1
- 128 Jakobs, Hartmut: *Simulation nicht-isothermer Gas-Wasser-Prozesse in komplexen Kluft-Matrix-Systemen*, 2004, ISBN 3-933761-31-X
- 129 Li, Chen-Chien: *Deterministisch-stochastisches Berechnungskonzept zur Beurteilung der Auswirkungen erosiver Hochwasserereignisse in Flusstauhaltungen*, 2004, ISBN 3-933761-32-8
- 130 Reichenberger, Volker; Helmig, Rainer; Jakobs, Hartmut; Bastian, Peter; Niessner, Jennifer: *Complex Gas-Water Processes in Discrete Fracture-Matrix Systems: Up-scaling, Mass-Conservative Discretization and Efficient Multilevel Solution*, 2004, ISBN 3-933761-33-6
- 131 Hrsg.: Barczewski, Baldur; Koschitzky, Hans-Peter; Weber, Karolin; Wege, Ralf: *VEGAS - Statuskolloquium 2004*, Tagungsband zur Veranstaltung am 05. Oktober 2004 an der Universität Stuttgart, Campus Stuttgart-Vaihingen, 2004, ISBN 3-933761-34-4
- 132 Asie, Kemal Jabir: *Finite Volume Models for Multiphase Multicomponent Flow through Porous Media*. 2005, ISBN 3-933761-35-2
- 133 Jacoub, George: *Development of a 2-D Numerical Module for Particulate Contaminant Transport in Flood Retention Reservoirs and Impounded Rivers*, 2004, ISBN 3-933761-36-0
- 134 Nowak, Wolfgang: *Geostatistical Methods for the Identification of Flow and Transport Parameters in the Subsurface*, 2005, ISBN 3-933761-37-9
- 135 Süß, Mia: *Analysis of the influence of structures and boundaries on flow and transport processes in fractured porous media*, 2005, ISBN 3-933761-38-7
- 136 Jose, Surabhin Chackiath: *Experimental Investigations on Longitudinal Dispersive Mixing in Heterogeneous Aquifers*, 2005, ISBN: 3-933761-39-5
- 137 Filiz, Fulya: *Linking Large-Scale Meteorological Conditions to Floods in Mesoscale Catchments*, 2005, ISBN 3-933761-40-9
- 138 Qin, Minghao: *Wirklichkeitsnahe und recheneffiziente Ermittlung von Temperatur und Spannungen bei großen RCC-Staumauern*, 2005, ISBN 3-933761-41-7
- 139 Kobayashi, Kenichiro: *Optimization Methods for Multiphase Systems in the Subsurface - Application to Methane Migration in Coal Mining Areas*, 2005, ISBN 3-933761-42-5
- 140 Rahman, Md. Arifur: *Experimental Investigations on Transverse Dispersive Mixing in Heterogeneous Porous Media*, 2005, ISBN 3-933761-43-3
- 141 Schrenk, Volker: *Ökobilanzen zur Bewertung von Altlastensanierungsmaßnahmen*, 2005, ISBN 3-933761-44-1
- 142 Hundecha, Hirpa Yeshewatesfa: *Regionalization of Parameters of a Conceptual Rainfall-Runoff Model*, 2005, ISBN: 3-933761-45-X
- 143 Wege, Ralf: *Untersuchungs- und Überwachungsmethoden für die Beurteilung natürlicher Selbstreinigungsprozesse im Grundwasser*, 2005, ISBN 3-933761-46-8

- 144 Breiting, Thomas: *Techniken und Methoden der Hydroinformatik - Modellierung von komplexen Hydrosystemen im Untergrund*, 2006, ISBN 3-933761-47-6
- 145 Hrsg.: Braun, Jürgen; Koschitzky, Hans-Peter; Müller, Martin: *Ressource Untergrund: 10 Jahre VEGAS: Forschung und Technologieentwicklung zum Schutz von Grundwasser und Boden*, Tagungsband zur Veranstaltung am 28. und 29. September 2005 an der Universität Stuttgart, Campus Stuttgart-Vaihingen, 2005, ISBN 3-933761-48-4
- 146 Rojanschi, Vlad: *Abflusskonzentration in mesoskaligen Einzugsgebieten unter Berücksichtigung des Sickerraumes*, 2006, ISBN 3-933761-49-2
- 147 Winkler, Nina Simone: *Optimierung der Steuerung von Hochwasserrückhaltebeckensystemen*, 2006, ISBN 3-933761-50-6
- 148 Wolf, Jens: *Räumlich differenzierte Modellierung der Grundwasserströmung alluvialer Aquifere für mesoskalige Einzugsgebiete*, 2006, ISBN: 3-933761-51-4
- 149 Kohler, Beate: *Externe Effekte der Laufwasserkraftnutzung*, 2006, ISBN 3-933761-52-2
- 150 Hrsg.: Braun, Jürgen; Koschitzky, Hans-Peter; Stuhmann, Matthias: *VEGAS-Statuskolloquium 2006*, Tagungsband zur Veranstaltung am 28. September 2006 an der Universität Stuttgart, Campus Stuttgart-Vaihingen, 2006, ISBN 3-933761-53-0
- 151 Niessner, Jennifer: *Multi-Scale Modeling of Multi-Phase - Multi-Component Processes in Heterogeneous Porous Media*, 2006, ISBN 3-933761-54-9
- 152 Fischer, Markus: *Beanspruchung eingeeerdeter Rohrleitungen infolge Austrocknung bindiger Böden*, 2006, ISBN 3-933761-55-7
- 153 Schneck, Alexander: *Optimierung der Grundwasserbewirtschaftung unter Berücksichtigung der Belange der Wasserversorgung, der Landwirtschaft und des Naturschutzes*, 2006, ISBN 3-933761-56-5
- 154 Das, Tapash: *The Impact of Spatial Variability of Precipitation on the Predictive Uncertainty of Hydrological Models*, 2006, ISBN 3-33761-57-3
- 155 Bielinski, Andreas: *Numerical Simulation of CO₂ sequestration in geological formations*, 2007, ISBN 3-933761-58-1
- 156 Mödinger, Jens: *Entwicklung eines Bewertungs- und Entscheidungsunterstützungssystems für eine nachhaltige regionale Grundwasserbewirtschaftung*, 2006, ISBN 3-933761-60-3
- 157 Manthey, Sabine: *Two-phase flow processes with dynamic effects in porous media - parameter estimation and simulation*, 2007, ISBN 3-933761-61-1
- 158 Pozos Estrada, Oscar: *Investigation on the Effects of Entrained Air in Pipelines*, 2007, ISBN 3-933761-62-X
- 159 Ochs, Steffen Oliver: *Steam injection into saturated porous media – process analysis including experimental and numerical investigations*, 2007, ISBN 3-933761-63-8
- 160 Marx, Andreas: *Einsatz gekoppelter Modelle und Wetterradar zur Abschätzung von Niederschlagsintensitäten und zur Abflussvorhersage*, 2007, ISBN 3-933761-64-6
- 161 Hartmann, Gabriele Maria: *Investigation of Evapotranspiration Concepts in Hydrological Modelling for Climate Change Impact Assessment*, 2007, ISBN 3-933761-65-4
- 162 Kebede Gurmessa, Tesfaye: *Numerical Investigation on Flow and Transport Characteristics to Improve Long-Term Simulation of Reservoir Sedimentation*, 2007, ISBN 3-933761-66-2
- 163 Trifković, Aleksandar: *Multi-objective and Risk-based Modelling Methodology for Planning, Design and Operation of Water Supply Systems*, 2007, ISBN 3-933761-67-0
- 164 Göttinger, Jens: *Distributed Conceptual Hydrological Modelling - Simulation of Climate, Land Use Change Impact and Uncertainty Analysis*, 2007, ISBN 3-933761-68-9
- 165 Hrsg.: Braun, Jürgen; Koschitzky, Hans-Peter; Stuhmann, Matthias: *VEGAS – Kolloquium 2007*, Tagungsband zur Veranstaltung am 26. September 2007 an der Universität Stuttgart, Campus Stuttgart-Vaihingen, 2007, ISBN 3-933761-69-7
- 166 Freeman, Beau: *Modernization Criteria Assessment for Water Resources Planning; Klamath Irrigation Project, U.S.*, 2008, ISBN 3-933761-70-0

- 167 Dreher, Thomas: *Selektive Sedimentation von Feinstschwebstoffen in Wechselwirkung mit wandnahen turbulenten Strömungsbedingungen*, 2008, ISBN 3-933761-71-9
- 168 Yang, Wei: *Discrete-Continuous Downscaling Model for Generating Daily Precipitation Time Series*, 2008, ISBN 3-933761-72-7
- 169 Kopecki, Ianina: *Calculational Approach to FST-Hemispheres for Multiparametrical Benthos Habitat Modelling*, 2008, ISBN 3-933761-73-5
- 170 Brommundt, Jürgen: *Stochastische Generierung räumlich zusammenhängender Niederschlagszeitreihen*, 2008, ISBN 3-933761-74-3
- 171 Papafotiou, Alexandros: *Numerical Investigations of the Role of Hysteresis in Heterogeneous Two-Phase Flow Systems*, 2008, ISBN 3-933761-75-1
- 172 He, Yi: *Application of a Non-Parametric Classification Scheme to Catchment Hydrology*, 2008, ISBN 978-3-933761-76-7
- 173 Wagner, Sven: *Water Balance in a Poorly Gauged Basin in West Africa Using Atmospheric Modelling and Remote Sensing Information*, 2008, ISBN 978-3-933761-77-4
- 174 Hrsg.: Braun, Jürgen; Koschitzky, Hans-Peter; Stuhmann, Matthias; Schrenk, Volker: *VEGAS-Kolloquium 2008 Ressource Fläche III*, Tagungsband zur Veranstaltung am 01. Oktober 2008 an der Universität Stuttgart, Campus Stuttgart-Vaihingen, 2008, ISBN 978-3-933761-78-1
- 175 Patil, Sachin: *Regionalization of an Event Based Nash Cascade Model for Flood Predictions in Ungauged Basins*, 2008, ISBN 978-3-933761-79-8
- 176 Assteerawatt, Anongnart: *Flow and Transport Modelling of Fractured Aquifers based on a Geostatistical Approach*, 2008, ISBN 978-3-933761-80-4
- 177 Karnahl, Joachim Alexander: *2D numerische Modellierung von multifraktionalem Schwebstoff- und Schadstofftransport in Flüssen*, 2008, ISBN 978-3-933761-81-1
- 178 Hiester, Uwe: *Technologieentwicklung zur In-situ-Sanierung der ungesättigten Bodenzone mit festen Wärmequellen*, 2009, ISBN 978-3-933761-82-8
- 179 Laux, Patrick: *Statistical Modeling of Precipitation for Agricultural Planning in the Volta Basin of West Africa*, 2009, ISBN 978-3-933761-83-5
- 180 Ehsan, Saqib: *Evaluation of Life Safety Risks Related to Severe Flooding*, 2009, ISBN 978-3-933761-84-2
- 181 Prohaska, Sandra: *Development and Application of a 1D Multi-Strip Fine Sediment Transport Model for Regulated Rivers*, 2009, ISBN 978-3-933761-85-9
- 182 Kopp, Andreas: *Evaluation of CO₂ Injection Processes in Geological Formations for Site Screening*, 2009, ISBN 978-3-933761-86-6
- 183 Ebigbo, Anozie: *Modelling of biofilm growth and its influence on CO₂ and water (two-phase) flow in porous media*, 2009, ISBN 978-3-933761-87-3
- 184 Freiboth, Sandra: *A phenomenological model for the numerical simulation of multiphase multicomponent processes considering structural alterations of porous media*, 2009, ISBN 978-3-933761-88-0
- 185 Zöllner, Frank: *Implementierung und Anwendung netzfreier Methoden im Konstruktiven Wasserbau und in der Hydromechanik*, 2009, ISBN 978-3-933761-89-7
- 186 Vasin, Milos: *Influence of the soil structure and property contrast on flow and transport in the unsaturated zone*, 2010, ISBN 978-3-933761-90-3
- 187 Li, Jing: *Application of Copulas as a New Geostatistical Tool*, 2010, ISBN 978-3-933761-91-0
- 188 AghaKouchak, Amir: *Simulation of Remotely Sensed Rainfall Fields Using Copulas*, 2010, ISBN 978-3-933761-92-7
- 189 Thapa, Pawan Kumar: *Physically-based spatially distributed rainfall runoff modelling for soil erosion estimation*, 2010, ISBN 978-3-933761-93-4
- 190 Wurms, Sven: *Numerische Modellierung der Sedimentationsprozesse in Retentionsanlagen zur Steuerung von Stoffströmen bei extremen Hochwasserabflussereignissen*, 2011, ISBN 978-3-933761-94-1

- 191 Merkel, Uwe: *Unsicherheitsanalyse hydraulischer Einwirkungen auf Hochwasserschutzdeiche und Steigerung der Leistungsfähigkeit durch adaptive Strömungsmodellierung*, 2011, ISBN 978-3-933761-95-8
- 192 Fritz, Jochen: *A Decoupled Model for Compositional Non-Isothermal Multiphase Flow in Porous Media and Multiphysics Approaches for Two-Phase Flow*, 2010, ISBN 978-3-933761-96-5
- 193 Weber, Karolin (Hrsg.): *12. Treffen junger WissenschaftlerInnen an Wasserbauinstituten*, 2010, ISBN 978-3-933761-97-2
- 194 Blifernicht, Jan-Geert: *Probability Forecasts of Daily Areal Precipitation for Small River Basins*, 2011, ISBN 978-3-933761-98-9
- 195 Hrsg.: Koschitzky, Hans-Peter; Braun, Jürgen: *VEGAS-Kolloquium 2010 In-situ-Sanierung - Stand und Entwicklung Nano und ISCO -*, Tagungsband zur Veranstaltung am 07. Oktober 2010 an der Universität Stuttgart, Campus Stuttgart-Vaihingen, 2010, ISBN 978-3-933761-99-6
- 196 Gafurov, Abror: *Water Balance Modeling Using Remote Sensing Information - Focus on Central Asia*, 2010, ISBN 978-3-942036-00-9
- 197 Mackenberg, Sylvia: *Die Quellstärke in der Sickerwasserprognose: Möglichkeiten und Grenzen von Labor- und Freilanduntersuchungen*, 2010, ISBN 978-3-942036-01-6
- 198 Singh, Shailesh Kumar: *Robust Parameter Estimation in Gauged and Ungauged Basins*, 2010, ISBN 978-3-942036-02-3
- 199 Doğan, Mehmet Onur: *Coupling of porous media flow with pipe flow*, 2011, ISBN 978-3-942036-03-0
- 200 Liu, Min: *Study of Topographic Effects on Hydrological Patterns and the Implication on Hydrological Modeling and Data Interpolation*, 2011, ISBN 978-3-942036-04-7
- 201 Geleta, Habtamu Itafa: *Watershed Sediment Yield Modeling for Data Scarce Areas*, 2011, ISBN 978-3-942036-05-4
- 202 Franke, Jörg: *Einfluss der Überwachung auf die Versagenswahrscheinlichkeit von Staustufen*, 2011, ISBN 978-3-942036-06-1
- 203 Bakimchandra, Oinam: *Integrated Fuzzy-GIS approach for assessing regional soil erosion risks*, 2011, ISBN 978-3-942036-07-8
- 204 Alam, Muhammad Mahboob: *Statistical Downscaling of Extremes of Precipitation in Mesoscale Catchments from Different RCMs and Their Effects on Local Hydrology*, 2011, ISBN 978-3-942036-08-5
- 205 Hrsg.: Koschitzky, Hans-Peter; Braun, Jürgen: *VEGAS-Kolloquium 2011 Flache Geothermie - Perspektiven und Risiken*, Tagungsband zur Veranstaltung am 06. Oktober 2011 an der Universität Stuttgart, Campus Stuttgart-Vaihingen, 2011, ISBN 978-3-933761-09-2
- 206 Haslauer, Claus: *Analysis of Real-World Spatial Dependence of Subsurface Hydraulic Properties Using Copulas with a Focus on Solute Transport Behaviour*, 2011, ISBN 978-3-942036-10-8
- 207 Dung, Nguyen Viet: *Multi-objective automatic calibration of hydrodynamic models – development of the concept and an application in the Mekong Delta*, 2011, ISBN 978-3-942036-11-5
- 208 Hung, Nguyen Nghia: *Sediment dynamics in the floodplain of the Mekong Delta, Vietnam*, 2011, ISBN 978-3-942036-12-2
- 209 Kuhlmann, Anna: *Influence of soil structure and root water uptake on flow in the unsaturated zone*, 2012, ISBN 978-3-942036-13-9
- 210 Tuhtan, Jeffrey Andrew: *Including the Second Law Inequality in Aquatic Ecodynamics: A Modeling Approach for Alpine Rivers Impacted by Hydropeaking*, 2012, ISBN 978-3-942036-14-6
- 211 Tolossa, Habtamu: *Sediment Transport Computation Using a Data-Driven Adaptive Neuro-Fuzzy Modelling Approach*, 2012, ISBN 978-3-942036-15-3

- 212 Tatomir, Alexandru-Bodgan: *From Discrete to Continuum Concepts of Flow in Fractured Porous Media*, 2012, ISBN 978-3-942036-16-0
- 213 Erbertseder, Karin: *A Multi-Scale Model for Describing Cancer-Therapeutic Transport in the Human Lung*, 2012, ISBN 978-3-942036-17-7
- 214 Noack, Markus: *Modelling Approach for Interstitial Sediment Dynamics and Reproduction of Gravel Spawning Fish*, 2012, ISBN 978-3-942036-18-4
- 215 De Boer, Cjestmir Volkert: *Transport of Nano Sized Zero Valent Iron Colloids during Injection into the Subsurface*, 2012, ISBN 978-3-942036-19-1
- 216 Pfaff, Thomas: *Processing and Analysis of Weather Radar Data for Use in Hydrology*, 2013, ISBN 978-3-942036-20-7
- 217 Lebreuz, Hans-Henning: *Addressing the Input Uncertainty for Hydrological Modeling by a New Geostatistical Method*, 2013, ISBN 978-3-942036-21-4
- 218 Darcis, Melanie Yvonne: *Coupling Models of Different Complexity for the Simulation of CO₂ Storage in Deep Saline Aquifers*, 2013, ISBN 978-3-942036-22-1
- 219 Beck, Ferdinand: *Generation of Spatially Correlated Synthetic Rainfall Time Series in High Temporal Resolution - A Data Driven Approach*, 2013, ISBN 978-3-942036-23-8
- 220 Guthke, Philipp: *Non-multi-Gaussian spatial structures: Process-driven natural genesis, manifestation, modeling approaches, and influences on dependent processes*, 2013, ISBN 978-3-942036-24-5
- 221 Walter, Lena: *Uncertainty studies and risk assessment for CO₂ storage in geological formations*, 2013, ISBN 978-3-942036-25-2
- 222 Wolff, Markus: *Multi-scale modeling of two-phase flow in porous media including capillary pressure effects*, 2013, ISBN 978-3-942036-26-9
- 223 Mosthaf, Klaus Roland: *Modeling and analysis of coupled porous-medium and free flow with application to evaporation processes*, 2014, ISBN 978-3-942036-27-6
- 224 Leube, Philipp Christoph: *Methods for Physically-Based Model Reduction in Time: Analysis, Comparison of Methods and Application*, 2013, ISBN 978-3-942036-28-3
- 225 Rodríguez Fernández, Jhan Ignacio: *High Order Interactions among environmental variables: Diagnostics and initial steps towards modeling*, 2013, ISBN 978-3-942036-29-0
- 226 Eder, Maria Magdalena: *Climate Sensitivity of a Large Lake*, 2013, ISBN 978-3-942036-30-6
- 227 Greiner, Philipp: *Alkoholinjektion zur In-situ-Sanierung von CKW Schadensherden in Grundwasserleitern: Charakterisierung der relevanten Prozesse auf unterschiedlichen Skalen*, 2014, ISBN 978-3-942036-31-3
- 228 Lauser, Andreas: *Theory and Numerical Applications of Compositional Multi-Phase Flow in Porous Media*, 2014, ISBN 978-3-942036-32-0
- 229 Enzenhöfer, Rainer: *Risk Quantification and Management in Water Production and Supply Systems*, 2014, ISBN 978-3-942036-33-7
- 230 Faigle, Benjamin: *Adaptive modelling of compositional multi-phase flow with capillary pressure*, 2014, ISBN 978-3-942036-34-4
- 231 Oladyshkin, Sergey: *Efficient modeling of environmental systems in the face of complexity and uncertainty*, 2014, ISBN 978-3-942036-35-1
- 232 Sugimoto, Takayuki: *Copula based Stochastic Analysis of Discharge Time Series*, 2014, ISBN 978-3-942036-36-8
- 233 Koch, Jonas: *Simulation, Identification and Characterization of Contaminant Source Architectures in the Subsurface*, 2014, ISBN 978-3-942036-37-5
- 234 Zhang, Jin: *Investigations on Urban River Regulation and Ecological Rehabilitation Measures, Case of Shenzhen in China*, 2014, ISBN 978-3-942036-38-2
- 235 Siebel, Rüdiger: *Experimentelle Untersuchungen zur hydrodynamischen Belastung und Standsicherheit von Deckwerken an überströmbaren Erddämmen*, 2014, ISBN 978-3-942036-39-9

- 236 Baber, Katherina: *Coupling free flow and flow in porous media in biological and technical applications: From a simple to a complex interface description*, 2014, ISBN 978-3-942036-40-5
- 237 Nuske, Klaus Philipp: *Beyond Local Equilibrium — Relaxing local equilibrium assumptions in multiphase flow in porous media*, 2014, ISBN 978-3-942036-41-2
- 238 Geiges, Andreas: *Efficient concepts for optimal experimental design in nonlinear environmental systems*, 2014, ISBN 978-3-942036-42-9
- 239 Schwenck, Nicolas: *An XFEM-Based Model for Fluid Flow in Fractured Porous Media*, 2014, ISBN 978-3-942036-43-6
- 240 Chamorro Chávez, Alejandro: *Stochastic and hydrological modelling for climate change prediction in the Lima region, Peru*, 2015, ISBN 978-3-942036-44-3
- 241 Yulizar: *Investigation of Changes in Hydro-Meteorological Time Series Using a Depth-Based Approach*, 2015, ISBN 978-3-942036-45-0
- 242 Kretschmer, Nicole: *Impacts of the existing water allocation scheme on the Limarí watershed – Chile, an integrative approach*, 2015, ISBN 978-3-942036-46-7
- 243 Kramer, Matthias: *Luftbedarf von Freistrahlturbinen im Gegendruckbetrieb*, 2015, ISBN 978-3-942036-47-4
- 244 Hommel, Johannes: *Modeling biogeochemical and mass transport processes in the subsurface: Investigation of microbially induced calcite precipitation*, 2016, ISBN 978-3-942036-48-1
- 245 Germer, Kai: *Wasserinfiltration in die ungesättigte Zone eines makroporösen Hanges und deren Einfluss auf die Hangstabilität*, 2016, ISBN 978-3-942036-49-8
- 246 Hörning, Sebastian: *Process-oriented modeling of spatial random fields using copulas*, 2016, ISBN 978-3-942036-50-4
- 247 Jambhekar, Vishal: *Numerical modeling and analysis of evaporative salinization in a coupled free-flow porous-media system*, 2016, ISBN 978-3-942036-51-1
- 248 Huang, Yingchun: *Study on the spatial and temporal transferability of conceptual hydrological models*, 2016, ISBN 978-3-942036-52-8
- 249 Kleinknecht, Simon Matthias: *Migration and retention of a heavy NAPL vapor and remediation of the unsaturated zone*, 2016, ISBN 978-3-942036-53-5
- 250 Kwakye, Stephen Oppong: *Study on the effects of climate change on the hydrology of the West African sub-region*, 2016, ISBN 978-3-942036-54-2
- 251 Kissinger, Alexander: *Basin-Scale Site Screening and Investigation of Possible Impacts of CO₂ Storage on Subsurface Hydrosystems*, 2016, ISBN 978-3-942036-55-9
- 252 Müller, Thomas: *Generation of a Realistic Temporal Structure of Synthetic Precipitation Time Series for Sewer Applications*, 2017, ISBN 978-3-942036-56-6
- 253 Grüninger, Christoph: *Numerical Coupling of Navier-Stokes and Darcy Flow for Soil-Water Evaporation*, 2017, ISBN 978-3-942036-57-3
- 254 Suroso: *Asymmetric Dependence Based Spatial Copula Models: Empirical Investigations and Consequences on Precipitation Fields*, 2017, ISBN 978-3-942036-58-0
- 255 Müller, Thomas; Mosthaf, Tobias; Gunzenhauser, Sarah; Seidel, Jochen; Bárdossy, András: *Grundlagenbericht Niederschlags-Simulator (NiedSim3)*, 2017, ISBN 978-3-942036-59-7
- 256 Mosthaf, Tobias: *New Concepts for Regionalizing Temporal Distributions of Precipitation and for its Application in Spatial Rainfall Simulation*, 2017, ISBN 978-3-942036-60-3
- 257 Fenrich, Eva Katrin: *Entwicklung eines ökologisch-ökonomischen Vernetzungsmodells für Wasserkraftanlagen und Mehrzweckspeicher*, 2018, ISBN 978-3-942036-61-0
- 258 Schmidt, Holger: *Microbial stabilization of lotic fine sediments*, 2018, ISBN 978-3-942036-62-7

- 259 Fetzer, Thomas: *Coupled Free and Porous-Medium Flow Processes Affected by Turbulence and Roughness – Models, Concepts and Analysis*, 2018, ISBN 978-3-942036-63-4
- 260 Schröder, Hans Christoph: *Large-scale High Head Pico Hydropower Potential Assessment*, 2018, ISBN 978-3-942036-64-1
- 261 Bode, Felix: *Early-Warning Monitoring Systems for Improved Drinking Water Resource Protection*, 2018, ISBN 978-3-942036-65-8
- 262 Gebler, Tobias: *Statistische Auswertung von simulierten Talsperrenüberwachungsdaten zur Identifikation von Schadensprozessen an Gewichtsstaumauern*, 2018, ISBN 978-3-942036-66-5
- 263 Harten, Matthias von: *Analyse des Zuppinger-Wasserrades – Hydraulische Optimierungen unter Berücksichtigung ökologischer Aspekte*, 2018, ISBN 978-3-942036-67-2
- 264 Yan, Jieru: *Nonlinear estimation of short time precipitation using weather radar and surface observations*, 2018, ISBN 978-3-942036-68-9
- 265 Beck, Martin: *Conceptual approaches for the analysis of coupled hydraulic and geomechanical processes*, 2019, ISBN 978-3-942036-69-6
- 266 Haas, Jannik: *Optimal planning of hydropower and energy storage technologies for fully renewable power systems*, 2019, ISBN 978-3-942036-70-2
- 267 Schneider, Martin: *Nonlinear Finite Volume Schemes for Complex Flow Processes and Challenging Grids*, 2019, ISBN 978-3-942036-71-9
- 268 Most, Sebastian Christopher: *Analysis and Simulation of Anomalous Transport in Porous Media*, 2019, ISBN 978-3-942036-72-6
- 269 Buchta, Rocco: *Entwicklung eines Ziel- und Bewertungssystems zur Schaffung nachhaltiger naturnaher Strukturen in großen sandgeprägten Flüssen des norddeutschen Tieflandes*, 2019, ISBN 978-3-942036-73-3
- 270 Thom, Moritz: *Towards a Better Understanding of the Biostabilization Mechanisms of Sediment Beds*, 2019, ISBN 978-3-942036-74-0

Die Mitteilungshefte ab der Nr. 134 (Jg. 2005) stehen als pdf-Datei über die Homepage des Instituts: www.iws.uni-stuttgart.de zur Verfügung.